On the Formulation of a Hybrid Discontinuous Galerkin Finite Element Method (DG-FEM) for Multi-layered Shell Structures

Tianyu Li

Thesis submitted to the faculty of the Virginia Polytechnic Institute and State University in partial fulfillment of the requirement for the degree of

Master of Science

In

Aerospace Engineering

Rakesh K. Kapania, Chair

Gary D. Seidel

Mayuresh Patil

September 23, 2016

Blacksburg, VA

Keywords: hybrid discontinuous Galerkin finite element method; Multi-layered and stiffened plates and shells; large deformation and strain; Dirac's delta function; Orthogonal basis function

Copyright 2016 by Tianyu Li

On the Formulation of a Hybrid Discontinuous Galerkin Finite Element Method (DG-FEM) for Multi-layered Shell Structures

Tianyu Li

Abstract

A high-order hybrid discontinuous Galerkin finite element method (DG-FEM) is developed for multi-layered curved panels having large deformation and finite strain. The kinematics of the multi-layered shells is presented at first. The Jacobian matrix and its determinant are also calculated. The weak form of the DG-FEM is next presented. In this case, the discontinuous basis functions can be employed for the displacement basis functions. The implementation details of the nonlinear FEM are next presented. Then, the Consistent Orthogonal Basis Function Space is developed. Given the boundary conditions and structure configurations, there will be a unique basis function space, such that the mass matrix is an accurate diagonal matrix. Moreover, the Consistent Orthogonal Basis Functions are very similar to mode shape functions. Based on the DG-FEM, three dedicated finite elements are developed for the multi-layered pipes, curved stiffeners and multi-layered stiffened hydrofoils. The kinematics of these three structures are presented. The smooth configuration is also obtained, which is very important for the buckling analysis with large deformation and finite strain. Finally, five problems are solved, including sandwich plates, 2-D multi-layered pipes, 3-D multi-layered pipes, stiffened plates and stiffened multi-layered hydrofoils. Material and geometric nonlinearities are both considered. The results are verified by other papers' results or ANSYS.

On the Formulation of a Hybrid Discontinuous Galerkin Finite Element Method (DG-FEM) for Multi-layered Shell Structures

Tianyu Li

General audience abstract

A novel computational method is developed for the composite structures with multiple layers and stiffeners, which possess high ratio of strength-to-weight and have wide applications in the aerospace engineering. The present method has the potential to use fewer calculations to obtain high accuracy. Five typical and important problems are solved by this method and the results are also verified by other papers or commercial software. For the first problem, the Sandwich plate problem, the water pressure is applied on the top surface and the deformation as well as stress field are both analyzed. The second problem is a two-dimensional multi-layered pipe's collapse. The critical collapse failure point is found as a function of geometrical imperfection. The third problem is the three-dimensional multi-layered pipe's unstable deformation analysis. The critical point of the unstable deformation is found and a device is also analyzed to increase the strength. For the last two problems, they are the stiffened plates and shells. In this case, we use stiffeners to increase the strength of the structure and the deformation of the stiffened plates/shells is analyzed. For the stiffened plate problem, we analyze a rectangular plate reinforced by a parabolic stiffener. For the stiffened shell problem, we analyze the airfoil/hydrofoil structure stiffened by ribs. All these problems are important for aerospace vehicles.

Acknowledgement

First of all, the author of the thesis wants to say many thanks to my advisor Dr. Kapania. Thank you so much for the support and encourage in my Masters program and your help with my research of multi-layered structures. Your words become my power to move forward in my research. Next, the author wants to say thanks to Dr. Seidel and Dr. Patil. Thank you for your time and comment on my work. Next, the author wants to say thanks to my parents and my fiancee. My interest in Mathematics and Mechanics encourage me to be a researcher. Thanks for your understanding in my career choice. I also want to say thanks to myself. Thanks for the true love and pure interest of Mathematics and Mechanics.

TABLE OF CONTENTS

Chapter 1 Introduction

Multi-layered shells have wide applications due to their high strength-to-weight ratio. In the analysis of multi-layered structures, finite element method has proven to be reliable. The nonlinear finite element material is available in [1]. In the papers [2-3], the multi-layered beam/plate development history is detailed. Static and dynamic analysis with large deformation are both included. The constitutive theory in this thesis is based on the material available in the book [4]. In [5], a multi-layered beam finite element is developed wherein the shear force effect is considered. The multi-layered plate buckling problem is solved in [6], wherein the geometrical imperfections are considered. The layerwise theory is applied to solve the multi-layered plate vibration problem in [7]. The stiffened panel buckling analysis is available in [8]. A honeycomb type structure is inserted into two multi-layered skins and the buckling analysis is presented in [9]. A multi-layered shell finite element is developed in [10]. The shell buckling problem with geometrical imperfection is described in [11]. In [12-13], the multi-layered shell element is applied to solve the thermoviscoelastic problem of multi-layered shells. An enriched in-plane displacement mode is given for laminated plate structure in [14]. In this reference method, a high-order in-plane displacement basis function is obtained. In [15-16], a multi-variable variation principle (Hellinger-Reissner(HR) variation principle) is applied for laminated plate structures and the shear force DOF is employed. A layer-wise theory is used for studying displacements in the laminated

plates in [17]. Multi-layered shell analysis with continuous shear force across the thickness direction is available in [18]. In this reference, the displacement is given such that the shear force is continuous for adjacent layers and zero on the top and bottom surface. In [19], the buckling and vibration of a multi-layered plate by using different plate theories are presented. Multi-layered plate/shell coupled with electric field is detailed in [20-22]. The multi-layered pipe element developed in this thesis is based on the author's previous work in [23]. The pipe element is also referred to [24]. The multi-layered pipe element can be used to solve many problems [25-27].

A high-order hybrid discontinuous Galerkin finite element method (DG-FEM) is developed for the stiffened multi-layered structure analysis with large deformation and finite strain. The DG-FEM developed in this thesis is very accurate for the problems in the field of multi-layered structures while using a much fewer number of DOF (degree-of-freedom) comparing with traditional FEM.

The DG-FEM is used for the multi-layered structures in this thesis because:

(1) DG-FEM can easily employ high-order modal displacement mode with much fewer number of DOFs;

(2) DG-FEM doesn't require a conforming basis function space;

(3) DG-FEM has weaker limitations of continuity in the selection of basis function space so that the optimization of basis is more feasible;

(4) DG-FEM has the DOFs of both the displacement field and the traction field (shear force, membrane force).

(5) The traction force (shear force, membrane force etc) is continuous across adjacent layers, even for large deformation plastic problems.

For the DG-FEM in this thesis, the basis function space of displacement is further studied based on orthogonal polynomial theory. An *accurate* diagonal mass matrix is obtained without any numerical approximations (such as lumped mass matrix or the artificial diagonal mass matrix by Gauss-Lobatto numerical integration). The lumped diagonal mass matrix is studied in [34]. The spectral element method with Legendre polynomials is studied in [35] with a diagonal mass matrix. The dynamical study of the Legendre spectral element is presented in [36]. In reference [37], the Legendre spectral element method is applied to analyze the composite plates. In [38], the incompressible material is studied with the Legendre spectral element. The spectral element method for composite strips is studied in [39]. The diagonal mass matrix is obtainable for all the references from [34-39] in the applications of solid mechanics. In [40], the diagonal mass matrix is even obtained for fluid mechanics. However, the uniqueness of the structure configuration and the boundary conditions are not considered in the design of the basis functions. In this thesis, given the structure and boundary conditions, there is a unique basis function space. For different structures or boundary conditions, the basis function spaces are different. The Consistent Orthogonal Basis Function Space also has the following advantages:

(1) It generates the basis functions that are quite similar to the mode shape functions without solving the eigenvalue problem for the structure;

(2) The basis function space is uniquely determined by the structure configuration and boundary conditions;

(3) The use of space leads to very high accuracy by using only a few number of DOF;

(4) A diagonal mass matrix is accurately obtained, which makes explicit dynamic analysis faster because of total decoupling of the degree-of-freedom.

It is noted that, the Consistent Orthogonal Basis Function Space not only gives a diagonal mass matrix, which is meaningful for explicit dynamical analysis, but also gives a good high-order basis function space that shows high accuracy in both static and dynamical analysis.

For the success of the above-mentioned Consistent Orthogonal Basis Function Space with an accurate diagonal mass matrix, a new kinematics of multi-layered plate/shell is formulated. The kinematics has the following advantages:

(1) The kinematics can be used to represent most complex plate/shell structures;

(2) The Jacobian matrix between material coordinates and natural coordinates and its determinant could be pre-calculated explicitly and the formulation is simple;

The DG-FEM implementation details are also presented for the completeness of the thesis. Geometric nonlinearity is considered by using the Green strain and the corresponding second Piola Kirchhoff stress in the calculation of the strain energy. The material tangent stiffness, geometric stiffness and the load tangent stiffness matrices are all derived. Both external force vector and the internal force vector are also given. The traction term is also derived.

Based on the DG-FEM, a more specific multi-layered pipe element is developed for the multi-layered pipe structures, which has the potential to be embedded into an

existent commercial FEM package's beam element framework. Since most of the beam elements available in the commercial FEM package uses Lagrangian interpolation function, in this case of multi-layered pipe element, the axial basis function is also chosen as Lagrangian interpolation function. The kinematics of the multi-layered pipe structure is derived here. For this multi-layered pipe element, the cross-section can be considered to have an arbitrary shape and it can vary along the pipe axial direction. The Consistent Orthogonal Basis Function Space is applied in displacement field in the radial and circumferential directions. The pipe structure is discretized in axial direction and the Lagrange interpolation functions are used as the basis functions to describe axial displacement. A multi-layered hydrofoil finite element is developed, which also uses Lagrangian interpolation in the hydrofoil span direction. The hydrofoil finite element is able to represent the complex hydrofoil structure using a fewer number of elements as compared to the traditional finite element method. The hydrofoil finite element is also able to solve the stiffened hydrofoils, in which the stiffener and the hydrofoil are both modeled. A curved stiffener element is also developed. The stiffener could be any curved 3-D beam in space. 3-D curved stiffener and in-plane 2-D curved stiffener are both considered. By using this stiffener element, a stiffened plate structure is analyzed.

The outline of the thesis is as follows. In Chapter 2, the nonlinear solid continuum mechanics is reviewed for completeness. The hybrid DG-FEM weak form is derived. The kinematics of the general multi-layered plate/shell is presented. The constitutive model for large-deformation problem is also given. In Chapter 3, the hybrid DG-FEM implementation details are presented. In Chapter 4, the Consistent

Orthogonal Basis Function Space is developed. The procedure of how to develop the basis functions based on structural configuration and boundary conditions is presented. Based on the general DG-FEM theory developed from Chapter 2 to Chapter 4, the multi-layered pipe element, the stiffener element and the multi-layered hydrofoil element are developed in Chapter 5. In Chapter 6, the numerical tests are presented. All the codes are developed in Matlab environment and the results are verified with results obtained using ANSYS. In Chapter 7, key conclusion is given: the DG-FEM developed in the thesis is very accurate for the multi-layered structures and it uses a much fewer number of DOF as compared to the traditional finite element method.

Chapter 2 DG-FEM for multi-layered structures

In this Chapter, the basic equations for solid mechanics and the continuum mechanics are briefly reviewed. Large deformations and finite strain components are considered. The Green strain and second Piola-Kirchhoff stress are used for strain energy. The Jaumann stress and the objective linear strain rate are used for constitutive equations. The relation between Jaumann stress and Piola-Kirchhoff stress are set up. The weak form of DG-FEM is derived. The kinematics of multi-layered plate/shell structures with multiple layers are discussed. The constitutive theory is also reviewed.

2.1 Large deformation continua mechanics

In this thesis, the Einstein's notation is used, where the repeated index is assumed to sum up from 1 to 3. The set of governing equations describing the motion of a solid is given as:

$$\rho \ddot{u}_i = b_i + \sigma_{ij,j} \quad \text{in} \quad \Omega_t$$

$$u_i = \overline{u}_i \quad \text{on} \quad \Gamma_t^u \qquad \text{(1a, b, c)}$$

$$n_j \sigma_{ij} = \overline{T}_i \quad \text{on} \quad \Gamma_t^\sigma$$

where u_i is the displacement tensor, b_i is the body force tensor, σ_{ij} is the Cauchy stress tensor, ρ is density, $\overline{u}_i$ is the given displacement boundary condition tensor, $\overline{T}_i$ is the traction force tensor, n_j is the outward normal vector tensor, Ω_t is the

reference configuration space at time t, Γ_t^u and Γ_t^σ are displacement boundary and traction boundary, respectively.

For a dynamical problem, the initial condition must also be given:

$$u_i = \overline{u}_{i0}$$
$$\frac{\partial u_i}{\partial t} = \frac{\partial \overline{u}_{i0}}{\partial t} \quad \text{in } \Omega_t, \text{for } t = 0 \qquad \text{(2a, b)}$$

In a small deformation analysis, the Cauchy stress can be approximated as the engineering stress. However, in a large deformation and finite strain analysis, the Cauchy stress tensor based on the current configuration must be distinguished from the engineering stress. However, for the nonlinear continua mechanics, the Cauchy stress tensor based on unknown configuration can't be used for analysis because the current configuration is unknown and needs to be determined. Instead, the second Piola Kirchhoff stress tensor and corresponding Green strain tensor based on the reference configuration are used to represent the state of stress and strain, respectively.

The essentials of non-linear continuum mechanics is reviewed in the rest of this section.

The deformation from time 0 to time t can be denoted as:

$$^t x_i = {}^t x_i ({}^0 x_1, {}^0 x_2, {}^0 x_3), \quad i = 1,2,3 \qquad (3)$$

This is a mapping from the initial configuration $^0 x_i, i = 1,2,3$ to the current configuration $^t x_i, i = 1,2,3$.

The inverse mapping is also existent and is unique:

$$^0 x_i = {}^0 x_i ({}^t x_1, {}^t x_2, {}^t x_3), i = 1,2,3 \qquad (4)$$

In this case, by using the derivative chain rule:

$$d^t x_i = \frac{\partial^t x_i}{\partial^0 x_j} d^0 x_j$$
$$d^0 x_i = \frac{\partial^0 x_i}{\partial^t x_j} d^t x_j \qquad \text{(5a, b)}$$

For any two points in the initial configuration, the distance between them is:

$$\left({}^0 ds\right)^2 = d^0 x_i \, d^0 x_i = \left(\frac{\partial^0 x_i}{\partial^t x_m} d^t x_m\right)\left(\frac{\partial^0 x_i}{\partial^t x_n} d^t x_n\right) = \frac{\partial^0 x_i}{\partial^t x_m}\frac{\partial^0 x_i}{\partial^t x_n} d^t x_m d^t x_n \qquad \text{(6a)}$$

For any two points in the current configuration, the distance between them is:

$$\left({}^t ds\right)^2 = d^t x_i \, d^t x_i = \left(\frac{\partial^t x_i}{\partial^0 x_m} d^0 x_m\right)\left(\frac{\partial^t x_i}{\partial^0 x_n} d^0 x_n\right) = \frac{\partial^t x_i}{\partial^0 x_m}\frac{\partial^t x_i}{\partial^0 x_n} d^0 x_m d^0 x_n \qquad \text{(6b)}$$

Thus, the change of the length can be formulated as:

$$\left({}^t ds\right)^2 - \left({}^0 ds\right)^2 = \left(\frac{\partial^t x_i}{\partial^0 x_m}\frac{\partial^t x_i}{\partial^0 x_n} - \delta_{mn}\right) d^0 x_m d^0 x_n \qquad \text{(7a)}$$

or

$$\left({}^t ds\right)^2 - \left({}^0 ds\right)^2 = \left(\delta_{mn} - \frac{\partial^0 x_i}{\partial^t x_m}\frac{\partial^0 x_i}{\partial^t x_n}\right) d^t x_m d^t x_n \qquad \text{(7b)}$$

Thus, we define the Green strain tensor and Almansi strain tensor as:

$${}^t_0\varepsilon_{ij} = \frac{1}{2}\left(\frac{\partial^t x_k}{\partial^0 x_i}\frac{\partial^t x_k}{\partial^0 x_j} - \delta_{ij}\right) \qquad \text{(8a)}$$

$${}^0_t\varepsilon^A_{ij} = \frac{1}{2}\left(\delta_{ij} - \frac{\partial^0 x_k}{\partial^t x_i}\frac{\partial^0 x_k}{\partial^t x_j}\right) \qquad \text{(8b)}$$

The total displacement tensor is:

$${}^t u_i = {}^t x_i - {}^0 x_i \qquad \text{(9)}$$

where the left-top corner t is for the time of the displacement, the right-bottom index is for displacement dimension.

Thus, material derivatives are calculated as:

$$ {}^{t}_{0}x_{i,j} = {}^{t}_{0}u_{i,j} + {}^{0}_{0}x_{i,j} = {}^{t}_{0}u_{i,j} + \delta_{ij} \tag{10a} $$

$$ {}^{0}_{t}x_{i,j} = -{}^{t}_{t}u_{i,j} + {}^{t}_{t}x_{i,j} = -{}^{t}_{t}u_{i,j} + \delta_{ij} \tag{10b} $$

where the left-bottom corner t is for the time of the configuration, based on which the derivatives are calculated.

In this case, we can reformulate the two strain tensors based on displacement as:

$$ {}^{t}_{0}\varepsilon_{ij} = \frac{1}{2}\left(\frac{\partial^{t}x_{k}}{\partial^{0}x_{i}} \frac{\partial^{t}x_{k}}{\partial^{0}x_{j}} - \delta_{ij} \right) = \frac{1}{2}\left({}^{t}_{0}u_{i,j} + {}^{t}_{0}u_{j,i} + \left({}^{t}_{0}u_{k,i} \right)\left({}^{t}_{0}u_{k,j} \right) \right) \tag{11a} $$

$$ {}^{0}_{t}\varepsilon^{A}_{ij} = \frac{1}{2}\left(\delta_{ij} - \frac{\partial^{0}x_{k}}{\partial^{t}x_{i}} \frac{\partial^{0}x_{k}}{\partial^{t}x_{j}} \right) = \frac{1}{2}\left({}^{0}_{t}u_{i,j} + {}^{0}_{t}u_{j,i} - \left({}^{0}_{t}u_{k,i} \right)\left({}^{0}_{t}u_{k,j} \right) \right) \tag{11b} $$

The second Piola Kirchhoff stress tensor is defined as:

$$ {}^{t}_{0}S_{ij} = \frac{{}^{0}\rho}{{}^{t}\rho}\left({}^{0}_{t}x_{i,m} \right)\left({}^{0}_{t}x_{j,n} \right)\left({}^{t}\sigma_{mn} \right) \tag{12} $$

where ${}^{t}\rho, {}^{0}\rho$ are the density for the time $t, 0$.

The second Piola Kirchhoff stress tensor is the conjugate with the Green strain tensor when obtaining the expression for virtual work. Moreover, the second Piola Kirchhoff stress and its corresponding Green strain are based on the known reference configuration. Thus, the strain energy is calculated by the second Piola Kirchhoff stress and Green strain, instead of Cauchy stress and Euler strain. However, a more accurate constitutive model is based on the Jaumann stress tensor and linear strain rate tensor:

$$ {}^{t}\dot{\sigma}_{ij}^{J} = D_{ijkl}^{J}\left({}^{t}\dot{e}_{kl}\right) \tag{13} $$

$$ {}^{t}\dot{\sigma}_{ij}^{J} = {}^{t}\dot{\sigma}_{ij} - {}^{t}\sigma_{ip}\left({}^{t}\Omega_{pj}\right) - {}^{t}\sigma_{jp}\left({}^{t}\Omega_{pi}\right) \tag{14} $$

where

$$ {}^{t}\dot{e}_{ij} = \frac{1}{2}\left({}^{t}\dot{u}_{i,j} + {}^{t}\dot{u}_{j,i}\right) \tag{15a} $$

$$ {}^{t}\Omega_{ij} = \frac{1}{2}\left({}_{t}^{t}\dot{u}_{j,i} - {}_{t}^{t}\dot{u}_{i,j}\right) \tag{15b} $$

Since the virtual work is derived based on second Kirchhoff stress tensor and Green strain tensor while the constitutive model is based on Jaumann stress tensor and linear strain rate tensor, it is necessary to relate the second Kirchhoff stress tensor with the Jaumann stress tensor [1]:

$$ {}_{t}S_{sl}^{k} = \sigma_{sl}^{k} - {}^{t}\sigma_{sp}^{k}({}_{t}u_{l,p}^{k}) - {}^{t}\sigma_{lp}^{k}({}_{t}u_{s,p}^{k}) \tag{16} $$

2.2 Weak form of the Hybrid Discontinuous Galerkin Finite Element Method (DG-FEM)

In this section, the weak form of DG-FEM is derived. The PDE (1) is multiplied with a trial function $\delta u_i = \delta\tilde{u}^T w_i^T$, and integrated over the reference domain to obtain the weak form as below:

$$ \delta\tilde{u}^T\left\langle w_i^T, \rho\ddot{u}_i\right\rangle_{\Omega_t} - \delta\tilde{u}^T\left\langle w_i^T, b_i\right\rangle_{\Omega_t} - \delta\tilde{u}^T\left\langle w_i^T, \sigma_{ij,j}\right\rangle_{\Omega_t} = 0 \tag{17a} $$

where

$$ \left\langle w, v\right\rangle_{\Omega_t} = \int_{\Omega_t} wv d\Omega\,. \tag{17b} $$

The divergence theorem is applied for the last term of (17a), thus:

$$\delta\tilde{u}^T\left\langle w_i^T,\rho\ddot{u}_i\right\rangle_{\Omega_t}-\delta\tilde{u}^T\left\langle w_i^T,b_i\right\rangle_{\Omega_t}+\left\langle\delta^{t+dt}e_{ij},{}^{t+dt}\sigma_{ij}\right\rangle_{\Omega_t}-\left\langle\delta u_i,\overline{T}_i\right\rangle_{\Gamma_t^\sigma}=0$$
$$\overline{T}_i=n_j\sigma_{ij} \qquad \text{(18a, b)}$$

With the mass conservation law, we have

$$\delta\tilde{u}^T\left\langle w_i^T,\rho\ddot{u}_i\right\rangle_{\Omega_t}=\delta\tilde{u}^T\left\langle w_i^T,\rho_0\ddot{u}_i\right\rangle_{\Omega_0},\forall t \qquad (19)$$

In this thesis, the large deformation and finite strain are considered. Thus, the Green strain tensor ${}_t^{t+dt}\varepsilon_{ij}$ and the corresponding second Piola Kirchhoff stress tensor ${}_t^{t+dt}S_{ij}$ are used. Then, (18a) becomes:

$$\delta\tilde{u}^T\left\langle w_i^T,\rho_0\ddot{u}_i\right\rangle_{\Omega_0}+\left\langle\delta_t^{t+dt}\varepsilon_{ij},{}_t^{t+dt}S_{ij}\right\rangle_{\Omega_t}-\delta\tilde{u}^T\left\langle w_i^T,b_i\right\rangle_{\Omega_t}-\left\langle\delta u_i,\overline{T}_i\right\rangle_{\Gamma_t^\sigma}=0 \qquad (20)$$

where ${}_t^{t+dt}\varepsilon_{ij}$ and ${}_t^{t+dt}S_{ij}$ are the Green strain tensor and the second Piola Kirchhoff stress tensor at Ω_{t+dt} with reference to Ω_t.

In the above equation, we have used the relation that $\delta_t^{t+dt}\varepsilon_{ij}S_{ij}=\delta^{t+dt}e_{ij}\sigma_{ij}$ [1].

Assume the multi-layered plate/shell structure has n_l layers. The top surface and bottom surface are denoted as $\Gamma_{t,k}^{\pm}$, $k=1,2,3,\cdots,n_l$. We also define $\Gamma_{t,k}^i$ as the interface between the k th layer and the $k+1$ th layer. Thus, we have $\Gamma_{t,k}^i=\Gamma_{t,k}^+=\Gamma_{t,k+1}^-$. The space at time $t+dt$ for the k th layer is denoted as $\Omega_{t,k}$, as Figure 1a shows.

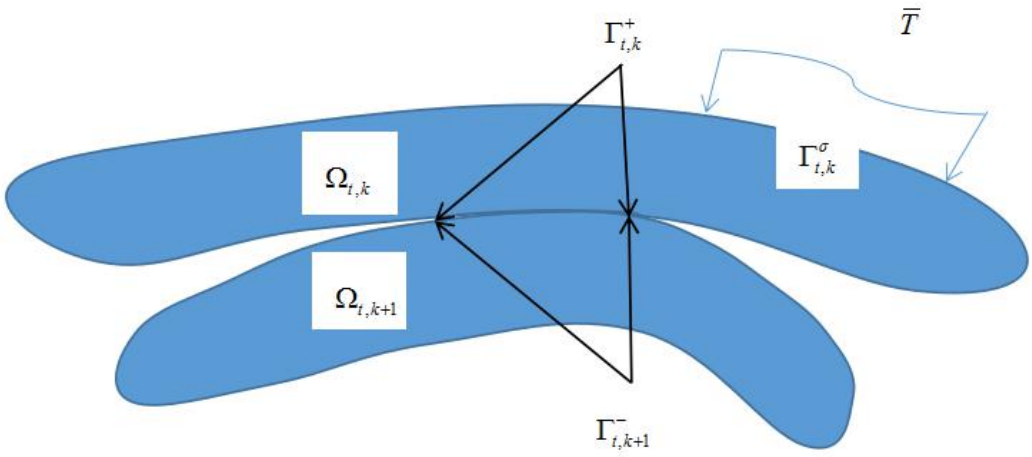

Figure 1a The notations of multi-layered shell structure

With these notations, for the k th layer, the weak form will be:

$$\delta\tilde{u}^{kT}\left\langle w_i^{kT}, \rho_0^k \ddot{u}_i^k \right\rangle_{\Omega_{0,k}} + \left\langle \delta_t^{t+dt}\varepsilon_{ij}^k, {}_t^{t+dt}S_{ij}^k \right\rangle_{\Omega_{t,k}} - \delta\tilde{u}^{kT}\left\langle w_i^{kT}, b_i^k \right\rangle_{\Omega_{t,k}} - \left\langle \delta u_i^k, \bar{T}_i^k \right\rangle_{\Gamma^{\sigma}_{t,k}} - \left\langle \delta u_i^k, T_i^k \right\rangle_{\Gamma^{\pm}_{t,k}} = 0 \tag{21}$$

For the hybrid DG-FEM method, the traction force T_i defined on the interior boundaries are also introduced as the variable to be interpolated and thus determined independently. In the DG-FEM, the traction force is also primary variable to be determined. This is different from traditional finite element, in which the stress is obtained from constitutive theory. The advantage of the DG-FEM is that the traction is continuous at the interfaces, even for large deformation and strain analysis. For the traditional finite element method, the stress obtained from constitutive theory is not continuous at the interfaces.

Thus, the weak form becomes:

$$\sum_{k=1}^{n_l}\delta\tilde{u}^{kT}\left\langle w_i^{kT},\rho_0^k\ddot{u}_i^k\right\rangle_{\Omega_{0,k}}+\sum_{k=1}^{n_l}\left\langle\delta_t^{t+dt}\varepsilon_{ij}^{k},_t^{t+dt}S_{ij}^k\right\rangle_{\Omega_{t,k}}-\sum_{k=1}^{n_l}\delta\tilde{u}^{kT}\left\langle w_i^{kT},b_i^k\right\rangle_{\Omega_{t,k}}$$
$$-\sum_{k=1}^{n_l}\left\langle\delta u_i^k,\overline{T}_i^k\right\rangle_{\Gamma_{t,k}^{\sigma}}-\sum_{k=1}^{n_l}\left\langle\delta u_i^k,T_i^k\right\rangle_{\Gamma_{t,k}^{\pm}}-\sum_{k=1}^{n_l}\left\langle\delta T_i^k,u_i^k\right\rangle_{\Gamma_{t,k}^{\pm}}=0 \tag{22}$$

Based on the idea of DG and hybrid FEM, the following weak form is adopted in this paper after some re-arrangement from (22):

$$\sum_{k=1}^{n_l}\delta\tilde{u}^{T}\left\langle w_i^{T},\rho_0\ddot{u}_i\right\rangle_{\Omega_{0,k}}+\sum_{k=1}^{n_l}\left\langle\delta_t^{t+dt}\varepsilon_{ij},_t^{t+dt}S_{ij}\right\rangle_{\Omega_{t,k}}-\sum_{k=1}^{n_l}\delta\tilde{u}^{T}\left\langle w_i^{T},b_i\right\rangle_{\Omega_{t,k}}$$
$$-\sum_{k=1}^{n_l}\left\langle\delta u_i,\overline{T}_i\right\rangle_{\Gamma_{t,k}^{\sigma}}-\sum_{k=1}^{n_l-1}\left\langle\delta u_i^{k+\frac{1}{2}},T_i^k-T_i^{k+1}\right\rangle_{\Gamma_{t,k}^{i}}-\sum_{k=1}^{n_l-1}\left\langle\delta T_i^{k+\frac{1}{2}},u_i^k-u_i^{k+1}\right\rangle_{\Gamma_{t,k}^{i}}=0 \tag{23}$$

where

$$\delta u_i^{k+\frac{1}{2}}=\frac{1}{2}\left(\delta u_i^k+\delta u_i^{k+1}\right)$$
$$\delta T_i^{k+\frac{1}{2}}=\frac{1}{2}\left(\delta T_i^k+\delta T_i^{k+1}\right) \tag{24a, b}$$

For the last term $\left\langle\delta T_i^{k+\frac{1}{2}},u_i^k-u_i^{k+1}\right\rangle_{\Gamma_{t,k}^{i}}$ in (23), it could also be understood as the penalty term to reinforce the displacement continuity condition $u_i^k-u_i^{k+1},k=1,2,3,\cdots,n_l-1$ at interfaces. The weight of the penalty term is the variation of the traction, which is consistent in the sense of energy variation. For the term $\left\langle\delta u_i^{k+\frac{1}{2}},T_i^k-T_i^{k+1}\right\rangle_{\Gamma_{t,k}^{i}}$, the traction force is also forced to be continuous. It is also possible to satisfy the traction continuity condition in the strong sense. In this case, this term will vanish and the traction field is only defined on the interfaces.

2.3 Kinematics of multi-layered plate/shell

In this section, the kinematics of multi-layered plate/shell structures is discussed. The well-known kinematics of multi-layered plate/shell structures is first reviewed in section 2.3.1. In section 2.3.2, a different kinematics for single-curvature dominated shell is presented. For the so-called single-curvature dominated shell, the curvature of one dimension is much smaller than the other, such as pipe structures or ship hull structures etc. In section 2.3.3, another kinematics for doubly-curvature dominating shell is presented. In this case, the curvatures of the two dimensions are comparable. In section 2.3.4, the kinematics for the plate structure is discussed.

2.3.1 Traditional kinematics for plate/shell

In this part, the well-known kinematics for multi-layered shell structure is reviewed. A local coordinate system is given, in which one axis is normal to the reference surface and the other two axes are tangent with the reference surface. The reference surface mapping is based on NURBS, in which a high-order smooth function is used to set up the mapping from natural coordinate system to the material coordinate system. In this well-known kinematics for multi-layered plate/shell, the normal vector of the reference surface has to be calculated and updated because the reference configuration is the deformed structure configuration in the previous load step.

The change in the normal vector is significant, especially for those large-deformation problems that are focused in this thesis.

The local coordinate system is defined in the Figure 1b.

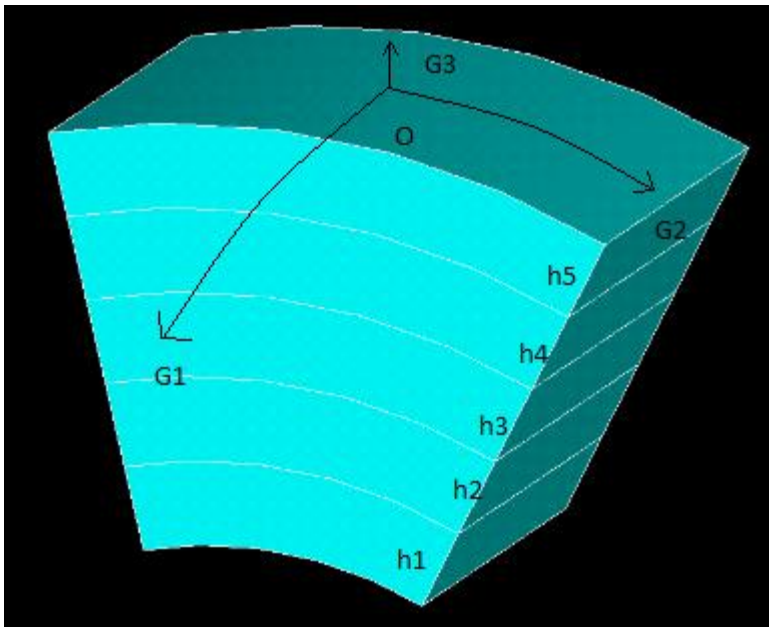

Figure 1b Laminated Shell Configuration and Notations

The first step is to develop the natural coordinate system for the reference surface. The natural coordinate system is also called parameterization coordinates, which belong to the interval $[-1,1]$ or $[0,1]$. There are many numerical tools to map a complex structure to a regular natural coordinate system. For the traditional FEM, we can use high order Lagrange interpolation to model the mid surface of the shell. Recently, the isogeometrical analysis has been developed [41] and a more accurate and smooth description of complex structures is possible.

For the k th layer shell, the initial mid-surface can be formulated as:

$$ {}^{0}X_i^k = \sum_{m=1}\sum_{n=1} \Psi_{m,n}\left(\xi_1,\xi_2\right) B_{i,m,n} \tag{25} $$

where ${}^{0}X_i^k$ is the initial mid surface coordinates for the k th layer, $\Psi_{m,n}\left(\xi_1,\xi_2\right)$ are the basis functions to describe the configuration, $B_{i,m,n}$ are parameters to control the contribution of $\Psi_{m,n}\left(\xi_1,\xi_2\right)$ to ${}^{0}X_i^k$.

For the case of higher order Lagrange interpolation,

$$\Psi_{m,n}(\xi_1,\xi_2)=N_L^m(\xi_1)N_L^n(\xi_2) \tag{26}$$

where $N_L^i(\xi)$ is the Lagrange interpolation function for the i th node:

$$N_L^i(\xi^j)=\delta_{ij} \tag{27}$$

In this case, B^{mn} is the node (m,n) coordinates.

For the case of IGA, the NURBS are used to describe the configuration of structures.

A knot vector is defined as:

$$\Xi=\left[\bar{\xi}_1 \quad \bar{\xi}_2 \quad \cdots \quad \bar{\xi}_{n+p+1}\right] \tag{28}$$

where n is the number of NURBS basis functions and p is the order of NURBS functions.

The NURBS function is defined as:

$$N_{i,0}(\xi)=1 \qquad \text{if } \xi\in[\bar{\xi}_i,\bar{\xi}_{i+1})$$

$$N_{i,0}(\xi)=0 \qquad \text{if } \xi\notin[\bar{\xi}_i,\bar{\xi}_{i+1}) \tag{29a, b, c}$$

$$N_{i,p}(\xi)=\frac{\xi-\bar{\xi}_i}{\bar{\xi}_{i+p}-\bar{\xi}_i}N_{i,p-1}(\xi)+\frac{\bar{\xi}_{i+p+1}-\xi}{\bar{\xi}_{i+p+1}-\bar{\xi}_{i+1}}N_{i+1,p-1}(\xi)$$

The derivative of NURBS is:

$$\frac{dN_{i,p}(\xi)}{d\xi}=\frac{p}{\bar{\xi}_{i+p}-\bar{\xi}_i}N_{i,p-1}(\xi)-\frac{p}{\bar{\xi}_{i+p+1}-\bar{\xi}_{i+1}}N_{i+1,p-1}(\xi) \tag{30}$$

If the knot vector is equally spaced,

$$N_{i,p}(\xi)=\frac{\xi-\bar{\xi}_i}{p\Delta\bar{\xi}}N_{i,p-1}(\xi)+\frac{\bar{\xi}_{i+p+1}-\xi}{p\Delta\bar{\xi}}N_{i+1,p-1}(\xi) \tag{31}$$

$$\frac{dN_{i,p}(\xi)}{d\xi}=\frac{1}{\Delta\overline{\xi}}\left(N_{i,p-1}(\xi)-N_{i+1,p-1}(\xi)\right) \tag{32}$$

where

$$\Delta\overline{\xi}=\overline{\xi}_2-\overline{\xi}_1=\overline{\xi}_3-\overline{\xi}_2=\cdots=\overline{\xi}_{n+p+1}-\overline{\xi}_{n+p} \tag{33}$$

A more general case is applied for the multi- dimensional case. A tensor product is applied.

$$R^{p_1,p_2}_{i_1,i_2}(\xi_1,\xi_2)=\frac{\omega_{i_1,i_2}N^1_{i_1,p_1}(\xi_1)N^2_{i_2,p_2}(\xi_2)}{\sum_{i_1=1}\sum_{i_2=1}\omega_{i_1,i_2}N^1_{i_1,p_1}(\xi_1)N^2_{i_2,p_2}(\xi_2)} \tag{34}$$

where ω_{i_1,i_2} is weight.

In this case, the mid surface can be formulated as:

$$^0X^k_i=\sum_{m=1}\sum_{n=1}\Psi_{i_1,i_2}(\xi_1,\xi_2)B_{i,i_1,i_2}=\sum_{i_1=1}\sum_{i_2=1}\left(R_{i_1,i_2}\right)\left(^0B^k_{i,i_1,i_2}\right) \tag{35a, b}$$

$$\Psi_{i_1,i_2}=R_{i_1,i_2}$$

where $^0B^k_{i,i_1,i_2}$ is the control point i th component for the k th layer corresponding with R_{i_1,i_2}.

Using NURBS, we have successfully set up the configuration of mid surface. We can always find a mapping from a regular natural coordinates $(\xi_1,\xi_2),\xi_{1,2}\in[-1,1]$ to $^0X^k_i$.

When the mapping of the shell reference surface is set up, we can get the local coordinate system.

On the mid surface of the k th layer, a local coordinate system is defined:

$$G^k_i=\frac{\partial^0X^k}{\partial\xi_i},i=1,2 \tag{36}$$

where ${}^0X^k = \left[{}^0X_1^k \quad {}^0X_2^k \quad {}^0X_3^k \right]^T$

and

$$G_3^k = \frac{G_1^k \times G_2^k}{\left| G_1^k \times G_2^k \right|} \tag{37}$$

Thus, the configuration of the k th layer is:

$${}^0x^k = {}^0X^k + \frac{h_k}{2} G_3^k \xi_3 \quad \xi_3 \in [-1,1] \tag{38}$$

In the programming, we need to calculate the derivatives of ${}^0x_i^k$ with respect to natural coordinates (ξ_1, ξ_2, ξ_3). Thus:

$$\frac{\partial {}^0x^k}{\partial \xi_3} = \frac{h_k}{2} G_3^k \tag{39}$$

$$\frac{\partial {}^0x^k}{\partial \xi_\alpha} = \frac{\partial {}^0X^k}{\partial \xi_\alpha} + \xi_3 \frac{h_k}{2} \frac{\partial G_3^k}{\partial \xi_\alpha} \qquad a = 1,2 \tag{40}$$

The calculation of $\frac{\partial G_3^k}{\partial \xi_\alpha}$, $\alpha = 1,2$ is a little complex. Instead, we can calculate it in this way:

First of all, we can use the same function Ψ_{i_1,i_2} in ${}^0X_i^k$ to define the G_3^k.

$$G_3^k = \sum_{i_1=1} \sum_{i_2=1} \left(\Psi_{i_1,i_2}(\xi_1, \xi_2) \right) \left({}^0B_{i_1,i_2}^{k,G} \right) \tag{41a, b}$$
$$\Psi_{i_1,i_2} = R_{i_1,i_2}$$

where $\left({}^0B_{i_1,i_2}^{k,G} \right)$ is G_3^k calculated at the control point (i_1, i_2) by using $G_3^k = \frac{G_1^k \times G_2^k}{\left| G_1^k \times G_2^k \right|}$

In this case, we can have:

$$
\begin{aligned}
{}^0x_i^k &= {}^0X^k + \frac{h_k}{2} G_3^k \xi_3 \\
&= \sum_{i_1=1}\sum_{i_2=1} \Psi_{i_1,i_2}(\xi_1,\xi_2)\left({}^0B^k_{i_1,i_2} + {}^0B^{k,G}_{i_1,i_2}\xi_3 \frac{h_k}{2} \right)
\end{aligned}
\tag{42}
$$

Then, the local coordinate system is defined as:

$$
g_i^k = \frac{\partial^0 x^k}{\partial \xi_i} = \frac{\partial^0 X_i^k}{\partial \xi_i} + \xi_3 \frac{h_k}{2} \frac{\partial G_3^k}{\partial \xi_i}, i = 1,2 \tag{43a}
$$

$$
g_3^k = \frac{g_1^k \times g_2^k}{\left| g_1^k \times g_2^k \right|} \tag{43b}
$$

where $g_{1,2}$ and g_3 are the local tangential and local normal vectors for the surface $\xi_3 \neq 0$.

In this local coordinate system, g_3^k is normal to the reference surface (mid-surface) and $g_i^k, i = 1,2$ are tangential to the reference surface.

The displacement basis function spaces are given below:

$$
V_\phi^k = \{\phi_{u_i}^{m_0} \mid \phi_{u_i}^m(\xi_1) \in P^m(\xi_1), \xi_1 \in [0,1], m = 1,2,3,\cdots,m_0\}
$$

$$
V_\psi^k = \{\psi_{u_i}^{n_0} \mid \psi_{u_i}^n(\xi_2) \in P^n(\xi_2), \xi_2 \in [0,1], n = 1,2,3,\cdots,n_0\}
$$

$$
V_\varphi^k = \{\varphi_{u_i}^{s_0} \mid \varphi_{u_i}^s(\xi_3) \in P^s(\xi_3), \xi_3 \in [0,1], s = 1,2,3,\cdots,s_0\}
$$

where $P^\alpha(\xi)$ is the polynomial function space, in which the highest order of the polynomial function is α.

Then, the displacement field is given as:

$$u_1^k = f_{u_1}^{\xi_1} f_{u_1}^{\xi_2} f_{u_1}^{\xi_3} \sum_{m,n,s=1}^{m_0,n_0,s_0} A_{mns}^k \phi_{u_1}^m(\xi_1)\psi_{u_1}^n(\xi_2)\varphi_{u_1}^s(\xi_3)$$

$$u_2^k = f_{u_2}^{\xi_1} f_{u_2}^{\xi_2} f_{u_2}^{\xi_3} \sum_{m,n,s=1}^{m_0,n_0,s_0} B_{mns}^k \phi_{u_2}^m(\xi_1)\psi_{u_2}^n(\xi_2)\varphi_{u_2}^s(\xi_3) \tag{44}$$

$$u_3^k = f_{u_3}^{\xi_1} f_{u_3}^{\xi_2} f_{u_3}^{\xi_3} \sum_{m,n,s=1}^{m_0,n_0,s_0} C_{mns}^k \phi_{u_3}^m(\xi_1)\psi_{u_3}^n(\xi_2)\varphi_{u_3}^s(\xi_3)$$

where $\phi_{u_i}^m(\xi_1), \psi_{u_i}^n(\xi_2), \varphi_{u_i}^s(\xi_3)$ are the basis functions described in terms of natural coordinates ξ_1, ξ_2, ξ_3 for u_i, $A_{mns}, B_{mns}, C_{mns}$ are the degree-of-freedom, m, n, k are the number of basis functions, m_0, n_0, s_0 are the total order of the basis functions for u_1, u_2 and u_3 components of displacement, respectively. $f_{u_i}^{\xi_j}, (i = 1,2,3,\ j = 1,2,3)$ is the displacement boundary condition function, which is used to define displacement boundary conditions for $u_i, (i = 1,2,3)$ about the coordinate $\xi_j, (j = 1,2,3)$.

Thus, the current configuration will be:

$${}^t x_i^k = {}^0 x_i^k + {}^t u_i^k \tag{45}$$

Then, the Jacobian matrix will be:

$$J^k = \left[J_{ij}^k\right]$$

$$J_{ij}^k = \frac{\partial^t x_i^k}{\partial \xi_i} = \frac{\partial^0 x_i^k}{\partial \xi_i} + \frac{\partial^t u_j^k}{\partial \xi_i} \tag{46a, b}$$

Then we can calculate the material derivatives by the chain rule:

$$\frac{\partial}{\partial \xi_i} = \frac{\partial}{\partial^t x_r^k} \frac{\partial^t x_r^k}{\partial \xi_i} \tag{47}$$

In the FEM code, the material derivatives are calculated as:

$$\begin{bmatrix} \frac{\partial \Phi}{\partial \xi_1} \\ \frac{\partial \Phi}{\partial \xi_2} \\ \frac{\partial \Phi}{\partial \xi_3} \end{bmatrix} = \left[J_{ij}^k \right] \begin{bmatrix} \frac{\partial \Phi}{\partial^t x_1^k} \\ \frac{\partial \Phi}{\partial^t x_2^k} \\ \frac{\partial \Phi}{\partial^t x_3^k} \end{bmatrix}$$

$$\begin{bmatrix} \frac{\partial \Phi}{\partial^t x_1^k} \\ \frac{\partial \Phi}{\partial^t x_2^k} \\ \frac{\partial \Phi}{\partial^t x_3^k} \end{bmatrix} = \left[J_{ij}^k \right]^{-1} \begin{bmatrix} \frac{\partial \Phi}{\partial \xi_1} \\ \frac{\partial \Phi}{\partial \xi_2} \\ \frac{\partial \Phi}{\partial \xi_3} \end{bmatrix} \tag{48a, b}$$

where Φ is any entity.

In this case, the normal vector at current time t will be:

$${}^t g_i^k = \frac{\partial^t x^k}{\partial \xi_i} = \frac{\partial^0 X^k}{\partial \xi_i} + \xi_3 \frac{h_k}{2} \frac{\partial G_3^k}{\partial \xi_i} + \frac{\partial^t u^k}{\partial \xi_i}, i = 1,2 \tag{49a}$$

$${}^t g_3^k = \frac{{}^t g_1^k \times {}^t g_2^k}{\left| {}^t g_1^k \times {}^t g_2^k \right|} \tag{49b}$$

The traction defined on the top/bottom surface are given as:

$$\begin{aligned} T_1^k &= \sum_{m,n=1}^{m_0,n_0} a_{mn}^k \phi_{T_1}^m (\xi_1) \psi_{T_1}^n (\xi_2) \\ T_2^k &= \sum_{m,n=1}^{m_0,n_0} b_{mn}^k \phi_{T_2}^m (\xi_1) \psi_{T_2}^n (\xi_2) \\ T_3^k &= \sum_{m,n=1}^{m_0,n_0} c_{mn}^k \phi_{T_3}^m (\xi_1) \psi_{T_3}^n (\xi_2) \end{aligned} \tag{50}$$

It is noted that traction force is only a function about $\xi_{1,2}$ and it is only defined on the interface.

2.3.2 Single-curvature dominating plate/shell kinematics

In this section, a new kinematics for shells with a dominating curvature in one dimension is presented. The so-called single-curvature dominating shell means that the structure has a much larger curvature in one dimension than the other one dimension, like pipe structures or ship hull etc.

The natural coordinates ξ_1, ξ_2, ξ_3 are defined as below.

$$\xi_1 = \frac{z}{L} \in [0,1]$$
$$\xi_2 = \frac{2\theta}{\pi} \in [0,1] \qquad \text{(51a, b, c)}$$
$$\xi_3 = \frac{\rho - R}{t_w} \in [0,1]$$

where ρ, θ, z are the polar coordinates, z is the direction that the shell has a much smaller curvature; L is the total characteristic length of the structure in the z direction; O' is the point on the z axis, as the Figure 2 below. This Figure represents the shell cross-section that $z = z_0$ (z_0 is a constant).

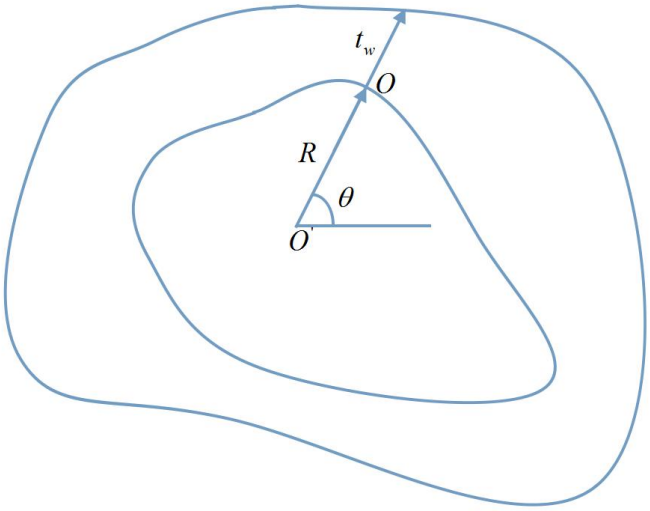

Figure 2 Single curvature shell cross-section

Assume there is a radial line orienting from O' that makes an angle of θ with the horizontal direction. The radial line will intersect with the inner surface of the shell at O. The function R is defined as the distance between the inner surface point O and the z axis' point O'. The radial line will also intersect with the outer surface of the shell. The distance between the outer surface point and the point O' is defined as the wall thickness function t_w. It is noted that t_w and R could be the functions of axial distance (z) and circumferential coordinate (θ). Thus, from (56a, b), it is obvious that t_w and R are functions of ξ_1, ξ_2, $t_w = t_w(\xi_1, \xi_2)$ and $R = R(\xi_1, \xi_2)$.

It is also noted that the z coordinate could be placed anywhere, as long as it is inside the shell and the shell could be seen from the point O'.

If the wall-thickness t_w and the radius vector R are constants, which is the case of a common pipe, the pipe configuration can be described as:

$$r^0 = \begin{bmatrix} x_1^0 \\ x_2^0 \\ x_3^0 \end{bmatrix} = \begin{bmatrix} L\xi_1 \\ (R + t_w\xi_3)\cos(2\pi\xi_2) \\ (R + t_w\xi_3)\sin(2\pi\xi_2) \end{bmatrix} \tag{52}$$

J_0 is denoted as the initial configuration's Jacobian matrix. So from the configuration r^0 in (52), we have

$$J_0 = \begin{bmatrix} L & 0 & 0 \\ 0 & -2\pi(R + t_w\xi_3)\sin(2\pi\xi_2) & 2\pi(R + t_w\xi_3)\cos(2\pi\xi_2) \\ 0 & t_w\cos(2\pi\xi_2) & t_w\sin(2\pi\xi_2) \end{bmatrix} \tag{53}$$

The absolute value of the determinant of J_0 is

$$\det(J_0) = 2\pi L t_w (R + t_w\xi_3) \tag{54}$$

Equation (54) is the formulation of the initial Jacobian matrix's determinant, in which the wall-thickness t_w and the inner radius R are constants.

If the wall-thickness t_w and the inner radius R are arbitrary functions, denoted as $R(\xi_1, \xi_2)$ and $t_w(\xi_1, \xi_2)$, then the shell structure's initial configuration is

$$r^0 = \begin{bmatrix} x_1^0 \\ x_2^0 \\ x_3^0 \end{bmatrix} = \begin{bmatrix} L\xi_1 \\ (R(\xi_1, \xi_2) + t_w(\xi_1, \xi_2)\xi_3)\cos(2\pi\xi_2) \\ (R(\xi_1, \xi_2) + t_w(\xi_1, \xi_2)\xi_3)\sin(2\pi\xi_2) \end{bmatrix} \tag{55}$$

In this case, the initial Jacobian matrix will become:

$$J_0 = \begin{bmatrix} J_{11} & J_{12} & J_{13} \\ J_{21} & J_{22} & J_{23} \\ J_{31} & J_{32} & J_{33} \end{bmatrix} \tag{56}$$

where

$$\begin{aligned}
J_{11} &= L \\
J_{21} &= J_{31} = 0 \\
J_{12} &= (\frac{\partial R}{\partial \xi_1} + \frac{\partial t_w}{\partial \xi_1}\xi_3)\cos(2\pi\xi_2) \\
J_{13} &= (\frac{\partial R}{\partial \xi_1} + \frac{\partial t_w}{\partial \xi_1}\xi_3)\sin(2\pi\xi_2) \\
J_{22} &= (R + t_w\xi_3)(-2\pi\sin(2\pi\xi_2)) + \cos(2\pi\xi_2)(\frac{\partial R}{\partial \xi_2} + \frac{\partial t_w}{\partial \xi_2}\xi_3) \\
J_{23} &= (R + t_w\xi_3)(2\pi\cos(2\pi\xi_2)) + \sin(2\pi\xi_2)(\frac{\partial t_w}{\partial \xi_2}\xi_3 + \frac{\partial R}{\partial \xi_2}) \\
J_{32} &= t_w\cos(2\pi\xi_2) \\
J_{33} &= t_w\sin(2\pi\xi_2)
\end{aligned} \tag{57}$$

The determinant of the Jacobian matrix will be:

$$\det(J_0) = 2L\pi t_w(\xi_1, \xi_2)(R(\xi_1, \xi_2) + t_w(\xi_1, \xi_2)\xi_3) \tag{58}$$

It is observed that, when t_w and R become arbitrary functions, the Jacobian matrix becomes more complex. However, the determinant of the Jacobian matrix is still as simple as that of (54). The Jacobian matrix's determinant is very important for the following work.

2.3.3 Doubly curvature plate/shell kinematics

In this section, a doubly-curvature shell structure kinematics is developed based on the spherical coordinate system. Different from the 2.3.2, it allows comparable curvature in the two dimensions. The wall-thickness t_w is still an arbitrary function and the inner surface R is arbitrary curved surface. The kinematics developed in this part is very suitable for the shell structures with comparable curvature fields in two of the dimensions.

The natural coordinates are defined as:

$$\begin{aligned}\xi_1 &= \frac{\theta}{2\pi} \in [0,1] \\ \xi_2 &= \frac{\alpha}{\pi} \in [0,1] \\ \xi_3 &= \frac{\rho - R}{t_w} \in [0,1]\end{aligned} \tag{59}$$

where ρ, θ, α are the conventional spherical coordinates.

If the wall-thickness and the inner surface's position radius are constants, the configuration can be described as:

$$r^0 = \begin{bmatrix} x_1^0 \\ x_2^0 \\ x_3^0 \end{bmatrix} = \begin{bmatrix} (R+\xi_3 t_w)\sin(\pi\xi_2)\cos(2\pi\xi_1) \\ (R+\xi_3 t_w)\sin(\pi\xi_2)\sin(2\pi\xi_1) \\ (R+\xi_3 t_w)\cos(\pi\xi_2) \end{bmatrix} \tag{60}$$

where R is the inner radius and t_w is the wall-thickness.

The absolute value of the determinant of the initial Jacobian matrix is:

$$\det(J) = \frac{1}{4}\pi^2 t \sin(\pi\xi_2)(R + t\xi_3)^2 \tag{61}$$

If the inner radius R and the wall-thickness t_w are generalized to be arbitrary functions about ξ_1, ξ_2, the shell configuration will be:

$$r^0 = \begin{bmatrix} x_1^0 \\ x_2^0 \\ x_3^0 \end{bmatrix} = \begin{bmatrix} [R(\xi_1,\xi_2) + \xi_3 t_w(\xi_1,\xi_2)]\sin(\pi\xi_2)\cos(2\pi\xi_1) \\ [R(\xi_1,\xi_2) + \xi_3 t_w(\xi_1,\xi_2)]\sin(\pi\xi_2)\sin(2\pi\xi_1) \\ [R(\xi_1,\xi_2) + \xi_3 t_w(\xi_1,\xi_2)]\cos(\pi\xi_2) \end{bmatrix} \tag{62}$$

Fortunately, even if both the inner radius and the wall-thickness have been generalized to be arbitrary functions and the formulation of the Jacobian matrix becomes more complicated, the formulation of the Jacobian matrix's determinant remains as simple as (61).

$$\det(J) = \frac{1}{4}\pi^2 t(\xi_1,\xi_2)\sin(\pi\xi_2)(R(\xi_1,\xi_2) + t_w(\xi_1,\xi_2)\xi_3)^2 \tag{63}$$

It is noted that the simple and accurate Jacobian matrix and its determinant are significant for the success of deriving the Consistent Orthogonal Basis Function Space and the corresponding diagonal mass matrix.

A special case is considered. If we define:

$$R(\xi_1,\xi_2) = 0 \tag{64}$$

In this case, the configuration and the Jacobian matrix determinant will be simplified as:

$$r^0 = \begin{bmatrix} x_1^0 \\ x_2^0 \\ x_3^0 \end{bmatrix} = \begin{bmatrix} [\xi_3 t(\xi_1, \xi_2)]\sin(\pi\xi_2)\cos(2\pi\xi_1) \\ [\xi_3 t(\xi_1, \xi_2)]\sin(\pi\xi_2)\sin(2\pi\xi_1) \\ [\xi_3 t(\xi_1, \xi_2)]\cos(\pi\xi_2) \end{bmatrix} \tag{65}$$

$$\det(J) = \frac{1}{4}\pi^2[t(\xi_1, \xi_2)]^3 \sin(\pi\xi_2)(\xi_3)^2 \tag{66}$$

This is applicable for non-hollow structures.

2.3.4 Kinematics for the plate structure

In this section, a new kinematics is presented for the parameterization of plate structures, as the Figure 3 shows.

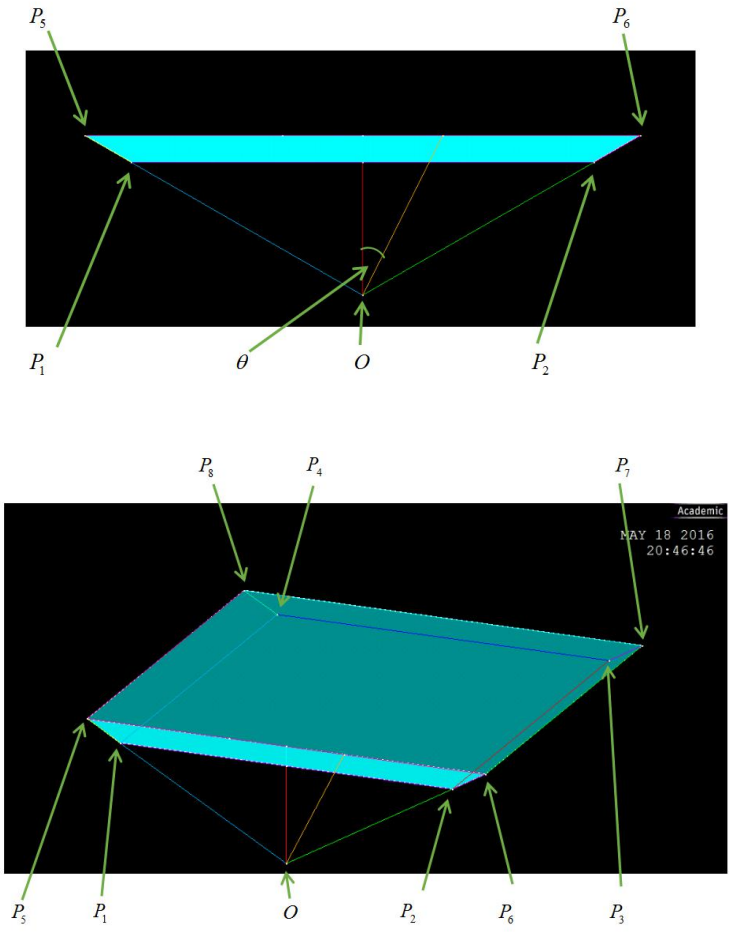

Figure 3 Plate structure notations

The kinematics and the natural coordinates are defined as:

$$r_l = \begin{bmatrix} L\xi_1 \\ (H + t\xi_3)\xi_2 \tan\theta_0 \\ H + t\xi_3 \end{bmatrix}$$
$$\xi_1 \in [0,1] \qquad \text{(67a, b, c, d)}$$
$$\xi_2 = \frac{\tan\theta}{\tan\theta_0} \in [-1,1]$$
$$\xi_3 \in [0,1]$$

where H is the distance between O and the plate's bottom surface, θ_0 is the angle between line OP_2 and the vertical direction.

The local rotation matrix is defined as:

$$R_l = \left[\vec{e}_l^{\,1} \quad \vec{e}_l^{\,2} \quad \vec{e}_l^{\,3}\right] \qquad (68)$$

where

$$\vec{e}_l^{\,1} = P_1 P_4$$
$$\vec{e}_l^{\,2} = P_1 P_2 \qquad (69)$$
$$\vec{e}_l^{\,3} = OP_{12}$$

where P_{12} is the center point of line $P_1 P_2$

Thus, the global position vector of the plate is

$$r_g = r_O + R_l r_l \qquad (70)$$

where r_O is the global coordinate vector of the point O (the origin point of the local coordinate system $\vec{e}_l^{\,1}, \vec{e}_l^{\,2}, \vec{e}_l^{\,3}$).

Thus, the Jacobian matrix will be:

$$J = R_l J_l$$
$$J_l = \begin{bmatrix} L & 0 & 0 \\ 0 & (H + t\xi_3)\tan\theta_0 & 0 \\ 0 & t\xi_2 \tan\theta_0 & t \end{bmatrix} \quad (71a, b)$$

The determinant of the Jacobian matrix is:

$$\begin{aligned} &\det(J) \\ &= \det(R_l)\det(J_l) \\ &= \det(J_l) \\ &= Lt(H + t\xi_3)\tan\theta_0 \end{aligned} \quad (72)$$

Thus, the kinematics of the plate is set up. The Jacobian matrix's determinant is still simple.

It is also noted that the regular plate will be reproduced if the local origin point O is defined far away from the plate. In this case, the value of H will be large and the regular plate's kinematics is also reproduced by the (67a).

2.4 Constitutive Theory

In this section, the constitutive model that is used throughout the thesis is presented. For an isotropic elastic constitutive material, we have:

$$\sigma_{ij} = C_{ijkl}\varepsilon_{kl} \quad (73)$$

where σ_{ij} is the stress tensor, ε_{kl} is the strain tensor, C_{ijkl} is the 4th-order constitutive tensor.

For a small deformation problem, the engineering stress and strain can be used for approximation of the Cauchy stress and Euler strain. However, for the problem with large deformation and even large strain, the objective strain tensor must be used.

The objective strain tensor refers to those strain definitions that are always zero in a finite rigid motion and rotation. In this thesis, we use the Jaumann stress tensor and the strain rate tensor to set up the constitutive relation:

$$\sigma_{ij}^{J} = C_{ijkl}^{J} e_{kl} \tag{74}$$

Then, by using the relation between Jaumann stress tensor and the second Piola Kirchhoff stress tensor, we can replace the stress by displacement in the weak form of finite element formulation.

In this thesis, the isotropic elastic constitutive model is used for the plate analysis and the large strain plastic constitutive model is used for the shell analysis. For each layer of the multi-layered structures, the 3-D solid isotropic constitutive theory is used.

Chapter 3 Hybrid DG-FEM implementation details

In this chapter, the DG-FEM implementation details are presented [1, 23]. We re-write the displacement in a matrix form. Then, the displacement matrix is taken into the weak form DG-FEM discrete equations and all the tangent stiffness matrix including material nonlinearity, geometrical nonlinearity and load nonlinearity are derived. The external force vector and internal force vector are also derived.

The displacement and the traction field are re-written in matrix form as:

$$u^k = N_u \widetilde{u}^k$$
$$T^k = N_T \widetilde{T}^k \qquad (75a, b)$$

where $\widetilde{u}^k, \widetilde{T}^k$ are vectors of DOFs ($A_{mns}, B_{mns}, C_{mns}, a_{mn}, b_{mn}, c_{mn}$). N_u, N_T are matrix of basis functions.

It's noted that for the displacement variables, the displacement increment and the displacement variation are:

$$u_i^k = {}^{t+dt}u_i^k - {}^{t}u_i^k$$
$$\delta u_i^k = \delta\, {}^{t+dt}u_i^k \qquad (76a, b)$$

where ${}^{t+dt}u_i^k$, ${}^{t}u_i^k$ are the i th displacement component for the k th layer at $t+dt$ and t time configuration.

The Green strain tensor and its variation have the formulation as below:

$${}_{t}^{t+dt}\varepsilon_{ij}^k = {}_t\varepsilon_{ij}^k = {}_t e_{ij}^k + {}_t\eta_{ij}^k$$
$$\delta\, {}_{t}^{t+dt}\varepsilon_{ij}^k = \delta_t \varepsilon_{ij}^k = \delta_t e_{ij}^k + \delta_t \eta_{ij}^k \qquad (77a, b)$$

where ${}_t\varepsilon_{ij}^k$, is the Green strain tensor increment, ${}_t\varepsilon_{ij}^k = {}_t^{t+dt}\varepsilon_{ij}^k - {}_t^t\varepsilon_{ij}^k = {}_t^{t+dt}\varepsilon_{ij}^k$;

${}_te_{ij}^k = \frac{1}{2}(u_{i,j}^k + u_{j,i}^k)$ is the linear part of ${}_t\varepsilon_{ij}^k$; ${}_t\eta_{ij} = \frac{1}{2}u_{s,i}^k u_{s,j}^k$ is the nonlinear part of ${}_t\varepsilon_{ij}^k$.

The left-low corner t in ${}_t\varepsilon_{ij}^k$, ${}_te_{ij}^k$ and ${}_t\eta_{ij}^k$ means that the derivatives are calculated to the t time configuration coordinate.

The Kirchhoff stress tensor has the formulation as below.

$${}_t^{t+dt}S_{ij}^k = {}_tS_{ij}^k + {}_t^tS_{ij}^k = {}_tS_{ij}^k + {}^t\sigma_{ij}^k \tag{78}$$

where ${}_tS_{ij}^k$ is the increment of the Kirchhoff stress tensor based on the configuration at time t and ${}^t\sigma_{ij}^k$ is the Cauchy stress tensor at time t.

Based on the relation between Kirchhoff and the Cauchy stresses, we have:

$${}_tS_{sl}^k = \sigma_{sl}^k - {}^t\sigma_{sp}^k({}_tu_{l,p}^k) - {}^t\sigma_{lp}^k({}_tu_{s,p}^k) \tag{79}$$

Based on the Jaumann constitutive theory, we have

$${}_tS_{ij}^k = D_{ijsl}^J({}_te_{sl}^k) - {}^t\sigma_{ip}^k({}_te_{jp}^k) - {}^t\sigma_{jp}^k({}_te_{ip}^k) \tag{80}$$

where D_{ijsl}^J is the Jaumann elastic-plastic constitutive tensor and ${}^t\sigma_{ij}^k$ is the Cauchy stress tensor at time t.

The Jaumann stress tensor is used in the constitutive model in this thesis, which is necessary for large deformation analysis. The Jaumann stress tensor and its corresponding strain rate tensor are objective.

Take (77a, b) and (78) into the variation of strain energy and consider (79, 80), the variation of the strain energy will be:

$$\int_{\Omega_{t,h}} {}_t^{t+dt}S_{ij}^k \delta_t^{t+dt}\varepsilon_{ij}^k d^tV = \int_{\Omega_{t,h}} D_{ijsl}^J ({}_t e_{sl}^k)(\delta_t e_{ij}^k) d^tV + \int_{\Omega_{t,h}} {}^t\sigma_{ij}^k \delta[{}_t\eta_{ij}^k - ({}_t e_{pi}^k)({}_t e_{pj}^k)] d^tV + \int_{\Omega_{t,h}} {}^t\sigma_{ij}^k \delta_t e_{ij}^k d^tV \tag{81}$$

A vector is defined for convenience.

$$\vec{\delta}_s = [\delta_{s1}, \delta_{s2}, \delta_{s3}] \tag{82}$$

where

$$\delta_{ij} = 1, i = j$$
$$\delta_{ij} = 0, i \neq j \tag{83a, b}$$

Thus

$$u_s^k = \vec{\delta}_s u^k \tag{84}$$

where

$$u^k = [u_1^k, u_2^k, u_3^k]^T = N_u \tilde{u}^k \tag{85}$$

So

$$u_s^k = \vec{\delta}_s N_u \tilde{u}^k \tag{86}$$

Thus, the ${}_t e_{ij}^k$ can be represented as:

$${}_t e_{ij}^k = \frac{1}{2}({}_t u_{i,j}^k + {}_t u_{j,i}^k) = \frac{1}{2}({}_t(\vec{\delta}_i N_u)_{,j} + {}_t(\vec{\delta}_j N_u)_{,i})\tilde{u}^k \tag{87}$$

Similarly, the variation of the linear strain tensor is:

$$\delta_t e_{ij}^k = \delta\frac{1}{2}({}_t u_{i,j}^k + {}_t u_{j,i}^k) = \frac{1}{2}({}_t(\vec{\delta}_i N_u)_{,j} + {}_t(\vec{\delta}_j N_u)_{,i})\delta\tilde{u}^k \tag{88}$$

Thus, the first term of the variation of the strain energy is:

$$\int_{{}^tV} D^J_{ijsl}({}_t e^k_{sl})(\delta_t e^k_{ij})d^tV =$$

$$\frac{1}{4}\delta\tilde{u}^{kT}[\int_{{}^tV} D^J_{ijsl}({}_t(\vec{\delta}_i N_u)_{,j} + {}_t(\vec{\delta}_j N_u)_{,i})^T({}_t(\vec{\delta}_k N_u)_{,l} + {}_t(\vec{\delta}_l N_u)_{,s})d^tV]\tilde{u}^k \tag{89}$$

It is noted that $\vec{\delta}_i N_u$ is essentially the i row of N_u.

The second term of the strain energy variation is:

$$\begin{aligned}
&\int_{\Omega_{t,k}} \delta_t \eta^k_{ij}({}^t\sigma^k_{ij})dV \\
&= \int_{\Omega_{t,k}} \frac{1}{2}\delta[({}_t u^k_{s,i})({}_t u^k_{s,j})]({}^t\sigma^k_{ij})dV \\
&= \int_{\Omega_{t,k}} \frac{1}{2}[(\delta_t u^k_{s,i})({}_t u^k_{s,j}) + ({}_t u^k_{s,i})(\delta_t u^k_{s,j})]({}^t\sigma^k_{ij})dV \\
&= \int_{\Omega_{t,k}} \frac{1}{2}\begin{pmatrix}[{}_t(\vec{\delta}_s N_u)_{,i}(\delta\tilde{u}^k)][{}_t(\vec{\delta}_s N_u)_{,j}(\tilde{u}^k)] \\ +[{}_t(\vec{\delta}_s N_u)_{,i}(\tilde{u}^k)][{}_t(\vec{\delta}_s N_u)_{,j}(\delta\tilde{u}^k)]\end{pmatrix}({}^t\sigma^k_{ij})dV \\
&= \delta\tilde{u}^{kT}\left(\int_{\Omega_{t,k}}[{}_t(\vec{\delta}_s N_u)^T_{,i}]({}^t\sigma_{ij})[{}_t(\vec{\delta}_s N_u)_{,j}]dV\right)\tilde{u}^k
\end{aligned} \tag{90}$$

The third term of the strain energy variation is:

$$\begin{aligned}
&\int_{\Omega_{t,k}} {}^t\sigma^k_{ij}\delta[({}_t e^k_{pi})({}_t e^k_{pj})]dV \\
&= \int_{\Omega_{t,k}} 2{}^t\sigma^k_{ij}(\delta_t e^k_{pi})({}_t e^k_{pj})dV \\
&= \delta\tilde{u}^{kT}\left(\int_{\Omega_{t,k}} \frac{1}{2}[{}_t(\vec{\delta}_i N_u)_{,p} + {}_t(\vec{\delta}_p N_u)_{,i}]^T({}^t\sigma^k_{ij})[{}_t(\vec{\delta}_j N_u)_{,p} + {}_t(\vec{\delta}_p N_u)_{,j}]dV\right)\tilde{u}^k
\end{aligned} \tag{91}$$

$$\int_{\Omega_{t,k}} {}^t\sigma^k_{ij}\delta_t e^k_{ij}dV = \delta\tilde{u}^{kT}\left(\int_{\Omega_{t,k}} \frac{1}{2}[({}^t\sigma^k_{ij})({}_t(\vec{\delta}_i N_u)_{,j} + {}_t(\vec{\delta}_j N_u)_{,i})]^T dV\right) \tag{92}$$

For the body force term and external distributed force, we have:

$$
\begin{aligned}
{}^{t+dt}W^k &= \int_{{}^{t+dt}\Gamma^{\pm}} {}^{t+dt}_{t+dt}t_s^k \delta u_s^k d^{t+dt}S + \int_{\Omega_{t+dt,k}} {}^{t+dt}_{t+dt}f_s^k \delta u_s^k d^{t+dt}V \\
&= \delta\tilde{u}^{kT}\left(\int_{{}^{t+dt}\Gamma^{\pm}} {}^{t+dt}_{t+dt}t_s^k (\vec{\delta}_s N_u)^T d^{t+dt}S \right) + \delta\tilde{u}^{kT}\left(\int_{\Omega_{t+dt,k}} {}^{t+dt}_{t+dt}f_s^k (\vec{\delta}_s N_u)^T d^{t+dt}V \right)
\end{aligned} \tag{93}
$$

where f_s^k is the body force and t_s^k is the external traction force for the k th layer.

Then the tangential stiffness matrices are obtained:

$$
K_l = \frac{1}{4}[\int_{{}^tV} D_{ijsl}^J ({}_t(\vec{\delta}_i N_u)_{,j} + {}_t(\vec{\delta}_j N_u)_{,i})^T ({}_t(\vec{\delta}_k N_u)_{,l} + {}_t(\vec{\delta}_l N_u)_{,s}) d^tV] \tag{94}
$$

$$
K_{n1} = \left(\int_{\Omega_{t,k}} [{}_t(\vec{\delta}_s N_u)_{,i}^T]({}^t\sigma_{ij})[{}_t(\vec{\delta}_s N_u)_{,j}] dV \right) \tag{95}
$$

$$
K_{n2} = \frac{1}{2}\int_{\Omega_{t,k}} [{}_t(\vec{\delta}_i N_u)_{,p} + {}_t(\vec{\delta}_p N_u)_{,i}]^T ({}^t\sigma_{ij}^k)[{}_t(\vec{\delta}_j N_u)_{,p} + {}_t(\vec{\delta}_p N_u)_{,j}] d^tV \tag{96}
$$

And the internal/external force vector are:

$$
F = \left(\int_{\Omega_{t,k}} \frac{1}{2}[({}^t\sigma_{ij}^k)({}_t(\vec{\delta}_i N_u)_{,j} + {}_t(\vec{\delta}_j N_u)_{,i})]^T dV \right) \tag{97}
$$

$$
Q = \left(\int_{{}^{t+dt}\Gamma^{\pm}} {}^{t+dt}_{t+dt}t_s^k (\vec{\delta}_s N_u)^T d^{t+dt}S \right) + \left(\int_{\Omega_{t+dt,k}} {}^{t+dt}_{t+dt}f_s^k (\vec{\delta}_s N_u)^T d^{t+dt}V \right) \tag{98}
$$

The load tangential stiffness matrix is also considered, for example, for the case of fluid pressure that is always normal to the deformed structure's outer surface:

$$
Q = \int_{{}^{t+dt}\Gamma^{\sigma}} ({}^{t+dt}_{t+dt}n_s)(\vec{\delta}_s N_u)^T p d^{t+dt}S = \int_{{}^{t+dt}\Gamma^{\sigma}} (N_u)^T ({}^{t+dt}_{t+dt}n) p d^{t+dt}S \tag{99}
$$

where p is the fluid pressure; n_s is the s th component of the unit normal vector pointing outside $\vec{n}$, $\vec{n} = [n_1, n_2, n_3]^T$; $t+dt$ refers to the current time.

Then, assuming the fluid pressure is applied on the surface $\xi_3 = 1$

$$d^{t+dt}\vec{S} = ({}^{t+dt}_{t+dt}\vec{n})d^{t+dt}S = \det\begin{bmatrix} \vec{i} & \vec{j} & \vec{k} \\ \dfrac{\partial^{t+dt}x_1}{\partial\xi_1} & \dfrac{\partial^{t+dt}x_2}{\partial\xi_1} & \dfrac{\partial^{t+dt}x_3}{\partial\xi_1} \\ \dfrac{\partial^{t+dt}x_1}{\partial\xi_2} & \dfrac{\partial^{t+dt}x_2}{\partial\xi_2} & \dfrac{\partial^{t+dt}x_3}{\partial\xi_2} \end{bmatrix} d\xi_1\, d\xi_2 \tag{100}$$

$${}^{t+dt}x_i^k = {}^{t}x_i^k + u_i^k \tag{101}$$

where $\vec{i}, \vec{j}, \vec{k}$ are the basis vector of space rectangular coordinate system;

$\xi_i, i = 1,2,3$ are the natural coordinates; ${}^{t+dt}x_i$ is the configuration i coordinate at time $t+dt$; ${}^{t}x_i$ is the configuration i coordinate at time t.

Thus, the area nominal vector is:

$$\begin{aligned} d^{t+dt}\vec{S} &= \begin{bmatrix} \dfrac{\partial^{t+dt}x_2^k}{\partial\xi_1}\dfrac{\partial^{t+dt}x_3^k}{\partial\xi_2} - \dfrac{\partial^{t+dt}x_2^k}{\partial\xi_2}\dfrac{\partial^{t+dt}x_3^k}{\partial\xi_1} \\ \dfrac{\partial^{t+dt}x_3^k}{\partial\xi_1}\dfrac{\partial^{t+dt}x_1^k}{\partial\xi_2} - \dfrac{\partial^{t+dt}x_1^k}{\partial\xi_1}\dfrac{\partial^{t+dt}x_3^k}{\partial\xi_2} \\ \dfrac{\partial^{t+dt}x_1^k}{\partial\xi_1}\dfrac{\partial^{t+dt}x_2^k}{\partial\xi_2} - \dfrac{\partial^{t+dt}x_1^k}{\partial\xi_2}\dfrac{\partial^{t+dt}x_2^k}{\partial\xi_1} \end{bmatrix} d\xi_1\, d\xi_2 \\ &= \begin{bmatrix} \dfrac{\partial({}^{t}x_2^k + u_2^k)}{\partial\xi_1}\dfrac{\partial({}^{t}x_3^k + u_3^k)}{\partial\xi_2} - \dfrac{\partial({}^{t}x_2^k + u_2^k)}{\partial\xi_2}\dfrac{\partial({}^{t}x_3^k + u_3^k)}{\partial\xi_1} \\ \dfrac{\partial({}^{t}x_3^k + u_3^k)}{\partial\xi_1}\dfrac{\partial({}^{t}x_1^k + u_1^k)}{\partial\xi_2} - \dfrac{\partial({}^{t}x_1^k + u_1^k)}{\partial\xi_1}\dfrac{\partial({}^{t}x_3^k + u_3^k)}{\partial\xi_2} \\ \dfrac{\partial({}^{t}x_1^k + u_1^k)}{\partial\xi_1}\dfrac{\partial({}^{t}x_2^k + u_2^k)}{\partial\xi_2} - \dfrac{\partial({}^{t}x_1^k + u_1^k)}{\partial\xi_2}\dfrac{\partial({}^{t}x_2^k + u_2^k)}{\partial\xi_1} \end{bmatrix} d\xi_1\, d\xi_2 \end{aligned} \tag{102}$$

The linear part from (99) can be picked up as the load tangential stiffness matrix, denoted as K_Q, thus

$$K_Q = \int_{-1}^{1}\int_{-1}^{1} p \begin{bmatrix} [\frac{\partial^t x_2^k}{\partial \xi_1}(\vec{\delta}_3 N_u)_{,2} + \frac{\partial^t x_3^k}{\partial \xi_2}(\vec{\delta}_2 N_u)_{,1}] - [\frac{\partial^t x_2^k}{\partial \xi_2}(\vec{\delta}_3 N_u)_{,1} + \frac{\partial^t x_3^k}{\partial \xi_1}(\vec{\delta}_2 N_u)_{,2}] \\ [\frac{\partial^t x_3^k}{\partial \xi_1}(\vec{\delta}_1 N_u)_{,2} + \frac{\partial^t x_1^k}{\partial \xi_2}(\vec{\delta}_3 N_u)_{,1}] - [\frac{\partial^t x_1^k}{\partial \xi_1}(\vec{\delta}_3 N_u)_{,2} + \frac{\partial^t x_3^k}{\partial \xi_2}(\vec{\delta}_1 N_u)_{,1}] \\ [\frac{\partial^t x_1^k}{\partial \xi_1}(\vec{\delta}_2 N_u)_{,2} + \frac{\partial^t x_2^k}{\partial \xi_2}(\vec{\delta}_1 N_u)_{,1}] - [\frac{\partial^t x_2^k}{\partial \xi_1}(\vec{\delta}_1 N_u)_{,2} + \frac{\partial^t x_1^k}{\partial \xi_2}(\vec{\delta}_2 N_u)_{,1}] \end{bmatrix} d\xi_1 \, d\xi_2$$

(103)

If the water pressure is applied on the surface $\xi_2 - \xi_3$, the load tangential stiffness matrix will be:

$$K_Q = \int_{-1}^{1}\int_{-1}^{1} p \begin{bmatrix} [\frac{\partial^t x_2^k}{\partial \xi_2}(\vec{\delta}_3 N_u)_{,3} + \frac{\partial^t x_3^k}{\partial \xi_3}(\vec{\delta}_2 N_u)_{,2}] - [\frac{\partial^t x_2^k}{\partial \xi_3}(\vec{\delta}_3 N_u)_{,2} + \frac{\partial^t x_3^k}{\partial \xi_2}(\vec{\delta}_2 N_u)_{,3}] \\ [\frac{\partial^t x_3^k}{\partial \xi_2}(\vec{\delta}_1 N_u)_{,3} + \frac{\partial^t x_1^k}{\partial \xi_3}(\vec{\delta}_3 N_u)_{,2}] - [\frac{\partial^t x_1^k}{\partial \xi_2}(\vec{\delta}_3 N_u)_{,3} + \frac{\partial^t x_3^k}{\partial \xi_3}(\vec{\delta}_1 N_u)_{,2}] \\ [\frac{\partial^t x_1^k}{\partial \xi_2}(\vec{\delta}_2 N_u)_{,3} + \frac{\partial^t x_2^k}{\partial \xi_3}(\vec{\delta}_1 N_u)_{,2}] - [\frac{\partial^t x_2^k}{\partial \xi_2}(\vec{\delta}_1 N_u)_{,3} + \frac{\partial^t x_1^k}{\partial \xi_3}(\vec{\delta}_2 N_u)_{,2}] \end{bmatrix} d\xi_2 \, d\xi_3$$

(104)

where p is the distributed pressure function.

For the i th component of the traction field, we have:

$$T_i^{k+\frac{1}{2}} = \vec{\delta}_i \, T^{k+\frac{1}{2}} \tag{105}$$

where $\vec{\delta}_i$ is defined in (82-83), $T^{k+\frac{1}{2}} = \begin{bmatrix} T_1 \\ T_2 \\ T_3 \end{bmatrix}^{k+\frac{1}{2}}$.

Taking the interpolation matrix of traction field defined in (75b) into (105):

$$T^{k+\frac{1}{2}} = N_T \widetilde{T}^{k+\frac{1}{2}} \tag{106}$$

where $\widetilde{T}$ is the degree-of-freedom vector for traction field.

Thus, consider (105), we have:

$$T_i^{k+\frac{1}{2}} = \left(\vec{\delta}_i \; N_T\right)\widetilde{T}^{k+\frac{1}{2}} \tag{107}$$

For the term containing interface traction $\left\langle \delta T_i^{k+\frac{1}{2}}, u_i^k - u_i^{k+1} \right\rangle_{\Gamma_{t,k}^i}$, we have:

$$\begin{aligned} &\left(\widetilde{T}^{k+\frac{1}{2}}\right)^T \left(\int_{\Gamma_{t,k}^i} \left(\vec{\delta}_i \; N_T\right)^T \left(\vec{\delta}_i \; N_u\right) dS \right) \left(\widetilde{u}^k - \widetilde{u}^{k+1}\right) \\ &= \left(\widetilde{T}^{k+\frac{1}{2}}\right)^T \left(\int_{\Gamma_{t,k}^i} \left(N_T\right)^T \left(N_u\right) dS \right) \left(\widetilde{u}^k - \widetilde{u}^{k+1}\right) \end{aligned} \tag{108}$$

where $T_i^{k+\frac{1}{2}}$ is the i th traction component of the traction vector $T^{k+\frac{1}{2}}$, which has been defined in (24a, b), N_T is the interpolation matrix for traction field, $\widetilde{T}^{k+\frac{1}{2}}$ is the degree-of-freedom of traction to be determined.

Chapter 4 Consistent Orthogonal Basis Function Space

In this chapter, the orthogonal polynomial theory is applied to develop the so-called Consistent Orthogonal Basis Function Space for displacement field. A systematical method to design the Consistent Orthogonal Basis Function Space is presented so that a dedicated basis function space is developed for the structure of interest and an accurate diagonal mass matrix is always obtained for the multi- layered shells. To develop a diagonal mass matrix is not a new idea, but it is the first time to develop an *accurate* diagonal mass matrix for multi-layered structures, which also considers the uniqueness due to the structural configuration and boundary conditions. For the so-called *accurate* diagonal mass matrix, we don't use any unreasonable approximations throughout this method. Moreover, when we develop the Consistent Orthogonal Basis Function Space, we consider the contribution of displacement boundary conditions and the structure configurations. As long as the structure and its boundary conditions are known accurately, the method will yield a unique orthogonal basis functions space for this specific structure, such that an accurate diagonal mass matrix is obtained. For different structures, the Consistent Orthogonal Basis Functions Spaces are different. For the same structure with different boundary conditions, the Consistent Orthogonal Basis Function spaces are still different. Thus, the method presents a unique orthogonal basis function space for a given specific structure. This is analogous to the mode shape functions or buckling mode functions, which are also uniquely determined by the structure

configuration and boundary conditions. Thus, it is reasonable to state that this thesis's basis functions are very similar the mode shape functions. It is also interesting that the mode shape functions are also orthogonal with respect to each other and a diagonal mass matrix is also obtained if the mode shape functions are used as the basis functions. However, analytic mode shape functions are not easy to obtain for complex structures. The analytic solution of mode shape analysis is only possible for simple beams or plates. For complex structures, we may only be able to obtain the discrete mode shapes, instead of mode shape functions.

The basis function space in this thesis is not a serendipitous function space. It is not an arbitrarily defined basis function space, but a systematically derived basis function space, which considers the uniqueness of structures (configuration and boundary conditions). In the traditional finite element method or any finite element methods before, the basis function space never considers the uniqueness of the structure itself. They either use the same basis functions for every part of the structure or simply increase the displacement order for some particular region where a larger gradient displacement occurs. This is one reason why the traditional FEM is so powerful, however, it also induces a problem that the number of DOF is often too large. In this method, we can develop different basis functions for different structures. With this method, a user can obtain accurate results by using a much fewer number of elements. With an accurate diagonal mass matrix, the explicit Galerkin dynamical system of equations will become totally decoupled. For the implicit dynamics, the system will be diagonally dominated by using smaller time step. Moreover, the Consistent Orthogonal Basis Functions developed in this thesis

also provide greater accuracy even by using a fewer number of degrees-of-freedom in both static and dynamical analysis (This is shown in the numerical tests in the last two chapters).

For completeness of the mathematics, the basic property of orthogonal polynomial is simply reviewed. The orthogonal polynomials have the property that:

$$\begin{aligned} &\left\langle p_i , p_j \right\rangle_w = \delta_{ij} \\ &\delta_{ij} = 1, i = j \\ &\delta_{ij} = 0, i \neq j \end{aligned} \qquad \text{(109a, b, c)}$$

where p_i , p_j are the i, j term of the orthogonal polynomial; w is the weighting function. It is noted that the weighting function w refers to the orthogonal polynomial only.

On the other hand, once a weighting function w is given, we can always find an orthogonal polynomial series, such that (109a) holds.

$$\begin{aligned} &p_0 = 1 \\ &p_1 = \xi - \alpha_0 \\ &p_{n+1} = (\xi - \alpha_n) p_n - \beta_n p_{n-1}, n \geq 1 \end{aligned} \qquad \text{(110a, b, c)}$$

where

$$\begin{aligned} &\alpha_n = \frac{\left\langle x p_n , p_n \right\rangle_w}{\left\| p_n \right\|_w^2}, n \geq 0 \\ &\beta_n = \frac{\left\| p_n \right\|_w^2}{\left\| p_{n-1} \right\|_w^2}, n \geq 1 \end{aligned} \qquad \text{(111a, b)}$$

In this case, an orthogonal polynomial series about coordinate ξ is calculated. Once the weighting function is given, we can uniquely determine an orthogonal polynomial series in (110-111).

The displacement defined in (44) is re-written in matrix form as:

$$u = N_u \widetilde{u} \tag{112}$$

where

$$N_u = \begin{bmatrix} N_{111} & N_{211} & \cdots & N_{m11} & N_{121} & \cdots & N_{m21} & \cdots & N_{mn1} & \cdots & N_{mnk} \end{bmatrix}$$
$$\widetilde{u} = \begin{bmatrix} \widetilde{u}_{111}^T & \widetilde{u}_{211}^T & \cdots & \widetilde{u}_{m11}^T & \widetilde{u}_{121}^T & \cdots & \widetilde{u}_{m21}^T & \cdots & \widetilde{u}_{mn1}^T & \cdots & \widetilde{u}_{mnk}^T \end{bmatrix}$$

For the convenience of mathematical derivations, some matrices are defined below:

$$N_{mnk} = N_m^{\varphi} N_n^{\psi} N_k^{\phi}$$

$$N_m^{\varphi} = \begin{bmatrix} f_{u_1}^{\xi_1} \varphi_{u_1}^{m} & 0 & 0 \\ 0 & f_{u_2}^{\xi_1} \varphi_{u_2}^{m} & 0 \\ 0 & 0 & f_{u_3}^{\xi_1} \varphi_{u_3}^{m} \end{bmatrix}$$

$$N_n^{\psi} = \begin{bmatrix} f_{u_1}^{\xi_2} \psi_{u_1}^{n} & 0 & 0 \\ 0 & f_{u_2}^{\xi_2} \psi_{u_2}^{n} & 0 \\ 0 & 0 & f_{u_3}^{\xi_2} \psi_{u_3}^{n} \end{bmatrix} \tag{113a, b, c, d}$$

$$N_k^{\phi} = \begin{bmatrix} f_{u_1}^{\xi_3} \phi_{u_1}^{k} & 0 & 0 \\ 0 & f_{u_2}^{\xi_3} \phi_{u_2}^{k} & 0 \\ 0 & 0 & f_{u_3}^{\xi_3} \phi_{u_3}^{k} \end{bmatrix}$$

$$\widetilde{u}_{mnk} = \begin{bmatrix} A_{mnk} \\ B_{mnk} \\ C_{mnk} \end{bmatrix} \tag{114}$$

The mass matrix is defined as:

$$M_m = \rho_s \int N_u^T N_u d\Omega$$
$$= \rho_s \int N_u^T N_u \det(J_0) d\xi_1 d\xi_2 d\xi_3 \quad (115)$$

where J_0 is the Jacobian matrix calculated from configuration and $\det(J_0)$ is the determinant of the Jacobian matrix J_0.

Substitute (113a) into (115), the mass matrix can be written as:

$$M_m = \begin{bmatrix} M_{11} & M_{21} & \cdots & M_{1n_d} \\ M_{21} & M_{22} & \cdots & M_{2n_d} \\ \vdots & \vdots & \ddots & \vdots \\ M_{n_d 1} & M_{n_d 2} & \cdots & M_{n_d n_d} \end{bmatrix} \quad (116)$$

where

$$M_{i_1 i_2} = \rho_s \int \int \int (N_{m_1}^{\phi} N_{m_2}^{\phi} N_{n_1}^{\psi} N_{n_2}^{\psi} N_{k_1}^{\varphi} N_{k_2}^{\varphi}) \det(J_0) d\xi_1 d\xi_2 d\xi_3 \quad (117)$$

$$i_1 = m_1 + (n_1 - 1)m^0 + (k_1 - 1)m^0 n^0$$
$$i_2 = m_2 + (n_2 - 1)m^0 + (k_2 - 1)m^0 n^0 \quad (118a, b)$$

$$1 < m_1, m_2 < m^0$$
$$1 < n_1, n_2 < n^0$$
$$1 < k_1, k_2 < k^0 \quad (119a, b, c)$$

where $m_1, m_2, n_1, n_2, k_1, k_2$ are sub-script, and m^0, n^0, k^0 are the order of basis functions.

It's assumed that $\det(J_0)$ can be reformulated as:

$$\det(J_0) = f_{\det}^{\xi_1}(\xi_1) f_{\det}^{\xi_2}(\xi_2) f_{\det}^{\xi_3}(\xi_3) \quad (120)$$

where (120) $f_{\det}^{\xi_i}, i = 1,2,3$ is only a function of ξ_i.

This assumption will be discussed later. It is noted that for the five typical problems in the field of multi-layered shells solved in this thesis, this assumption is valid.

Then, we have

$$M_{i_1 i_2} = \rho_s \int_{-1}^{1} (N_{m_1}^{\phi} N_{m_2}^{\phi} f_{\det}^{\xi_1}) d\xi_1 \int_{-1}^{1} (N_{n_1}^{\psi} N_{n_2}^{\psi} f_{\det}^{\xi_2}) d\xi_2 \int_{-1}^{1} (N_{k_1}^{\varphi} N_{k_2}^{\varphi} f_{\det}^{\xi_3}) d\xi_3 \tag{121}$$

Substitute the (113a-d) into (121), thus,

$$M_{i_1 i_2} = \rho_s R_0^2 \begin{bmatrix} m_a & 0 & 0 \\ 0 & m_b & 0 \\ 0 & 0 & m_c \end{bmatrix} \tag{122}$$

where

$$m_a = \int_{-1}^{1} [(f_{u_1}^{\xi_1})^2 f_{\det}^{\xi_1}] \phi_{u_1}^{m_1} \phi_{u_1}^{m_2} d\xi_1 \int_{-1}^{1} [(f_{u_1}^{\xi_2})^2 f_{\det}^{\xi_2}] \psi_{u_1}^{n_1} \psi_{u_1}^{n_2} d\xi_2 \int_{-1}^{1} [(f_{u_1}^{\xi_3})^2 f_{\det}^{\xi_3}] \varphi_{u_1}^{k_1} \varphi_{u_1}^{k_2} d\xi_3$$
$$m_b = \int_{-1}^{1} [(f_{u_2}^{\xi_1})^2 f_{\det}^{\xi_1}] \phi_{u_2}^{m_1} \phi_{u_2}^{m_2} d\xi_1 \int_{-1}^{1} [(f_{u_2}^{\xi_2})^2 f_{\det}^{\xi_2}] \psi_{u_2}^{n_1} \psi_{u_2}^{n_2} d\xi_2 \int_{-1}^{1} [(f_{u_2}^{\xi_3})^2 f_{\det}^{\xi_3}] \varphi_{u_2}^{k_1} \varphi_{u_2}^{k_2} d\xi_3$$
$$m_c = \int_{-1}^{1} [(f_{u_3}^{\xi_1})^2 f_{\det}^{\xi_1}] \phi_{u_3}^{m_1} \phi_{u_3}^{m_2} d\xi_1 \int_{-1}^{1} [(f_{u_3}^{\xi_2})^2 f_{\det}^{\xi_2}] \psi_{u_3}^{n_1} \psi_{u_3}^{n_2} d\xi_2 \int_{-1}^{1} [(f_{u_3}^{\xi_3})^2 f_{\det}^{\xi_3}] \varphi_{u_3}^{k_1} \varphi_{u_3}^{k_2} d\xi_3$$

(123a, b, c)

If ϕ_{u_i} $(i = 1,2,3)$ is selected as the orthogonal series with weighting function $f_{\det}^{\xi_1} (f_{u_i}^{\xi_1})^2$ in the interval $[-1,1]$ and ψ_{u_i} $(i = 1,2,3)$ is selected as the orthogonal series with weighting function $f_{\det}^{\xi_2} (f_{u_i}^{\xi_2})^2$ in the interval $[-1,1]$ and φ_{u_i} $(i = 1,2,3)$ is selected as the orthogonal series with weighting function $f_{\det}^{\xi_3} (f_{u_i}^{\xi_3})^2$ in the interval $[-1,1]$, then

$$\int_{-1}^{1} [(f_{u_i}^{\xi_1})^2 f_{\det}^{\xi_1}] \phi_{u_i}^{m_1} \phi_{u_i}^{m_2} d\xi_1 = \delta_{m_1 m_2}, (i = 1,2,3)$$
$$\int_{-1}^{1} [(f_{u_i}^{\xi_2})^2 f_{\det}^{\xi_2}] \psi_{u_i}^{n_1} \psi_{u_i}^{n_2} d\xi_2 = \delta_{n_1 n_2}, (i = 1,2,3) \tag{124a, b, c}$$
$$\int_{-1}^{1} [(f_{u_i}^{\xi_3})^2 f_{\det}^{\xi_3}] \varphi_{u_i}^{k_1} \varphi_{u_i}^{k_2} d\xi_3 = \delta_{k_1 k_2}, (i = 1,2,3)$$

Thus

$$M_{i_1 i_2} = \rho_s \delta_{m_1 m_2} \delta_{n_1 n_2} \delta_{k_1 k_2} I \tag{125}$$

In this case, the mass matrix is a diagonal matrix. For the specific formulations of $\phi_{u_i}\ (i=1,2,3)$, $\psi_{u_i}\ (i=1,2,3)$ and $\varphi_{u_i}\ (i=1,2,3)$, it is easy to obtain in (110-111) by taking $f_{\det}^{\xi_1}(f_{u_i}^{\xi_1})^2$, $f_{\det}^{\xi_2}(f_{u_i}^{\xi_2})^2$ and $f_{\det}^{\xi_3}(f_{u_i}^{\xi_3})^2$ as the weight functions. Thus, for different structures (different in the Jacobian matrix's determinant $f_{\det}^{\xi_i}, i=1,2,3$) and/or different boundary conditions (different in the boundary condition functions $f_{u_i}^{\xi_j}, (i=1,2,3,\ j=1,2,3)$), there exists a unique basis function space, which is totally different from other structures.

Let us give some simple examples. In these simple examples, the analytic solution of mode shapes are available. We develop orthogonal basis function space for these simple examples. It is very interesting that, the orthogonal basis functions developed in this thesis are quite identical with those analytic mode shape functions.

For a 2-D uniform beam with fixed-fixed boundary conditions, the mid-surface displacement of deflection is assumed to be:

$$w = f_w^{\xi_1} \sum_{m=1}^{m_0} A_m \phi_w^m(\xi_1) \tag{126}$$

where $\xi_1 = \frac{x}{L}$, L is the length of the beam. A_m is the DOF to be solved, $\phi_w^m(\xi_1)$ is the basis functions to be determined, the boundary conditions will be defined as $f_w^{\xi_1} = \xi_1^2(1-\xi_1)^2$, which means that the deflection is zero for the beam's end points ($\xi_1 = 0,1$).

Based on the orthogonal basis function space developed in (123-124), we have:

$\phi_w^m(\xi_1)$ is the orthogonal polynomial with the weight function $\left(\xi_1^2(1-\xi_1)^2\right)^2$;

Then, we plot the first 6 basis functions of $\phi_w^m(\xi_1)$ in Figure 4, we see that the $\phi_w^m(\xi_1)$ are so identical with the mode shape functions of a fixed-fixed beam.

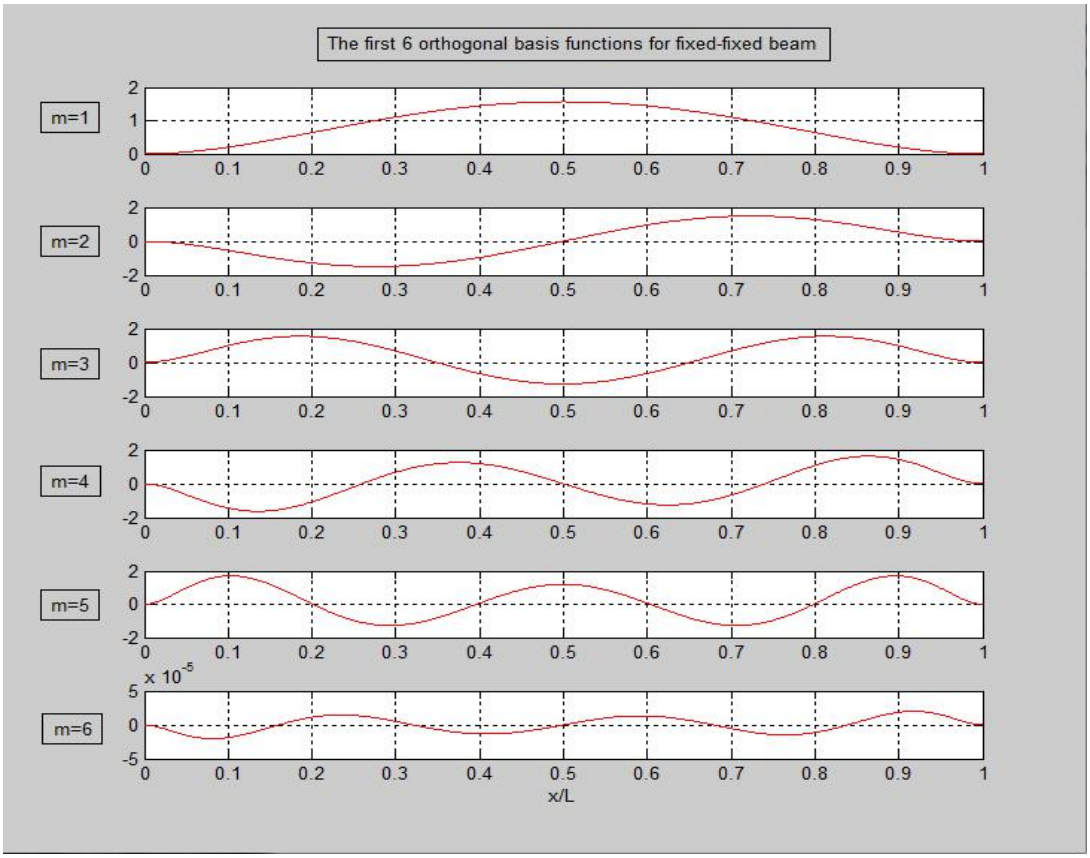

Figure 4 Orthogonal basis functions for fixed-fixed uniform beam

If we change to boundary conditions to fixed-free case, based on (123-124), we have that $\phi_w^m(\xi_1)$ is the orthogonal polynomial with the weight function $\left(\xi_1^2\right)^2$. Thus, the plot of $\phi_w^m(\xi_1)$ is presented in Figure 5.

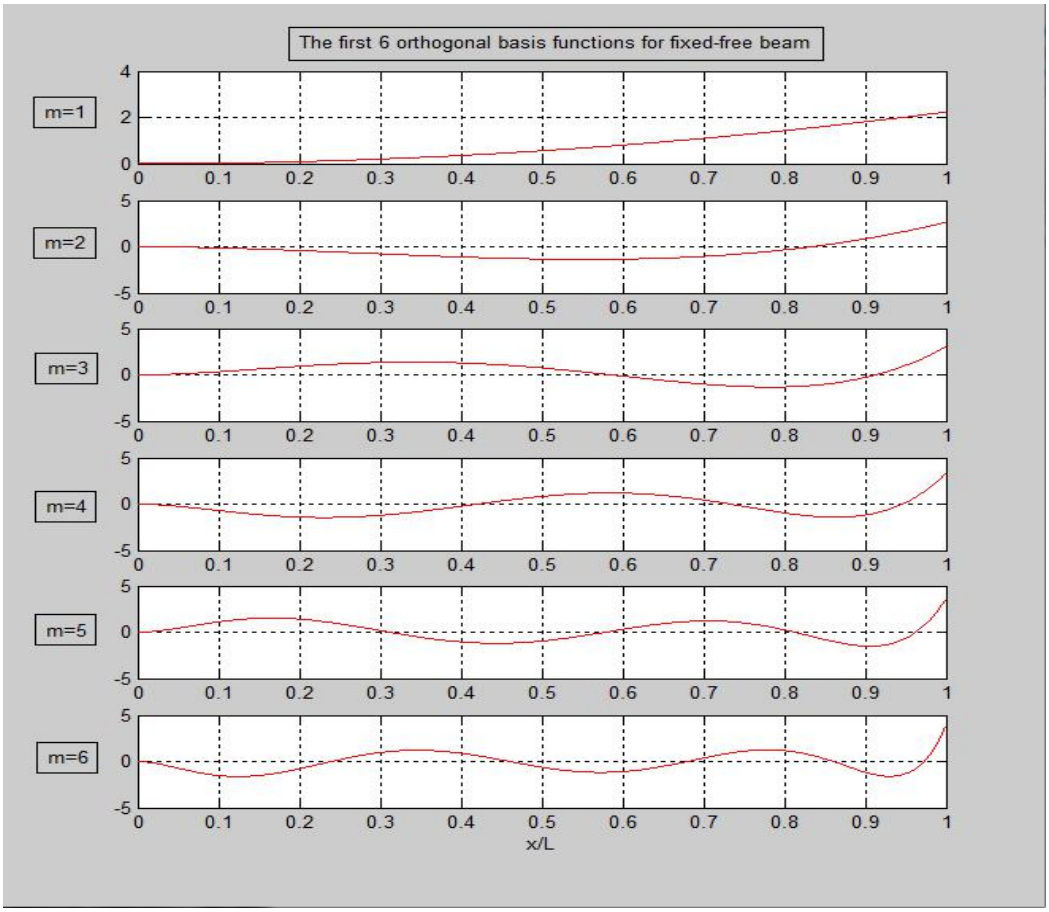

Figure 5 Orthogonal basis functions for fixed-free uniform beam

From the Figure 5, we can tell that $\phi_w^m(\xi_1)$ are quite identical to the mode shapes of a fixed-free beam.

Let us analyze another example. In this case, the beam's cross-section area is a function of axial coordinate: $A(x) = A_0(1+\frac{x}{L})$

Where we just assume that $A_0 = 1, L = 1$. In this case, the beam's stiffness will be a function of x. Stiffness will increase from left to right.

The fixed-fixed boundary conditions are applied. Thus, based on the (123-124), the weight of $\phi_w^m(\xi_1)$ will be $\left(\xi_1^2\left(1-\xi_1\right)^2\right)^2\left(1+\xi_1\right)$. Thus, the plot of $\phi_w^m(\xi_1)$ is presented in Figure 6.

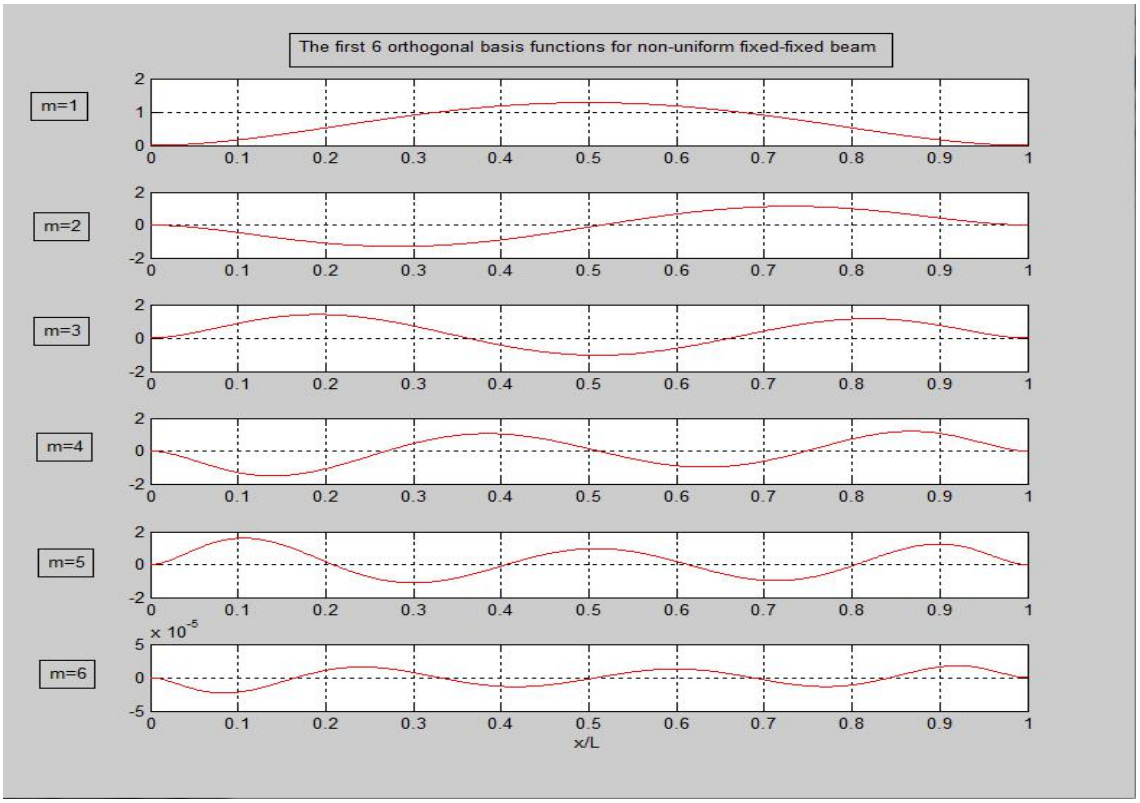

Figure 6 Orthogonal basis functions for fixed-fixed non-uniform beam

From the Figure 6, it is interesting to observe that, these orthogonal basis functions have a larger value on the left part. For this beam, the left part's stiffness is smaller than that of right part due to $A(x)=A_0(1+\frac{x}{L})$.

If we change the boundary conditions to fix-free, we will the functions $\phi_w^m(\xi_1)$ with a weight of $\left(\xi_1^2\right)^2(1+\xi_1)$. In this case, the plot of $\phi_w^m(\xi_1)$ is presented in Figure 7.

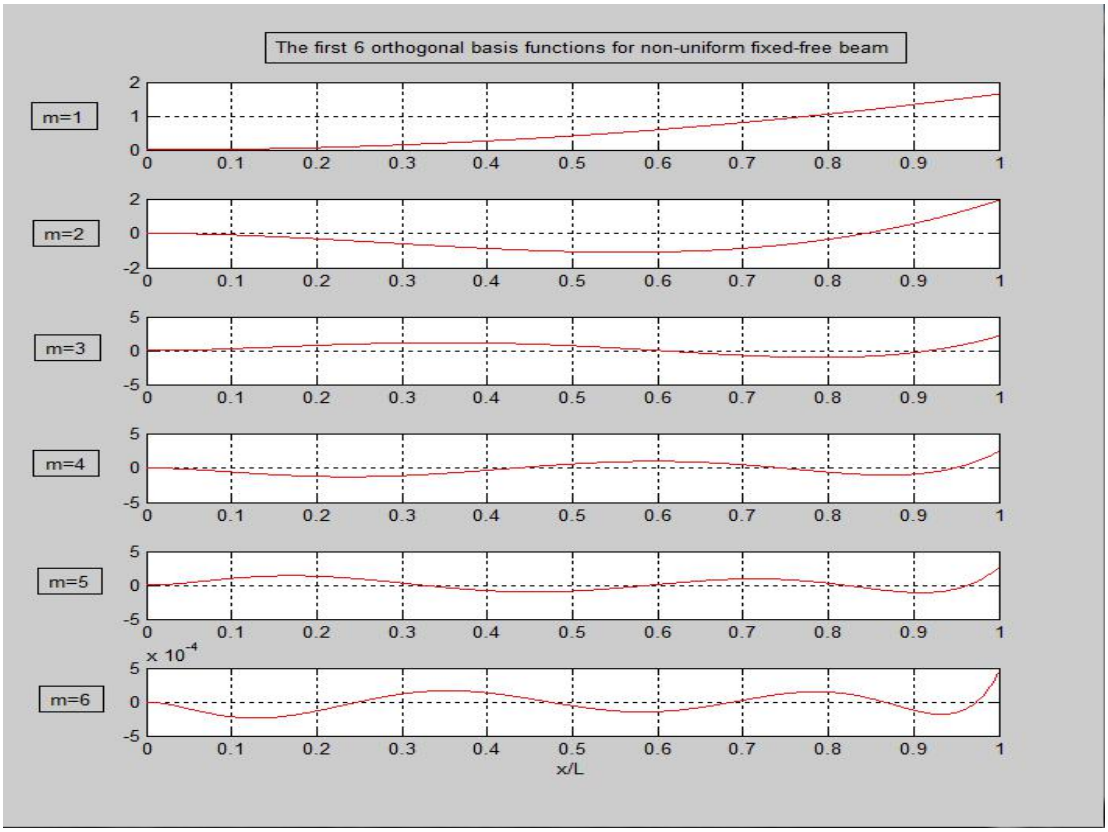

Figure 7 Orthogonal basis functions for fixed-free non-uniform beam

Comparing the plot in the Figure 7 with those in the Figure 5, it is found that the basis functions' value is reduced on its right side. This is quite consistent with mode shapes because the beam's stiffness on right side is higher.

Thus, it is valid to state that, the orthogonal basis function space developed in this thesis is a good representation of mode shape functions. However, analytic mode shape functions can not be obtainable for complex structures.

Chapter 5 Multi-layered and stiffened pipe, stiffener and hydrofoil element

In this chapter, three types of beam elements are developed based on the DG-FEM: multi-layered pipe, stiffener and hydrofoil element. The motivation of the work in this chapter is to embed the thesis's method into existent finite element code package in future. At first, the stiffener and hydrofoil structure is regarded as a beam.

The multi-layered pipe element based on the previous DG-FEM is developed in section 5.1. In this case, the interpolation functions in the beam length direction are prescribed as Lagrange interpolation functions, which makes it possible to combine the multi-layered pipe element with any commercial software's beam element. For the adjacent layers of multi-layered pipe structures, DG-FEM is applied. The orthogonal function spaces are also used in the circumferential and radial basis function spaces. A diagonal mass matrix is obtained for every cross section of the multi-layered pipe and a tri-diagonal mass matrix is obtained for the 3-D multi-layered pipe structure. Based on the author's work, the reference surface and wall thickness for each layer can be arbitrary functions along the axial and circumferential directions. Because of these assumptions, the multi-layered pipe element will have a wide application in marine and aerospace engineering.

The multi-layered stiffener element is developed in section 5.2. The stiffener is an arbitrary 3-D or 2-D curved beam, which can be coupled with plate/shell structures that are reinforced in the deflection direction. The DG-FEM is also applied to this

multi-layered stiffener element as is the case for the multi-layered pipe in section 5.1.

The multi-layered hydrofoil element is developed in section 5.3. For the first time, the hydrofoil structure with multi-layers and stiffeners are considered as a nonlinear beam. The stiffener of the hydrofoil is modeled along with the hydrofoil and it can be of arbitrary shape. The DG-FEM idea is also applied to the hydrofoil element.

5.1 Multi-layered Pipe Element

5.1.1 Kinematics of the multi-layered pipe element

In this section, the kinematics of the multi-layered pipe element is set up. The natural coordinate system $\xi_{1,2,3}$ is defined based on section 2.4.2. The mapping from natural coordinate system to the configuration of multi-layered pipe with variable wall thickness for every layer is first determined. The Jacobian matrix is obtained, and the determinant of the Jacobian matrix is also calculated in an explicit form. Then, the inverse of the Jacobian matrix is also obtained. It is noted that whatever the wall thickness functions are, there always exists the explicit formulation of the Jacobian matrix, its determinant and its inverse, which all are of vital importance. The basis function space is given for displacement field. A tensor product is used to define the multi-dimensional displacement field.

The multi-layered pipe structure with constant wall thickness is shown in Figure 8. For this kind of common multi-layered pipe, the wall thickness for each layer is a constant (the wall thickness can be different from layers to layers but it is a constant for a given layer).

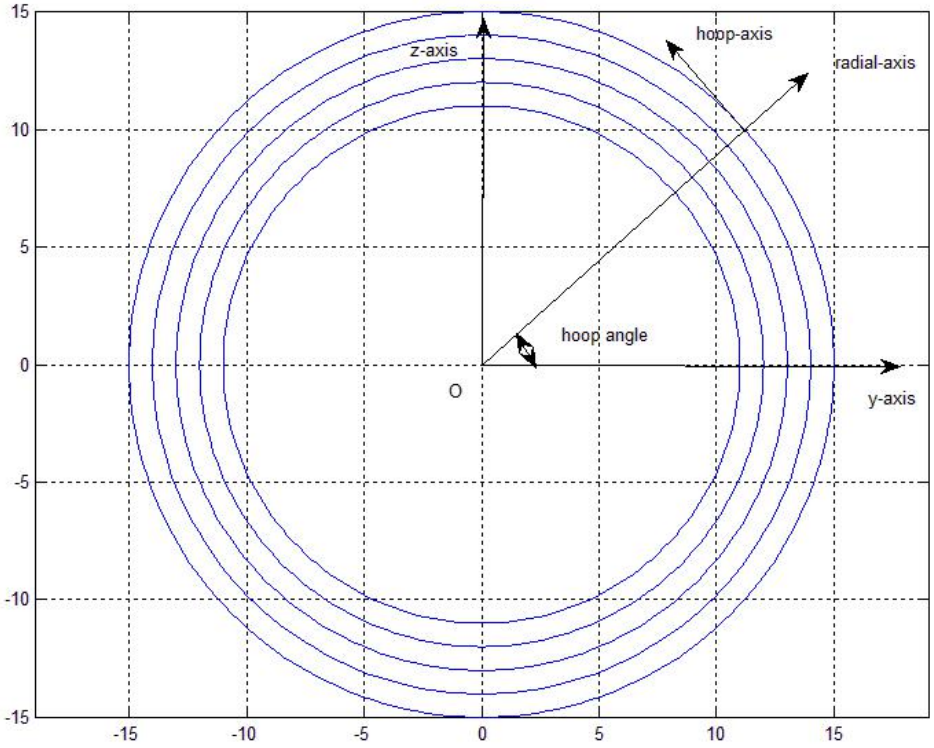

Figure 8 Multi-layered pipe structure cross-section with uniform wall thickness

For the so-called variable multi-layered pipe structure, the cross-section can be of any shape. The multi-layered pipe has many layers. For any cross section, the interface between adjacent layers can be formulated as a function of the circumferential coordinate.

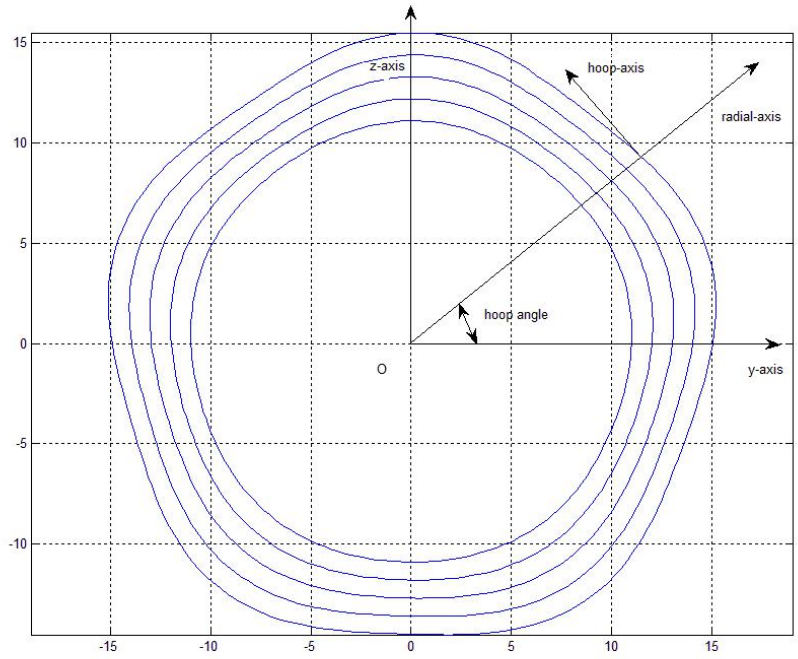

Figure 9 Variable wall thickness multi-layered pipe cross-section

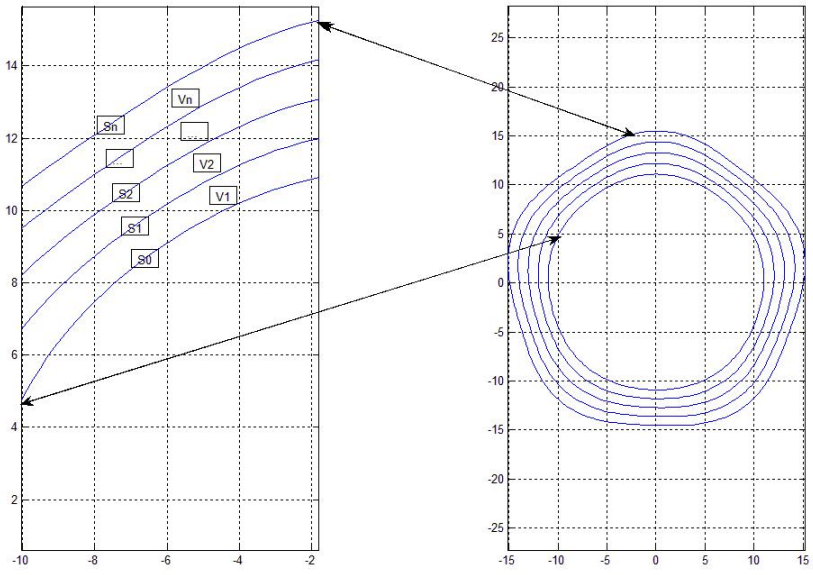

Figure 10 Multi-layered pipe structure notations

where ρ and θ are the polar coordinates, $V_k\ (k=1,2,3,\cdots,n_c)$ is denoted as the k th layer, n_c is the total number of layers, $S_k\,(k=0,1,2,\cdots,n_c)$ are the interfaces, S_0 is the bottom surface of V_1 , S_{n_c} is the top surface of V_{n_c} , $S_k\,(k=1,2,\cdots,n_c-1)$ is the interface between V_k and V_{k+1}.

If we extrude the cross-section along the pipe axial line, the 3-D multi-layered pipe structure will be formed. During the extrusion, the cross section could be changing. Thus, the interface is also a function of the axial coordinate.

The natural coordinates ξ_1, ξ_2, ξ_3^k are defined as:

$$\xi_1 = \frac{z}{L} \in [0,1]$$
$$\xi_2 = \frac{\theta}{2\pi} \in [0,1] \qquad \text{(127a, b, c)}$$
$$\xi_3^k = \frac{\rho - R_b^k(\xi_1,\xi_2)}{t_w^k(\xi_1,\xi_2)} \in [0,1]$$

where L is the total length of the pipe element, $R_b^k = R_b^k(\xi_1,\xi_2)$ is the bottom surface function of the k th layer, $R_{top}^k = R_{top}^k(\xi_1,\xi_2)$ is the top surface function of the k th layer, and $t_w^k(\xi_1,\xi_2) = R_{top}^k(\xi_1,\xi_2) - R_b^k(\xi_1,\xi_2)$ is the wall thickness of the k th layer.

The so-called bottom and top surface functions $R_b^k = R_b^k(\xi_1,\xi_2)$ and $R_{top}^k = R_{top}^k(\xi_1,\xi_2)$ measure the distance between the origin and the material point on the bottom/top surface. Assume that there is a radial line originating from the origin at an angle θ with respect to the x_2 axis. The line intersects with the interface $k, (k=1,2,3,\cdots,n_c)$. Then, the distance between the interacting point and the origin point is the surface

function. Obviously, the top surface of layer k is the bottom surface of layer $k+1$: $R_b^{k+1} = R_t^k$.

$R_b^k = R_b^k(\xi_1, \xi_2)$ and $R_{top}^k = R_{top}^k(\xi_1, \xi_2)$ are functions of ξ_2 because the radial line is controlled by $\theta = 2\pi\xi_2$. The surface functions are also functions about the axial direction ξ_1 because the cross-section could be changed during the extrusion.

For the mapping (127a, b, c), it is easy to verify that, when $\xi_3^k = 0$, $\rho = R_b^k$, which is the bottom surface of the k th layer; when $\xi_3^k = 1$, $\rho = R_b^k + t_w^k = R_{top}^k$, which is the top surface of the k th layer.

The variable wall-thickness pipe's element configuration can be formulated as

$$ {}^0\vec{r} = \begin{bmatrix} {}^0x_1 \\ {}^0x_2 \\ {}^0x_3 \end{bmatrix} = \begin{bmatrix} L\xi_1 \\ (R_b^k(\xi_1, \xi_2) + t_w^k(\xi_1, \xi_2)\xi_3)\cos(2\pi\xi_2) \\ (R_b^k(\xi_1, \xi_2) + t_w^k(\xi_1, \xi_2)\xi_3)\sin(2\pi\xi_2) \end{bmatrix} \tag{128} $$

where ${}^0\vec{r}$ is the initial configuration positive vector.

The Jacobian matrix is

$$ J_0 = \left[J_{ij}\right]_{3\times 3} \tag{129} $$

where

$$J_{11} = L$$

$$J_{12} = \frac{\partial(R_b^k + t_w^k \xi_3)}{\partial \xi_1} \cos(2\pi\xi_2)$$

$$J_{13} = \frac{\partial(R_b^k + t_w^k \xi_3)}{\partial \xi_1} \sin(2\pi\xi_2)$$

$$J_{21} = 0$$

$$J_{22} = \frac{\partial(R_b^k + t_w^k \xi_3)}{\partial \xi_2} \cos(2\pi\xi_2) - \frac{\pi}{2}(R + t_w^k \xi_3)\sin(2\pi\xi_2) \qquad \text{(130a, b, c, d, e, f, g, h, i)}$$

$$J_{23} = \frac{\partial(R_b^k + t_w^k \xi_3)}{\partial \xi_2} \sin(2\pi\xi_2) + \frac{\pi}{2}(R + t_w^i \xi_3)\cos(2\pi\xi_2)$$

$$J_{31} = 0$$

$$J_{32} = t_w^k \cos(2\pi\xi_2)$$

$$J_{33} = t_w^k \sin(2\pi\xi_2)$$

The absolute value of the Jacobian matrix's determinant is

$$\det(J_0) = \frac{\pi}{2} L t_w^k (R_b^k + t_w^k \xi_3) \qquad (131)$$

It's noted that even if the wall-thickness t_w^k and R_b^k are functions of ξ_1 , ξ_2 , the formulation of the determinant of the Jacobian matrix is a simple expression. With the application of variable t_w^k and R_b^k , more complex structure configurations can also be described with a simple expression for the Jacobian matrix determinant.

With the explicit formulation of the determinant of the Jacobian matrix, one can get the explicit formulation of the Jacobian matrix's inverse.

The displacement trial function spaces are next discussed. Three function spaces are defined as below; for $i = 1,2,3$:

$$V_\phi^k = \{\phi_{u_i}^{m_0} \mid \phi_{u_i}^m(\xi_1) \in P^m(\xi_1), \xi_1 \in [0,1], m = 1,2,3,\cdots,m_0\}$$

$$V_\psi^k = \{\psi_{u_i}^{n_0} \mid \psi_{u_i}^n(\xi_2) \in P^n(\xi_2), \xi_2 \in [0,1], n = 1,2,3,\cdots,n_0\} \qquad \text{(132a, b, c)}$$

$$V_{\varphi}^{k}=\{\varphi_{u_i}^{s_0}\mid \varphi_{u_i}^{s}(\xi_3)\in P^{s}(\xi_3),\xi_3\in[0,1],s=1,2,3,\cdots,s_0\}$$

where P^{l} is the polynomial function space whose highest order term is l.

Then, a tensor product is used to give the multi-dimensional displacement field as:

$$\begin{aligned}
u_1^k &= R_0 f_{u_1}^{\xi_1} f_{u_1}^{\xi_2} f_{u_1}^{\xi_3} \sum_{m,n,s=1}^{m_0,n_0,s_0} A_{mns}\phi_{u_1}^{m}(\xi_1)\psi_{u_1}^{n}(\xi_2)\varphi_{u_1}^{s}(\xi_3^k)\\
u_2^k &= R_0 f_{u_2}^{\xi_1} f_{u_2}^{\xi_2} f_{u_2}^{\xi_3} \sum_{m,n,s=1}^{m_0,n_0,s_0} B_{mns}\phi_{u_2}^{m}(\xi_1)\psi_{u_2}^{n}(\xi_2)\varphi_{u_2}^{s}(\xi_3^k) \qquad \text{(133a, b, c)}\\
u_3^k &= R_0 f_{u_3}^{\xi_1} f_{u_3}^{\xi_2} f_{u_3}^{\xi_3} \sum_{m,n,s=1}^{m_0,n_0,s_0} C_{mns}\phi_{u_3}^{m}(\xi_1)\psi_{u_3}^{n}(\xi_2)\varphi_{u_3}^{s}(\xi_3^k)
\end{aligned}$$

where u_1^k, u_2^k, u_3^k are denoted as the axial, circumferential and radial displacement; ξ_1, ξ_2, ξ_3^k are the natural coordinates (127a, b, c); m_0, n_0, s_0 are the highest orders for ξ_1, ξ_2, ξ_3^k; R_0 is a reference radius, which is only a constant to non-dimensionalize the degrees of freedom $A_{mns}^k, B_{mns}^k, C_{mns}^k$; $\phi_{u_i}^{m}(\xi_1)\in V_{\phi}^{k}, i=1,2,3$ are the Lagrangian interpolation functions about the axis coordinate ξ_1 for u_i; and $\psi_{u_i}^{n}(\xi_1)\in V_{\psi}^{k}, i=1,2,3$ and $\varphi_{u_i}^{s}(\xi_3^k)\in V_{\varphi}^{k}, i=1,2,3$ are the displacement basis functions about the circumferential coordinate ξ_2 and radial coordinate ξ_3^k, respectively. The specific formulation of $\psi_{u_i}, \varphi_{u_i}, i=1,2,3$ will be discussed later; $f_{u_i}^{\xi_j}$ is a displacement boundary condition function, which is used to define the displacement boundary condition about the circumferential coordinate ξ_j. If there is no displacement boundary condition about the circumferential coordinate, it is defined as 1. For the specific formulation of the displacement, we use Lagrange interpolation space for the axial displacement space (132a), and (132b, c) are still to be determined.

5.1.2 Traction DOF

The basis function space for the traction field T is defined by the Dirac's Delta function on the interior interface. The Dirac's Delta function $\delta(\xi-\xi_0)$ is located at the point ξ_0.

In order to define the interpolation function space for traction T, the collocation point vector is defined in the natural coordinate system $\xi_{1,2,3}$, and is denoted as

$$P_{ct}=\left[\xi_{ct1},\xi_{ct2},\xi_{ct3},\cdots,\xi_{ctn}\right] \tag{134}$$

Then, the traction is defined as:

$$T=N_T\widetilde{T}$$

$$\begin{aligned} &N_T(1,n_{ij})=\delta(\xi_1-\xi_{cti})\delta(\xi_2-\xi_{ctj}), i=1,2,\cdots n_1\,;\, j=1,2,\cdots n_2\\ &n_{ij}=(i-1)n_2+j \end{aligned} \tag{135a, b, c}$$

where $\delta(\xi-\xi_0)$ is the Dirac's Delta function:

$$\begin{aligned} &\int_S \delta(\xi-\xi_0)dS=1\\ &\int_S f(\xi)\delta(\xi-\xi_0)dS=f(\xi_0) \end{aligned} \tag{136a, b}$$

$n_{1,2}$ are the total collection points for the local direction $\xi_{1,2}$, $\widetilde{T}$ is the degree-of-freedom vector for traction field, $f(\xi)$ is any function.

The collection points vector $P_{ct}=\left[\xi_{ct1},\xi_{ct2},\xi_{ct3},\cdots,\xi_{ctn}\right]$ is defined as:

$$0<\xi_{ct1}<\xi_{ct2}<\xi_{ct3}<\cdots<\xi_{ctn}<1 \tag{137a}$$

$$(\xi-\xi_{ct1})(\xi-\xi_{ct2})\cdots(\xi-\xi_{ctn})=P_n^L(\xi) \tag{137b}$$

where $P_n^L(\xi)$ is the n th order Legendre orthogonal polynomial defined in [0,1].

Thus, $P_{ct} = \left[\xi_{ct1}, \xi_{ct2}, \xi_{ct3}, \cdots, \xi_{ctn}\right]$ is a vector of the Gauss integration points, where stress field's accuracy is 1-order higher than that of the other points.

5.1.3 Consistent Orthogonal Basis Function Space for pipe element

For multi-layered pipe element the mass matrix as derived in (116-125) becomes:

$$M_{i_1 i_2} = \rho_s R_0^2 \delta_{n_1 n_2} \delta_{k_1 k_2} \overline{M}_{m_1 m_2} \tag{138}$$

where

$$\overline{M}_{m_1 m_2} = diag\begin{pmatrix} \int [(f_{u_1}^{\xi_1})^2 f_{\det}^{\xi_1}] \phi_{u_1}^{m_1} \phi_{u_1}^{m_2} d\xi_1, \\ \int [(f_{u_2}^{\xi_1})^2 f_{\det}^{\xi_1}] \phi_{u_2}^{m_1} \phi_{u_2}^{m_2} d\xi_1, \\ \int [(f_{u_3}^{\xi_1})^2 f_{\det}^{\xi_1}] \phi_{u_3}^{m_1} \phi_{u_3}^{m_2} d\xi_1 \end{pmatrix} \tag{139}$$

From this formulation, it is obvious that, as long as $n_1 \neq n_2$ or $k_1 \neq k_2$, $M_{i_1 i_2}$ will be a zero matrix. When $n_1 = n_2$ and $k_1 = k_2$,

$$M_{i_1 i_2} = \rho_s R_0^2 \overline{M}_{m_1 m_2} \tag{140}$$

If a linear Lagrangian interpolation function is used in axial interpolation space, then, $m_0 = 2$ and

$$\begin{aligned} \phi_{u_i}^1 &= 1 - \xi_1 \\ \phi_{u_i}^2 &= \xi_1 \end{aligned} \tag{141a, b}$$

When $i_1 = i_2$, $n_1 = n_2$, $k_1 = k_2$:

Case (1), when $m_1 = m_2 = 1$, then

$$\overline{M}_{m_1 m_2} = \begin{vmatrix} \int [(f_{u_1}^{\xi_1})^2 f_{\det}^{\xi_1}](1-\xi_1)^2 d\xi_1 & 0 & 0 \\ 0 & \int [(f_{u_2}^{\xi_1})^2 f_{\det}^{\xi_1}](1-\xi_1)^2 d\xi_1 & 0 \\ 0 & 0 & \int [(f_{u_3}^{\xi_1})^2 f_{\det}^{\xi_1}](1-\xi_1)^2 d\xi_1 \end{vmatrix} \tag{142a}$$

Case (2), when $m_1 = m_2 = 2$, then

$$\overline{M}_{m_1 m_2} = \begin{vmatrix} \int [(f_{u_1}^{\xi_1})^2 f_{\det}^{\xi_1}]\xi_1^2 d\xi_1 & 0 & 0 \\ 0 & \int [(f_{u_2}^{\xi_1})^2 f_{\det}^{\xi_1}]\xi_1^2 d\xi_1 & 0 \\ 0 & 0 & \int [(f_{u_3}^{\xi_1})^2 f_{\det}^{\xi_1}]\xi_1^2 d\xi_1 \end{vmatrix} \tag{142b}$$

These are the diagonal elements of the mass matrix.

When $i_1 = i_2$, $n_1 = n_2$, $k_1 = k_2$ and $m_1 = 1, m_2 = 2$,

$$\overline{M}_{m_1 m_2} = \begin{vmatrix} \int [(f_{u_1}^{\xi_1})^2 f_{\det}^{\xi_1}](1-\xi_1)\xi_1 d\xi_1 & 0 & 0 \\ 0 & \int [(f_{u_2}^{\xi_1})^2 f_{\det}^{\xi_1}](1-\xi_1)\xi_1 d\xi_1 & 0 \\ 0 & 0 & \int [(f_{u_3}^{\xi_1})^2 f_{\det}^{\xi_1}](1-\xi_1)\xi_1 d\xi_1 \end{vmatrix} \tag{142c}$$

When $i_1 = i_2$, $n_1 = n_2$, $k_1 = k_2$ and $m_1 = 2, m_2 = 1$, it's the same case as (142c).

It's noted that, when $i_1 = i_2$, $n_1 = n_2$, $k_1 = k_2$ and $m_1 = 1, m_2 = 2$,

$$i_2 - i_1 = n_0 k_0 \tag{143a}$$

Similarly, when $i_1 = i_2$, $n_1 = n_2$, $k_1 = k_2$ and $m_1 = 2, m_2 = 1$,

$$i_1 - i_2 = n_0 k_0 \tag{143b}$$

In this case, the mass matrix will be like this:

$$\begin{vmatrix} \times 1 & & & o1 & & & \\ & \times 1 & & & o1 & & \\ & & \times 1 & & & o1 & \\ & & & \times 1 & & & o1 \\ o1 & & & \times 2 & & & \\ & o1 & & & \times 2 & & \\ & & o1 & & & \times 2 & \\ & & & o1 & & & \times 2 \end{vmatrix}$$

In this matrix, $\times 1$ represents (86a), $\times 2$ represents (86b), $o1$ represents (86c), other positions have zeros.

If a second order Lagrangian interpolation is used for ϕ_{u_i}, then

$$\begin{aligned} \phi^1_{u_i} &= (\xi_1 - 1)(2\xi_1 - 1) \\ \phi^2_{u_i} &= 4\xi_1 (1 - \xi_1) \\ \phi^3_{u_i} &= \xi_1 (2\xi_1 - 1) \end{aligned} \qquad \text{(144a, b, c)}$$

When $i_1 = i_2$, $n_1 = n_2$, $k_1 = k_2$:

Case (1), when $m_1 = m_2 = 1$, then

$$\overline{M}_{m_1 m_2} = \begin{vmatrix} \overline{M}^{11}_{m_1 m_2} & 0 & 0 \\ 0 & \overline{M}^{22}_{m_1 m_2} & 0 \\ 0 & 0 & \overline{M}^{33}_{m_1 m_2} \end{vmatrix} \qquad (145)$$

where

$$\overline{M}^{11}_{m_1 m_2} = \int [(f^{\xi_1}_{u_1})^2 f^{\xi_1}_{\det}][(\xi_1 - 1)(2\xi_1 - 1)]^2 d\xi_1$$
$$\overline{M}^{22}_{m_1 m_2} = \int [(f^{\xi_1}_{u_2})^2 f^{\xi_1}_{\det}][(\xi_1 - 1)(2\xi_1 - 1)]^2 d\xi_1 \qquad \text{(146a, b, c)}$$
$$\overline{M}^{33}_{m_1 m_2} = \int [(f^{\xi_1}_{u_3})^2 f^{\xi_1}_{\det}][(\xi_1 - 1)(2\xi_1 - 1)]^2 d\xi_1$$

Case (2), when $m_1 = m_2 = 2$, then

$$\overline{M}^{11}_{m_1 m_2} = \int [(f^{\xi_1}_{u_1})^2 f^{\xi_1}_{\det}][4\xi_1 (1 - \xi_1)]^2 d\xi_1$$
$$\overline{M}^{22}_{m_1 m_2} = \int [(f^{\xi_1}_{u_2})^2 f^{\xi_1}_{\det}][4\xi_1 (1 - \xi_1)]^2 d\xi_1 \qquad \text{(147a, b, c)}$$
$$\overline{M}^{33}_{m_1 m_2} = \int [(f^{\xi_1}_{u_3})^2 f^{\xi_1}_{\det}][4\xi_1 (1 - \xi_1)]^2 d\xi_1$$

Case (3), when $m_1 = m_2 = 3$, then

$$\overline{M}^{11}_{m_1 m_2} = \int [(f^{\xi_1}_{u_1})^2 f^{\xi_1}_{\det}][\xi_1 (2\xi_1 - 1)]^2 d\xi_1$$
$$\overline{M}^{22}_{m_1 m_2} = \int [(f^{\xi_1}_{u_2})^2 f^{\xi_1}_{\det}][\xi_1 (2\xi_1 - 1)]^2 d\xi_1 \qquad \text{(148a, b, c)}$$
$$\overline{M}^{33}_{m_1 m_2} = \int [(f^{\xi_1}_{u_3})^2 f^{\xi_1}_{\det}][\xi_1 (2\xi_1 - 1)]^2 d\xi_1$$

These are the diagonal elements of the mass matrix.

When $i_1 = i_2$, $n_1 = n_2$, $k_1 = k_2$ and $m_1 = 1, m_2 = 2$,

$$\overline{M}^{11}_{m_1 m_2} = \int [(f^{\xi_1}_{u_1})^2 f^{\xi_1}_{\det}][(\xi_1 - 1)(2\xi_1 - 1)4\xi_1 (1 - \xi_1)] d\xi_1$$
$$\overline{M}^{22}_{m_1 m_2} = \int [(f^{\xi_1}_{u_2})^2 f^{\xi_1}_{\det}][(\xi_1 - 1)(2\xi_1 - 1)4\xi_1 (1 - \xi_1)] d\xi_1 \qquad \text{(149a, b, c)}$$
$$\overline{M}^{33}_{m_1 m_2} = \int [(f^{\xi_1}_{u_3})^2 f^{\xi_1}_{\det}][(\xi_1 - 1)(2\xi_1 - 1)4\xi_1 (1 - \xi_1)] d\xi_1$$

When $i_1 = i_2$, $n_1 = n_2$, $k_1 = k_2$ and $m_1 = 2, m_2 = 1$, it is the same as (149a, b, c).

When $i_1 = i_2$, $n_1 = n_2$, $k_1 = k_2$ and $m_1 = 1, m_2 = 3$,

$$\overline{M}^{11}_{m_1 m_2} = \int [(f^{\xi_1}_{u_1})^2 f^{\xi_1}_{\det}][(\xi_1 - 1)(2\xi_1 - 1)\xi_1 (2\xi_1 - 1)]d\xi_1$$
$$\overline{M}^{22}_{m_1 m_2} = \int [(f^{\xi_1}_{u_2})^2 f^{\xi_1}_{\det}][(\xi_1 - 1)(2\xi_1 - 1)\xi_1 (2\xi_1 - 1)]d\xi_1 \qquad (150a, b, c)$$
$$\overline{M}^{33}_{m_1 m_2} = \int [(f^{\xi_1}_{u_3})^2 f^{\xi_1}_{\det}][(\xi_1 - 1)(2\xi_1 - 1)\xi_1 (2\xi_1 - 1)]d\xi_1$$

When $i_1 = i_2$, $n_1 = n_2$, $k_1 = k_2$ and $m_1 = 3, m_2 = 1$, it is the same as (150a, b, c).

When $i_1 = i_2$, $n_1 = n_2$, $k_1 = k_2$ and $m_1 = 2, m_2 = 3$,

$$\overline{M}^{11}_{m_1 m_2} = \int [(f^{\xi_1}_{u_1})^2 f^{\xi_1}_{\det}][4\xi_1 (1-\xi_1)\xi_1 (2\xi_1 - 1)]d\xi_1$$
$$\overline{M}^{22}_{m_1 m_2} = \int [(f^{\xi_1}_{u_2})^2 f^{\xi_1}_{\det}][4\xi_1 (1-\xi_1)\xi_1 (2\xi_1 - 1)]d\xi_1 \qquad (151a, b, c)$$
$$\overline{M}^{33}_{m_1 m_2} = \int [(f^{\xi_1}_{u_3})^2 f^{\xi_1}_{\det}][4\xi_1 (1-\xi_1)\xi_1 (2\xi_1 - 1)]d\xi_1$$

When $i_1 = i_2$, $n_1 = n_2$, $k_1 = k_2$ and $m_1 = 3, m_2 = 2$, it's the same as (151a, b, c).

These are the non-diagonal elements. The mass matrix will be like this:

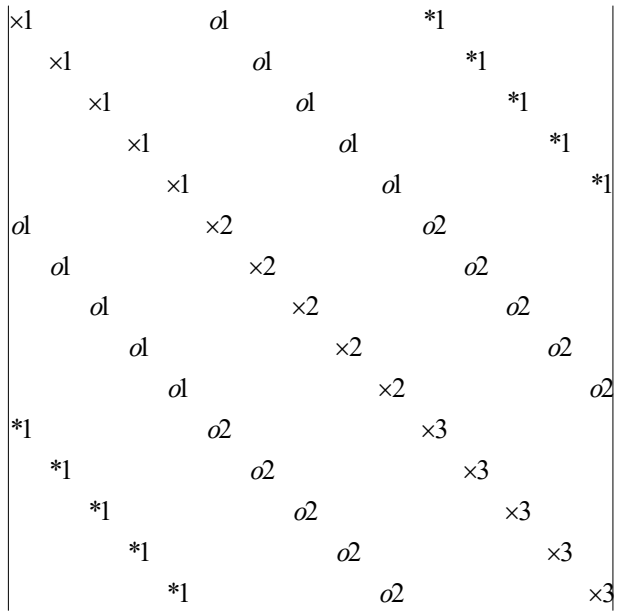

where $\times 1$ represents (146a, b, c), $\times 2$ represents (147a, b, c), $\times 3$ represents (148a, b, c), $o1$ represents (149a, b, c), $o2$ represents (150a, b, c), $*\ 1$ represents (151a, b, c).

In this case, the mass matrix will be a 5-diagonal matrix.

The determinant of the Jacobian matrix is important for the development of the orthogonal basis functions developed in this thesis. We next discuss the special consideration of the multi-layered pipe's Jacobian matrix.

Case (i): Thin multi-layered pipe

In this case, even if t_w^i and R_w^i are functions, $t_w^i << R_w^i$. So the mid-value theorem is used in ξ_3, which means:

$$\det(J_0) = 2\pi L^i t_w^i (R_w^i + t_w^i \xi_3) \approx 2\pi L^i t_w^i (R_w^i + t_w^i / 2) \tag{152}$$

Moreover, if the length of each pipe element is small enough(this is possible as long as more pipe elements are used in the axial direction), the mid-value theorem can be also used in ξ_1, thus

$$\begin{aligned} t_w^i(\xi_1, \xi_2) &= \sum_m \phi_m (1/2) t_m^i(\xi_2) = t_w^i(\xi_2) \\ R_w^i(\xi_1, \xi_2) &= \sum_m \phi_m (1/2) R_m^i(\xi_2) = R_w^i(\xi_2) \end{aligned} \tag{153a, b}$$

Thus,

$$\det(J_0) = 2\pi L^i t_w^i (R_w^i + t_w^i / 2) = 2\pi L^i t_w^i(\xi_2)[R_w^i(\xi_2) + t_w^i(\xi_2)/2] \tag{154}$$

Therefore, the determinant will approximately be a function of ξ_2. This result is valid because the circumferential size of the pipe element is much larger than the thickness (thin pipe) and axial size (by using more elements, and each element axial size will be small enough).

Case (ii): Thick multi-layered pipe

In this case, it is assumed that $R_w^i << t_w^i$ or even $R_w^i = 0$. Comparing with the case(i), this kind of structure will be much thicker and might not be hollow($R_w^i = 0$). The mid-value theorem can't be used for ξ_3 but can be used for ξ_1. In this case,

$$\det(J_0) \approx \frac{\pi}{2} L^i t_w^i(\xi_2) t_w^i(\xi_2) \xi_3 \tag{155}$$

So the assumption will still hold true. In this case, the determinant will be a function about ξ_2 and ξ_3. For ξ_3, it's just a simple linear function.

Case (iii): t_w^i and R_w^i are comparable. The mid-value theorem is first applied for ξ_1, we can get two kinds of results:

$$\begin{aligned} \det(J_0) &= \frac{\pi}{2} L^i t_w^i(\xi_2)[R_w^i(\xi_2) + t_w^i(\xi_2)\xi_3] \\ &= \frac{\pi}{2} L^i t_w^i(\xi_2) t_w^i(\xi_2)[\frac{R_w^i(\xi_2)}{t_w^i(\xi_2)} + \xi_3] \end{aligned} \tag{156a}$$

or

$$\begin{aligned} \det(J_0) &= \frac{\pi}{2} L^i t_w^i(\xi_2)[R_w^i(\xi_2) + t_w^i(\xi_2)\xi_3] \\ &= \frac{\pi}{2} L^i t_w^i(\xi_2) R_w^i(\xi_2)[1 + \frac{t_w^i(\xi_2)}{R_w^i(\xi_2)}\xi_3] \end{aligned} \tag{156b}$$

The mid-value theorem is applied for the term $\frac{R_w^i(\xi_2)}{t_w^i(\xi_2)}$ for (100a) and $\frac{t_w^i(\xi_2)}{R_w^i(\xi_2)}$ for (156b). Thus

$$\det(J_0) = \frac{\pi}{2} L^i t_w^i(\xi_2) t_w^i(\xi_2)[\frac{R_w^i(1/2)}{t_w^i(1/2)} + \xi_3] \tag{157a}$$

or

$$\det(J_0) = \frac{\pi}{2} L^i t_w^i(\xi_2) R_w^i(\xi_2)[1 + \frac{t_w^i(1/2)}{R_w^i(1/2)} \xi_3] \quad (157b)$$

In (157a, b), the assumption is also satisfied.

5.1.4 Static condensation

The discrete FEM equations with DOFs of displacement and traction force can be written as:

$$\begin{bmatrix} K & -H \\ -H^T & 0 \end{bmatrix} \begin{bmatrix} \widetilde{u} \\ \widetilde{T} \end{bmatrix} = \begin{bmatrix} R_f \\ 0 \end{bmatrix} \quad (158a, b)$$
$$R_f = Q - F$$

where K is the equivalent tangential stiffness matrix, and

$$H = \int_S N_u^T N_T dS \quad (158c)$$

For the case of static analysis, we have:

$$K = K_l + K_{n_1} - K_{n_2} + K_Q \quad (159a)$$

For the case of explicit dynamics analysis, we have

$$K = \frac{M}{dt^2} \quad (159b)$$

For the case of implicit dynamics analysis, we have:

$$K = K_l + K_{n_1} - K_{n_2} + K_Q + \alpha \frac{M}{dt^2} \quad (159c)$$

where α is a parameter dependent on the implicit time integration method.

Thus, from the first row of (158):

$$\widetilde{u} = K^{-1}\left(R_f + H\widetilde{T}\right) \quad (160)$$

Substituting (160) into the second row of (158),

$$
\begin{aligned}
&-H^T\left(K^{-1}\left(R_f+H\widetilde{T}\right)\right)=0\\
&\left(H^TK^{-1}H\right)\widetilde{T}=-H^TK^{-1}R_f\\
&\widetilde{T}=\left(H^TK^{-1}H\right)^{-1}\left(-H^TK^{-1}R_f\right)
\end{aligned}
\tag{161}
$$

Then, substitute (161) to (160)

$$\widetilde{u}=K^{-1}\left(R_f+H\left(\left(H^TK^{-1}H\right)^{-1}\left(-H^TK^{-1}R_f\right)\right)\right) \tag{162}$$

It is noted that the traction DOFs are eliminated. The augmented part ($-H$,$-H^T$) in (158) is removed. The unbalanced force R_f is modified to:

$$\left(R_f+H\left(\left(H^TK^{-1}H\right)^{-1}\left(-H^TK^{-1}R_f\right)\right)\right) \tag{163}$$

Thus, for the case of explicit dynamical analysis, where (159b) is true, the tri-diagonal mass matrix is maintained. If we use (158), the augmented part will make the whole system non tri-diagonal.

5.2 Curved stiffener element

The curve stiffener element is discussed in this section. In section 5.2.1, the general 3-D curved stiffener is discussed. In section 5.2.2, the 2-D curved stiffener is discussed, which has been widely used in the stiffened plate structure.

5.2.1 3-D Arbitrary curved stiffener element

In this section, the kinematics of the curved stiffener element is established. The spaced curved stiffener structure is formed this way: Given a cross section and a spaced curve, extrude the cross section along the spaced curve and keep the cross

section normal to the tangential direction of the spaced curve. During the extrusion, the cross section can change. The spaced curve is called curved stiffener axial line. A local coordinate system is set up based on the curved stiffener axial line. The first axis of the local coordinate system is tangential to the curved stiffener axial line. The other two axis of the local coordinate system are normal to the first axis and also normal to each other. Moreover, the second axis belongs to a fixed plane in the global coordinate system. With such a definition, we can formulate the rotation matrix between local coordinate system and global coordinate system. The rotation matrix is a function of the curve parameter coordinate ξ_s .

Then, the natural coordinate system $\xi_{1,2,3}$ is found. Here, ξ_1 is defined along the curved stiffener axial line and it is dependent on ξ_s . The other two natural coordinates, ξ_2 and ξ_3 are defined based on the variable wall thickness pipe element. Thus, we can get the configuration of the cross section in the local coordinate system for any given value of ξ_s . The rotation matrix at this value of ξ_s is also known. Thus, the global material coordinates of the curved stiffener element are found.

The global coordinate system and the local coordinate system are both set up, denoted as $\vec{e}_i^{\,g}, i = 1,2,3$ and $\vec{e}_i^{\,l}, i = 1,2,3$, respectively. The normal Cartesian coordinate system is applied. Thus,

$$\vec{e}_i^{\,g} \cdot \vec{e}_j^{\,g} = \delta_{ij}$$
$$\vec{e}_i^{\,l} \cdot \vec{e}_j^{\,l} = \delta_{ij} \qquad \text{(164a, b)}$$

The material coordinates defined in the global coordinate system $\vec{e}_i^{\,g}, i = 1,2,3$ are denoted as $x_i^g, i = 1,2,3$. In this case, the global position vector is defined as:

$$\vec{r}^{\,g} = \begin{bmatrix} x_1^g \\ x_2^g \\ x_3^g \end{bmatrix} \tag{165}$$

The material coordinates defined in the local coordinate system $\vec{e}_i^{\,l}, i = 1,2,3$ are denoted as $x_i^l, i = 1,2,3$. In this case, the local position vector is defined as:

$$\vec{r}^{\,l} = \begin{bmatrix} x_1^l \\ x_2^l \\ x_3^l \end{bmatrix} \tag{166}$$

A parameter coordinate ξ_s is defined for the spaced curve. In this case, the spaced curve positive vector can be formulated as:

$$\vec{r}^{\,o} = \begin{bmatrix} x_1^o(\xi_s) \\ x_2^o(\xi_s) \\ x_3^o(\xi_s) \end{bmatrix} \tag{167}$$

where $x_i^o, i = 1,2,3$ are the coordinates of the curve, $\xi_s \in [0, n_e]$, n_e is the total number of elements.

The nature coordinates are denoted as $\xi_i, i = 1,2,3$.

The local coordinate system is defined as in Figure 11. The $\vec{e}_i^{\,l}, i = 1,2,3$ are defined in equations (170-171).

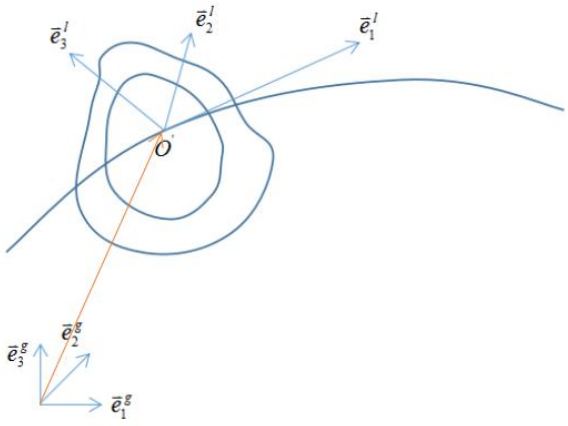

Figure 11 Curved stiffener structure (curved stiffener beam)

From this definition, $\vec{e}_i^{\,l}, i = 1,2,3$ satisfy:

$$\begin{aligned} &\vec{e}_1^{\,l} = \vec{n}_t \\ &\vec{e}_2^{\,l} \cdot \vec{e}_1^{\,l} = 0 \\ &\vec{e}_3^{\,l} \cdot \vec{e}_1^{\,l} = 0 \end{aligned} \qquad \text{(168a, b, c)}$$

where $\vec{n}_t$ is the tangential vector of the curve $\vec{r}^{\,o}$.

Thus, given the parameter function of the spaced curve, the tangential direction is:

$$\vec{e}_1^{\,l} = \frac{\dfrac{d\vec{r}^{\,o}}{d\xi_s}}{\left|\dfrac{d\vec{r}^{\,o}}{d\xi_s}\right|} = \frac{1}{\left|\dfrac{d\vec{r}^{\,o}}{d\xi_s}\right|}\begin{bmatrix} \dfrac{dx_1^o}{d\xi_s} \\ \dfrac{dx_2^o}{d\xi_s} \\ \dfrac{dx_3^o}{d\xi_s} \end{bmatrix} = \frac{1}{ne_1}\begin{bmatrix} \dfrac{dx_1^o}{d\xi_s} \\ \dfrac{dx_2^o}{d\xi_s} \\ \dfrac{dx_3^o}{d\xi_s} \end{bmatrix} \qquad \text{(169a, b)}$$

$$ne_1 = \sqrt{\left(\frac{dx_1^o}{d\xi_s}\right)^2 + \left(\frac{dx_2^o}{d\xi_s}\right)^2 + \left(\frac{dx_3^o}{d\xi_s}\right)^2}$$

where ne_1 is the norm of the vector $\vec{e}_1^{\,l}$.

In order to satisfy the condition (168b, c), we define the other two axis $\vec{e}_i^{\,l}, i = 2,3$ of the local coordinate system as:

$$\vec{e}_2^{\,l} = \frac{1}{ne_2}\begin{bmatrix} -\dfrac{dx_2^o}{d\xi_s} \\ \dfrac{dx_1^o}{d\xi_s} \\ \\ 0 \end{bmatrix} \tag{170a}$$

$$\vec{e}_3^{\,l} = \vec{e}_1^{\,l} \times \vec{e}_2^{\,l} = \frac{1}{ne_3}\begin{bmatrix} -\dfrac{dx_1^o}{d\xi_s}\dfrac{dx_3^o}{d\xi_s} \\ -\dfrac{dx_2^o}{d\xi_s}\dfrac{dx_3^o}{d\xi_s} \\ \left(\dfrac{dx_1^o}{d\xi_s}\right)^2 + \left(\dfrac{dx_2^o}{d\xi_s}\right)^2 \end{bmatrix} \tag{170b}$$

Where

$$ne_2 = \sqrt{\left(\frac{dx_2^o}{d\xi_s}\right)^2 + \left(\frac{dx_1^o}{d\xi_s}\right)^2} \tag{170c}$$

$$\begin{aligned} ne_3 &= \sqrt{\left(\frac{dx_1^o}{d\xi_s}\frac{dx_3^o}{d\xi_s}\right)^2 + \left(\frac{dx_2^o}{d\xi_s}\frac{dx_3^o}{d\xi_s}\right)^2 + \left(\left(\frac{dx_1^o}{d\xi_s}\right)^2 + \left(\frac{dx_2^o}{d\xi_s}\right)^2\right)^2} \\ &= \sqrt{\left(\frac{dx_3^o}{d\xi_s}\right)^2\left(\left(\frac{dx_1^o}{d\xi_s}\right)^2 + \left(\frac{dx_2^o}{d\xi_s}\right)^2\right) + \left(\left(\frac{dx_1^o}{d\xi_s}\right)^2 + \left(\frac{dx_2^o}{d\xi_s}\right)^2\right)^2} \\ &= \sqrt{\left(\left(\frac{dx_3^o}{d\xi_s}\right)^2 + \left(\frac{dx_1^o}{d\xi_s}\right)^2 + \left(\frac{dx_2^o}{d\xi_s}\right)^2\right)\left(\left(\frac{dx_1^o}{d\xi_s}\right)^2 + \left(\frac{dx_2^o}{d\xi_s}\right)^2\right)} \\ &= ne_1 \times ne_2 \end{aligned} \tag{170d}$$

It is noted that $\vec{e}_2^{\,l}$ is always in the plane of $x_1^g - x_2^g$ since its third component is always 0.

Then, the rotation matrix between the global coordinate system and the local coordinate system is obtained:

$$T=\left[\vec{e}_1^{\,l} \quad \vec{e}_2^{\,l} \quad \vec{e}_3^{\,l}\right]=\begin{bmatrix} \frac{1}{ne_1}\frac{dx_1^o}{d\xi_s} & -\frac{1}{ne_2}\frac{dx_2^o}{d\xi_s} & -\frac{1}{ne_1}\frac{1}{ne_2}\frac{dx_1^o}{d\xi_s}\frac{dx_3^o}{d\xi_s} \\ \frac{1}{ne_1}\frac{dx_2^o}{d\xi_s} & \frac{1}{ne_2}\frac{dx_1^o}{d\xi_s} & -\frac{1}{ne_1}\frac{1}{ne_2}\frac{dx_2^o}{d\xi_s}\frac{dx_3^o}{d\xi_s} \\ \frac{1}{ne_1}\frac{dx_3^o}{d\xi_s} & 0 & \frac{1}{ne_1}\frac{1}{ne_2}\left(\left(\frac{dx_1^o}{d\xi_s}\right)^2+\left(\frac{dx_2^o}{d\xi_s}\right)^2\right) \end{bmatrix} \tag{171}$$

The natural coordinate system is described.

First, the curve parameter coordinate ξ_s is discretized. For the element i, we defined the nature coordinate ξ_1 as:

$$\begin{aligned} &\xi_s = i-1+\xi_1 \\ &\xi_1 \in [0,1] \end{aligned} \tag{172a, b}$$

Where i is the stiffener element number, which is defined from 1 to n_{ele} from one end to the other end. n_{ele} is the total number of the stiffener element.

When $\xi_1 = 0, \xi_s = i-1$, which is the summation of the ξ_1 of the previous $i-1$ elements; when $\xi_1 = 1, \xi_s = i$, which is the summation of the ξ_1 of all these i elements. The novelty is, instead of discretizing arc length into elements, the curve parameter coordinate is discretized into uniform intervals. That's the reason why the interval of ξ_s is defined as $[0, n_{ele}]$.

Given the parameter curve formulation, one can uniquely determine the total arc length of the curve:

$$s=\int_0^{\xi_s}\sqrt{\left(\frac{dx_1^o}{d\xi_s}\right)^2+\left(\frac{dx_2^o}{d\xi_s}\right)^2+\left(\frac{dx_3^o}{d\xi_s}\right)^2}\,d\xi_s \tag{173}$$

Take (172) into (167) and (171), and it is also observed that $\frac{d}{d\xi_s}=\frac{d}{d\xi_1}\frac{d\xi_1}{d\xi_s}=\frac{d}{d\xi_1}$,

we have:

$$\vec{r}^{\,o}\left(\xi_1\right)=\begin{bmatrix} x_1^o(\xi_1,i) \\ x_2^o(\xi_1,i) \\ x_3^o(\xi_1,i) \end{bmatrix} \tag{174}$$

$$T=\begin{bmatrix} \frac{1}{ne_1}\frac{dx_1^o}{d\xi_1} & -\frac{1}{ne_2}\frac{dx_2^o}{d\xi_1} & -\frac{1}{ne_1}\frac{1}{ne_2}\frac{dx_1^o}{d\xi_1}\frac{dx_3^o}{d\xi_1} \\ \frac{1}{ne_1}\frac{dx_2^o}{d\xi_1} & \frac{1}{ne_2}\frac{dx_1^o}{d\xi_1} & -\frac{1}{ne_1}\frac{1}{ne_2}\frac{dx_2^o}{d\xi_1}\frac{dx_3^o}{d\xi_1} \\ \frac{1}{ne_1}\frac{dx_3^o}{d\xi_1} & 0 & \frac{1}{ne_1}\frac{1}{ne_2}\left(\left(\frac{dx_1^o}{d\xi_1}\right)^2+\left(\frac{dx_2^o}{d\xi_1}\right)^2\right) \end{bmatrix}$$

$$ne_1=\sqrt{\left(\frac{dx_1^o}{d\xi_1}\right)^2+\left(\frac{dx_2^o}{d\xi_1}\right)^2+\left(\frac{dx_3^o}{d\xi_1}\right)^2} \tag{175a, b, c}$$

$$ne_2=\sqrt{\left(\frac{dx_2^o}{d\xi_1}\right)^2+\left(\frac{dx_1^o}{d\xi_1}\right)^2}$$

For a given value ξ_1 and its element number i, the cross-section is uniquely located. Also, the local coordinate system is definite and the rotation matrix is calculated using (175). In the local coordinate system, the cross-section configuration is defined as:

$$\vec{r}^{\,l}=\begin{bmatrix} x_1^l \\ x_2^l \\ x_3^l \end{bmatrix}=\begin{bmatrix} 0 \\ \left(R(\xi_s,\xi_2)+\xi_3 t_w(\xi_s,\xi_2)\right)\cos(2\pi\xi_2) \\ \left(R(\xi_s,\xi_2)+\xi_3 t_w(\xi_s,\xi_2)\right)\sin(2\pi\xi_2) \end{bmatrix}=\begin{bmatrix} 0 \\ \left(R(\xi_1,\xi_2,i)+\xi_3 t_w(\xi_1,\xi_2,i)\right)\cos(2\pi\xi_2) \\ \left(R(\xi_1,\xi_2,i)+\xi_3 t_w(\xi_1,\xi_2,i)\right)\sin(2\pi\xi_2) \end{bmatrix} \tag{176}$$

It is noted that the cross-section's wall thickness and reference surface can be arbitrary. The point O' is the origin of the local coordinate system. It is determined

by the parameter curve in (174), once given a value of ξ_s. From the local coordinate system origin point $O^{'}$, there generates a radial line that interacts with the inner surface at point O. The distance between O and $O^{'}$ is defined as R. It is obvious that R is a function of ξ_2 and it is also changing with ξ_s. By extending the radial $O^{'}O$, the radial will intersect with the outer surface of the cross-section. The distance between this point and the point O is the wall thickness. As R, t_w is also a function of ξ_2 and ξ_s.

Given the local coordinates of each cross section, the rotation matrix and the spaced curve coordinate, we can get the global coordinates of the curved stiffener as:

$$\vec{r}^{\,g} = T(\xi_1, i)\vec{r}^{\,l}(\xi_1, \xi_2, \xi_3, i) + \vec{r}^{\,o}(\xi_1, i)$$

$$T(\xi_1, i) = \begin{bmatrix} \frac{1}{ne_1}\frac{dx_1^o}{d\xi_1} & -\frac{1}{ne_2}\frac{dx_2^o}{d\xi_1} & -\frac{1}{ne_1}\frac{1}{ne_2}\frac{dx_1^o}{d\xi_1}\frac{dx_3^o}{d\xi_1} \\ \frac{1}{ne_1}\frac{dx_2^o}{d\xi_1} & \frac{1}{ne_2}\frac{dx_1^o}{d\xi_1} & -\frac{1}{ne_1}\frac{1}{ne_2}\frac{dx_2^o}{d\xi_1}\frac{dx_3^o}{d\xi_1} \\ \frac{1}{ne_1}\frac{dx_3^o}{d\xi_1} & 0 & \frac{1}{ne_1}\frac{1}{ne_2}\left(\left(\frac{dx_1^o}{d\xi_1}\right)^2 + \left(\frac{dx_2^o}{d\xi_1}\right)^2\right) \end{bmatrix} \qquad \text{(177a, b, c, d)}$$

$$\vec{r}^{\,l}(\xi_1, \xi_2, \xi_3, i) = \begin{bmatrix} 0 \\ \left(R(\xi_1, \xi_2, i) + \xi_3 t_w(\xi_1, \xi_2, i)\right)\cos(2\pi\xi_2) \\ \left(R(\xi_1, \xi_2, i) + \xi_3 t_w(\xi_1, \xi_2, i)\right)\sin(2\pi\xi_2) \end{bmatrix}$$

$$\vec{r}^{\,o}(\xi_1, i) = \begin{bmatrix} x_1^o(\xi_1, i) \\ x_2^o(\xi_1, i) \\ x_3^o(\xi_1, i) \end{bmatrix}$$

The displacement trial function spaces are discussed. Three function spaces are defined as below for $i = 1,2,3$:

$$V_\phi = \{\phi_{u_i}^{m_0} \mid \phi_{u_i}^{m}(\xi_1) \in P^m(\xi_1), \xi_1 \in [0,1], m = 1,2,3,\cdots,m_0\}$$

$$V_{\psi} = \{\psi_{u_i}^{n_0} \mid \psi_{u_i}^{n}(\xi_2) \in P^n(\xi_2), \xi_2 \in [0,1], n = 1,2,3,\cdots,n_0\}$$

$$V_{\varphi} = \{\varphi_{u_i}^{k_0} \mid \varphi_{u_i}^{k}(\xi_3) \in P^k(\xi_3), \xi_3 \in [0,1], k = 1,2,3,\cdots,k_0\}$$

Where P^i is the polynomial function space whose highest order term has order i.

The multi-dimensional displacement field is defined in the natural coordinate system by a tensor product.

$$\begin{aligned} u_1 &= \sum_{m,n,k=1}^{m_0,n_0,k_0} A_{mnk}\phi_{u_1}^{m}(\xi_1)\psi_{u_1}^{n}(\xi_2)\phi_{u_1}^{k}(\xi_3) \\ u_2 &= \sum_{m,n,k=1}^{m_0,n_0,k_0} B_{mnk}\phi_{u_2}^{m}(\xi_1)\psi_{u_2}^{n}(\xi_2)\phi_{u_2}^{k}(\xi_3) \\ u_3 &= \sum_{m,n,k=1}^{m_0,n_0,k_0} C_{mnk}\phi_{u_3}^{m}(\xi_1)\psi_{u_3}^{n}(\xi_2)\phi_{u_3}^{k}(\xi_3) \end{aligned} \tag{178}$$

where $\phi_{u_i}^{m}(\xi_1), \psi_{u_i}^{n}(\xi_2), \phi_{u_i}^{k}(\xi_3)$ are the basis functions defined in terms of natural coordinate system ξ_1, ξ_2, ξ_3 for u_i, $A_{mnk}, B_{mnk}, C_{mnk}$ are the degrees-of-freedom, m, n, k are the number of basis functions, m_0, n_0, k_0 are the total order of the various basis functions.

The Jacobi matrix is defined as:

$$J = \begin{bmatrix} \frac{\partial r_1^g}{\partial \xi_1} & \frac{\partial r_2^g}{\partial \xi_1} & \frac{\partial r_3^g}{\partial \xi_1} \\ \frac{\partial r_1^g}{\partial \xi_2} & \frac{\partial r_2^g}{\partial \xi_2} & \frac{\partial r_3^g}{\partial \xi_2} \\ \frac{\partial r_1^g}{\partial \xi_3} & \frac{\partial r_2^g}{\partial \xi_3} & \frac{\partial r_3^g}{\partial \xi_3} \end{bmatrix} \tag{179}$$

With the definition of global configuration vector $\vec{r}^{\,g}$, the material derivatives are calculated as:

$$\frac{\partial}{\partial {}^t r_i^g} = \frac{\partial}{\partial \xi_k}\frac{\partial \xi_k}{\partial {}^t r_i^g}, k = 1,2,3 \tag{180}$$

Where the reference configuration is calculated as:

$${}^t r_i^g = r_i^g + {}^t u_i \tag{181}$$

${}^t u_i$ is the total displacement at time t in the dimension i.

The definition of the curved pipe axial line $\vec{r}^{\,o}$ is important for the success of the curved pipe element. The spaced curve is a function of ξ_s or ξ_1. NURBS are applied here to give the formulation of the spaced curve. For the orthogonal basis functions space and the DG-FEM implementation details, they are identical with the multi-layered pipe.

A special case is discussed. If the curved stiffener axial line is an in-plane curve, the global coordinate system can be defined according to this plane. The formulation can be simplified. The curve formulation can be defined as:

$$\vec{r}^{\,o}\left(\xi_1\right) = \begin{bmatrix} x_1^o(\xi_1) \\ x_2^o(\xi_1) \\ 0 \end{bmatrix} \tag{182}$$

By using (180), the global coordinate system's $x_1^g x_2^g$ plane is the plane where the curve belongs. In this case, the local coordinates will be:

$$\vec{e}_1^{\,l} = \frac{1}{ne_1}\begin{bmatrix} \dfrac{dx_1^o}{d\xi_s} \\ \dfrac{dx_2^o}{d\xi_s} \\ 0 \end{bmatrix}, ne_1 = \sqrt{\left(\frac{dx_1^o}{d\xi_s}\right)^2 + \left(\frac{dx_2^o}{d\xi_s}\right)^2} \tag{183a}$$

$$\vec{e}_2^{\,l} = \frac{1}{ne_2}\begin{bmatrix} -\dfrac{dx_2^o}{d\xi_s} \\ \dfrac{dx_1^o}{d\xi_s} \\ 0 \end{bmatrix}, ne_2 = ne_1 = \sqrt{\left(\frac{dx_2^o}{d\xi_s}\right)^2 + \left(\frac{dx_1^o}{d\xi_s}\right)^2} \tag{183b}$$

$$\vec{e}_3^{\,l} = \vec{e}_1^{\,l} \times \vec{e}_2^{\,l} = \begin{bmatrix} 0 \\ 0 \\ 1 \end{bmatrix} \tag{183c}$$

Then, the global configuration will become:

$$\begin{aligned}
\vec{r}^{\,g} &= T(\xi_1, i)\vec{r}^{\,l}(\xi_1, \xi_2, \xi_3, i) + \vec{r}^{\,o}(\xi_1, i) \\
&= \begin{bmatrix} \dfrac{1}{ne_1}\dfrac{dx_1^o}{d\xi_1} & -\dfrac{1}{ne_1}\dfrac{dx_2^o}{d\xi_1} & 0 \\ \dfrac{1}{ne_1}\dfrac{dx_2^o}{d\xi_1} & \dfrac{1}{ne_1}\dfrac{dx_1^o}{d\xi_1} & 0 \\ 0 & 0 & 1 \end{bmatrix} \begin{bmatrix} 0 \\ \left(R(\xi_1, \xi_2, i) + \xi_3 t_w(\xi_1, \xi_2, i)\right)\cos(2\pi\xi_2) \\ \left(R(\xi_1, \xi_2, i) + \xi_3 t_w(\xi_1, \xi_2, i)\right)\sin(2\pi\xi_2) \end{bmatrix} + \begin{bmatrix} x_1^o(\xi_1, i) \\ x_2^o(\xi_1, i) \\ x_3^o(\xi_1, i) \end{bmatrix} \\
&= \begin{bmatrix} -\dfrac{1}{ne_1}\dfrac{dx_2^o}{d\xi_1}\left(R(\xi_1, \xi_2, i) + \xi_3 t_w(\xi_1, \xi_2, i)\right)\cos(2\pi\xi_2) + x_1^o(\xi_1, i) \\ \dfrac{1}{ne_1}\dfrac{dx_1^o}{d\xi_1}\left(R(\xi_1, \xi_2, i) + \xi_3 t_w(\xi_1, \xi_2, i)\right)\cos(2\pi\xi_2) + x_2^o(\xi_1, i) \\ \left(R(\xi_1, \xi_2, i) + \xi_3 t_w(\xi_1, \xi_2, i)\right)\sin(2\pi\xi_2) + x_3^o(\xi_1, i) \end{bmatrix}
\end{aligned} \tag{184}$$

5.2.2 In-plane stiffener element

A more realistic case for stiffened plate structure is shown in Figure 12-13. In this case, the stiffener will be a single curvature curve.

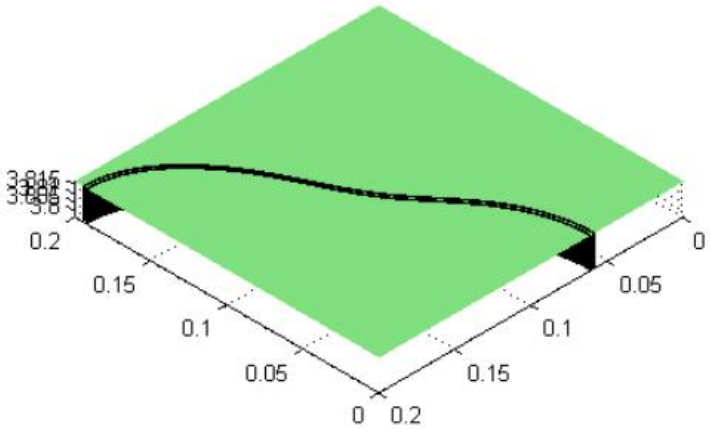

Figure 12 Stiffened plate structure with an arbitrary curved stiffener

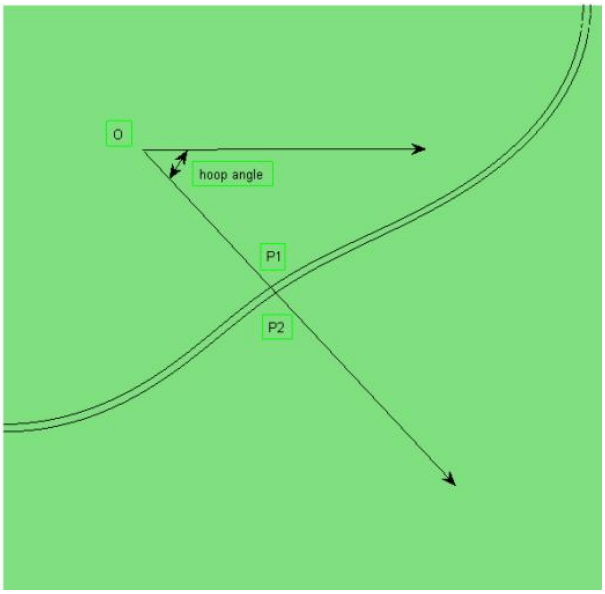

Figure 13 In-plane curved stiffener and notations

Assume that the stiffener's inner/outer outline could be formulated as:

$$y_1 = y_1(x)$$
$$y_2 = y_2(x) \qquad \text{(185a, b)}$$

Then, we define a point O on the plane of the stiffener, such that all the points on the stiffener could be seen from the point O. From the point O, a radial line is

generated and the radial line will intersect with the stiffener at point P_1 on the inner outline and at point P_2 on the outer outline. Thus, from the above formulation of the stiffener's reference line, it is possible to obtain the distance function as a function of θ,

$$\begin{aligned} R_1 &= dist(OP_1) = R_1(\theta) \\ R_2 &= dist(OP_2) = R_2(\theta) \end{aligned} \tag{186a, b}$$

where the radial line interacts with the stiffener's inner and outer line at the points of P_1 ,P_2 , respectively; θ is the hoop angle between line OP and the horizontal direction.

Assume that

$$\theta \in [\theta_1, \theta_2]$$

where $[\theta_1, \theta_2]$ is the interval of θ.

Then, the natural coordinate ξ_2 is defined as:

$$\xi_2 = \frac{\theta - \theta_1}{\theta_2 - \theta_1} \in [0,1] \tag{187}$$

Thus, the distance function could be re-written as:

$$\begin{aligned} R_1 &= dist(OP_1) = R_1(\xi_2) \\ R_2 &= dist(OP_2) = R_2(\xi_2) \end{aligned} \tag{188a, b}$$

Thus, the distance functions $R_{1,2}$ are obtained for the inner/outer outline of the curved in-plane stiffener structure.

Assume that the curved stiffener has the height of h_s, thus, the configuration of the curved stiffener could be represented as:

$$\vec{r}_s = \begin{bmatrix} \left(R_1(\xi_2)+\xi_3\left(R_2(\xi_2)-R_1(\xi_2)\right)\right)\sin\left(\theta_1+(\theta_2-\theta_1)\xi_2\right) \\ \left(R_1(\xi_2)+\xi_3\left(R_2(\xi_2)-R_1(\xi_2)\right)\right)\cos\left(\theta_1+(\theta_2-\theta_1)\xi_2\right) \\ h_s\xi_1 \end{bmatrix} \tag{189}$$

where $\xi_{1,2,3} \in [0,1]$ are the natural coordinates for the arbitrary in-plane curved stiffener structure. By using different functions of $R_{1,2}(\xi_2)$, different curved stiffener structure could be represented smoothly and accurately.

When $\xi_3 = 0$, then

$$\vec{r}_s = \begin{bmatrix} \left(R_1(\xi_2)\right)\sin\left(\theta_1+(\theta_2-\theta_1)\xi_2\right) \\ \left(R_1(\xi_2)\right)\cos\left(\theta_1+(\theta_2-\theta_1)\xi_2\right) \\ h_s\xi_1 \end{bmatrix} \tag{190}$$

The outer outline of the curved stiffener is described. When $\xi_3 = 1$, the stiffener's configuration function (189) will be:

$$\vec{r}_s = \begin{bmatrix} \left(R_2(\xi_2)\right)\sin\left(\theta_1+(\theta_2-\theta_1)\xi_2\right) \\ \left(R_2(\xi_2)\right)\cos\left(\theta_1+(\theta_2-\theta_1)\xi_2\right) \\ h_s\xi_1 \end{bmatrix} \tag{191}$$

The inner outline of the curved stiffener is described. When $\xi_1 = 0$, the stiffener's configuration function (189) will be:

$$\vec{r}_s = \begin{bmatrix} \left(R_1(\xi_2)+\xi_3\left(R_2(\xi_2)-R_1(\xi_2)\right)\right)\sin\left(\theta_1+(\theta_2-\theta_1)\xi_2\right) \\ \left(R_1(\xi_2)+\xi_3\left(R_2(\xi_2)-R_1(\xi_2)\right)\right)\cos\left(\theta_1+(\theta_2-\theta_1)\xi_2\right) \\ 0 \end{bmatrix} \tag{192}$$

The area where the stiffener is coupled with the plate is described.

A more general configuration is obtained:

$$\vec{r}_s = \begin{bmatrix} \left(R_1(\xi_1,\xi_2)+\xi_3\left(R_2(\xi_1,\xi_2)-R_1(\xi_1,\xi_2)\right)\right)\sin\left(\theta_1+(\theta_2-\theta_1)\xi_2\right) \\ \left(R_1(\xi_1,\xi_2)+\xi_3\left(R_2(\xi_1,\xi_2)-R_1(\xi_1,\xi_2)\right)\right)\cos\left(\theta_1+(\theta_2-\theta_1)\xi_2\right) \\ h_s\xi_1 \end{bmatrix} \tag{193}$$

In this more general case, the distance function $R_{1,2}$ will be also dependent on the natural coordinate ξ_1, the height direction of the stiffener.

The Jacobian matrix is calculated.

$$J=\left[J_{ij}\right]_{3\times 3} \tag{194}$$

where

$$J_{11}=\left(\frac{\partial R_1(\xi_1,\xi_2)}{\partial \xi_1}+\xi_3\left(\frac{\partial R_2(\xi_1,\xi_2)}{\partial \xi_1}-\frac{\partial R_1(\xi_1,\xi_2)}{\partial \xi_1}\right)\right)\sin\left(\theta_1+(\theta_2-\theta_1)\xi_2\right)$$

$$J_{12}=\left(\frac{\partial R_1(\xi_1,\xi_2)}{\partial \xi_1}+\xi_3\left(\frac{\partial R_2(\xi_1,\xi_2)}{\partial \xi_1}-\frac{\partial R_1(\xi_1,\xi_2)}{\partial \xi_1}\right)\right)\cos\left(\theta_1+(\theta_2-\theta_1)\xi_2\right)$$

$$J_{13}=h_s$$

$$J_{21}=\left(\frac{\partial R_1(\xi_1,\xi_2)}{\partial \xi_2}+\xi_3\left(\frac{\partial R_2(\xi_1,\xi_2)}{\partial \xi_2}-\frac{\partial R_1(\xi_1,\xi_2)}{\partial \xi_2}\right)\right)\sin\left(\theta_1+(\theta_2-\theta_1)\xi_2\right)+$$
$$(\theta_2-\theta_1)\left(R_1(\xi_1,\xi_2)+\xi_3\left(R_2(\xi_1,\xi_2)-R_1(\xi_1,\xi_2)\right)\right)\cos\left(\theta_1+(\theta_2-\theta_1)\xi_2\right)$$

$$J_{22}=\left(\frac{\partial R_1(\xi_1,\xi_2)}{\partial \xi_2}+\xi_3\left(\frac{\partial R_2(\xi_1,\xi_2)}{\partial \xi_2}-\frac{\partial R_1(\xi_1,\xi_2)}{\partial \xi_2}\right)\right)\cos\left(\theta_1+(\theta_2-\theta_1)\xi_2\right)-$$
$$(\theta_2-\theta_1)\left(R_1(\xi_1,\xi_2)+\xi_3\left(R_2(\xi_1,\xi_2)-R_1(\xi_1,\xi_2)\right)\right)\sin\left(\theta_1+(\theta_2-\theta_1)\xi_2\right)$$

$$J_{23}=0$$

$$J_{31}=\left(R_2(\xi_1,\xi_2)-R_1(\xi_1,\xi_2)\right)\sin\left(\theta_1+(\theta_2-\theta_1)\xi_2\right)$$

$$J_{32}=\left(R_2(\xi_1,\xi_2)-R_1(\xi_1,\xi_2)\right)\cos\left(\theta_1+(\theta_2-\theta_1)\xi_2\right)$$

$$J_{33}=0$$

(195a, b, c, d, e, f, g, h, i)

The Jacobian matrix's determinant is also calculated with a simple formulation as:

$$\det(J_0)=h_s(\theta_2-\theta_1)R_1(\xi_1,\xi_2)\left(R_1(\xi_1,\xi_2)+\xi_3\left(R_2(\xi_1,\xi_2)-R_1(\xi_1,\xi_2)\right)\right) \tag{196}$$

Another function is defined as:

$$R(\xi_1,\xi_2)=\frac{R_2(\xi_1,\xi_2)-R_1(\xi_1,\xi_2)}{R_1(\xi_1,\xi_2)} \tag{197}$$

Thus,

$$\det(J_0)=h_s(\theta_2-\theta_1)R_1^2(\xi_1,\xi_2)\left(1+\xi_3 R(\xi_1,\xi_2)\right) \tag{198}$$

It is reasonable to assume that the distance function could be in a separated coordinate form:

$$R_1(\xi_1,\xi_2)=R_{11}(\xi_1)R_{12}(\xi_2)$$
$$R_2(\xi_1,\xi_2)=R_{21}(\xi_1)R_{22}(\xi_2) \quad \text{(199a, b)}$$

Thus,

$$\det(J_0)=h_s(\theta_2-\theta_1)R_{11}^2(\xi_1)R_{12}^2(\xi_2)\left(1+\xi_3 R(\xi_1,\xi_2)\right) \quad (200)$$

5.2.3 DG-FEM implementation details and orthogonal basis function space

The definition of the curved pipe axial line $\vec{r}^{\,o}$ is important for the success of the curved pipe element. The spaced curve is a function of ξ_s or ξ_1 . NURBS is applied here to describe the spaced curve. The orthogonal basis functions space and the DG-FEM implementation for this example are identical to those for the layered pipe.

5.3 Multi-layered hydrofoil element

5.3.1 2-D hydrofoil cross-section kinematics

In this section, the kinematics of a typical 2-D hydrofoil cross section is set up. The general formulations of the natural coordinate system and the Jacobian matrix and Jacobian determinant are presented.

The 2-D cross section of the hydrofoil is described by a function as:

$$z=z(y)=z_t(y_t)$$
$$y_t=y/L_c \quad \text{(201a, b, c)}$$
$$0<y<L_c$$

where L_c is the chord line length, y is the coordinate of horizontal direction, z is the coordinate of the lift direction.

By using the above equation, the hydrofoil outline can be described in Figure 14.

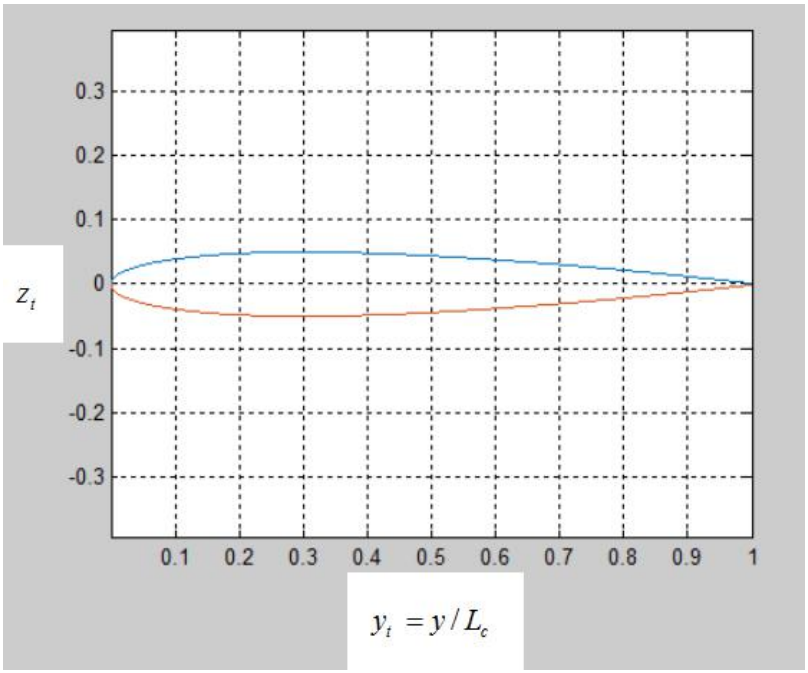

Figure 14 NACA hydrofoil cross section

The hydrofoil is a hollow shell structure. The Figure 14 only describes the outer outline of the hydrofoil and the inner outline configuration formulation is derived based on (201a, b, c).

The tangential direction angle is:

$$\theta_t = \arctan\left(\frac{dz(y)}{dy}\right) \tag{202}$$

Thus, the inner outline will be:

$$\begin{aligned} z' &= z + \frac{t_w}{\cos(\theta_t)} \\ &= z + t_w\sqrt{1+\left(\tan\left(\theta_t\right)\right)^2} \\ &= z + t_w\sqrt{1+\left(\frac{dz(y)}{dy}\right)^2} \end{aligned} \tag{203}$$

The natural coordinates are defined in Figure 15. In the natural coordinate system, a local origin O is placed inside the hydrofoil and the position of O is arbitrary. From the origin point O, a radial line is generated that makes an angle of θ with $y-axis$. The radial line interacts with the inner outline at point P and with the outer outline at point P'.

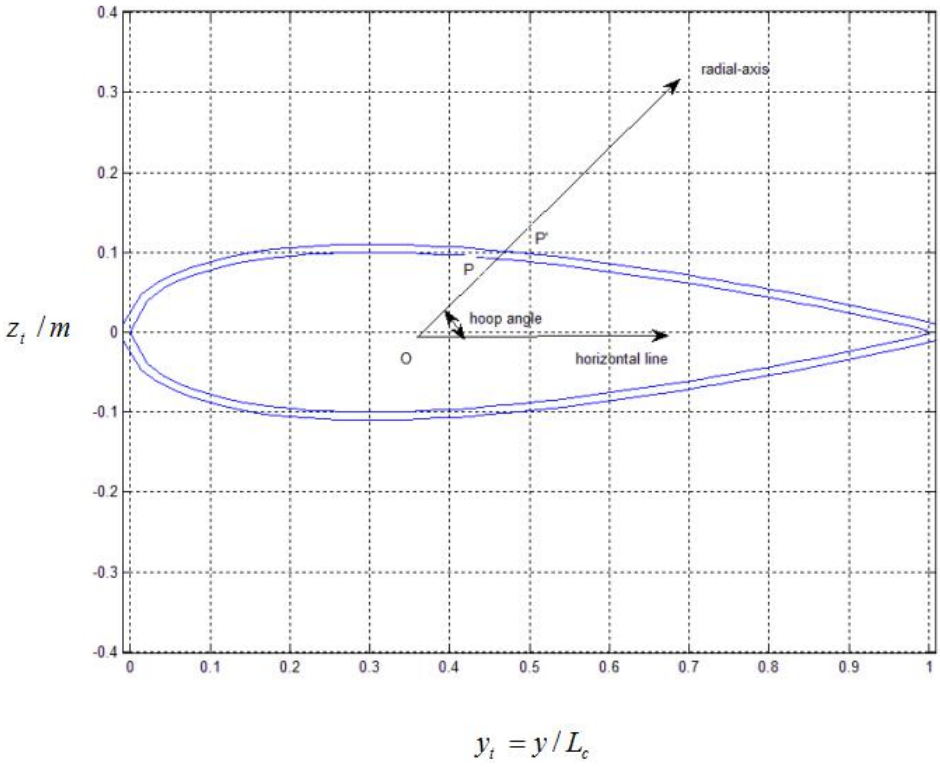

Figure 15 The hydrofoil kinematics notations

The natural coordinates ξ_1 ,ξ_2 are defined as:

$$\xi_1 = \frac{X}{L} \in [0,1]$$

$$\xi_2 = \frac{\theta}{2\pi} \in [0,1] \qquad (204a, b)$$

where L is the length in the hydrofoil span direction.

Then, we define the two functions:

$$R_b = dist(O,P) = R_b(\xi_1,\xi_2)$$
$$R_t = dist(O,P') = R_t(\xi_1,\xi_2) \qquad (205a, b)$$

where $dist(P_1,P_2)$ is the in-YOZ-plane distance function, which measures the distance between two points in the plane of YOZ.

We prove that $dist(P_1,P_2)$ is a function about ξ_1,ξ_2. According to the definition:

$$dist(O,P) = \sqrt{\left(y - y_0\right)^2 + \left(z'(y) - z_0\right)^2}$$
$$dist(O,P') = \sqrt{\left(y - y_0\right)^2 + \left(z(y) - z_0\right)^2} \qquad (206a, b)$$

where y_0, z_0 are the coordinates of origin point O in the YOZ plane.

For a 2-D hydrofoil cross-section, as in Figure 15, assume that the radial line OP makes a hoop angle θ with the $y-axis$. Then, the coordinates of point P will satisfy:

$$z = \tan(\theta)(y - y_0)$$
$$z = z(y) \qquad (207a, b)$$

For (207a), it means that point P is on the radial line OP, for the (207b), it means that point P is on the hydrofoil outline surface.

Then, we can solve the equations (207a, b) and get the solution as:

$$y = y(\theta) = y(\xi_2) \qquad (208a)$$

For the 3-D hydrofoil shell structure, the distance function $dist(P_1,P_2)$ is also dependent on the span direction, thus,

$$y = y(\theta, x) = y(\xi_1,\xi_2) \qquad (208b)$$

Thus,

$$dist(O,P)=\sqrt{\left(y(\xi_1,\xi_2)-y_0\right)^2+\left(z(y(\xi_1,\xi_2))-z_0\right)^2}$$
$$dist(O,P')=\sqrt{\left(y(\xi_1,\xi_2)-y_0\right)^2+\left(z'(y(\xi_1,\xi_2))-z_0\right)^2} \quad (209a, b)$$

They are functions of ξ_1,ξ_2.

Then, the natural coordinate ξ_3 is defined as:

$$\xi_3=\frac{\rho-R_b(\xi_1,\xi_2)}{R_t(\xi_1,\xi_2)-R_b(\xi_1,\xi_2)} \quad (210)$$

Thus, the hydrofoil configuration can be represented as:

$${}^0\vec{r}=\begin{bmatrix} L\xi_1 \\ \left(R_b+\xi_3(R_t-R_b)\right)\cos(2\pi\xi_2) \\ \left(R_b+\xi_3(R_t-R_b)\right)\sin(2\pi\xi_2) \end{bmatrix}=\begin{bmatrix} L\xi_1 \\ \left(R_b+\xi_3 t_w\right)\cos(2\pi\xi_2) \\ \left(R_b+\xi_3 t_w\right)\sin(2\pi\xi_2) \end{bmatrix} \quad (211)$$

where $t_w=(R_t-R_b)$ is defined as the wall thickness function.

It is noted that R_b,R_t are both functions of ξ_1,ξ_2.

The Jacobian matrix is:

$$J=\left[J_{ij}\right]$$
$$J_{ij}=\frac{\partial^0 r_j}{\partial\xi_i} \quad (212a, b)$$

The elements of the Jacobian matrix are:

$$
\begin{aligned}
J_{11} &= L \\
J_{12} &= \left(\frac{\partial R_b}{\partial \xi_1} + \xi_3 \left(\frac{\partial R_t}{\partial \xi_1} - \frac{\partial R_b}{\partial \xi_1} \right) \right) \cos(2\pi\xi_2) \\
J_{13} &= \left(\frac{\partial R_b}{\partial \xi_1} + \xi_3 \left(\frac{\partial R_t}{\partial \xi_1} - \frac{\partial R_b}{\partial \xi_1} \right) \right) \sin(2\pi\xi_2) \\
J_{21} &= 0 \\
J_{22} &= \left(\frac{\partial R_b}{\partial \xi_2} + \xi_3 \left(\frac{\partial R_t}{\partial \xi_2} - \frac{\partial R_b}{\partial \xi_2} \right) \right) \cos(2\pi\xi_2) - 2\pi \left(R_b + \xi_3 (R_t - R_b) \right) \sin(2\pi\xi_2) \\
J_{23} &= \left(\frac{\partial R_b}{\partial \xi_2} + \xi_3 \left(\frac{\partial R_t}{\partial \xi_2} - \frac{\partial R_b}{\partial \xi_2} \right) \right) \sin(2\pi\xi_2) + 2\pi \left(R_b + \xi_3 (R_t - R_b) \right) \cos(2\pi\xi_2) \\
J_{31} &= 0 \\
J_{32} &= \left(R_t - R_b \right) \cos(2\pi\xi_2) \\
J_{33} &= \left(R_t - R_b \right) \sin(2\pi\xi_2)
\end{aligned}
$$

(213a, b, c, d, e, f, g, h, i)

The Jacobian matrix determinant is:

$$
\det(J) = 2\pi L \left(R_t - R_b \right) \left(R_b + \xi_3 (R_t - R_b) \right) \tag{214a}
$$

It is seen that the Jacobian matrix determinant is quite simple even if R_b, R_t are both functions of ξ_1 and ξ_2. For a 2-D uniform hydrofoil model, R_b, R_t may be functions only of ξ_2.

For a thin hydrofoil, the Jacobian matrix may be approximated as:

$$
\det(J) \approx 2\pi L \left(R_t - R_b \right) \left(R_b + \frac{1}{2} (R_t - R_b) \right) \tag{214b}
$$

In this approximation, the mean value theorem is applied in ξ_3.

There could be more than one origin points, as shown in the Figure 16. Any arbitrary points can be chosen as the origin. The origins could be placed outside of the hydrofoil. In Figure 16, the hydrofoil is divided into 2 parts: the upper hydrofoil and the lower hydrofoil. For the upper hydrofoil, the origin is called O_1. The radial line makes an angle with horizontal line θ_1 and intersects with the hydrofoil inner/outer surface at the points P_1 ,$P_1^{'}$. For the lower hydrofoil part, the origin point is called O_2. The radial line makes an angle θ_2 with the horizontal line and interacts with the hydrofoil inner/outer surface at the points P_2 ,$P_2^{'}$.

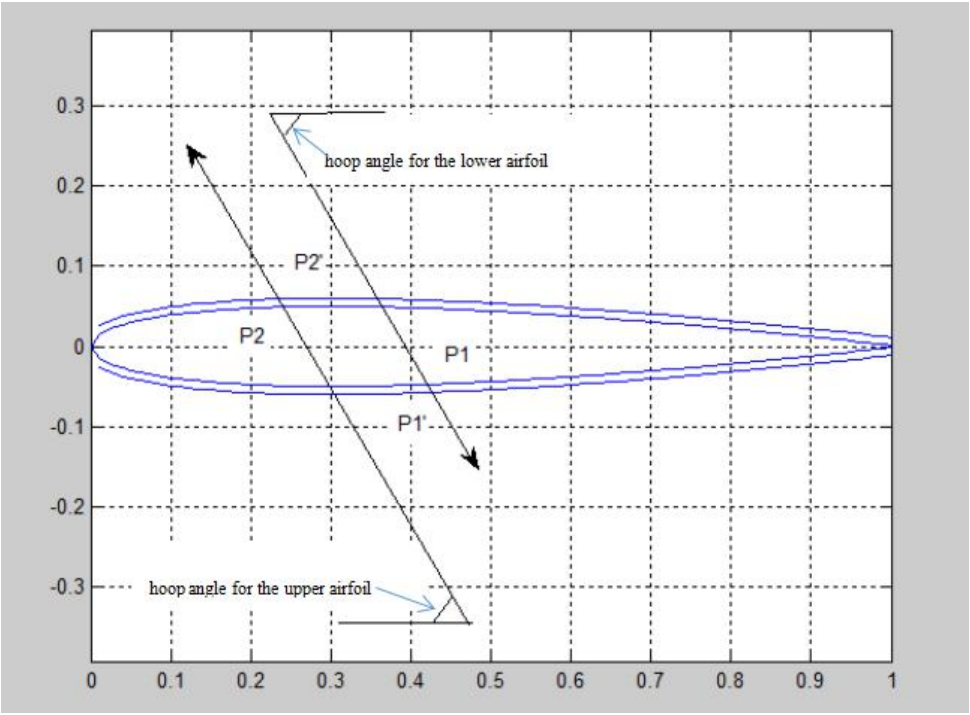

Figure 16 Hydrofoil kinematics definition for multi natural coordinate systems

The natural coordinates ξ_1^1,ξ_2^1 are defined for the upper hydrofoil as:

$$\xi_1^1 = \frac{X}{L} \in [0,1]$$

$$\xi_2^1 = \frac{\theta_1}{\pi} \in [0,1] \tag{215a, b}$$

The natural coordinates ξ_1^2, ξ_2^2 are defined for lower hydrofoil as:

$$\xi_1^2 = \frac{X}{L} \in [0,1]$$

$$\xi_2^2 = \frac{\theta_2}{\pi} \in [0,1] \tag{216a, b}$$

Then, the distance functions are defined for upper and lower hydrofoil as:

$$\begin{aligned} R_b^1 &= dist(O_1, P_1) = R_b^1(\xi_1^1, \xi_2^1) \\ R_t^1 &= dist(O_1, P_1') = R_t^1(\xi_1^1, \xi_2^1) \end{aligned} \tag{217a, b}$$

$$\begin{aligned} R_b^2 &= dist(O_2, P_2) = R_b^2(\xi_1^2, \xi_2^2) \\ R_t^2 &= dist(O_2, P_2') = R_t^2(\xi_1^2, \xi_2^2) \end{aligned} \tag{218a, b}$$

For the upper and low hydrofoil surface, the natural coordinates ξ_3^1, ξ_3^2 are defined as:

$$\xi_3^1 = \frac{\rho - R_b^1(\xi_1^1, \xi_2^1)}{R_t^1(\xi_1^1, \xi_2^1) - R_b^1(\xi_1^1, \xi_2^1)} \tag{219a}$$

$$\xi_3^2 = \frac{\rho - R_b^2(\xi_1^2, \xi_2^2)}{R_t^2(\xi_1^2, \xi_2^2) - R_b^2(\xi_1^2, \xi_2^2)} \tag{219b}$$

Thus, the hydrofoil configuration can be represented as:

$${}^0\vec{r}^1 = \begin{bmatrix} L\xi_1^1 \\ \left(R_b^1 + \xi_3^1(R_t^1 - R_b^1)\right)\cos(\pi\xi_2^1) \\ \left(R_b^1 + \xi_3^1(R_t^1 - R_b^1)\right)\sin(\pi\xi_2^1) \end{bmatrix} = \begin{bmatrix} L\xi_1^1 \\ \left(R_b^1 + \xi_3^1 t_w^1\right)\cos(\pi\xi_2^1) \\ \left(R_b^1 + \xi_3^1 t_w^1\right)\sin(\pi\xi_2^1) \end{bmatrix} \tag{220a}$$

$$
{}^{0}\vec{r}^{\,2} = \begin{bmatrix} L\xi_1^2 \\ \left(R_b^2 + \xi_3^2(R_t^2 - R_b^2)\right)\cos(\pi\xi_2^2) \\ \left(R_b^2 + \xi_3^2(R_t^2 - R_b^2)\right)\sin(\pi\xi_2^2) \end{bmatrix} = \begin{bmatrix} L\xi_1^2 \\ \left(R_b^2 + \xi_3^2 t_w^2\right)\cos(\pi\xi_2^2) \\ \left(R_b^2 + \xi_3^2 t_w^2\right)\sin(\pi\xi_2^2) \end{bmatrix} \tag{220b}
$$

It is also possible to divide the hydrofoil into more than 2 parts for a more complicated hydrofoil structure. The procedure is identical. In that case, the interior boundary will be considered as the interface between the adjacent parts.

Chapter 6 Numerical tests

In this chapter, five problems with large deformation are solved. For each problem, we discuss the dedicated orthogonal basis function space design for the specific structure. The results will be compared with commercial software ANSYS or experimental data from other papers if available. A convergence study is also presented for many examples.

The arc length method (Riks) [1, 23, 28] is applied to follow the post buckling equilibrium path in the static analysis. The traditional Newton iterative algorithm does not generally work for the post buckling analysis, where the tangential stiffness matrix may no longer be positive definite. A positive definite tangential stiffness matrix is an important requirement for the convergent solution in the Newton iterative method. From another viewpoint, in NR algorithm, we divide the load into several load steps. In each load step, we prescribe an increment in the load. For stable response, we can always find a corresponding equilibrium state by increasing the load. For unstable response (post-buckling etc), the structure resistance may be suddenly lost. In this case, if we continue to increase the load, there will be no corresponding equilibrium state. Thus, we can't use load to make a progress in the numerical simulation.

The arc length method (Riks) is a more general loading iterative algorithm. In this algorithm, any quantity could be used as 'load', as long as it varies monotonically. For example, the L2-norm of the displacement DOF vector may be defined as the

'load' because the L2-norm is always positive. However, a drawback of such a choice is that the L2-norm is nonlinear as a function of the DOF vector.

In this thesis, the close volume of the structure is defined as the arc length:

$$\Delta V = \tilde{u}^T A$$
$$A = \left(\int_S N_u^T n dS \right) \quad (221a, b)$$

where $\tilde{u}$ is the degree-of-freedom vector, n is the normal vector, S is the outer surface of the structure.

The advantages of the above definition of the arc length method are:

(a) ΔV is linear about $\tilde{u}$ in every load step, as seen in equation (221a, b);

(b) ΔV is monotonically decreasing, which means there always exists a static equilibrium for any prescribed value of ΔV.

In this case, for any FEM discrete equations:

$$K\tilde{u} = R_f \quad (222)$$

The corresponding arc length method discrete equations will be:

$$\begin{bmatrix} {}^t K & {}^t A \\ {}^t A^H & 0 \end{bmatrix} \begin{bmatrix} \tilde{u} \\ \tilde{p} \end{bmatrix} = \begin{bmatrix} {}^{t+dt} R_f - \left({}^t A \right) \left({}^t \tilde{p} \right) \\ \Delta V \end{bmatrix} \quad (223)$$

where

$$\tilde{p} = {}^{t+dt}\tilde{p} - {}^t\tilde{p}$$
$$\tilde{u} = {}^{t+dt}\tilde{u} - {}^t\tilde{u} \quad (224a, b)$$

It is also noted that the matrix A should be updated after every load step because the normal vector n changes with deformation.

When the equivalent tangential stiffness matrix K remains positive definite:

$0 < t < t_c \quad \min(\lambda_i, i = 1,2,3,\cdots,n_K, \det(\lambda_i I - {}^t K) = 0) > 0$

By prescribing a negative value of ΔV, we can always calculate a positive value of $\tilde{p}$. This is a valid result because the structure is still stable when $0 < t < t_c$.

When the tangential stiffness matrix has a zero eigenvalue, we have:

$t = t_c \ \min(\lambda_i, i = 1,2,3,\cdots,n_K, \det(\lambda_i I - {}^t K) = 0) = 0$

By prescribing a negative value of ΔV, we can calculate a zero value of $\tilde{p}$. This is the critical buckling point and the critical load ${}^{t_c}\tilde{p}$ has been found.

When the tangential stiffness matrix has a negative eigenvalue, we have:

$t > t_c \ \min(\lambda_i, i = 1,2,3,\cdots,n_K, \det(\lambda_i I - {}^t K) = 0) < 0$

By prescribing a negative value of ΔV, we can always calculate a negative value of $\tilde{p}$. This is valid because the structure has become unstable. The stiffness of the structure has reduced. There is no possible equilibrium state if we continue to increase the pressure beyond ${}^{t_c}\tilde{p}$. It has to be decreased for a possible equilibrium state.

The Ramberg-Osgood equation is used for the stress-strain relations:

$$\varepsilon = \frac{1}{E}\left[1 + \frac{3}{7}\left(\frac{\sigma}{\sigma_y}\right)^{n-1}\right] \tag{225}$$

where E is the elastic modulus, σ_y is the Ramberg-Osgood yield stress and $n = 10.7$ is the hardening parameter.

6.1 Sandwich plate

In this part, the sandwich plate structure is analyzed. The sandwich structure is shown in the Figure 17 below. There are three layers, namely the core later, top layer and bottom layer. For the three layers, we may use different materials.

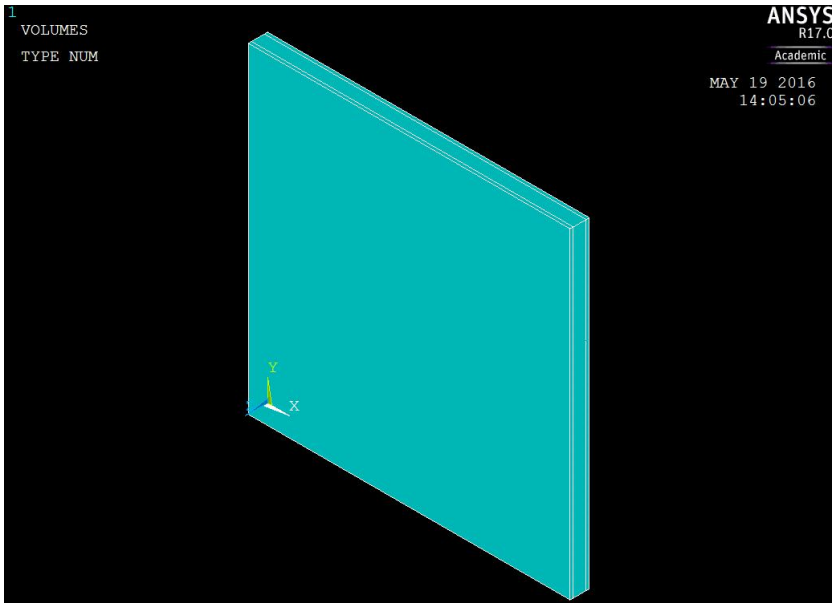

Figure 17 Sandwich plate structure

Test 1: Moderate thick sandwich plate static/vibration analysis

The water pressure is applied on the top surface of the top layer. The edges of the sandwich plate are clamped. The top and bottom layer' thickness are:

$t^1 = t^3 = 0.01m$

The core layer's thickness is:

$t_2 = n_m t_1, n_m = 4$

The plate is a $a \times b = 1 \times 1$ square plate. Elastic modulus for the top and bottom plates are $E_1 = E_3 = 2.06e11\,\text{Pa}$. For the core layer, we define the Young's Modulus as:

$E_2 = \beta E_1, \beta = 0.05$.

For the sandwich plate structure, the kinematics is simple and the Jacobian matrix's determinant is a constant, as presented in (226).

$$\det(J^k) = a \times b \times t^k \tag{226}$$

where $t^k, k = 1,2,3$ is the wall thickness of each layer.

For the boundary conditions, since all the boundaries are clamped, we could define the displacement as:

$$\begin{aligned} u_1^k &= R_0 \, f_{u_1}^{\xi_1} f_{u_1}^{\xi_2} f_{u_1}^{\xi_3^k} \sum_{m,n,s=1}^{m_0,n_0,s_0} A_{mns} \phi_{u_1}^m(\xi_1) \psi_{u_1}^n(\xi_2) \varphi_{u_1}^s(\xi_3^k) \\ u_2^k &= R_0 \, f_{u_2}^{\xi_1} f_{u_2}^{\xi_2} f_{u_2}^{\xi_3^k} \sum_{m,n,s=1}^{m_0,n_0,s_0} B_{mns} \phi_{u_2}^m(\xi_1) \psi_{u_2}^n(\xi_2) \varphi_{u_2}^s(\xi_3^k) \\ u_3^k &= R_0 \, f_{u_3}^{\xi_1} f_{u_3}^{\xi_2} f_{u_3}^{\xi_3^k} \sum_{m,n,s=1}^{m_0,n_0,s_0} C_{mns} \phi_{u_3}^m(\xi_1) \psi_{u_3}^n(\xi_2) \varphi_{u_3}^s(\xi_3^k) \end{aligned} \tag{227a, b, c}$$

where

$$\begin{aligned} f_{u_1}^{\xi_1} &= f_{u_2}^{\xi_1} = f_{u_3}^{\xi_1} = \xi_1(1-\xi_1) \\ f_{u_1}^{\xi_2} &= f_{u_2}^{\xi_2} = f_{u_3}^{\xi_2} = \xi_2(1-\xi_2) \\ f_{u_1}^{\xi_3^k} &= f_{u_2}^{\xi_3^k} = f_{u_3}^{\xi_3^k} = 1 \end{aligned} \tag{228a, b, c}$$

Thus, the orthogonal basis function space for the sandwich plate structure will be:

$\phi_{u_i}^{\xi_1}(i = 1,2,3)$ is the orthogonal polynomial series with weight function $\xi_1^2(1-\xi_1)^2$,

$\psi_{u_i}^{\xi_2}(i = 1,2,3)$ is the orthogonal polynomial series with weight function $\xi_2^2(1-\xi_2)^2$,

$\varphi_{u_i}^{\xi_1}(i = 1,2,3)$ is the orthogonal polynomial series with weight function 1.

In this case, the Consistent Orthogonal Basis Functions for ξ_1 and ξ_2 are plotted in Figure 18.

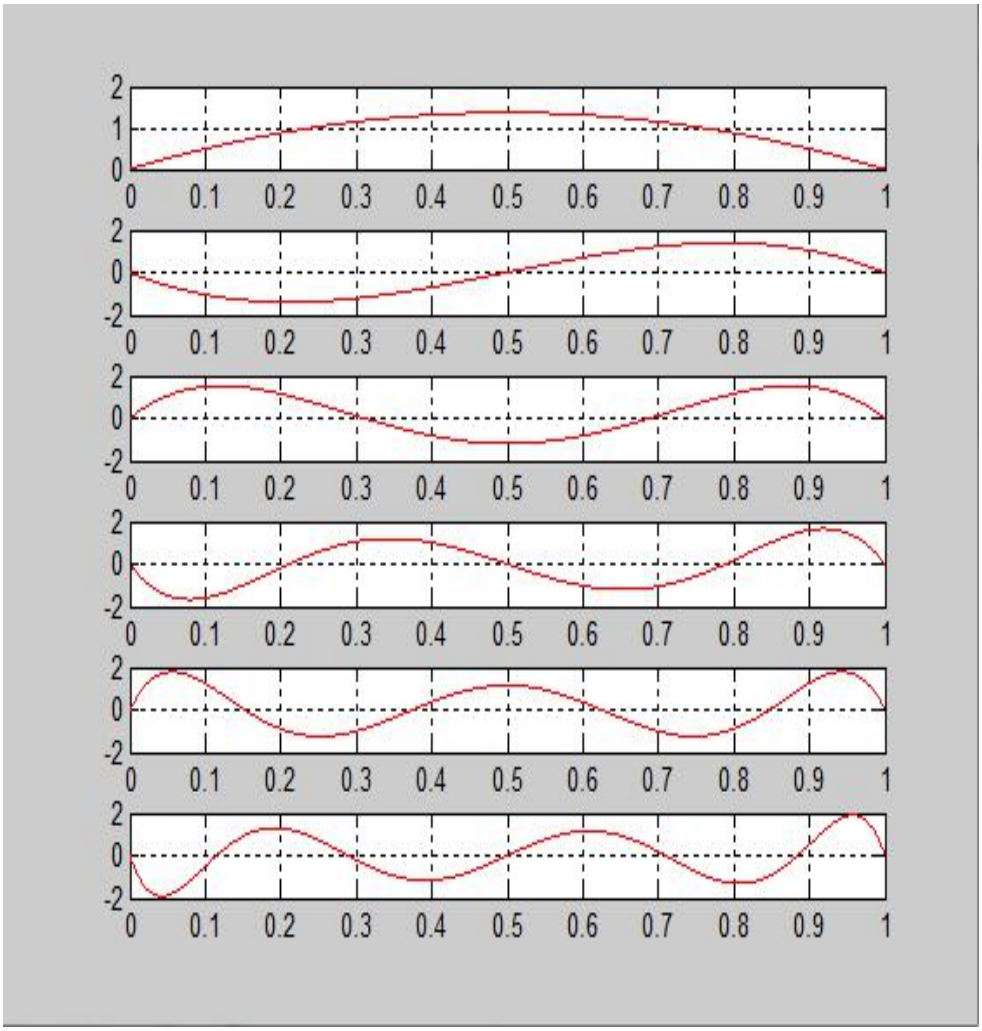

Figure 18 The Consistent Orthogonal Basis Functions for ξ_1 and ξ_2

For ξ_3 , the Consistent Orthogonal Basis Functions are plotted in Figure 19.

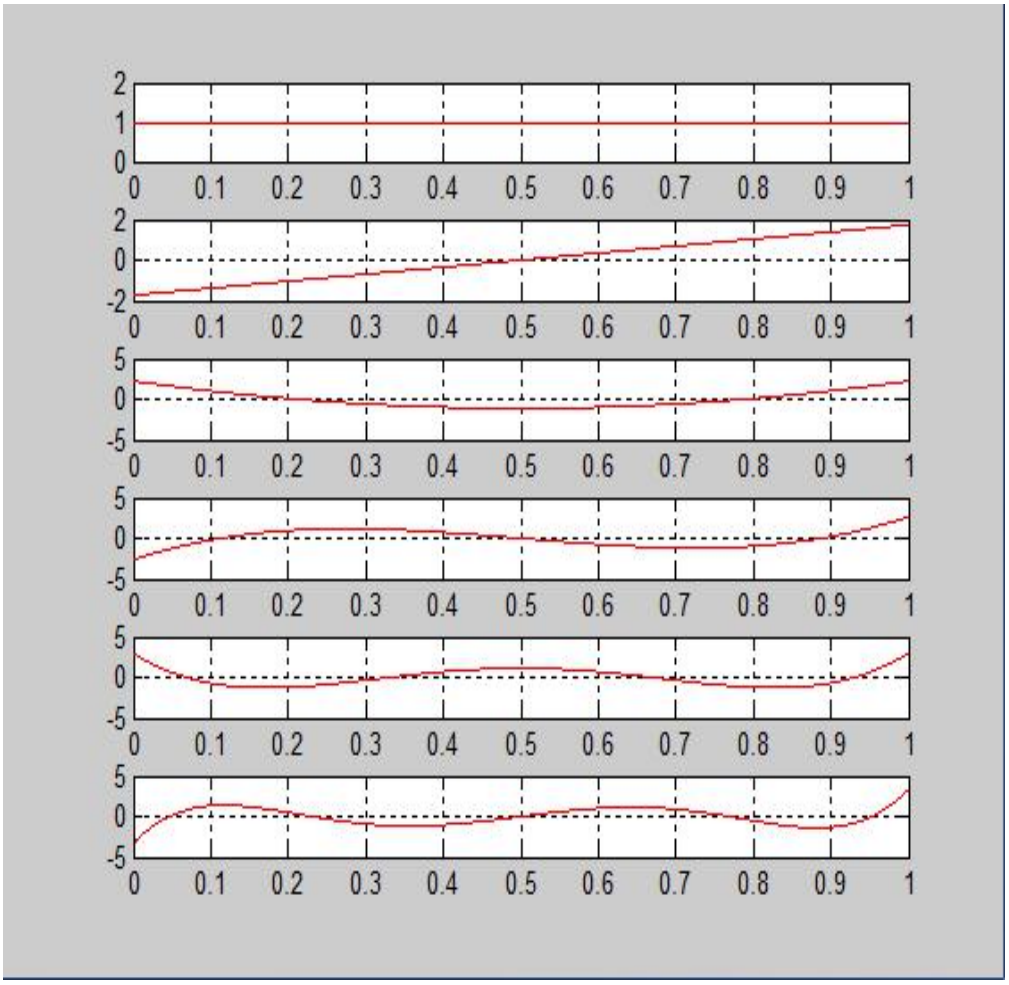

Figure 19 The Consistent Orthogonal Basis Functions for ξ_3

Another choice is also presented. The boundary conditions are defined as:

$$f_{u_1}^{\xi_1} = f_{u_2}^{\xi_1} = f_{u_3}^{\xi_1} = \xi_1^2(1-\xi_1)^2$$
$$f_{u_1}^{\xi_2} = f_{u_2}^{\xi_2} = f_{u_3}^{\xi_2} = \xi_2^2(1-\xi_2)^2 \qquad \text{(228a, b, c)}$$
$$f_{u_1}^{\xi_3} = f_{u_2}^{\xi_3} = f_{u_3}^{\xi_3} = 1$$

Thus, the orthogonal basis function space for the sandwich plate structure will be:

$\phi_{u_i}^{\xi_1}(i=1,2,3)$ is the orthogonal polynomial series with weight function $\left(\xi_1(1-\xi_1)\right)^4$,

$\psi_{u_j}^{\xi_2}(i=1,2,3)$ is the orthogonal polynomial series with weight function $\left(\xi_2(1-\xi_2)\right)^4$,

$\varphi_{u_i}^{\xi_1}$ (i=1,2,3) is the orthogonal polynomial series with weight function 1.

The Consistent Orthogonal Basis Functions for ξ_1 and ξ_2 are plotted in the Figure 20.

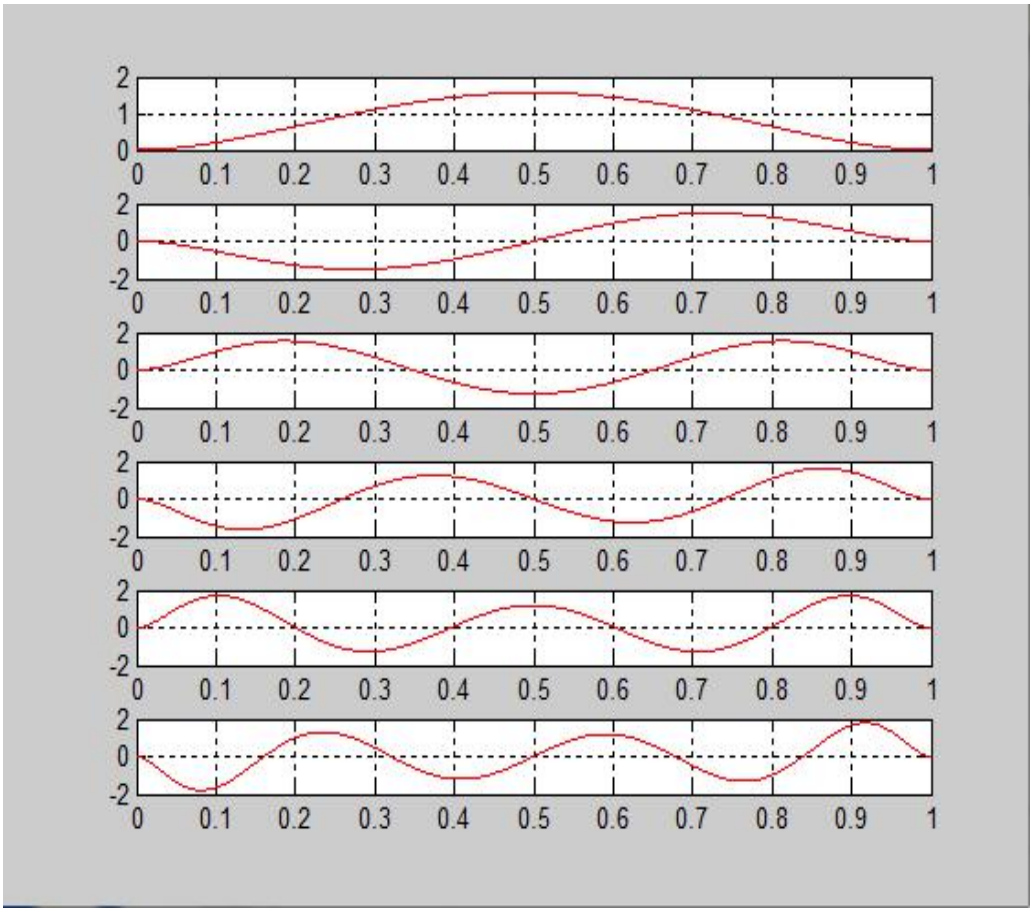

Figure 20 The Consistent Orthogonal Basis Functions for ξ_1 and ξ_2

The static analysis deformation of the sandwich plate under water pressure is shown below. In the Figure 21, the deflection of the plate at $x = 0.5m$ is plotted.

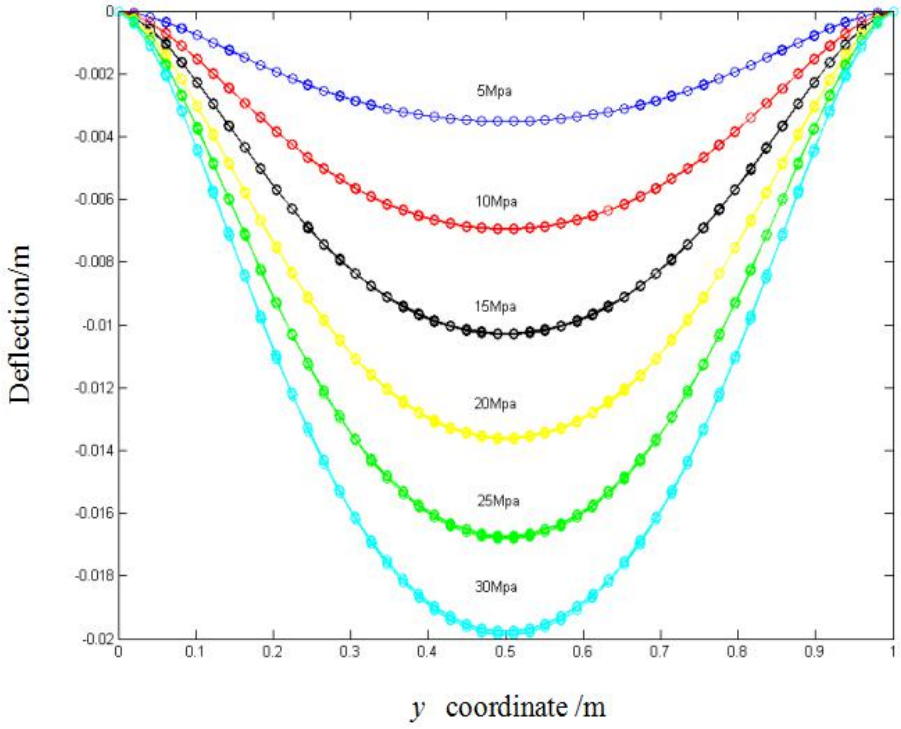

Figure 21 Plots of the deflection of the plate ($x=0.5$) under various water pressures

The traction between adjacent layers is analyzed. For the sandwich plate problem, the traction DOF will be the concentrated shear force and membrane force. When the Gauss integration points are defined as 8×8 , the shear traction contours are given in Figure 22 In Figure 22a, the shear traction magnitude of T_2 is plotted for the interface between layer 1 and layer 2. In Figure 22b, the results are verified by using ANSYS. The shear traction magnitude of T_1 is plotted in Figure23a and verified in Figure 23b. T_1 , T_2 are the shear traction in Y and X direction, respectively.

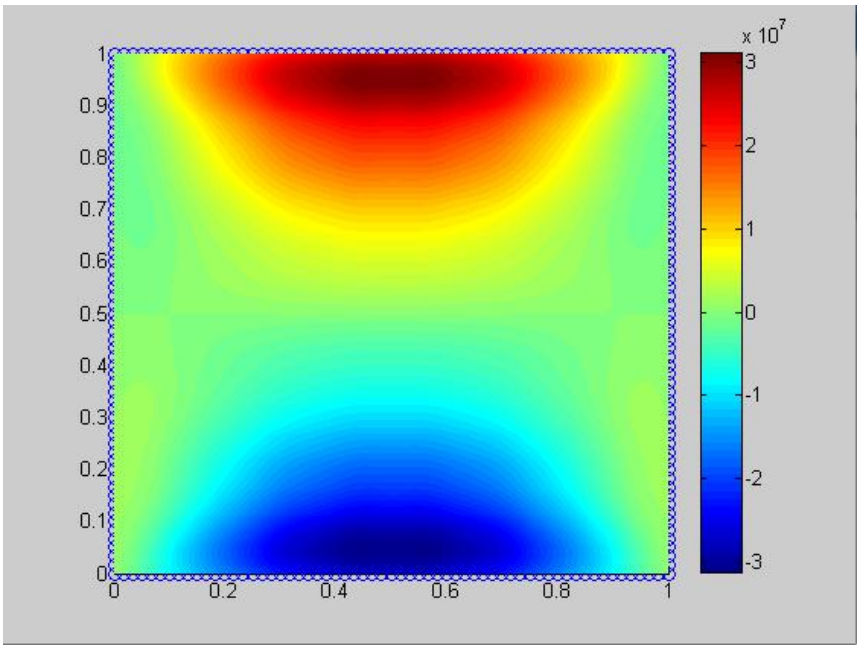

Figure 22a The shear traction T_2 (unit: Pa) magnitude contours for the interface between layer 1-2

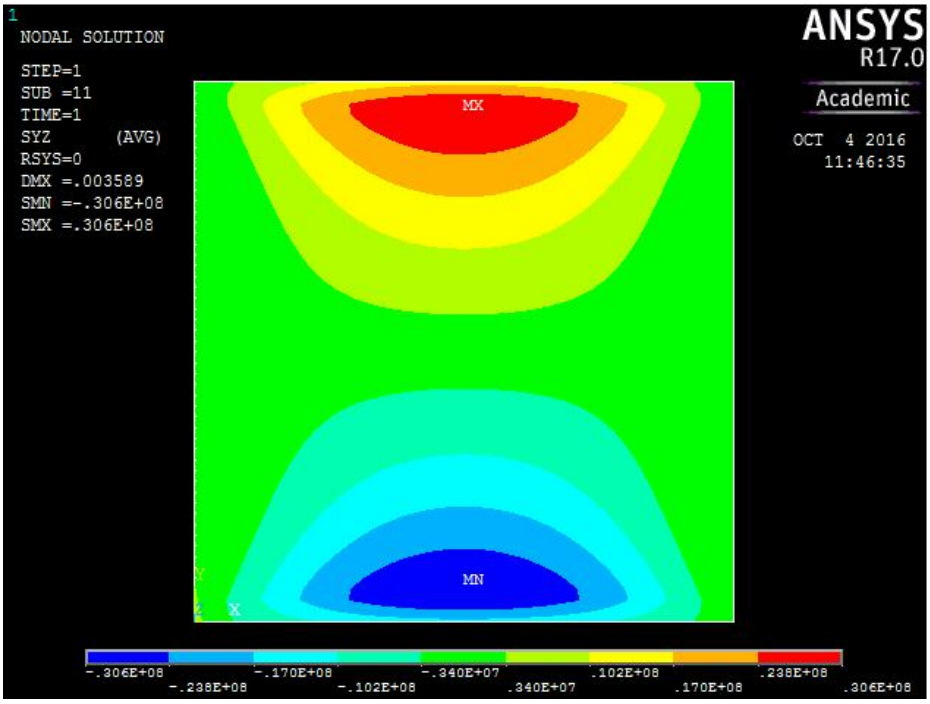

Figure 22b The shear traction T_2 (unit: Pa) magnitude contours for the interface between layer 1-2 (ANSYS verification)

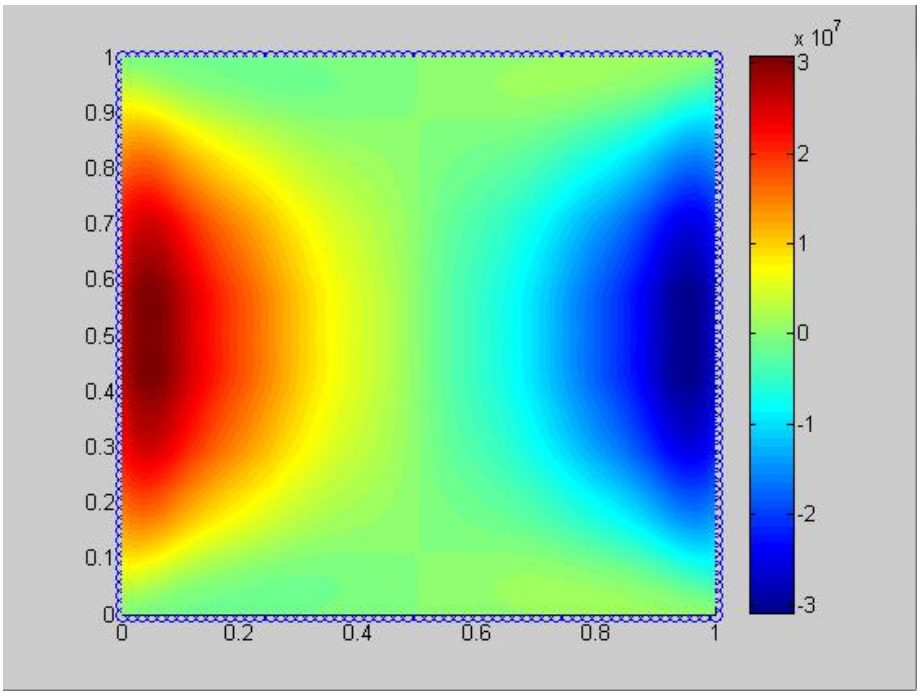

Figure 23a The shear traction T_1 (unit: Pa) magnitude contours for the interface between layer 1-2

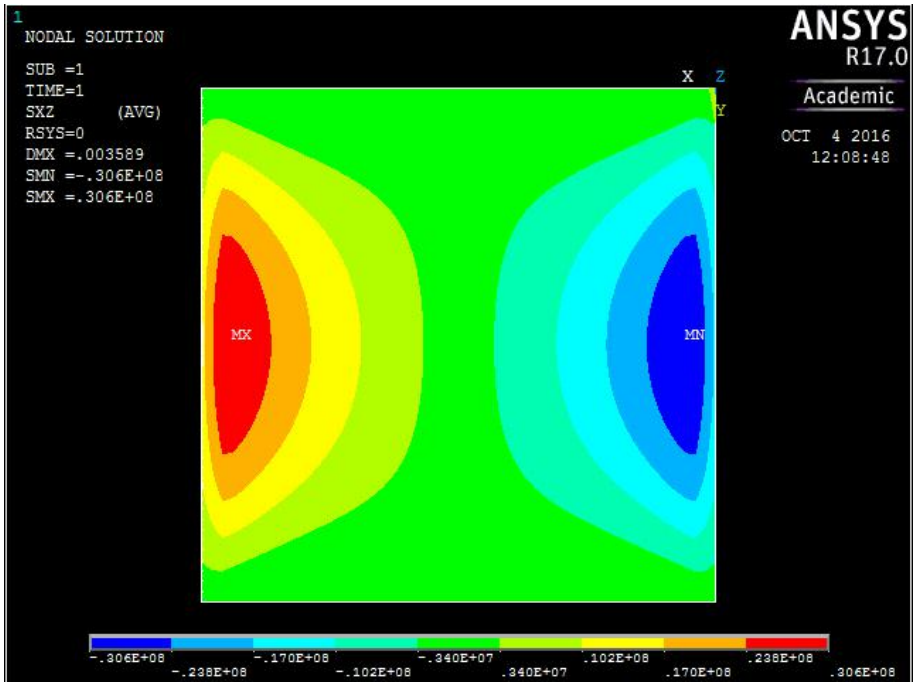

Figure 23b The shear traction T_1 (unit: Pa) magnitude contours for the interface between layer 1-2 (ANSYS verification)

The shear traction magnitude is compared in the Figure 24.

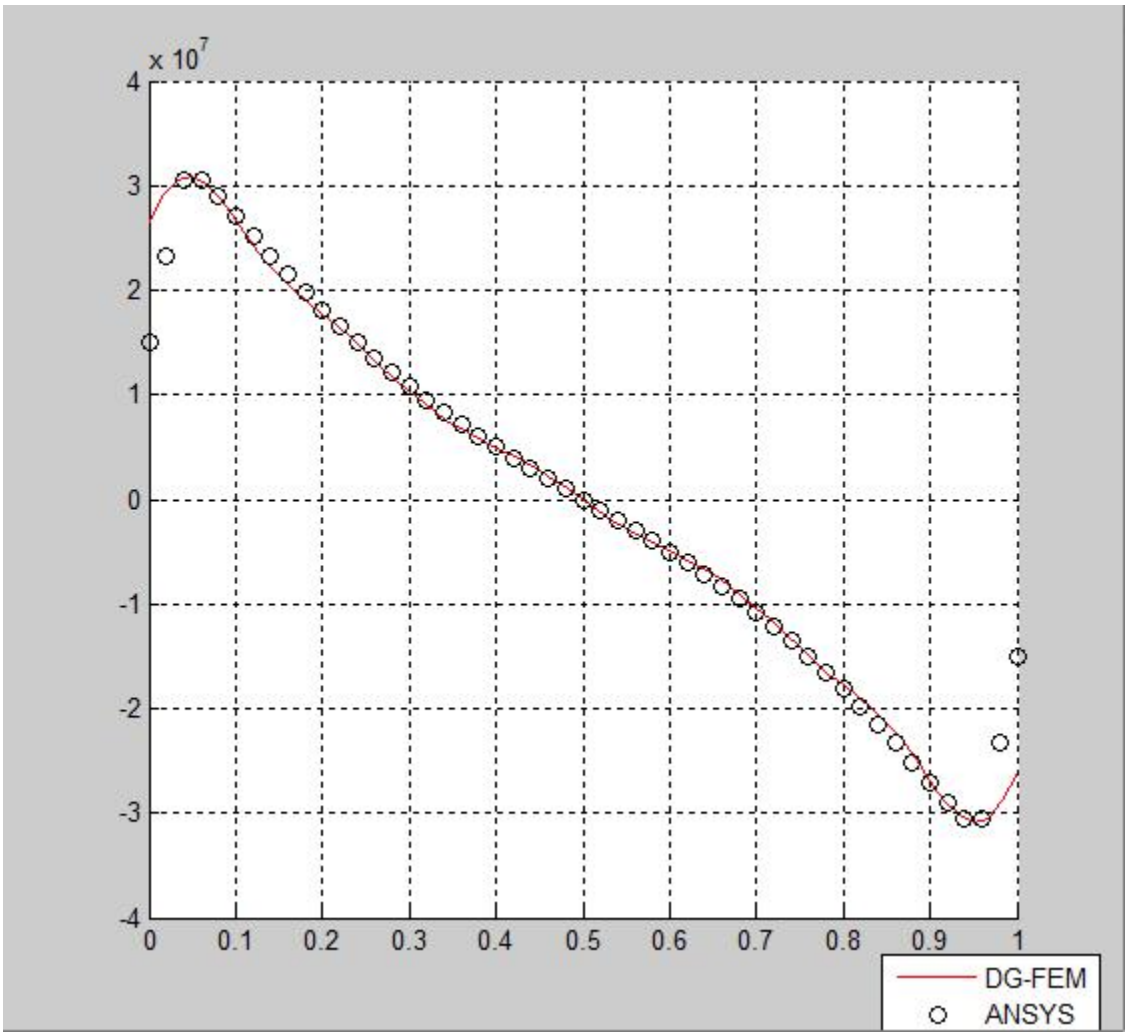

Figure 24 The shear traction T_2 (unit: Pa) magnitude for the interface between layer 1-2

From Figure 24, it is observed that the traction solution has a matching result with ANSYS for the main domain. But for the boundaries, the results obtained in the thesis are not able to capture the jump. This problem will be discussed in future work. Some enrichment function will be added for the traction to capture the jump. The convergence study for the traction are presented in the Figure 25.

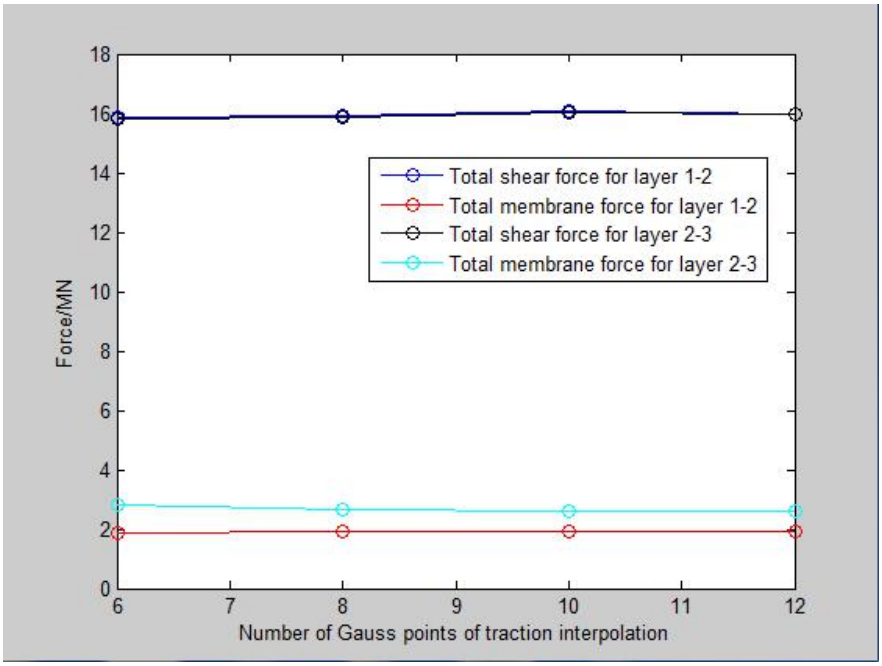

Figure 25 The convergence study of the traction

In Figure 25, the number of traction basis functions is increased and the total shear force and membrane force of the interfaces tend to be convergent.

The convergence study for displacement is presented here. As the number of DOFs is increased, the maximum deflection of the sandwich plate is recorded in the table under 10MPa, 20MPa and 30MPa. A relatively large deformation is observed.

The wall thickness displacement function order is prescribed as 4 and the in-plane displacement function order is increased from 5 to 10. The maximum displacement is recorded under several water pressure loads. Large deformation and finite strain occur. The maximum deflection is recorded in Table 1.

Table 1 Convergence study of in-plane displacement order

DOF (a,b,c)*	10MPa	20MPa	30MPa
(5,5,4)	6.856mm	13.500mm	19.700mm

(6,6,4)	6.923mm	13.600mm	19.700mm
(7,7,4)	7.236mm	14.200mm	20.700mm
(8,8,4)	7.311mm	14.200mm	20.800mm
(9,9,4)	7.247mm	14.100mm	20.600mm
(10,10,4)	7.236mm	14.200mm	20.700mm
ANSYS	7.134mm	14.049mm	20.591mm

*(a,b,c) refers to the displacement order in the plate x, y, z direction

A dynamical sandwich plate analysis is presented. The water pressure is a transient load shown in Figure 26.

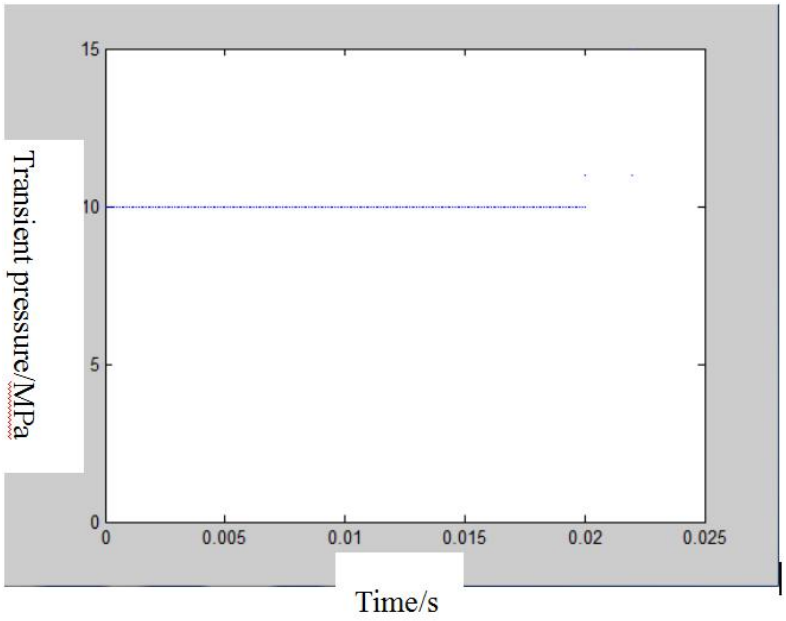

Figure 26 Transient water pressure versus time

Under such transient water pressure, the deflection history curve is recorded. The dynamical response of the point $x = 0.5, y = 0.5$ is given in Figure 27.

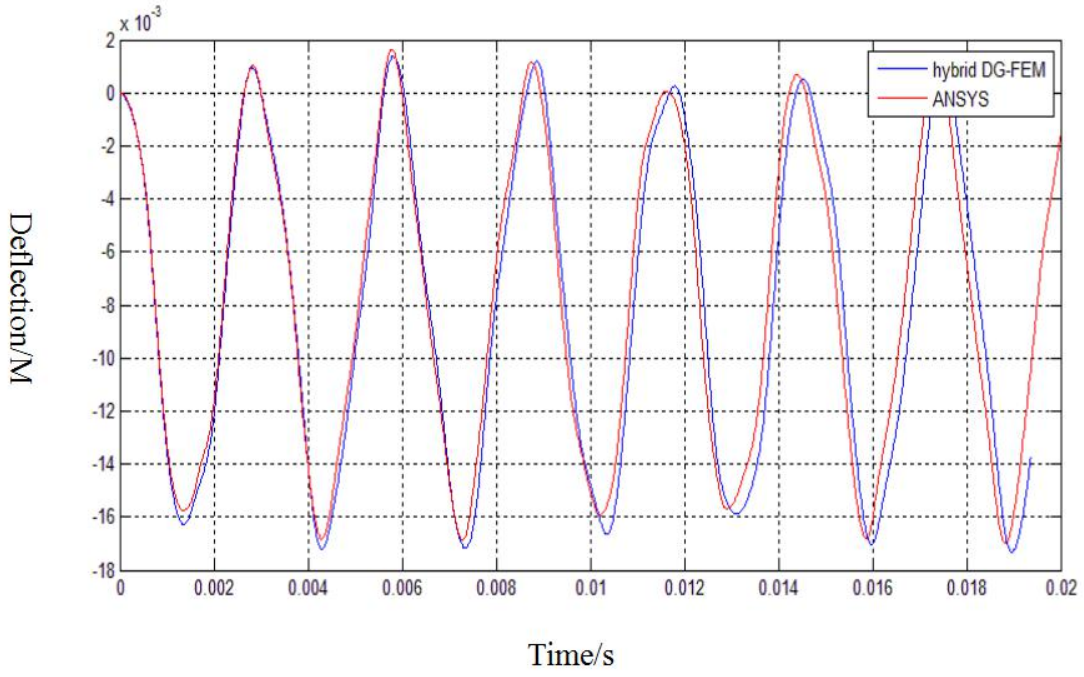

Figure 27 Deflection-time curve for the center point of the sandwich plate

The displacement contour is presented for several time steps and it is compared with results from ANSYS. For several typical time steps, the deflection contours are recorded and compared with results from ANSYS in Figure 28 and Figure 29. In the ANSYS results, the Solid 186 element, which uses 2 order Lagrange interpolation functions, is used. The element size is defined as the thickness of the top layer. The time step in ANSYS is 0.00001s.

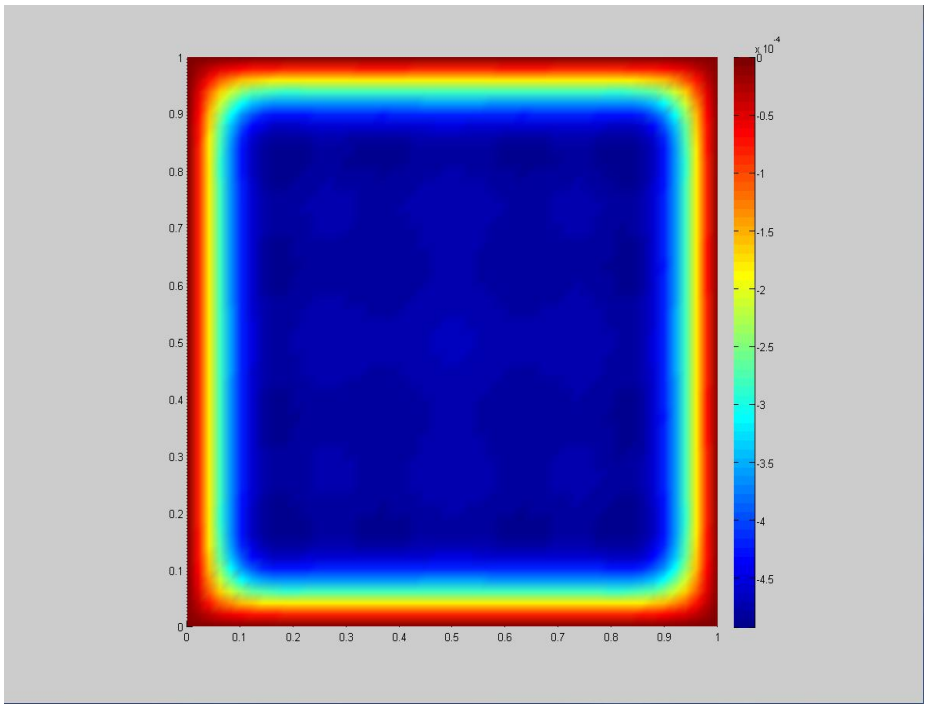

Figure 28a Deflection contour at time $t = 2e-4s$ from hybrid DG-FEM (unit: Meter)

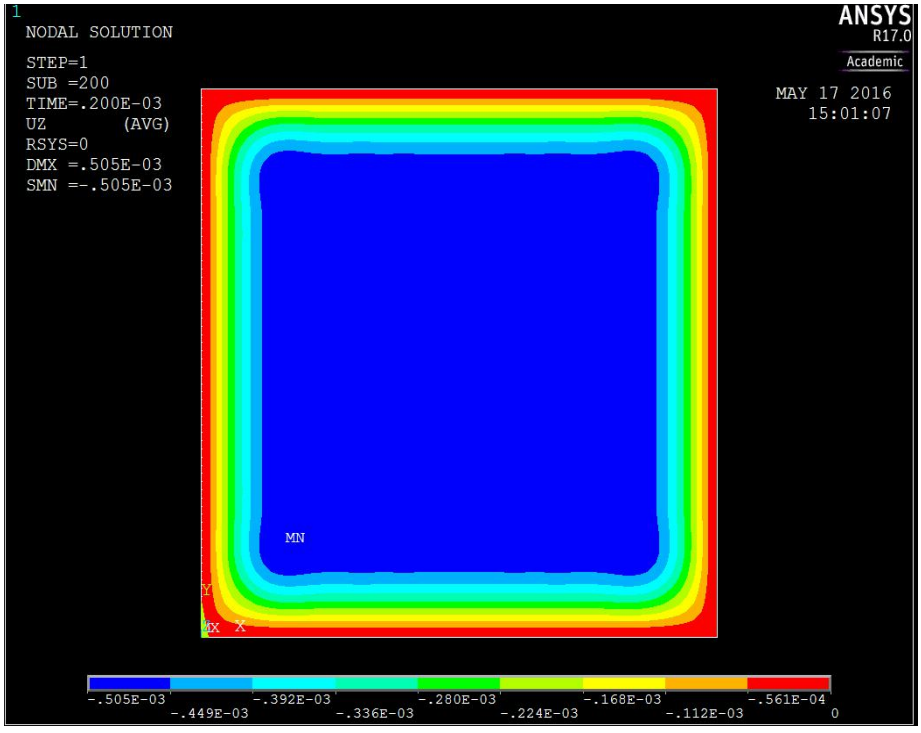

Figure 28b Deflection contour at time $t = 2e-4s$ from ANSYS (unit: Meter)

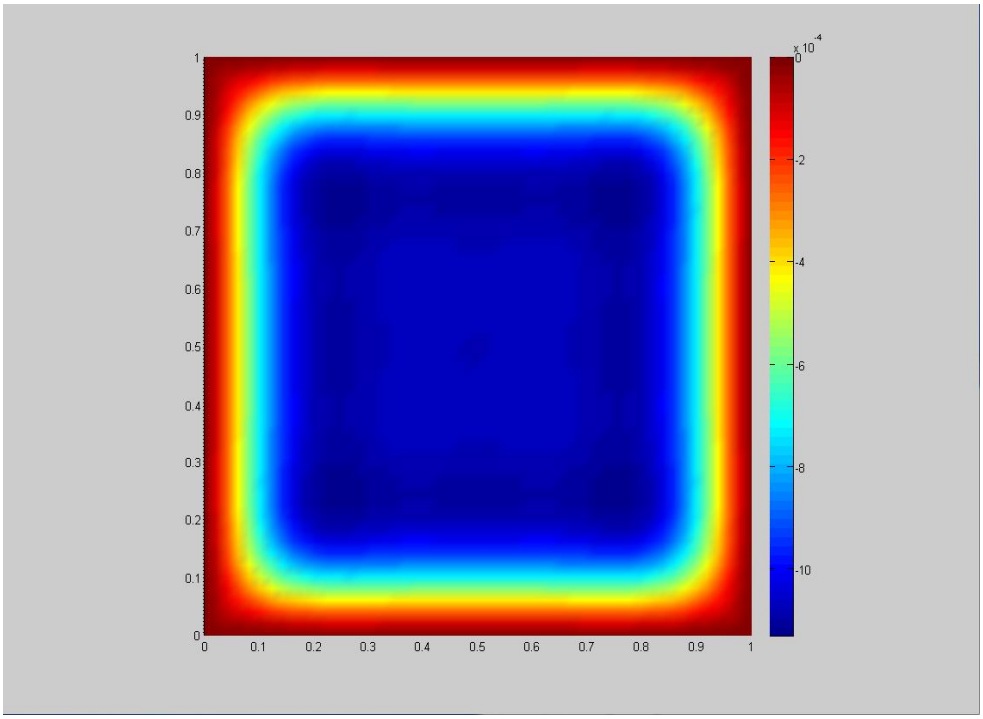

Figure 29a Deflection contour at time $t = 3e-4s$ from hybrid DG-FEM (unit: Meter)

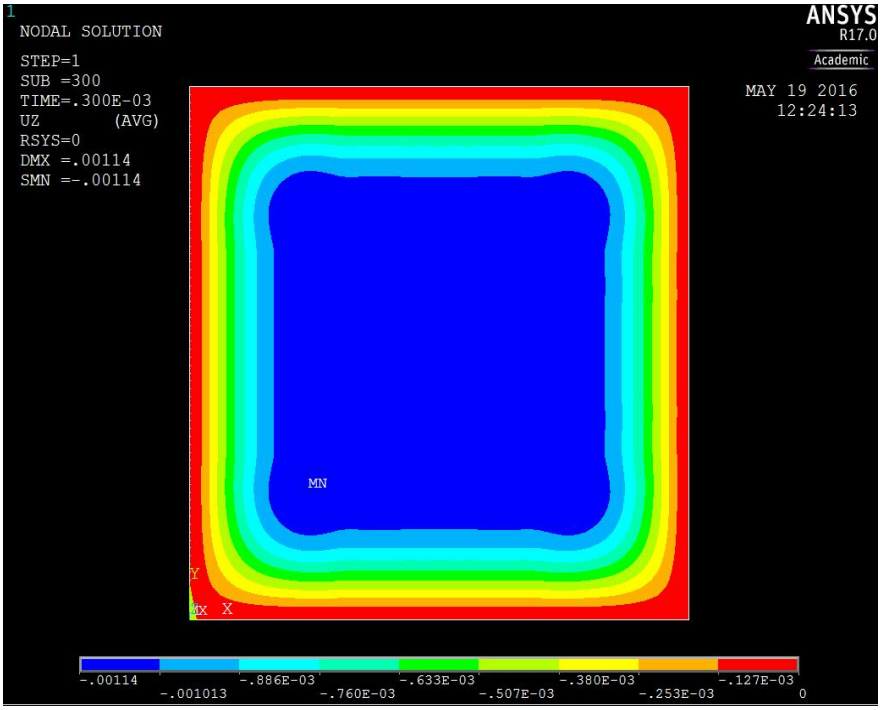

Figure 29b Deflection contour at time $t = 3e-4s$ from ANSYS (unit: Meter)

Test 2: Thick sandwich plate vibration analysis

In this test, the core later plate thickness is $t_2 = 6t_1$. For other parameters, they are same as Test 1.

The deflection history curve is shown in Figure 30.

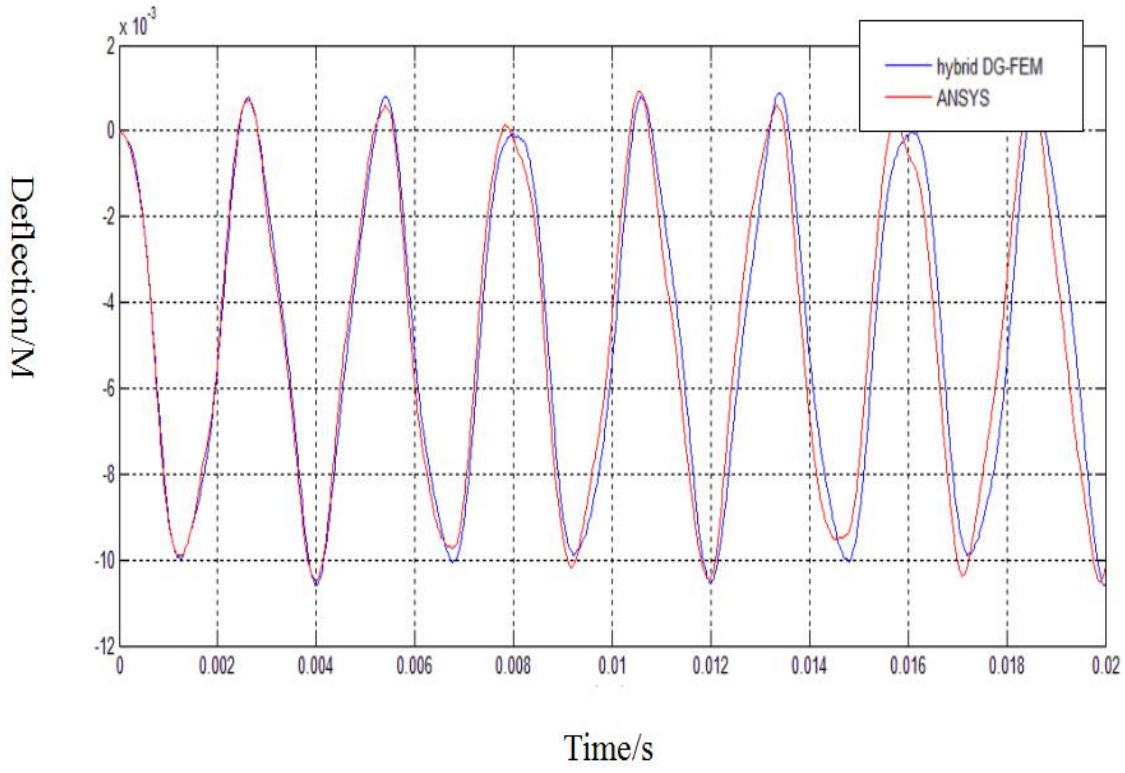

Figure 30 Deflection-time curve for the center point of the sandwich plate

In Figure 30, the deflection of the sandwich plate's point $(0.5,0.5)$ is recorded and compared with ANSYS.

The displacement contours are compared with ANSYS for some time steps in Figure 31-34. From these Figures' comparison, we can conclude that the method is accurate for conducting dynamic analysis of sandwich plates.

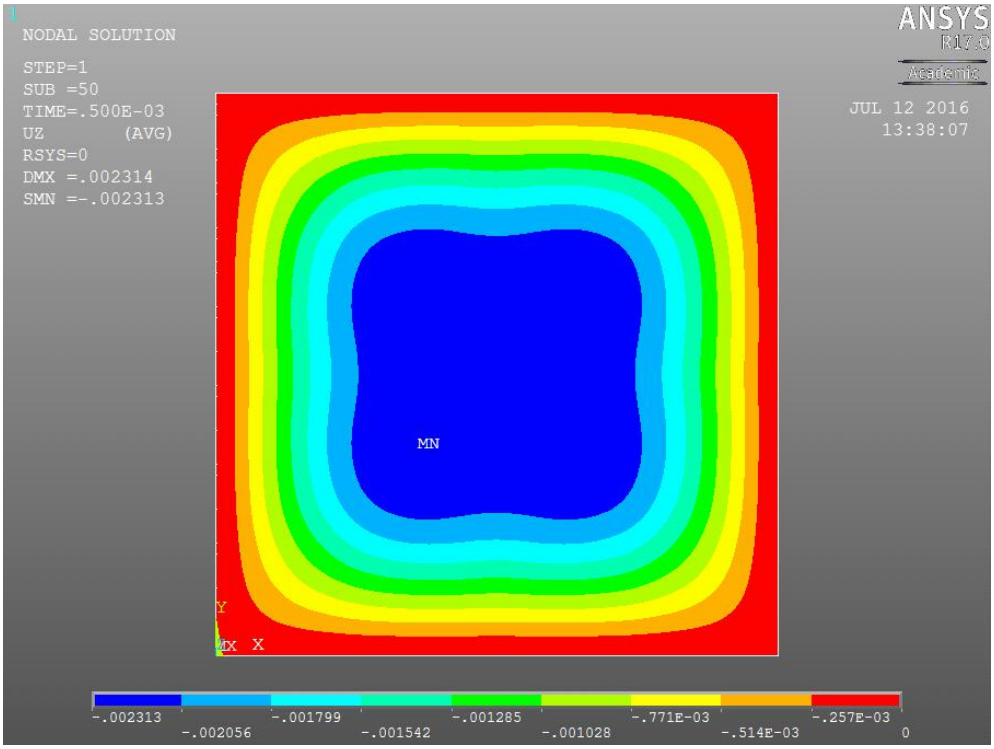

Figure 31a Displacement contour at time 5e-4s from ANSYS (unit: Meter)

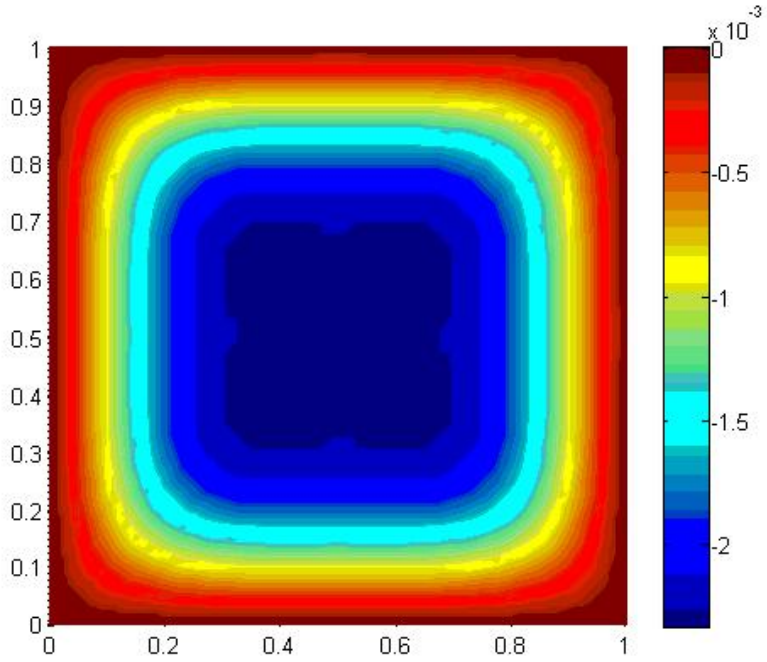

Figure 31b Displacement contour at time 5e-4s from DG-FEM (unit: Meter)

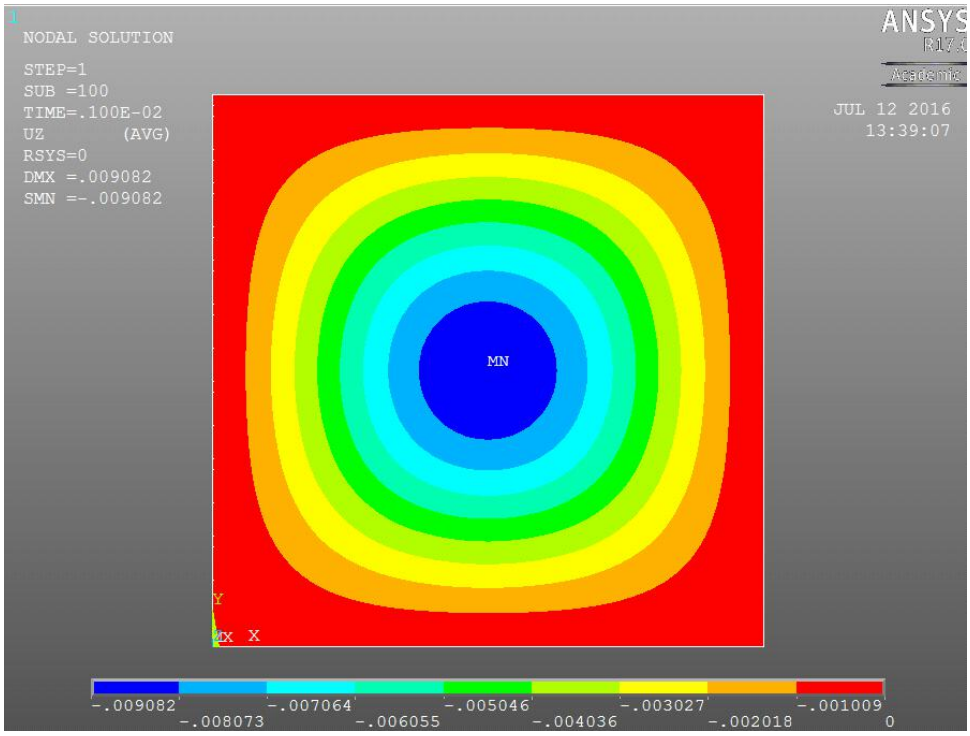

Figure 32a Displacement contour at time 1e-3s from ANSYS (unit: Meter)

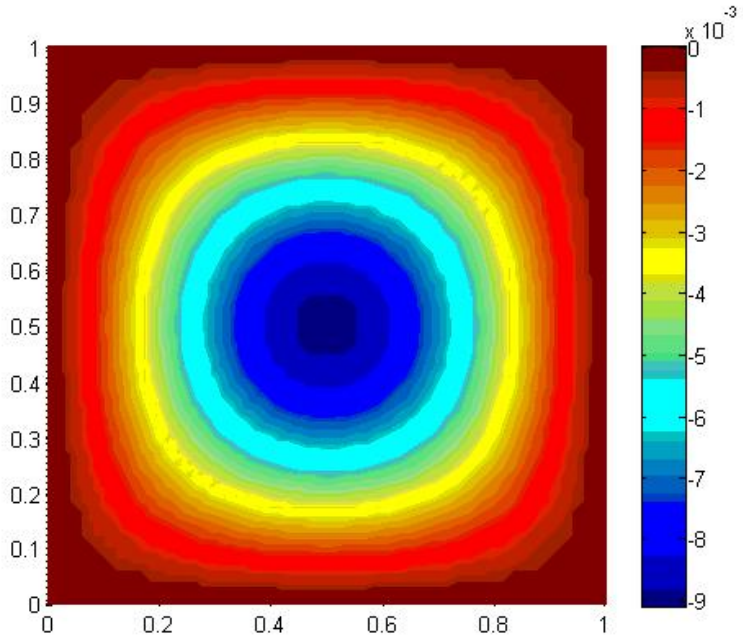

Figure 32b Displacement contour at time 1e-3s from DE-FEM (unit: Meter)

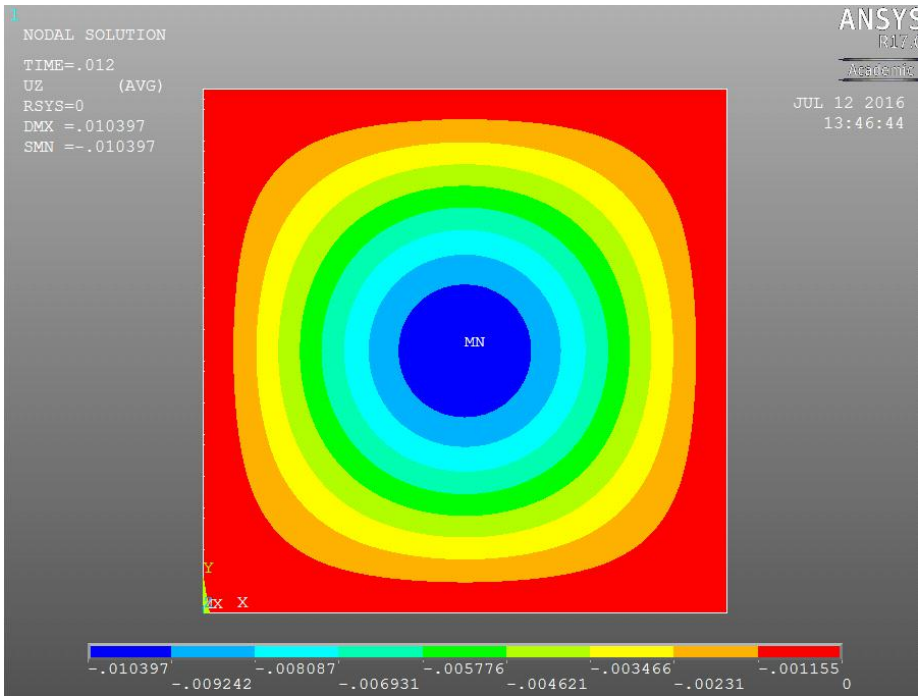

Figure 33a Displacement contour at time 12e-3s from ANSYS (unit: Meter)

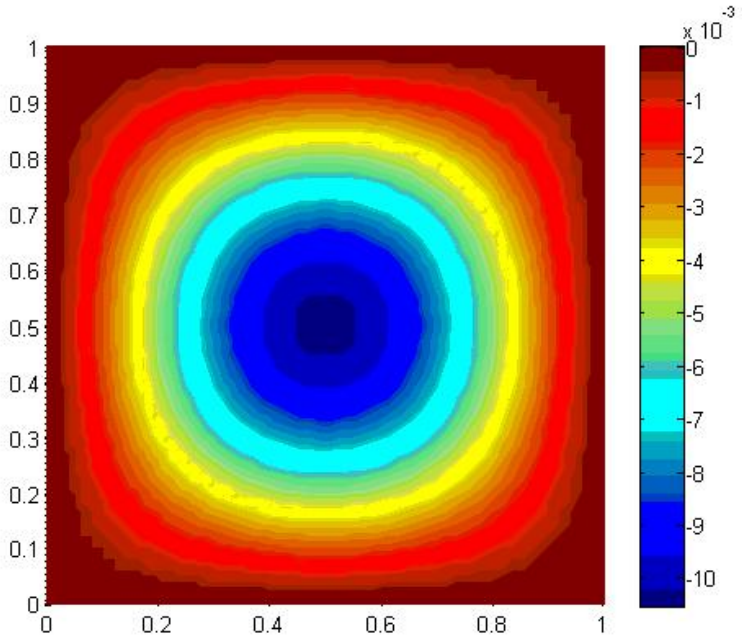

Figure 33b Displacement contour at time 12e-3s from DG-FEM (unit: Meter)

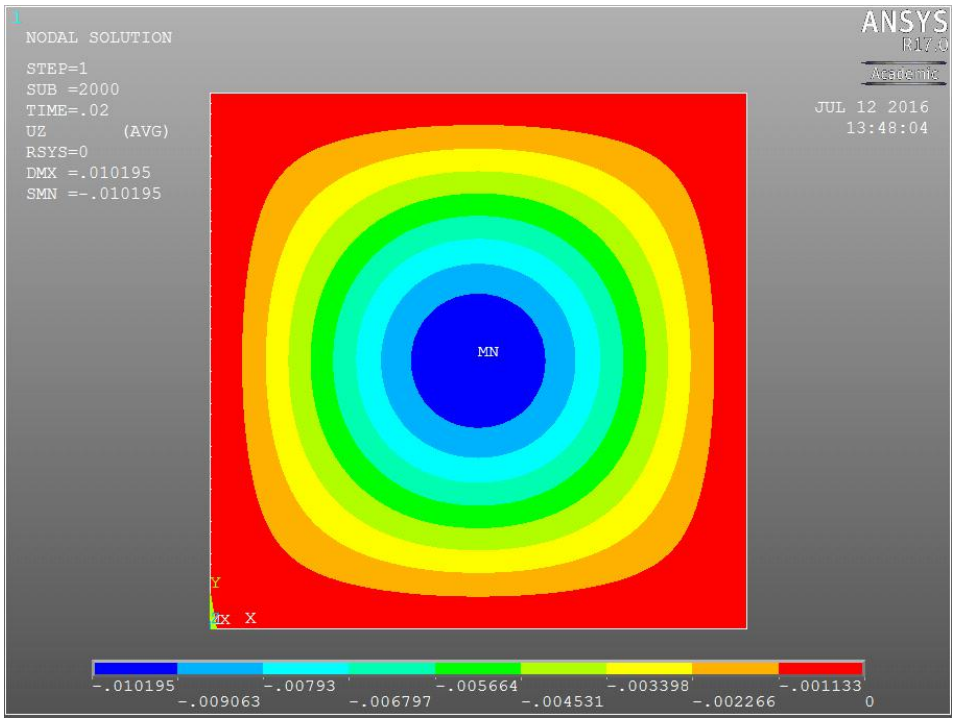

Figure 34a Displacement contour at time 2e-2s from ANSYS (unit: Meter)

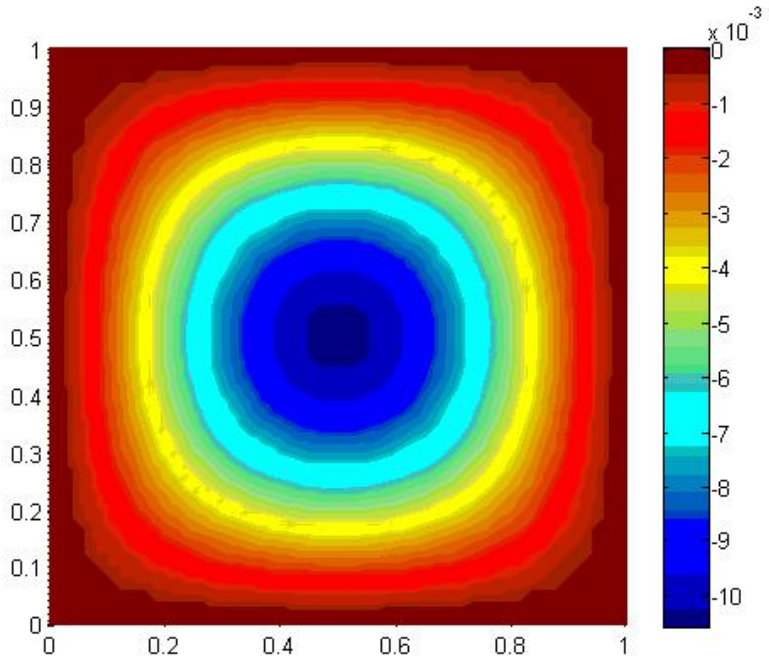

Figure 34b Displacement contour at time 2e-2s from DG-FEM (unit: Meter)

6.2 Multi-layered beam

In this section, the 2-D multi-layered curved beam is analyzed. The imperfect multi-layered pipe's buckling problem is solved. For the 2-D perfect pipe, we have the configuration as:

$$\vec{r}_0^{\,k} = \begin{bmatrix} \left(R^k + t_w^k \xi_3^k\right)\cos\left(2\pi\xi_2\right) \\ \left(R^k + t_w^k \xi_3^k\right)\sin\left(2\pi\xi_2\right) \end{bmatrix} \tag{229}$$

where R^k, t_w^k are the inner radius and wall thickness of the pipe's k^{th} layer. They are both constants for 2-D perfect pipe.

Thus, the Jacobian matrix is:

$$J = \begin{bmatrix} -2\pi\left(R^k + t_w^k \xi_3^k\right)\sin\left(2\pi\xi_2\right) & 2\pi\left(R^k + t_w^k \xi_3^k\right)\cos\left(2\pi\xi_2\right) \\ t_w^k \cos\left(2\pi\xi_2\right) & t_w^k \sin\left(2\pi\xi_2\right) \end{bmatrix} \tag{230}$$

The determinant of the Jacobian matrix will be:

$$\det(J) = 2\pi t_w^k \left(R^k + t_w^k \xi_3^k\right) = 2\pi\left(t_w^k\right)^2 \left(\frac{R^k}{t_w^k} + \xi_3^k\right) \tag{231}$$

For the 2-D imperfect pipe, we define the configuration as:

$$\vec{r}_0^{\,k} = \begin{bmatrix} \left(1+\Delta\cos\left(4\pi\xi_2\right)\right)\left(R^k + t_w^k \xi_3^k\right)\cos\left(2\pi\xi_2\right) \\ \left(1+\Delta\cos\left(4\pi\xi_2\right)\right)\left(R^k + t_w^k \xi_3^k\right)\sin\left(2\pi\xi_2\right) \end{bmatrix} \tag{232}$$

where Δ is the ovality of the imperfect pipe, which is used to control the magnitude of the imperfection.

Then, the determinant of the Jacobian matrix will be:

$$\det(\mathcal{J}) = 2\pi t_w^k \left(1+\Delta\cos\left(4\pi\xi_2\right)\right)\left(R^k + t_w^k \xi_3^k\right) = 2\pi\left(t_w^k\right)^2 \left(1+\Delta\cos\left(4\pi\xi_2\right)\right)\left(\frac{R^k}{t_w^k} + \xi_3^k\right) \quad (233)$$

For the 2-D multi-layered pipe's buckling problem, only $1/4$ pipe is considered because of symmetrical character of the problem. Thus, the circumferential displacement should vanish at the symmetrical surfaces.

Thus, the structural configuration is written as:

$$\vec{r}_0^k = \begin{bmatrix} \left(1+\Delta\cos\left(\pi\xi_2\right)\right)\left(R^k + t_w^k \xi_3^k\right)\cos\left(\pi\xi_2/2\right) \\ \left(1+\Delta\cos\left(\pi\xi_2\right)\right)\left(R^k + t_w^k \xi_3^k\right)\sin\left(\pi\xi_2/2\right) \end{bmatrix} \quad (234)$$

where Δ is called ovality, which is a parameter to control the magnitude of imperfection.

The determinant of the Jacobian matrix is:

$$\det(\mathcal{J}) = \frac{\pi}{2} t_w^k \left(1+\Delta\cos\left(\pi\xi_2\right)\right)\left(R^k + t_w^k \xi_3^k\right) = \frac{\pi}{2}\left(t_w^k\right)^2 \left(1+\Delta\cos\left(\pi\xi_2\right)\right)\left(\frac{R^k}{t_w^k} + \xi_3^k\right) \quad (235)$$

For the 2-D multi-layered pipe's buckling problem, the boundary conditions are discussed. There is no circumferential displacement at $\theta = 0, \pi/2$. Then the boundary condition functions will be defined as:

$$\begin{aligned} &f_{u_1}^{\xi_1} = f_{u_2}^{\xi_1} = f_{u_3}^{\xi_1} = 1 \\ &f_{u_2}^{\xi_2} = \xi_2(1-\xi_2) \\ &f_{u_1}^{\xi_2} = f_{u_3}^{\xi_2} = 1 \\ &f_{u_1}^{\xi_3^k} = f_{u_2}^{\xi_3^k} = f_{u_3}^{\xi_3^k} = 1 \end{aligned} \quad (236)$$

If we select the perfect pipe configuration as the initial time configuration, the orthogonal basis function spaces will be:

$\phi_{u_i}^{\xi_1}(i=1,2,3)$ is the orthogonal polynomial series with weighting function 1,

$\psi_{u_i}^{\xi_2}(i=1,3)$ is the orthogonal polynomial series with weighting function 1,

$\psi_{u_i}^{\xi_2}(i=2)$ is the orthogonal polynomial series with weighting function $\xi_2^2(1-\xi_2)^2$

$\varphi_{u_i}^{\xi_1}(i=1,2,3)$ is the orthogonal polynomial series with weighting function $\left(\frac{R^k}{t_w^k}+\xi_3^k\right)$.

If we select the imperfect pipe configuration as the initial configuration, the orthogonal basis function spaces will be:

$\phi_{u_i}^{\xi_1}(i=1,2,3)$ is the orthogonal polynomial series with weighting function 1,

$\psi_{u_i}^{\xi_2}(i=1,3)$ is the orthogonal polynomial series with weighting function

$\left(1+\Delta\cos\left(\pi\xi_2\right)\right)$,

$\psi_{u_i}^{\xi_2}(i=2)$ is the orthogonal polynomial series with weighting function

$\xi_2^2(1-\xi_2)^2\left(1+\Delta\cos\left(\pi\xi_2\right)\right)$,

$\varphi_{u_i}^{\xi_1}(i=1,2,3)$ is the orthogonal polynomial series with weighting function $\left(\frac{R^k}{t_w^k}+\xi_3^k\right)$.

These two choices are both valid. It depends on how the imperfection develops. If the imperfection is formed after the quenching, then the perfect configuration is the right choice. If the imperfection is formed before the quenching, the imperfect configuration is selected.

Thus, for the case of the perfect pipe, the circumferential basis functions are plotted in Figure 35.

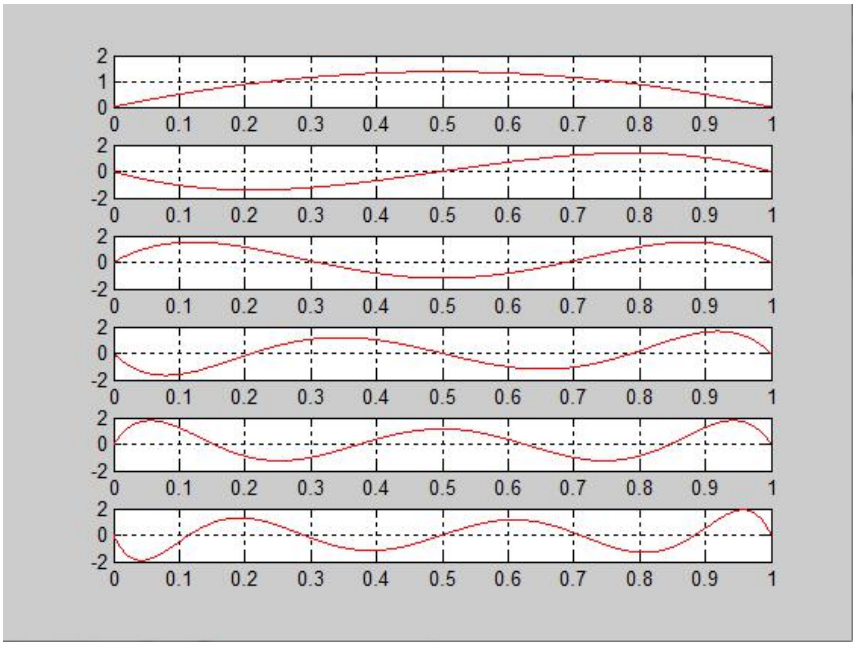

Figure 35 The plot of circumferential basis functions

The radial basis functions are plotted in the Figure 36.

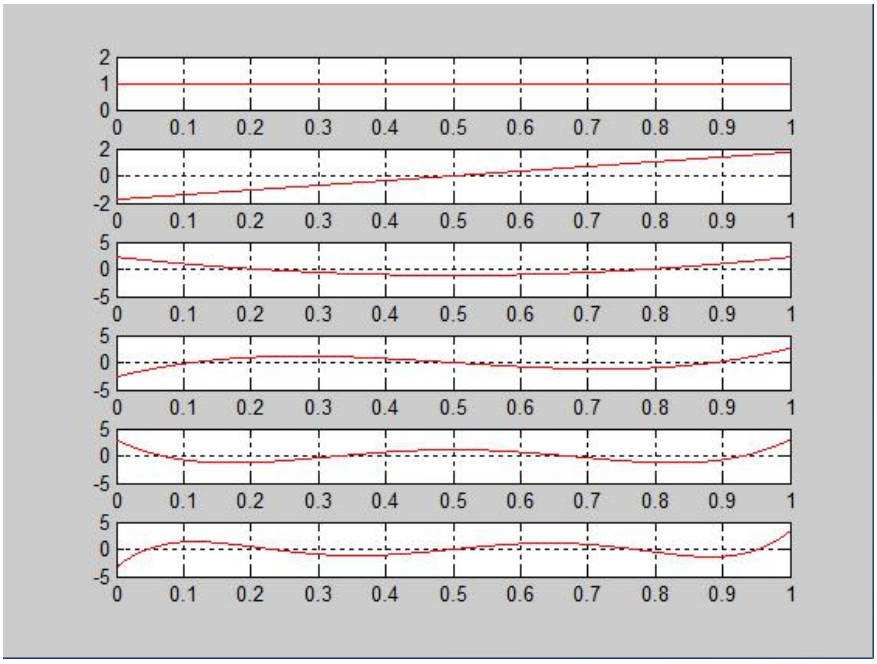

Figure 36 The plot of radial basis functions

For the case of imperfect pipe, the circumferential basis functions are plotted and compared with those of a perfect pipe in Figure 37.

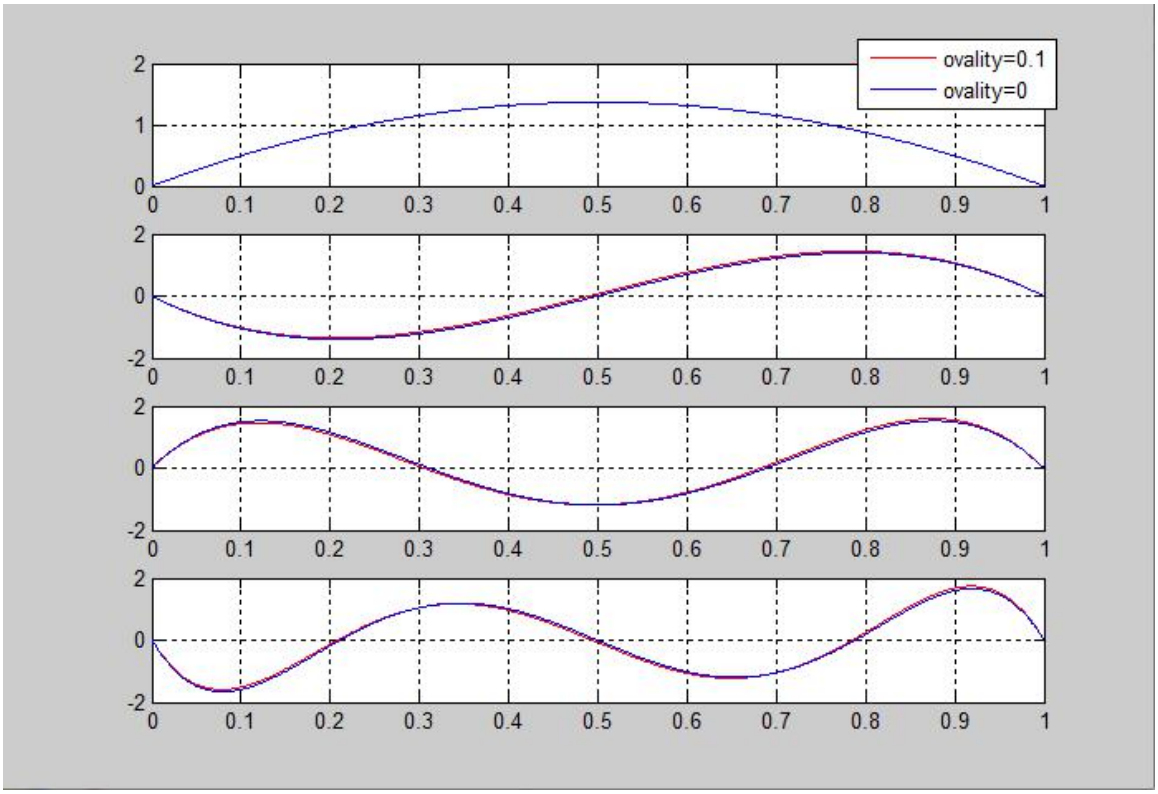

Figure 37 The comparison of the basis functions of perfect pipes and imperfect pipes

From Figure 37, it is observed that the imperfect pipes with a relatively large ovality (0.1) have an very identical basis function space with that of the perfect pipes.

The contact is also included in the problem of multi-layered pipe buckling. The Lagrangian multiplier method is used to apply the contact constraints. For the pipe buckling problems, the 1/4 pipe is used due to the symmetrical characters. Thus, the contact also occurs on the symmetrical surfaces. In the codes, once there is any material points penetrating the symmetrical surface, the point will be recorded and

the Lagrangian multiplier method will be applied for this point to constraint the normal displacement component.

The multi-layered pipe's post buckling response is shown in Figure 38.

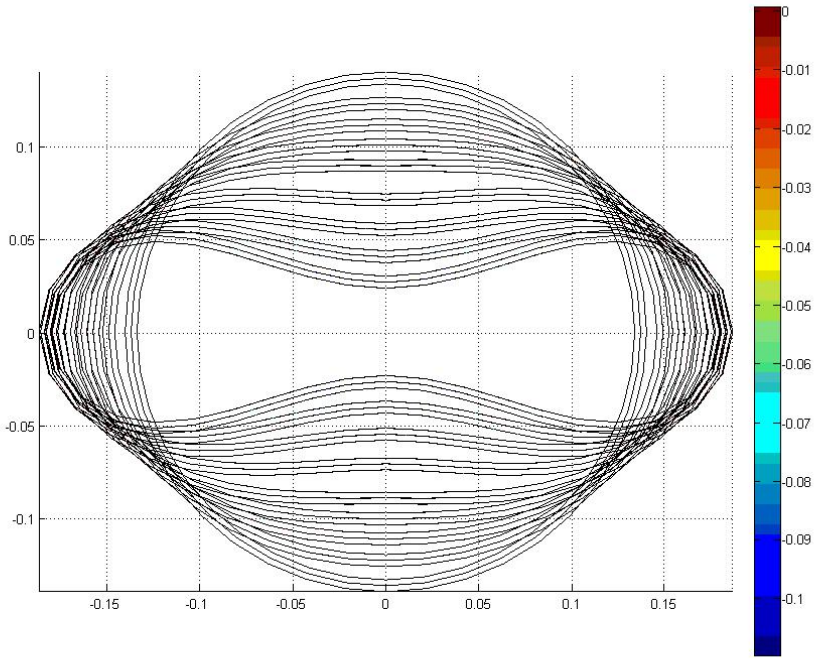

Figure 38 The post-buckling process for a multi-layered pipe under water pressure

In this Figure 38, the post buckling process of a 2-layered pipe is recorded. The water pressure is applied on the outer surface of the pipe. Due to the imperfection in the geometry, the structure will collapse.

Test 3: 2-D single-layered pipe collapse analysis

In this test, a 2-D single-layered pipe collapse analysis is presented. The multi-layered pipe element presented earlier is applied here.

The pipe outer diameter is $D_w = 406.4$ mm. The wall thickness is t_w =12.7 mm. The consistent ovality is $\Delta = 0.2\%$. The nominal yield stress is $448 Mpa$.

If we define this single-layer pipe by using 2 layers, then, for each layer we have:

$t_w^k = t_w / 2, k = 1,2.$

But for these two layers, the material parameters are the same.

The water pressure is applied on the outer surface and the pressure volume curve is shown in Figure 39.

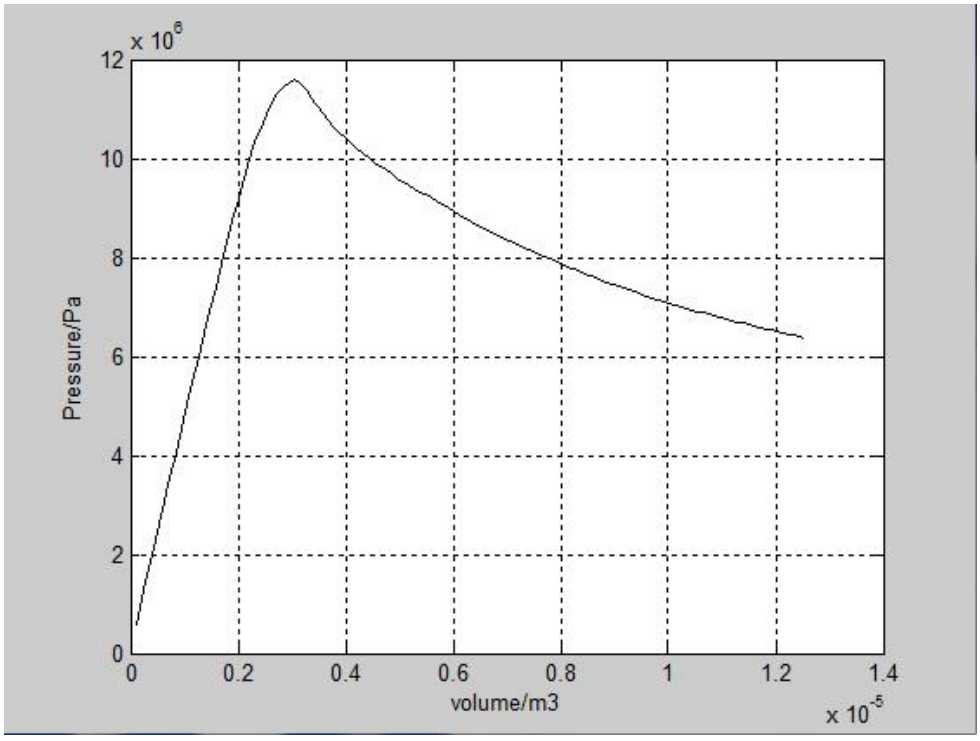

Figure 39 Pressure-volume curve for the single layer pipe

From the curve in Figure 39, the critical buckling pressure is 11.58MPa.

More single-layer pipe numerical tests are presented and compared with ANSYS in the Table 2.

Table 2 Critical buckling collapse pressure for single-layer pipes

D_w /mm	t_w /mm	Δ	σ_y / MPa	VCP /MPa	ANSYS /MPa
406.4	12.7	0.002	448	11.58	11.53
325	10	0.002	448	11.09	11.06
355.6	9.53	0.002	448	7.45	7.52
406	10	0.002	448	5.85	5.93
273	6.35	0.002	448	4.94	5.03

From these results, we can see that the multi-layered pipe element is reliable for a single-layer pipe's collapse analysis.

A convergence study is presented. The pipe outer diameter is 406.4 mm. The wall thickness is 12.7 mm. The consistent ovality is $\Delta = 0.2\%$. The nominal yield stress is $448 Mpa$.

The wall thickness displacement order is $s_0 = 2$ and the circumferential displacement order n_0 is increased from 5 to 11, as Figure 40 shows. In Figure 40, the post buckling response curves under increasing pressure are recorded for various values of the circumferential displacement function order.

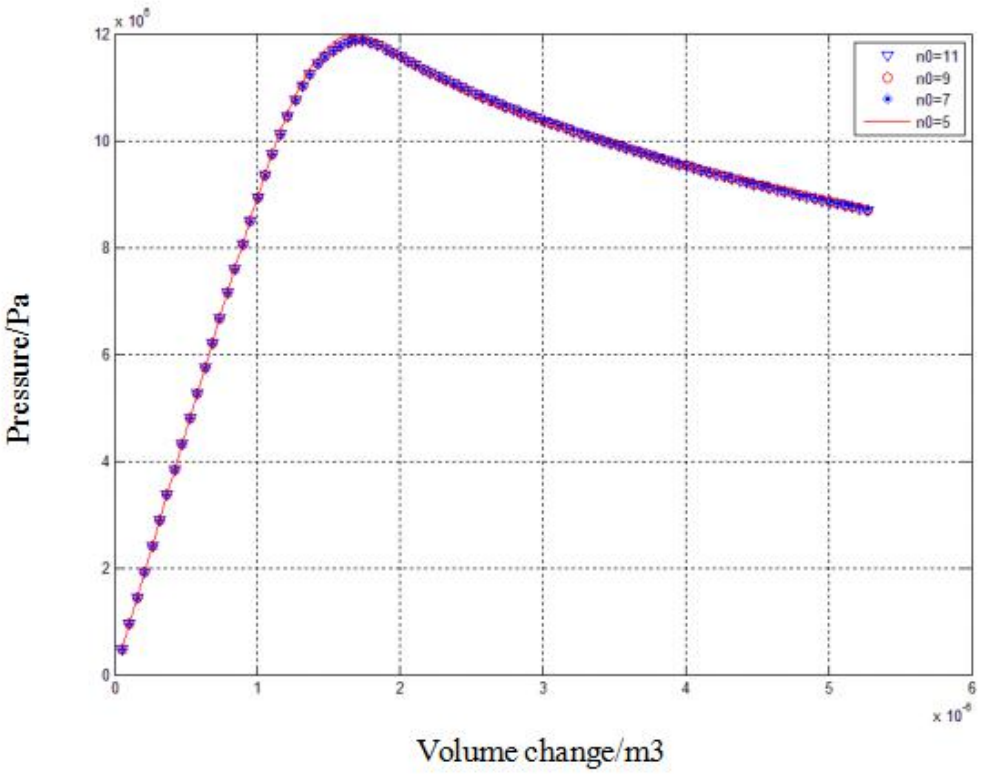

Figure 40 Convergence study of circumferential displacement order

From the pressure curves in Figure 40, it is observed that the pressure curves converge with an increase in the order of circumferential displacement functions. The wall thickness displacement function order is changed to $s_0 = 3$ and the circumferential displacement order n_0 is increased from 5 to 11 in Figure 41. The post buckling response curves are presented in Figure 41.

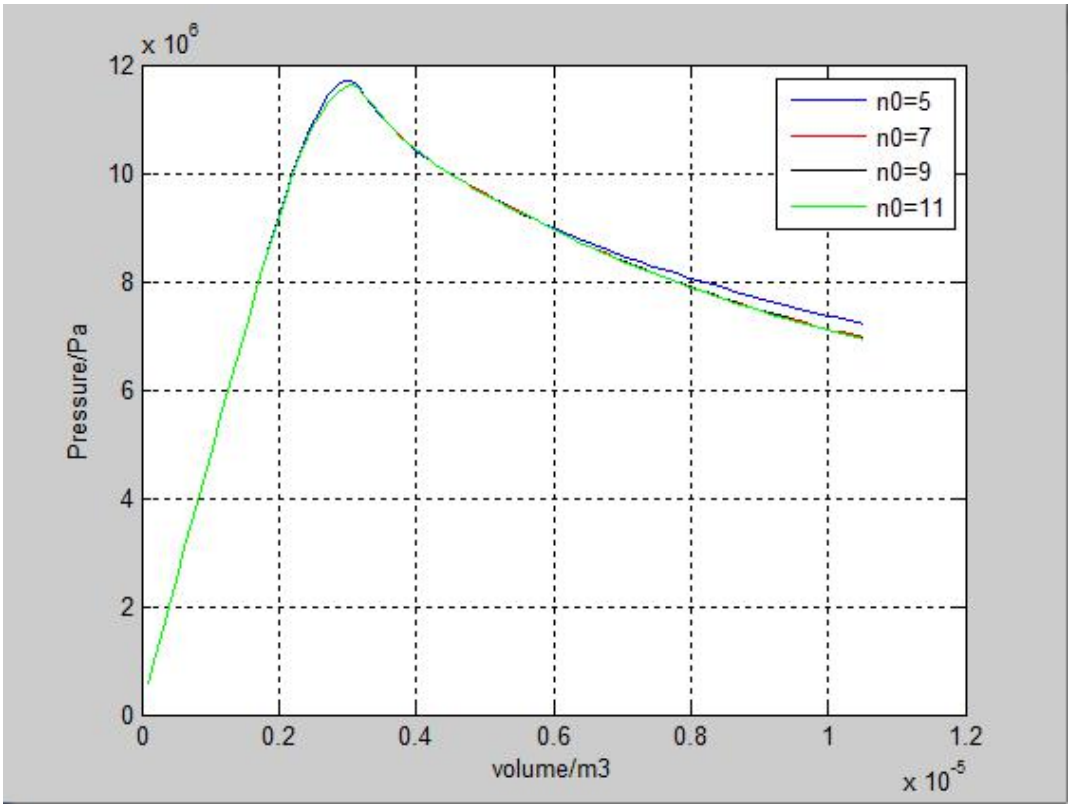

Figure 41 Convergence study of circumferential displacement order

From the curves in Figure 41, it is observed that the critical buckling pressure is smaller than that in Figure 40. Also, the results converge with the increase in circumferential displacement function order.

The wall thickness displacement order convergence study is presented. The circumferential displacement order is $n_0 = 9$ and the wall thickness displacement order s_0 is increased from 2 to 4 in Figure 42. The post buckling pressure curves are presented in Figure 42.

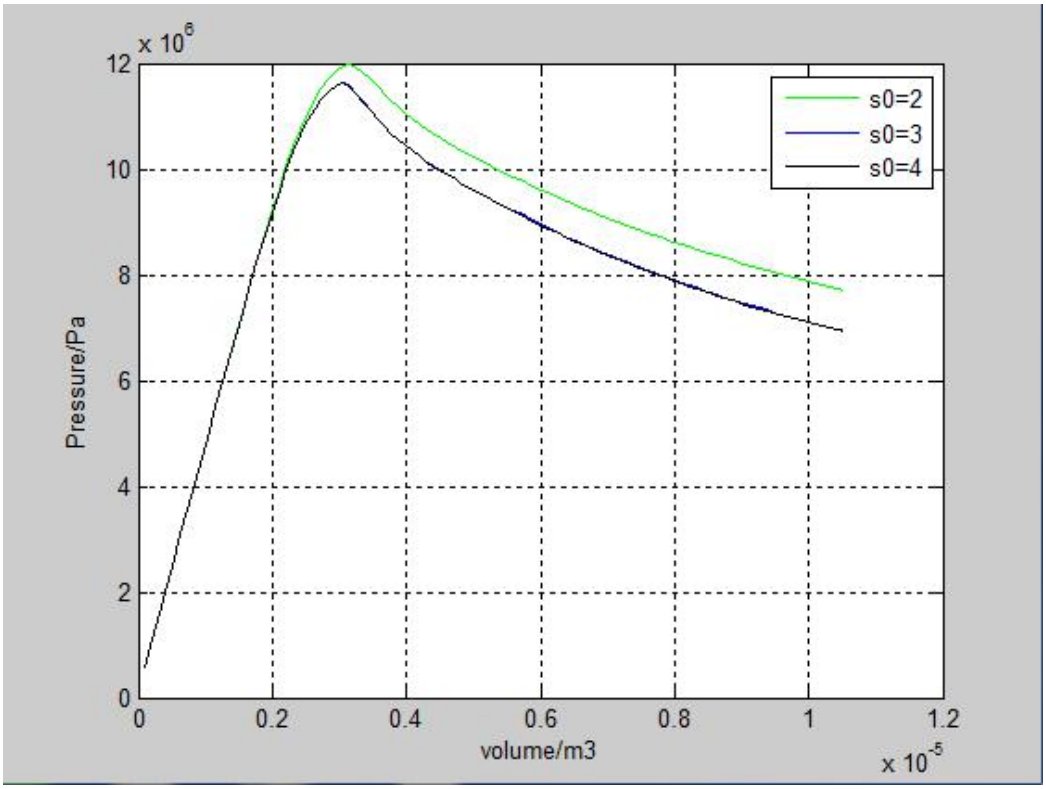

Figure 42 Convergence study of radial displacement order

From Figure 42, it is observed that, for the linear thickness displacement order case, the results are not satisfactory. When the wall thickness displacement order is greater than 3, the results converge. This shows that the three-dimensional effects are important.

Test 4: 2-D multi-layered pipe collapse analysis

A two-layered pipe buckling collapse analysis is next presented. The first layer is assumed to be elastic, with the Young's modulus 206Gpa, Poisson ratio 0.3. The second layer is assumed to be plastic. The yield stress is 448MPa. For the elastic-plastic stress-strain relation, the Ramberg-Osgood equation (225) is used.

The consistent ovality is:

$\Delta = 0.2\%$

The elastic-plastic critical buckling collapse pressure is listed in Table 3.

Table 3 Critical buckling collapse pressure for 2-layer pipes

D_w/mm	t_w/mm	Δ	P_c / *Mpa*	*Ansys*
406.4	12.7	0.002	11.69	11.82
355.6	9.53	0.002	7.49	7.64
406	10	0.002	5.86	5.99
273	6.35	0.002	4.96	5.06
325	10	0.002	11.16	11.32

From the Table 4, it is observed that the results obtained from this thesis are almost identical with those in ANSYS. Comparing with the single-layered pipe analyzed in Table 2, the critical buckling pressure is increased for the 2-layered pipe. At the point of collapse, the maximum equivalent plastic strain can be from 0.25% to 0.46%. For the post buckling, the equivalent plastic strain will be from 2.32% to 2.51%.

6.3 Multi-layered shell

The multi-layered shell analysis is presented for a 3-D multi-layered pipe. The pipe has geometrical imperfections. The single layer pipe buckling propagation analysis is presented in Test 5. In Test 6, the multi-layered pipe buckling propagation is solved. In Test 7, the multi-layered pipe structure with large ratio of materials is analyzed. In this case, the first layer's stiffness is much less than that of the second

layer. This is always hard in the field of numerical simulation. However, the method presented in this thesis also shows good robustness for this kind of structure. In Test 8, a single layer pipe buckling cross-over is solved using the multi-layered pipe element. For the background in buckling cross-over, the reader is referred to [23]. In Test 9, a multi-layer pipe buckling cross-over is analyzed. In Test 10, the buckling propagation problem with the strain rate effect is solved. In this case, the strain rate damping is considered. For the background of the strain rate buckling, the reader is referred to [29]. All the results are compared with paper [23, 28, 29] and ANSYS verification. In order to prove that the ANSYS is reliable, the pipe buckling cross-over problems are analyzed on ANSYS and verified with other papers, in which the ABAQUS is used and has been proved to be reliable[23, 28].

FEM calculations in ABAQUS by Lee and verification on ANSYS.

t_a/t_p	Lee/MPa	Verification
2	15.548	14.70875
2.25	18.651	18.12025
2.5	22.885	23.1546
2.75	27.539	28.6668
3	28.387	28.3294

Test 5: Single-layer pipe buckling propagation

In this section, the 3-D single-layer pipe buckling propagation is solved by the multi-layered pipe element. The critical buckling propagation pressure is obtained and compared with [23, 28]. The pipe outer diameter is 114.3mm. The wall thickness is 5.08mm. The nominal yielding stress is $516Mpa$. In this test, the single layer pipe is solved using multi-layered pipe elements. The same structure has been solved in [23]

using single layer pipe element developed by the author of this thesis and the results available in [28] using ABAQUS. By using the multi-layered pipe element to solve the same problem, we want to verify that the multi-layered pipe element is also applicable for the single-layered pipe structures.

The water pressure is applied on the outer surface of the pipe structure. For the single layer pipe, we still divide it into 2 layers with same material property. Each layer has the same wall thickness. The pressure-volume curve is shown in Figure 43.

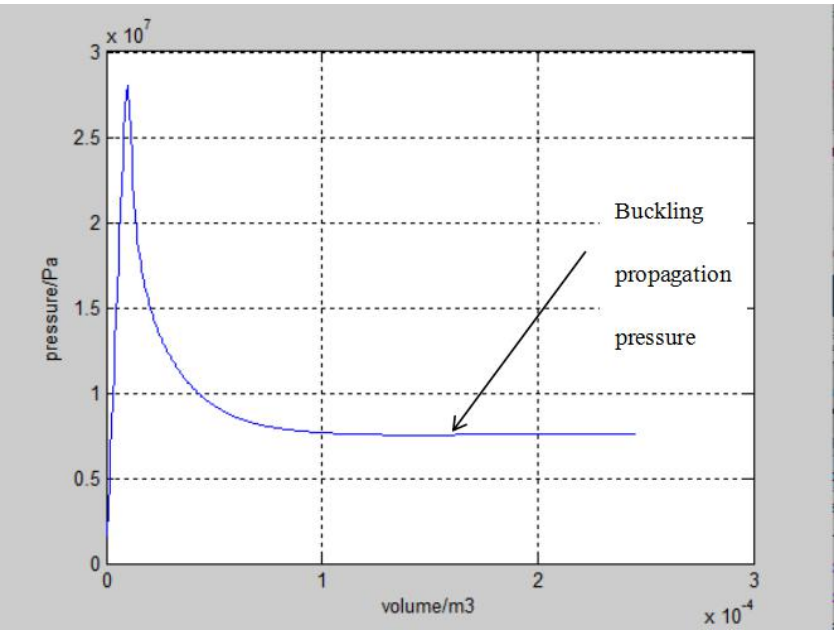

Figure 43 Pressure volume curve for single layer pipe buckling propagation

From the curve, we can get the critical buckling propagation pressure as 7.50MPa. The traditional FEM analysis gives the result of 7.65MPa [28]. The relative error is 1.96%.

The post buckling mode is shown in Figure 44.

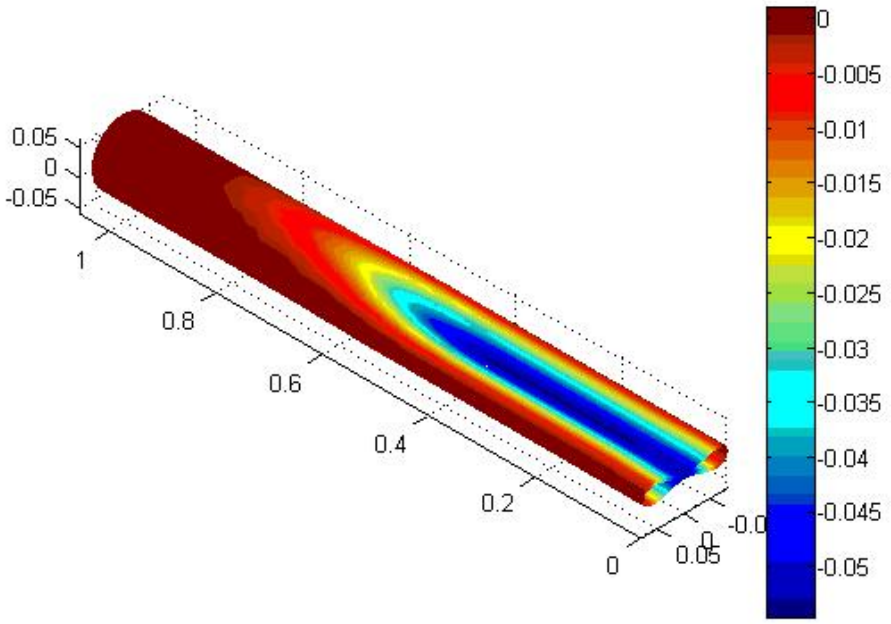

Figure 44 Displacement contours of buckling propagation (unit: Meter)

From the Figure 44, it is observed that the pipe has totally collapsed and the deformation is propagating along the pipeline. This is an unstable deformation, which means that the pipeline will be totally destroyed in absence of additional devices to arrest it. The inner surface's contact is also observed.

Test 6: Multi-layer pipe buckling propagation

A 2-layer pipe buckling propagation is analyzed. In this case, the first layer is assumed to be elastic. The second layer is assumed to be plastic with yield stress 516MPa. The Young's Modulus and Poisson's ratio are 206Gpa and 0.3, respectively. The water pressure is still applied on the outer surface, and the pressure curve obtained by this thesis is shown in Figure 45.

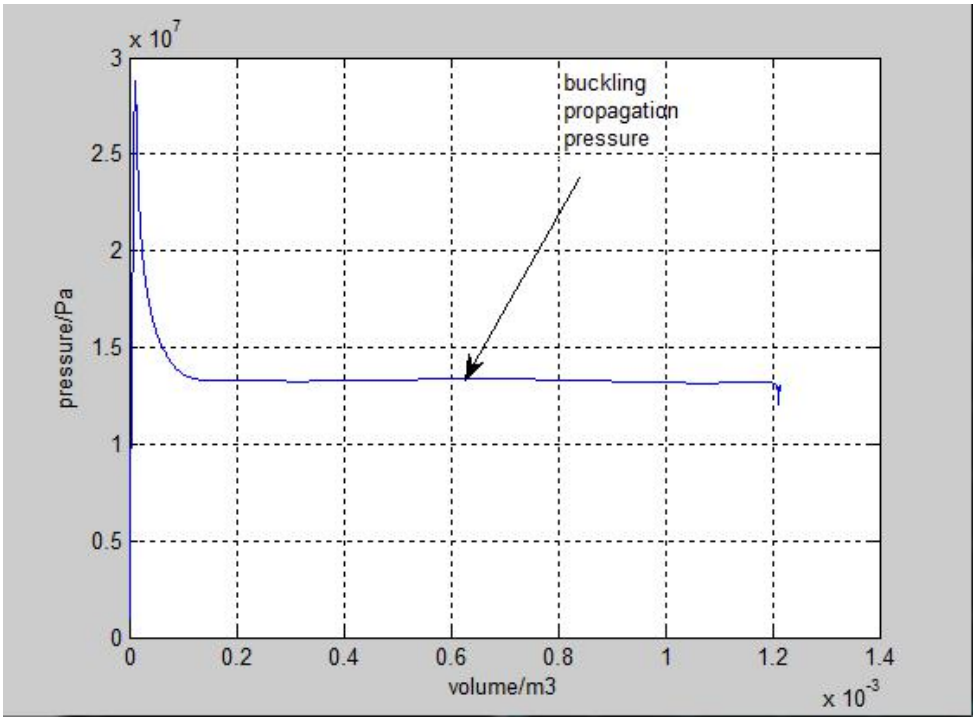

Figure 45 Pressure volume curve for 2-layer elastic-plastic pipe

From this pressure curve, the buckling propagation pressure is 13.4MPa.

The ANSYS Riks method gives the pressure curve shown in Figure 46.

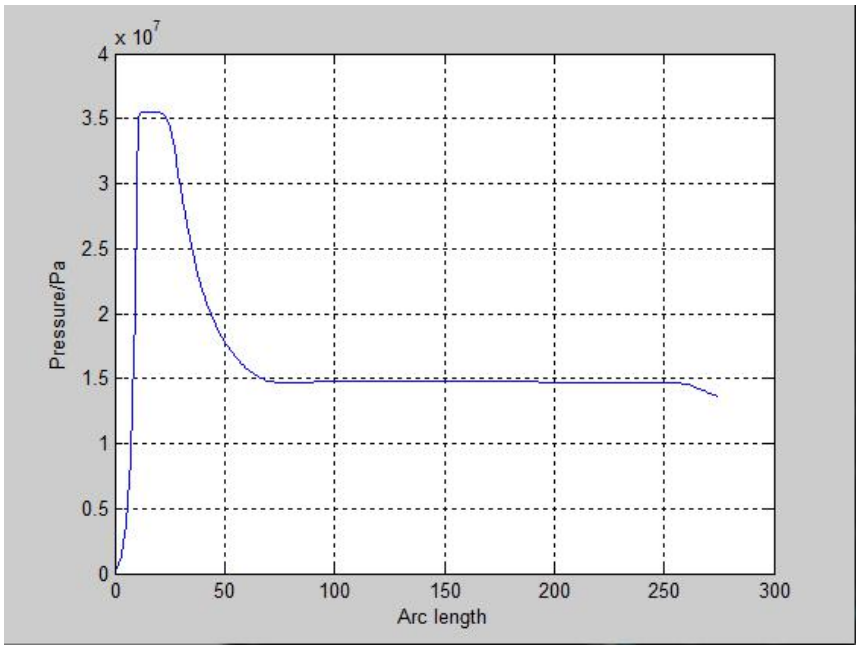

Figure 46 Pressure curve for 2-layer elastic-plastic pipe from ANSYS Riks

From Figure 46, the buckling propagation pressure is 14.6MPa. The relative error is 8.2%.

A relatively big error is observed in this analysis. The potential origin of the error is from the different plastic constitutive theory used in this thesis and in ANSYS. According to the papers [23, 28], the plastic deformation theory is more suitable for buckling problems and it is used in this thesis. For the deformation constitutive theory used in this thesis, it is referred to [33]. However, there is no deformation constitutive theory in ANSYS. The $J2$ flow theory has to be used in ANSYS. It is also reported that the $J2$ flow theory will produce a more rigid simulation, which is consistent with the results in the Figures 45 and 46.

The buckling propagation mode for the multi-layer pipe is shown in Figure 50.

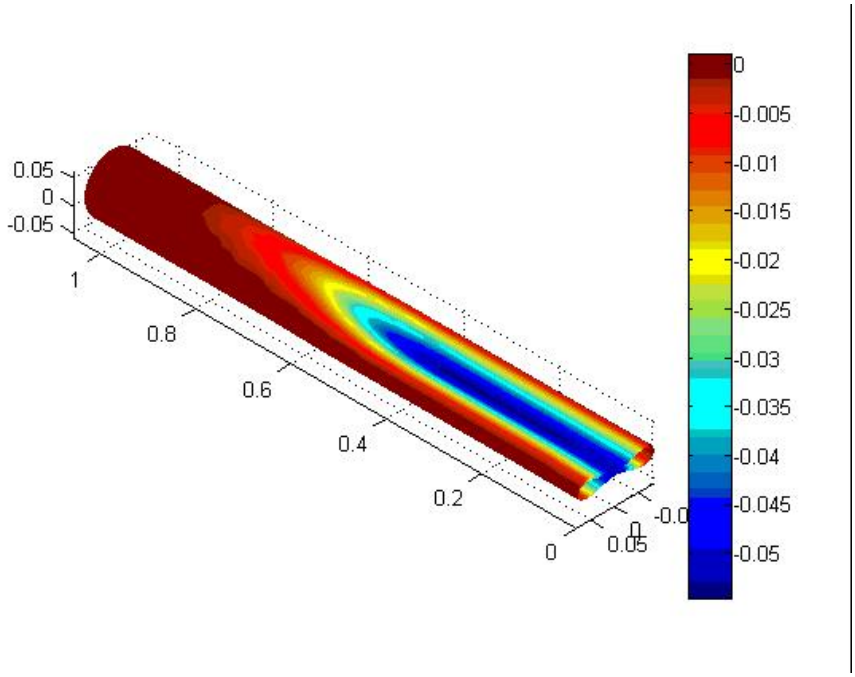

Figure 47 Displacement contours of buckling propagation for 2-layer elastic-plastic pipe (unit: Meter)

Test 7: Multi-layer pipe buckling propagation analysis with large strength ratio

In this case, a 2-layered pipe with large material ratio in the aspect of the yield stress is solved. The stiffness of the 2 layers differ significantly. In this case, a numerical difficulty may occur due to the large difference of stiffness matrix. The motivation of this analysis is to prove the robustness of the multi-layered pipe element. The first layer's nominal yielding stress is 50MPa. The second layer's nominal yielding stress is 488MPa. Thus, the first layer is plastic when the second layer is still elastic.

The geometrical parameters are the same as the last one. The first layer and the second layer have the same wall thickness $t_w^1 = t_w^2 = t_p / 2$. We want to test the case with a large ratio of stiffness.

The pressure volume curve obtained by the author is shown in Figure 48. The ANSYS Riks method gives the pressure curve in Figure 49. From the ANSYS, the critical buckling propagation pressure is 2.20MPa. The relative error is 3.9%.

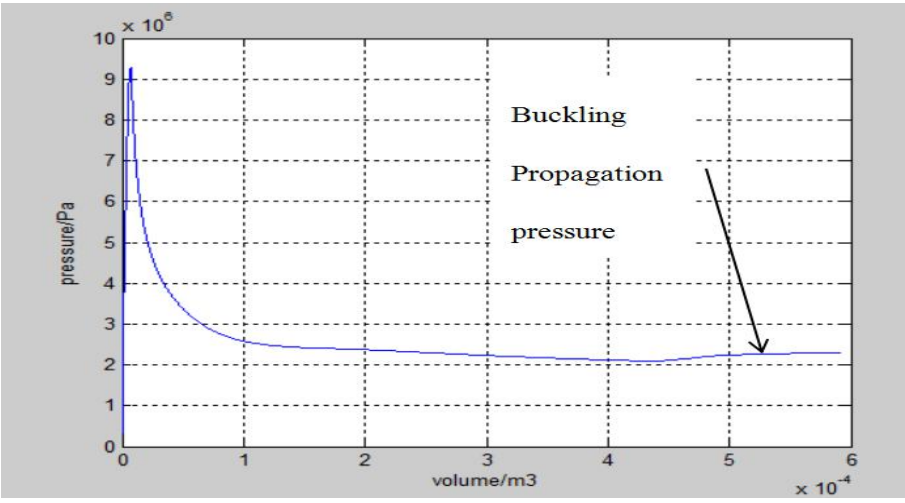

Figure 48 Pressure volume curve for 2-layer pipe with a large stiffness ratio

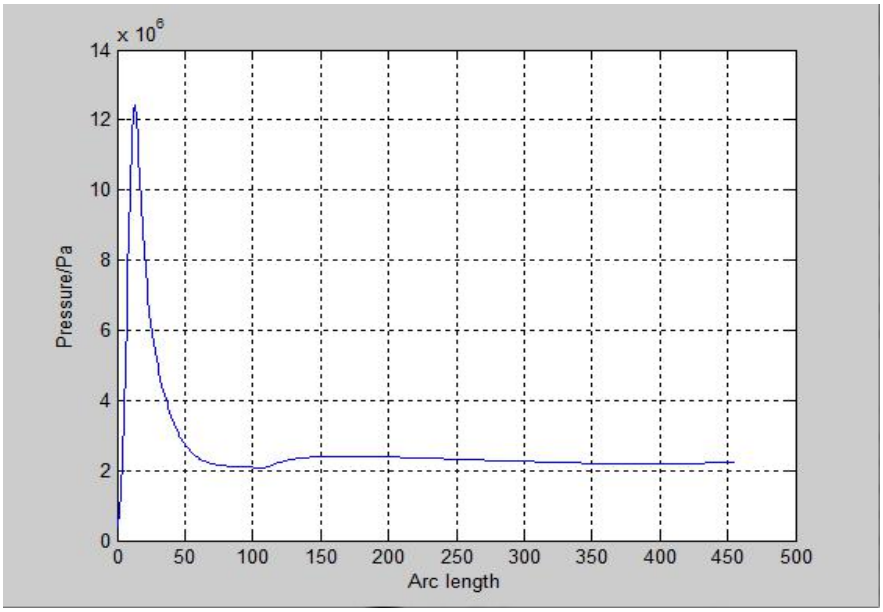

Figure 49 Pressure curve for a 2-layered pipe with a large stiffness ratio from ANSYS Riks

The post buckling behavior under the buckling propagation pressure is shown in Figure 50.

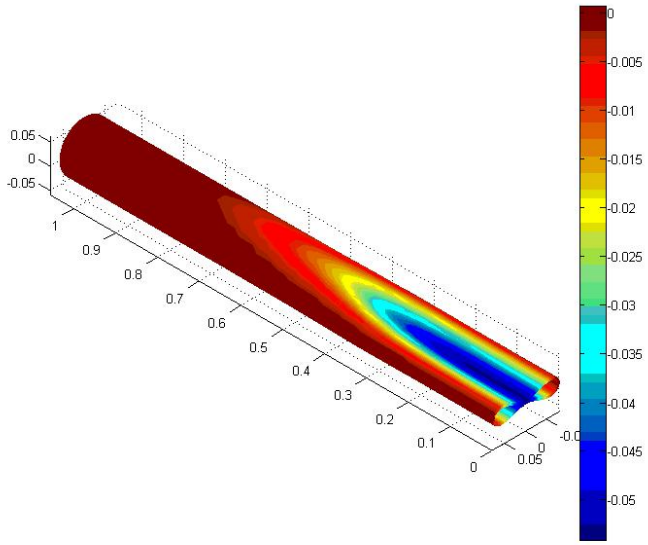

Figure 50 Displacement contours of buckling propagation (unit: Meter)

The critical buckling propagation pressure is 2.29MPa from the multi-layered pipe element.

Test 8: Pipe buckling cross-over analysis

In this case, the pipe buckling cross-over analysis is presented using the multi-layered pipe elements. For the problem of buckling cross-over, the arrestor [23, 28] is used, which is a local buckling arrestor device used for the pipeline. For the background of pipe buckling and arrestors, it is referred to the papers [23, 28, 29] and the references herein. The pipe buckling propagation analysis has been presented in the Test 5-7. It is noted that the buckling propagation is an unstable deformation, which means the whole pipeline will be destroyed without any types of arresting device to stop this propagation. The so-called arrestors are designed to enhance the pipeline locally. It is important to calculate the critical buckling cross-over pressure at which the arrestors fail to work. The critical buckling cross-over pressure is an important parameter in the ocean engineering. If the water pressure is larger than the critical cross-over pressure, the arrestors will fail to work and the unstable buckling deformation will jump over the arrestors. If the water pressure is smaller than the critical cross-over pressure, the arrestors will protect the whole pipeline. Even if there is a local collapse, the arrestors will stop the unstable buckling deformation from propagating along the whole pipeline.

The single-layer pipe buckling cross-over problem is solved at first. The pipe outer diameter is 114.3mm. The wall thickness is 5.08mm. The nominal yielding stress is $516Mpa$. The arrestor's wall thickness is 3 times the pipe's wall thickness. The

length of the arrestor is half the outer diameter of the pipe. Based on the thesis's multi-layered pipe element, the pressure curve is shown in Figure 51.

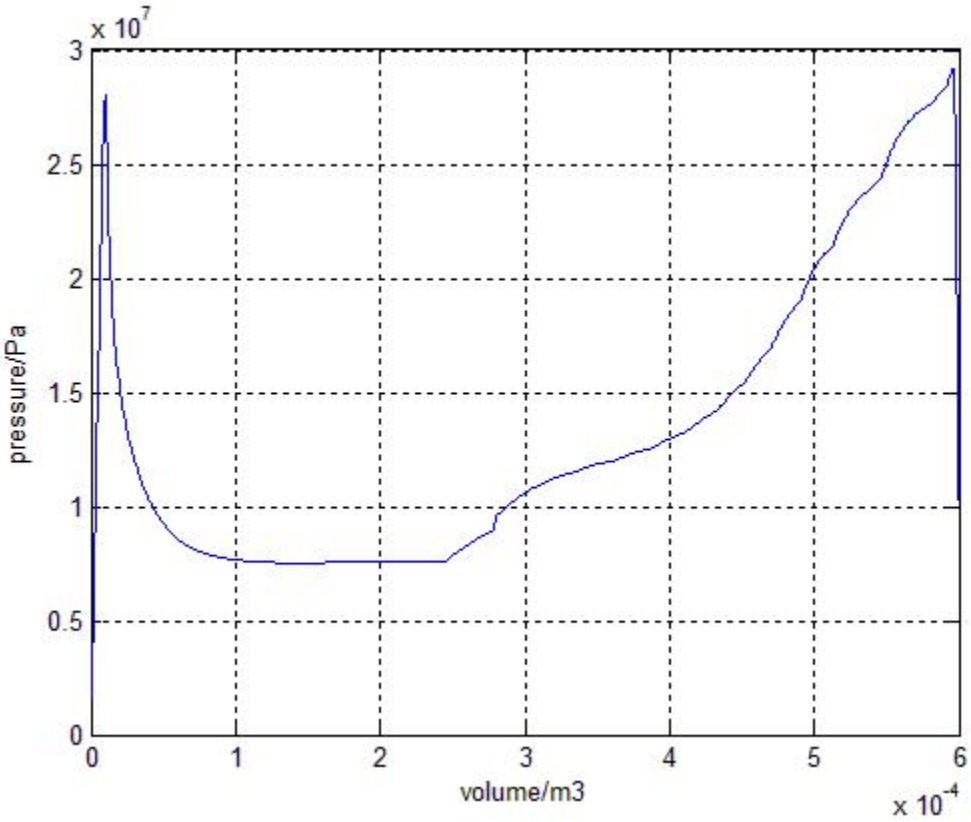

Figure 51 Pressure volume curve for single layer pipe cross-over

From the curve in Figure 51, we can get the critical buckling crossover pressure as 29.15MPa, which is the second peak value of the curve in Figure 51. The traditional ABAQUS FEM gives the result of 28.4 MPa[23, 28]. The relative error is 2.57%.

The arrestor's wall thickness is modified to 2 times the pipe's wall thickness.

The pressure curve is shown in Figure 52.

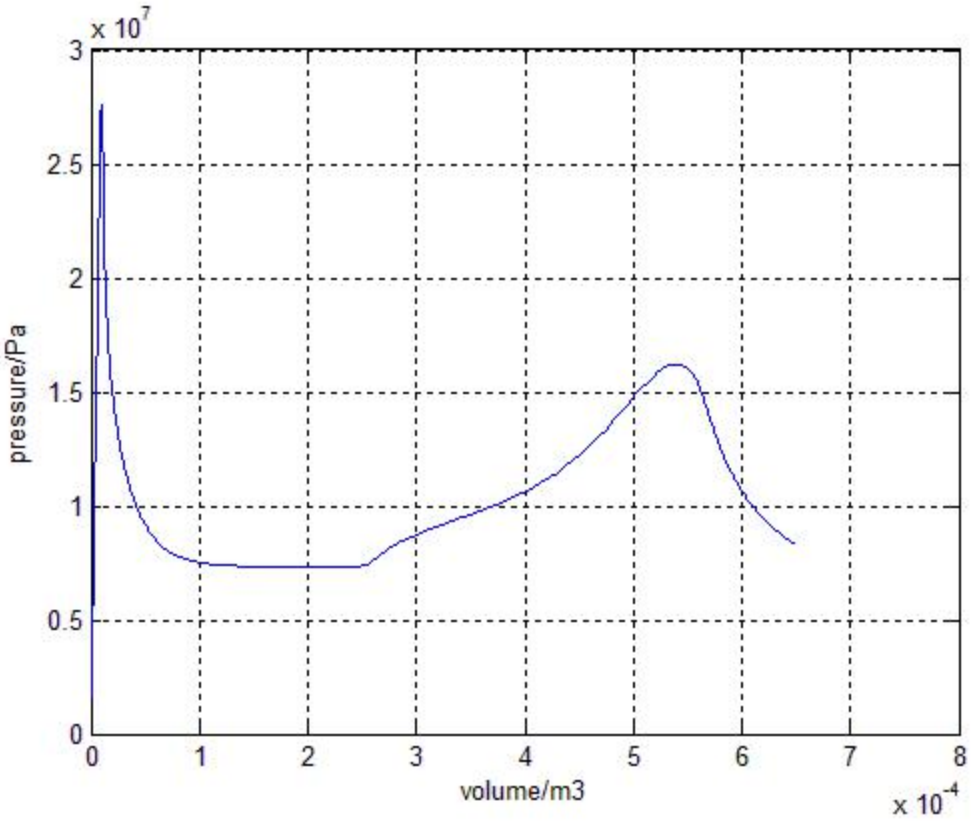

Figure 52 Pressure volume curve for single layer pipe cross-over

From the Figure 52, the multi-layered pipe gives the critical buckling crossover pressure as 15.2MPa (second peak value of the curve in Figure 52). The traditional ABAQUS FEM gives the result of 15.55MPa [23, 28]. The relative error is 2.25%. It is noted that, with the reduction of arrestors' thickness, the critical buckling cross-over pressure is reduced from 29.15 MPa to 15.2 MPa. In practice, the ratio of the arrestors' thickness to pipe thickness is always from 2 to 3 [23]. If we use an arrestor that has a thickness greater than 3 times that of the pipe, the critical buckling cross-over pressure will no longer increase [28, 29]. Comparing with Figure 51, the arrestor's thickness is smaller and the critical buckling pressure is also reduced.

The post buckling behavior is shown in Figure 53.

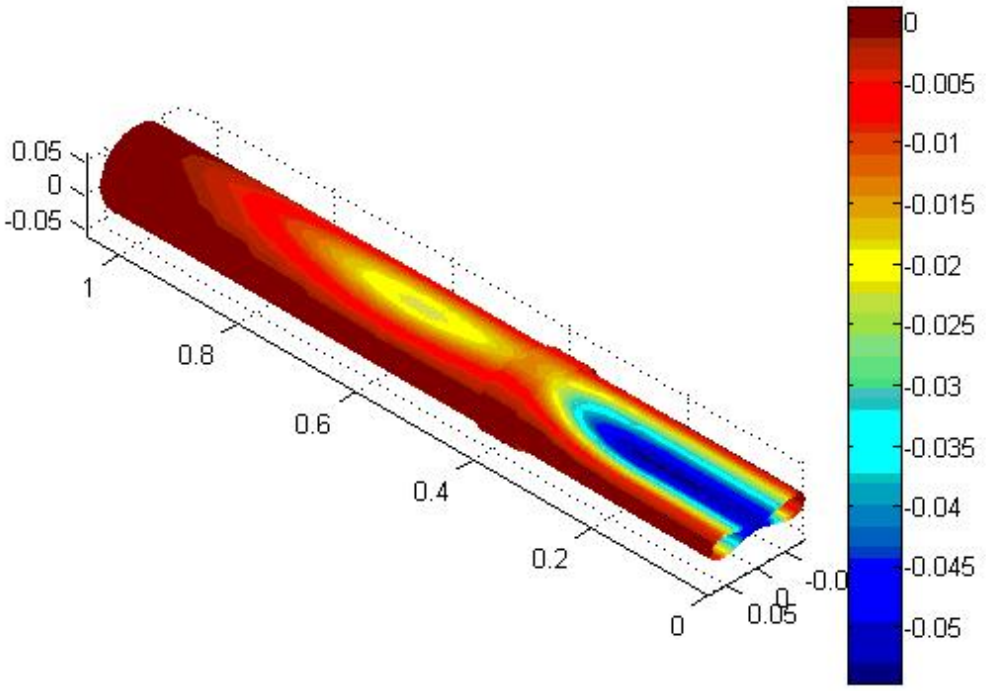

Figure 53 Displacement contours of buckling crossover (unit: Meter)

In the Figure 53, the buckling cross-over mode is clearly shown. The buckling deformation crosses over the so-called arrestor and destroy the pipeline behind the arrestor.

In this numerical test, the single layer pipe buckling cross-over problem is re-solved to verify the multi-layered pipe element developed in this thesis. Through the comparison with other papers, the method is proved to be accurate.

Test 9: Multi-layer pipe buckling cross-over

In this Test 9, the multi-layer pipe buckling cross-over problem is solved. In this case, we use different material for the pipe and arrestors. The pipe outer diameter is

114.3mm. The wall thickness is 5.08mm. The nominal yield stress is $516Mpa$. However, there are two layers with different material properties. The first layer has the yield stress of 50MPa while the second layer that of 516MPa. The Young's modulus is still $206Gpa$ and the Poisson ratio is 0.3. The convergence study is presented in the Figure 54. By increasing the number of pipe elements, the pressure curves tend to converge.

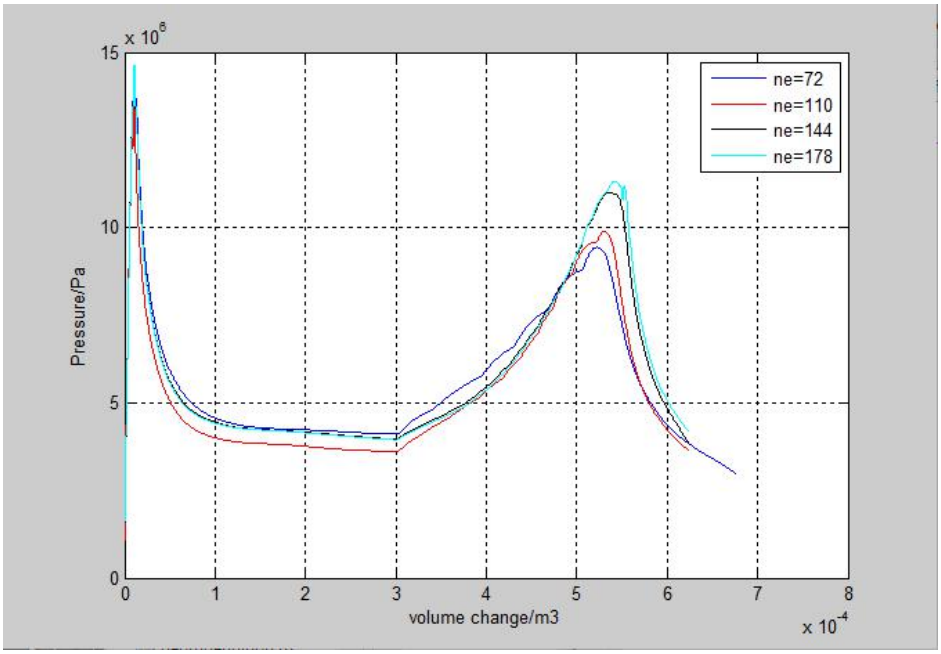

Figure 54 Convergence study of pressure curves of the multi-layered pipe element

From the pressure volume curve, the critical buckling crossover pressure for this multi-layered pipe structure is 11.25MPa (second peak value of the curves in Figure 54). The ANSYS Riks gives the pressure curve shown in Figure 55. The ANSYS Solid element 186 is used, which employs the second order Lagrange interpolation functions.

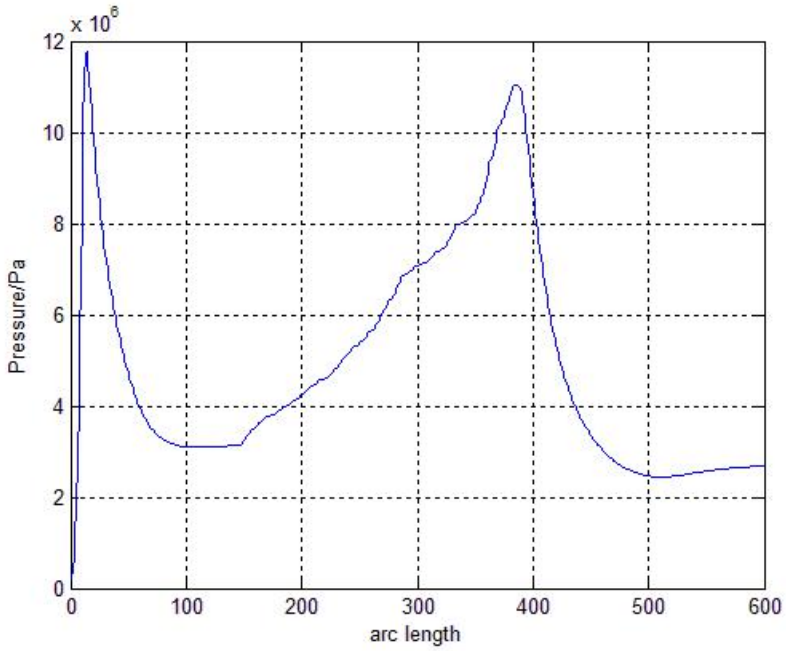

Figure 55 Pressure curve for the 2-layer pipe cross-over from ANSYS Riks

From the Figure 55, the critical buckling cross-over pressure for this multi-layer pipe structure with multi-layer arrestors is 11.05MPa. The relative error is 1.8%.

The buckling mode for the multi-layer pipe-arrestor structure is shown in Figure 56.

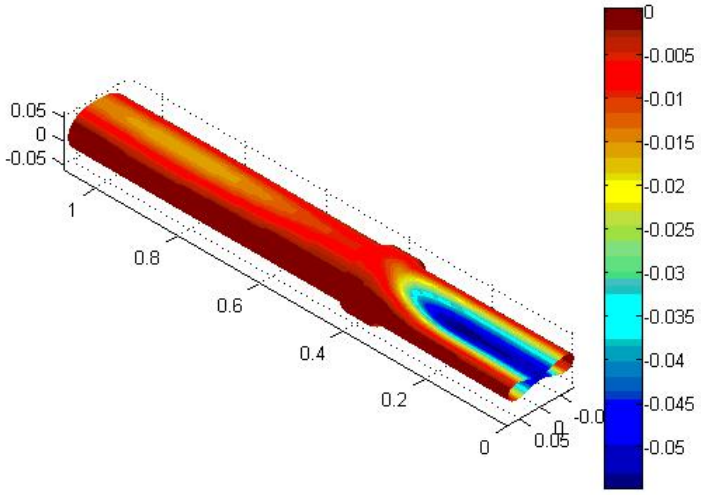

Figure 56 Displacement contours of buckling crossover (unit: Meter)

Test 10: Pipe buckling analysis with strain rate effect [33]

In this part, the buckling propagation that accounts for the strain rate effect is solved. Based on the reference [29], the real buckling propagation in the ocean environment must consider the strain rate effect when the applied water pressure is very high. For the background of strain rate effect, it is referred to [33]. The same strain rate constitutive theory is used in this thesis.

At first, a single-layer pipe's buckling propagation problem is solved. In [29], the experimental data for this pipe is available. The applied water pressure is 11.56MPa. The outer diameter is 44.53mm. The wall thickness is 1.671mm. The nominal yielding stress is 298MPa. The buckling propagation speed is measured by two time steps.

For the time $9e-4s$, the buckling propagation profile is shown in Figure 57.

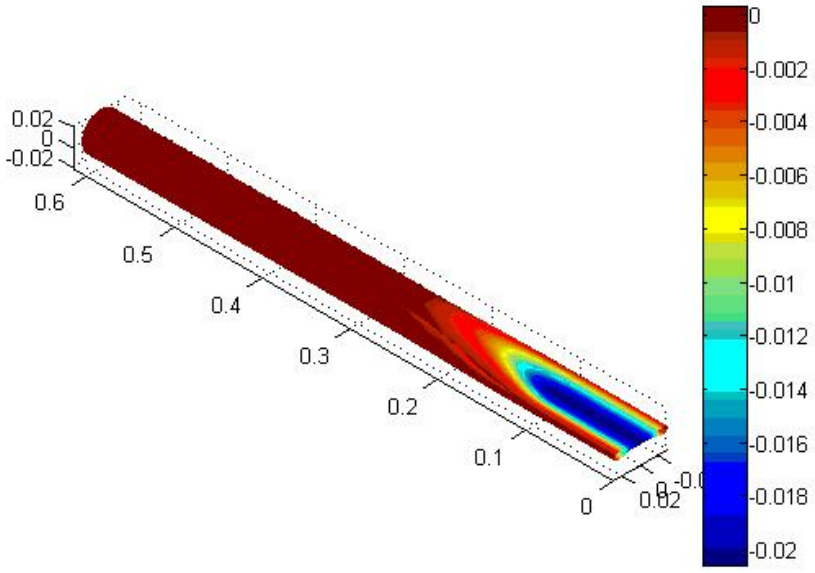

Figure 57 Dynamical buckling deformation contours at time 9e-4s (unit: Meter)

At the time $1.669e-3s$, the buckling propagation profile is shown in Figure 58.

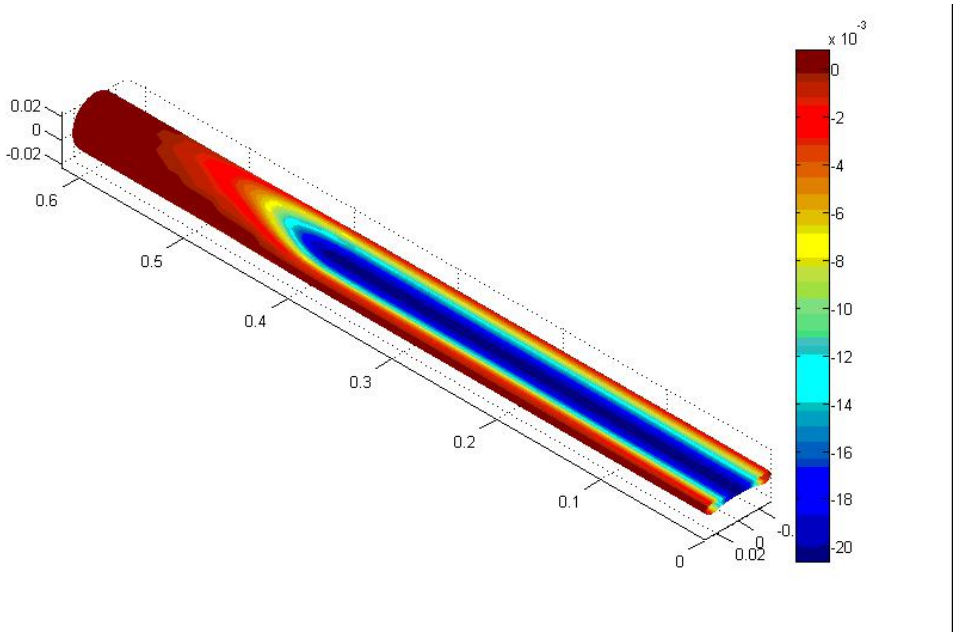

Figure 58 Dynamical buckling deformation contours at time 1.669e-3s (unit: Meter)

The buckling speed, according to [29], is measure by the contact length, which is the axial size of the contact area (In Figure 57 and 58, those blue regions are the contact area. For these regions, the pipe contact occurs).

Thus, the dynamical buckling propagation speed is:

$$v_p = \frac{l_2 - l_1}{\tau_2 - \tau_1} = 324 m/s \tag{237}$$

where l_1, l_2 are the length of the contact region for time τ_1, τ_2:

$l_1 = 0.1514m$

$\tau_1 = 0.0009s$

$l_2 = 0.40077m$

$\tau_2 = 0.001669s$

Comparing with the experimental results in [28-29], the dynamical buckling propagation speed is 324m/s in this simulation and 296m/s in the experiment [29]. The relative error is 8.6%.

A 2-layer pipe's dynamical buckling propagation with strain rate effect is solved. Comparing with the last case, the second layer's nominal yielding stress is changed to 30MPa. We want to test the multi-layered pipe element's robustness for the problems with big ratio of material strength. The transient water pressure is as 20MPa. According to the findings of the dynamical buckling propagation experiment in [28-29], there should be a flip-flop dynamical buckling mode under this water pressure. In this thesis's simulation, the flip-flop dynamical buckling propagation profile is found in Figure 59 at time $t = 0.72 \times 10^{-3} s$.

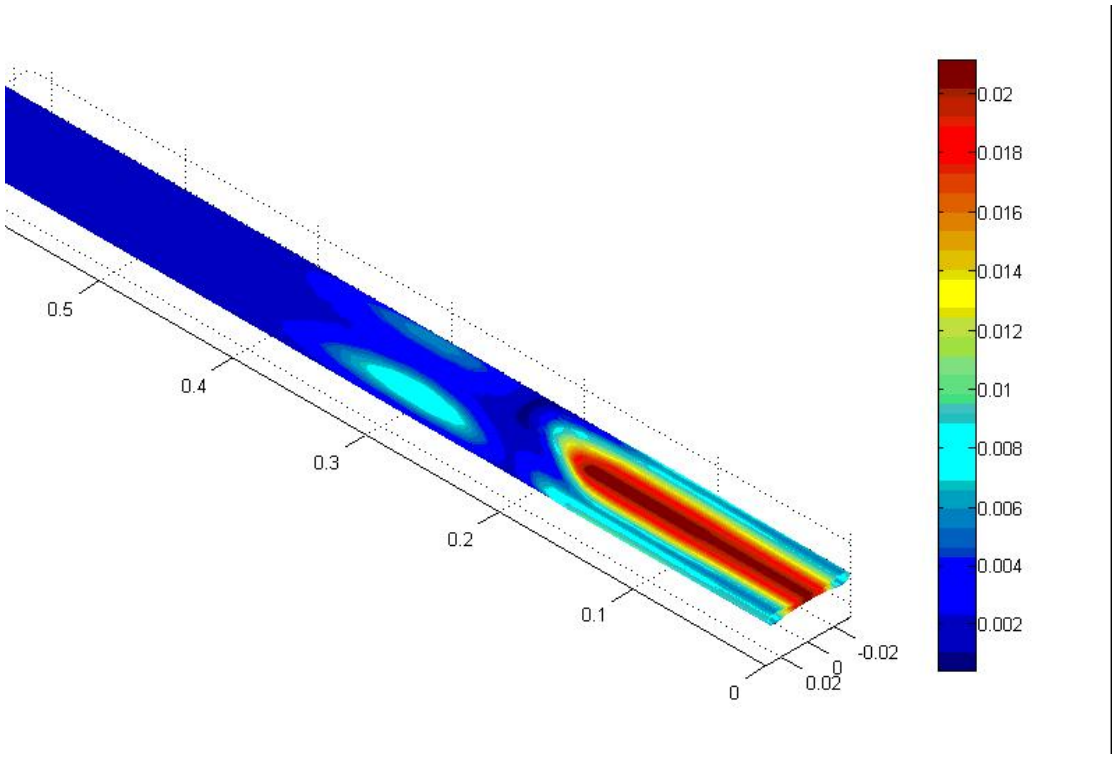

Figure 59 Flip-flop buckling propagation mode (unit: Meter)

From Figure 59, the so-called flip-flop buckling mode is a buckling mode that converts the deformation direction. This kind of buckling mode occurs only at a larger water pressure [29].

6.4 Stiffened plate

In this section, a problem about a stiffened plate structure with a parabolic stiffener structure is solved. The stiffened plate structure is shown in the Figure 60. The stiffener is a parabolic curve defined in Figure 61 [32].

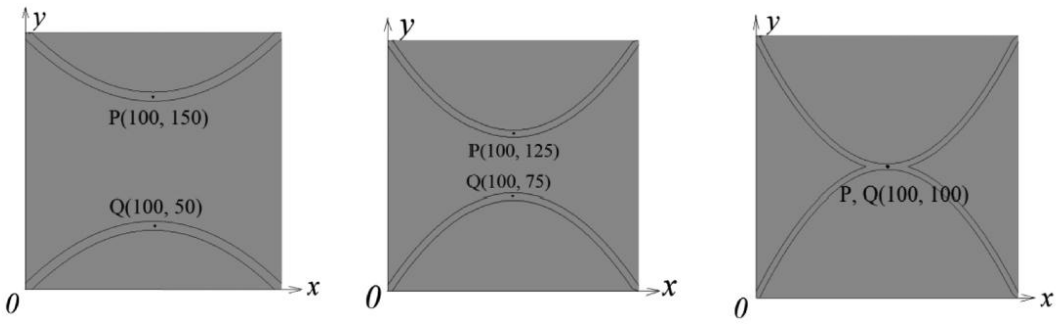

Figure 60 Stiffened plate and stiffeners

In this thesis, the plate has a dimension of $a_p \times b_p = 200mm \times 200mm$ and a thickness of $t_p = 2.5mm$. The two stiffeners, which are symmetrically placed, have a height of $h_s = 20mm$ along the z-direction(perpendicular to the paper plane) and a width of $b_s = 4mm$. To define the configuration of the stiffener based on the idea of this thesis, the local cylindrical coordinate is defined as Figure 61. The z-xis is in the perpendicular direction to the plane of the paper.

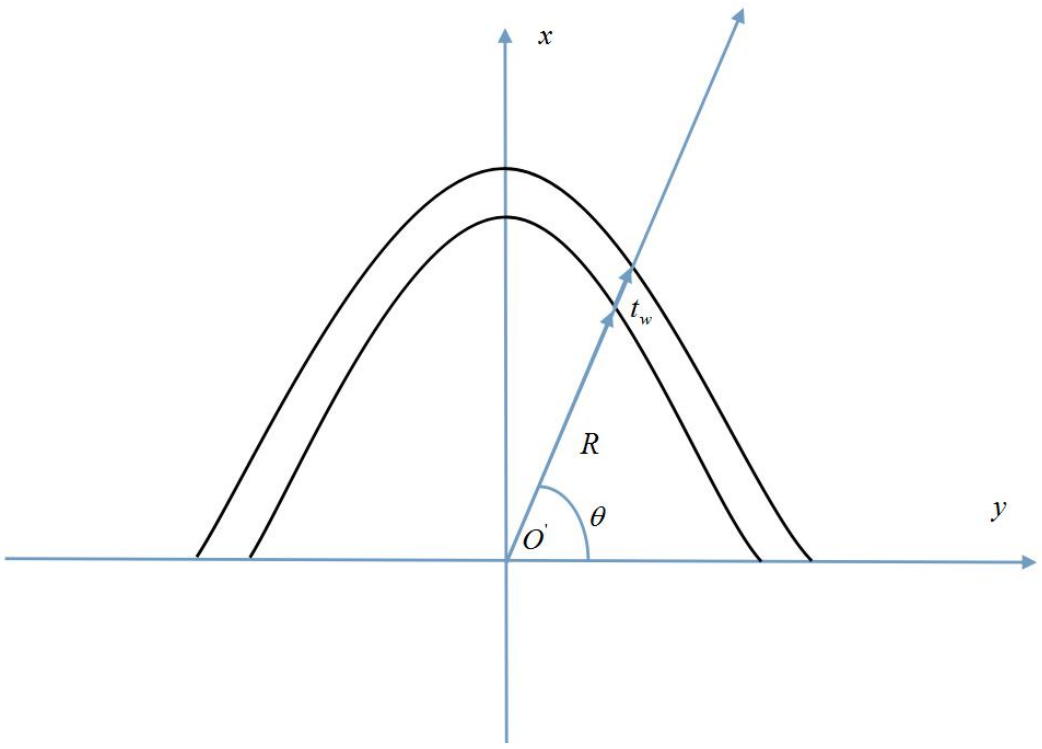

Figure 61 Stiffener's configuration and notations

The water pressure is applied on the top surface of the plate.

Based on the idea of stiffener element, the kinematics is derived for such a parabolic stiffener. The stiffener's inner surface can be formulated as:

$$x = d_p[1-(\frac{y}{e_p})^2] \tag{238}$$

Where the parabola intersects the x-axis at $x = d_p$ and intersects the y-axis at $y = \pm e_p$.

The equation of this parabola can be written in the polar coordinate form as:

$$\rho\sin(\theta) = d_p[1-(\frac{\rho\cos(\theta)}{e_p})^2]$$
$$\frac{d_p}{e_p^2}\rho^2[\cos(\theta)]^2 + \rho\sin(\theta) - d_p = 0 \tag{239a, b}$$

So

$$\rho = \frac{-b + \sqrt{b^2 - 4ac}}{2a}$$

$$a = \frac{d_p}{e_p^2}[\cos(\theta)]^2 \qquad \text{(240a, b, c, d)}$$

$$b = \sin(\theta)$$

$$c = -d_p < 0$$

So if $a \neq 0$

$$R(\theta) = \rho = \frac{-\sin(\theta) + \sqrt{[\sin(\theta)]^2 + 4\frac{d_p}{e_p^2}[\cos(\theta)]^2 d_p}}{\frac{2d_p}{e_p^2}[\cos(\theta)]^2} \qquad (241)$$

The other solution is discarded because ρ must be positive.

If $a = 0$

$$R(\theta) = \frac{-c}{b} = \frac{d_p}{\sin(\theta)} \qquad (242)$$

Thus, the natural coordinates ξ_i , $i = 1,2,3$ are defined as:

$$\xi_1 = \frac{z}{h_p}$$

$$\xi_2 = \frac{2\theta}{\pi} \qquad \text{(243a, b, c)}$$

$$\xi_3 = \frac{\rho - R}{t_w}$$

where

$$R(\theta) = \frac{-\sin(\pi\xi_2 / 2) + \sqrt{[\sin(\pi\xi_2 / 2)]^2 + 4\frac{d_p}{e_p^2}[\cos(\pi\xi_2 / 2)]^2 d_p}}{\frac{2d_p}{e_p^2}[\cos(\pi\xi_2 / 2)]^2} \qquad (244)$$

For the outer curve of the stiffener, we only need to adjust the parameter of d_p and e_p:

$$x = d_p^{'}[1-(\frac{y}{e_p^{'}})^2]$$
$$d_p^{'} = d_p + b_s \quad \text{(245a, b, c)}$$
$$e_p^{'} = e_p + b_s$$

In this way, the outer radius can be found as:

$$R^{'}(\theta) = \frac{-\sin(\pi\xi_2/2) + \sqrt{[\sin(\pi\xi_2/2)]^2 + 4\frac{d_p^{'}}{e_p^{'2}}[\cos(\pi\xi_2/2)]^2 d_p^{'}}}{\frac{2d_p^{'}}{e_p^{'2}}[\cos(\pi\xi_2/2)]^2} \quad (246)$$

So

$$t_w = R^{'} - R \quad (247)$$

Then, the stiffener's configuration will be:

$$r_{s0} = \begin{bmatrix} (R + t_w\xi_3)\sin(\pi\xi_2/2) \\ (R + t_w\xi_3)\cos(\pi\xi_2/2) \\ h_s\xi_1 \end{bmatrix} \quad (248)$$

$$J = [J_{ij}]_{3\times 3}$$
$$J_{11} = 0$$
$$J_{12} = 0$$
$$J_{13} = h_s$$
$$J_{21} = \frac{\pi}{2}(R + t_w\xi_3)\cos(\pi\xi_2/2) + (\frac{\partial R}{\partial \xi_2} + \frac{\partial t_w}{\partial \xi_2}\xi_3)\sin(\pi\xi_2/2)$$
$$J_{22} = -\frac{\pi}{2}(R + t_w\xi_3)\sin(\pi\xi_2/2) + (\frac{\partial R}{\partial \xi_2} + \frac{\partial t_w}{\partial \xi_2}\xi_3)\cos(\pi\xi_2/2) \quad \text{(249a, b, c, d, e, f, g, h, i, j)}$$
$$J_{23} = 0$$
$$J_{31} = t_w\sin(\pi\xi_2/2)$$
$$J_{32} = t_w\cos(\pi\xi_2/2)$$
$$J_{33} = 0$$

Thus, the determinant will be:

$$\det(J) = \frac{\pi}{2}t_w h_s(R + t_w\xi_3)$$
$$t_w = R' - R \quad \text{(250a, b)}$$

The mid-value theorem is applied for ξ_3, thus,

$$\det(J) = \frac{\pi}{4}h_s(R' - R)(R' + R)$$
$$= \frac{\pi}{4}h_s(R'^2 - R^2) \quad \text{(251)}$$

Since the problem is symmetrical, only 1/4 structure is analyzed and the symmetry boundary conditions are applied. Thus,

$$f_{u_i}^{\xi_2'} = (1-\xi_2)(\xi_2), i = 1,2,3$$
$$\xi_2 \in [0,1] \quad \text{(252)}$$

Thus,

$\phi_{u_i}^{\xi_1}(i = 1,2,3)$ is the orthogonal polynomial series with weighting function 1,

$\psi_{u_i}^{\xi_2}(i=2)$ is the orthogonal polynomial series with weighting function

$\det(J)\xi_2^2(1-\xi_2)^2$,

$\psi_{u_i}^{\xi_2}(i=1,3)$ is the orthogonal polynomial series with weighting function $\det(J)\xi_2^2$,

$\varphi_{u_i}^{\xi_1}(i=1,2,3)$ is the orthogonal polynomial series with weighting function 1.

Thus, the basis functions for ξ_1, ξ_3 are plotted in Figure 62.

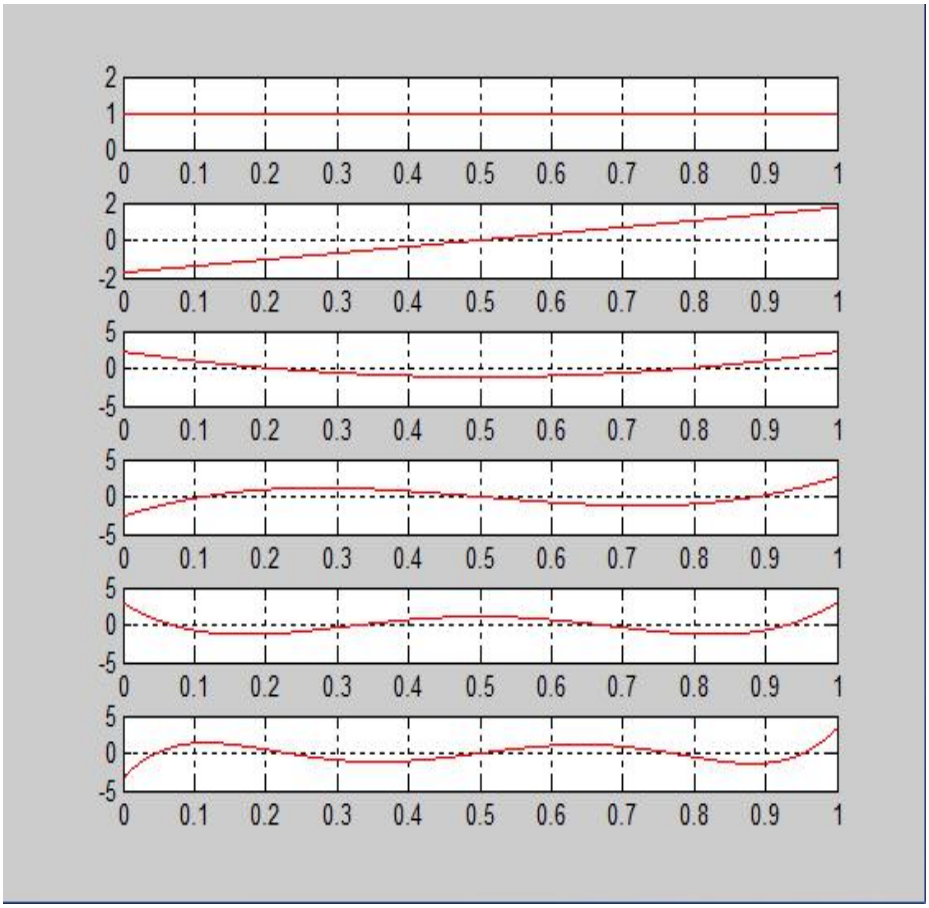

Figure 62 The basis functions for ξ_1, ξ_3

The basis functions $\psi_{u_i}, i=2$ for ξ_2 are plotted in Figure 63.

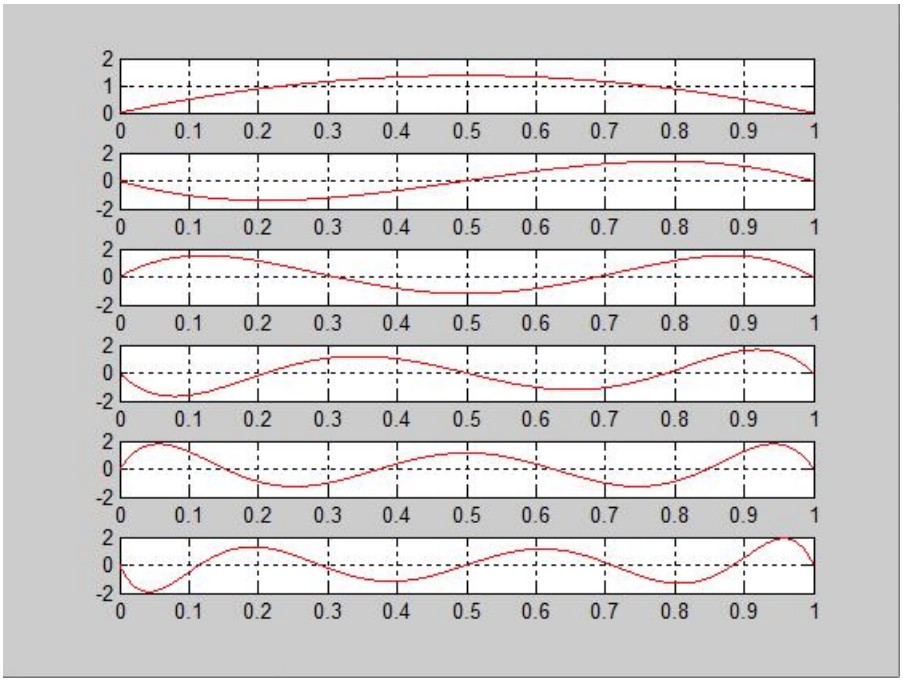

Figure 63 The basis functions $\psi_{u_i}, i = 2$ for ξ_2

The basis functions $\psi_{u_i}, i = 1,3$ for ξ_2 are plotted in Figure 64.

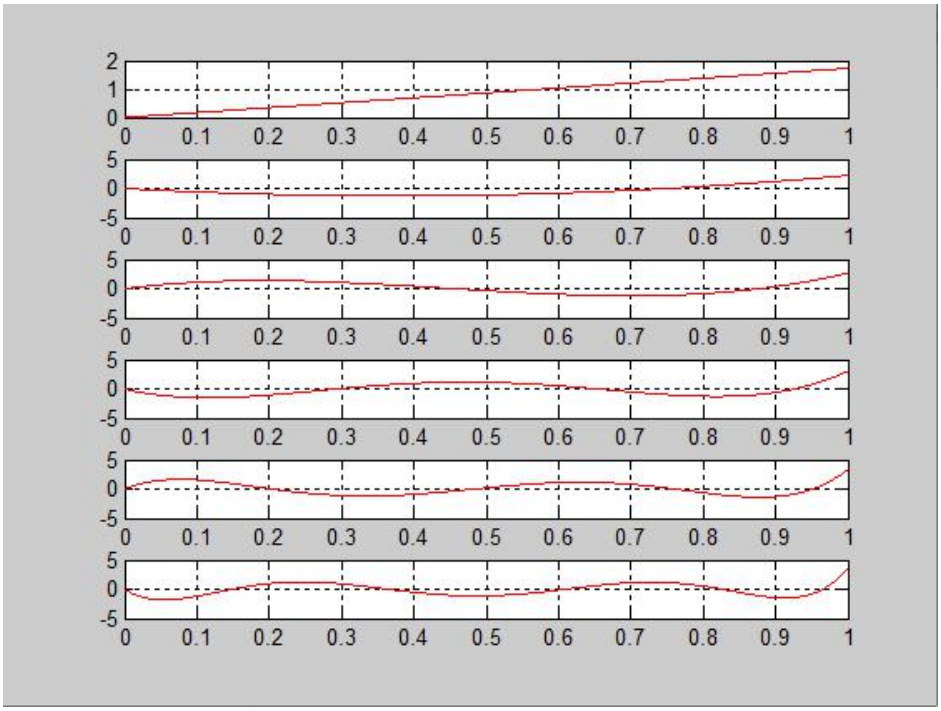

Figure 64 The basis functions $\psi_{u_i}, i = 1,3$ for ξ_2

Test 11: Small-deformation analysis of stiffened plates

Small deformation analysis is presented at first. The stiffener's geometry is changed by various values of parameter d_p. The applied pressure is 50kpa. The plate's maximum deflection is recorded and compared with the traditional FEM in ANSYS. All the boundaries are clamped, including the stiffeners'. The results are listed in Table 4 and plotted in Figure 65.

Table 4 Maximum deflection of the stiffened plate (small deformation analysis)

d_p/mm	This paper/mm	ANSYS verification/mm
100	0.124	0.123
90	0.122	0.130
80	0.144	0.138
70	0.174	0.164
60	0.227	0.215
50	0.317	0.301

From the comparison in Figure 65, it is noted that the small-deformation analysis is accurate.

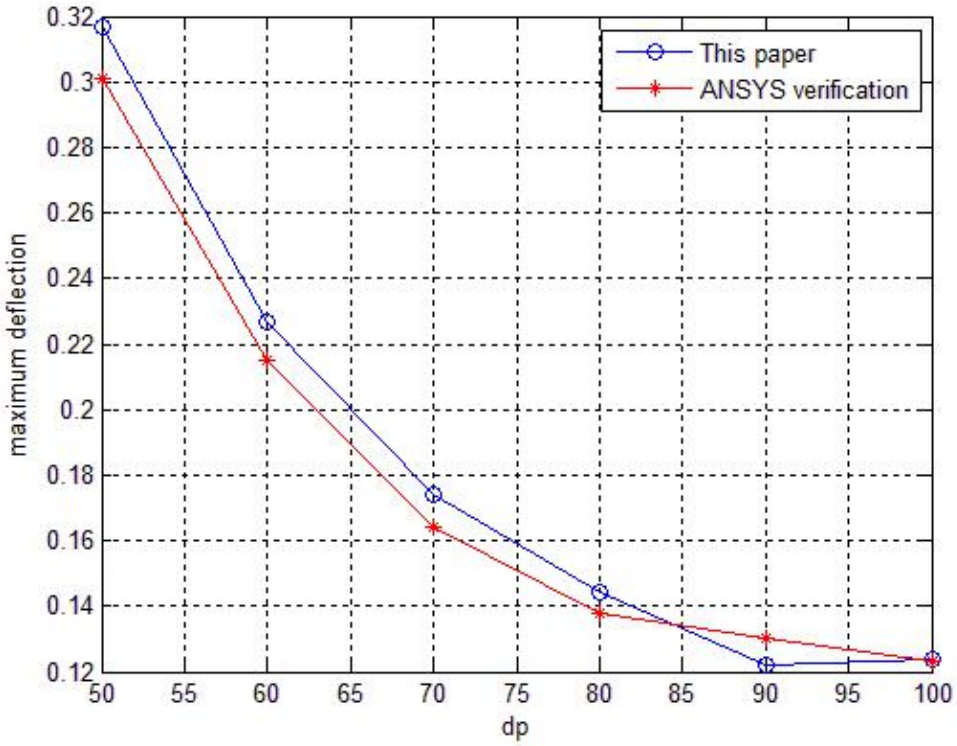

Figure 65 Maximum deflection(unit:Meter)of the stiffened plate (small deformation)

Test 12: Large deformation analysis of stiffened plates

Large deformation analysis is presented next. In this case, the arc length method is used. The arc length is defined as the volume of the space between the initial un-deformed plate and the deformed plate. The elastic analysis is presented. The Young's modulus considers to be 2.06×10^{11} Pa and the Poisson ratio is 0.3. By changing the parameter d_p, the shape of the stiffener will be changed.

The parameter d_p is 50mm. In this case, the stiffened plate is shown in Figure 66.

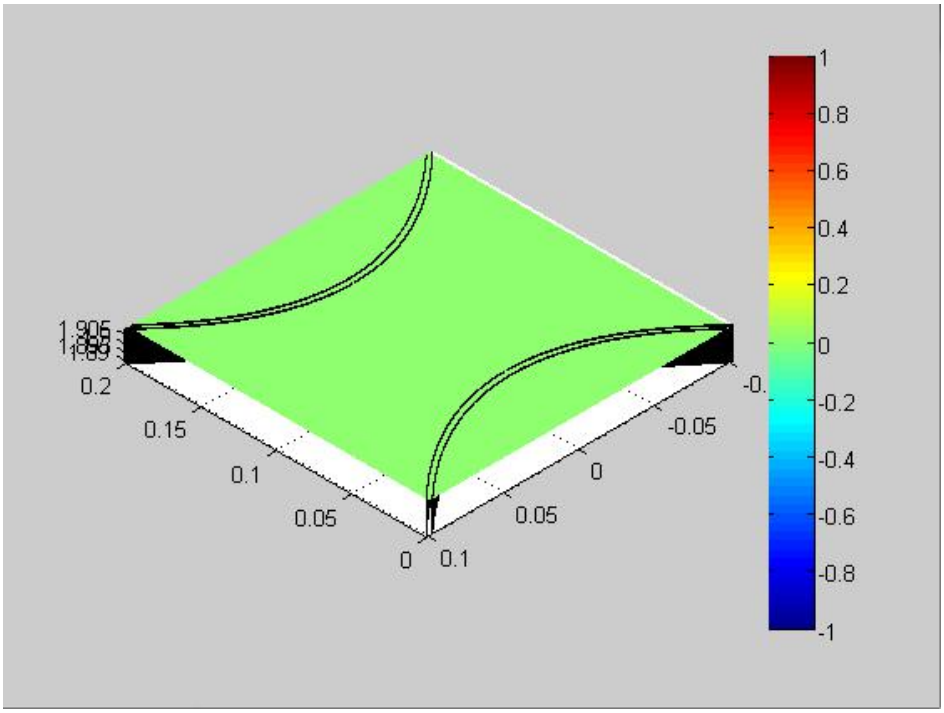

Figure 66 Stiffened plate structure for $d_p = 50mm$

In Figure 66, a plate with smooth stiffener is represented, which is essential for large deformation analysis that is always sensitive to geometrical imperfection.

The deflection of the stiffened plate under several water pressure levels are plotted in Figure 67 and 68. In Figure 67, the deflection is plotted against y coordinate for x=0.5. In Figure 68, the deflection is plotted against x coordinate for y=0.5. The results are compared with those obtained using ANSYS. The water pressure applied are 5MPa, 10MPa, 20MPa and 30MPa.

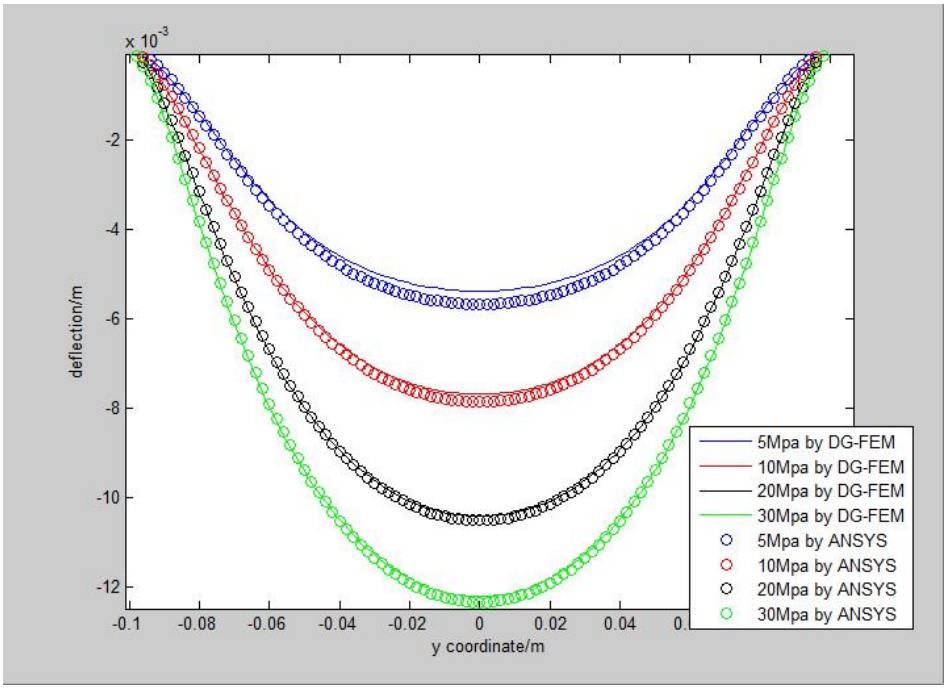

Figure 67 The comparison of the transverse deflection along the y direction at $x = 0.5m$

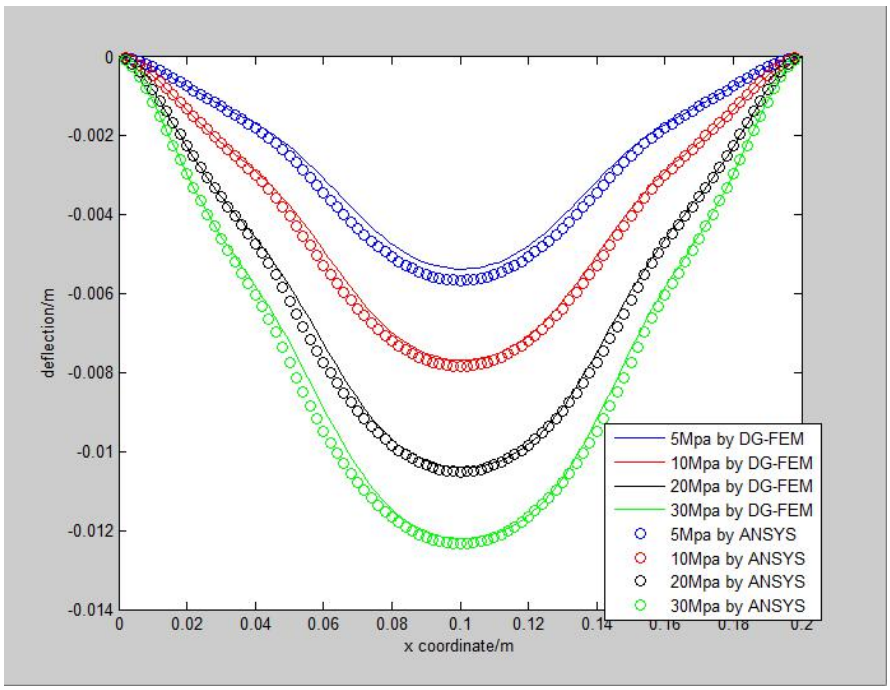

Figure 68 The comparison of the transverse deflection along the x direction at $y = 0.5m$

From Figure 67 and 68, it is observed that the present method is quite accurate. In Figure 67, the deflection is plotted for x=0.1m against the y coordinate. In Figure 68, the deflection is plotted for y=0 against the x coordinate.

The continuity of displacement between stiffeners and plates is investigated here. The deflection contours are plotted in Figure 69.

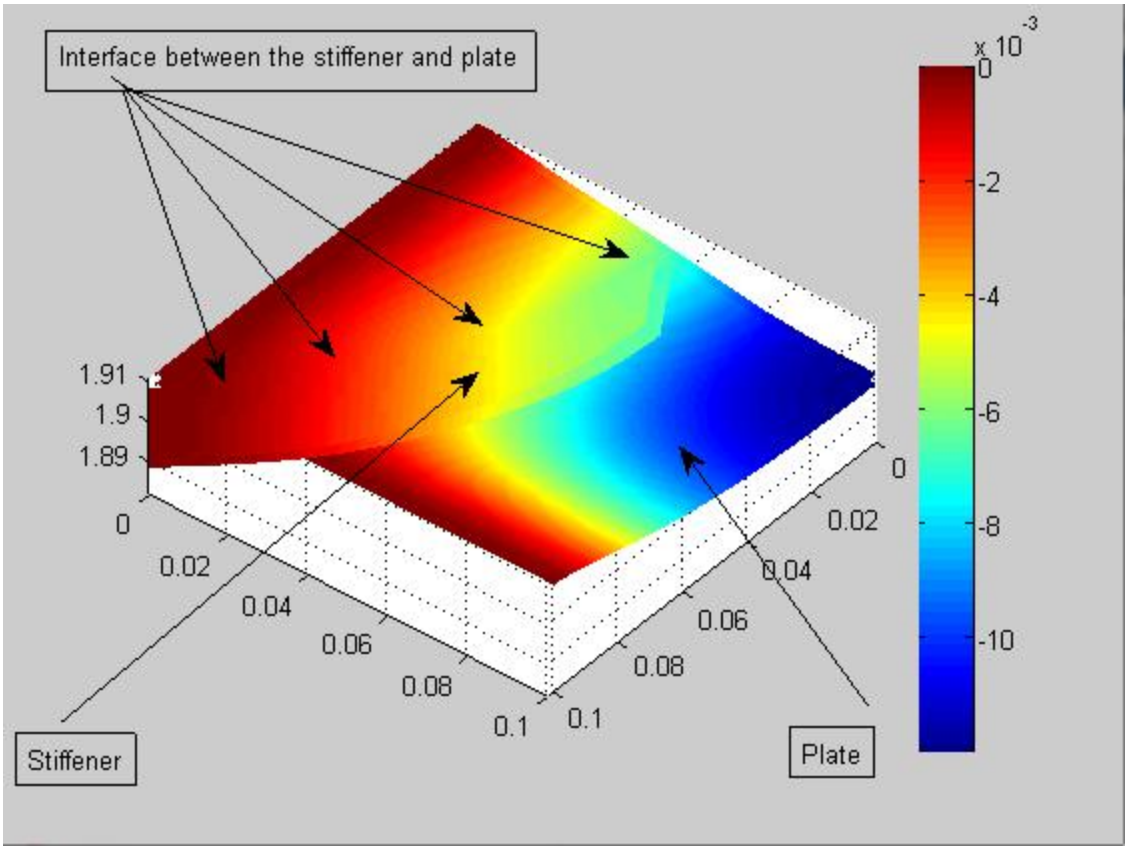

Figure 69 The deflection contours of the interface between stiffeners and plates

From Figure 69, it is observed that the continuity of displacement at the interface is good.

The convergence study is presented in Figure 70. It is noted that, with the increase of the in-plane displacement order k, the results tend to converge.

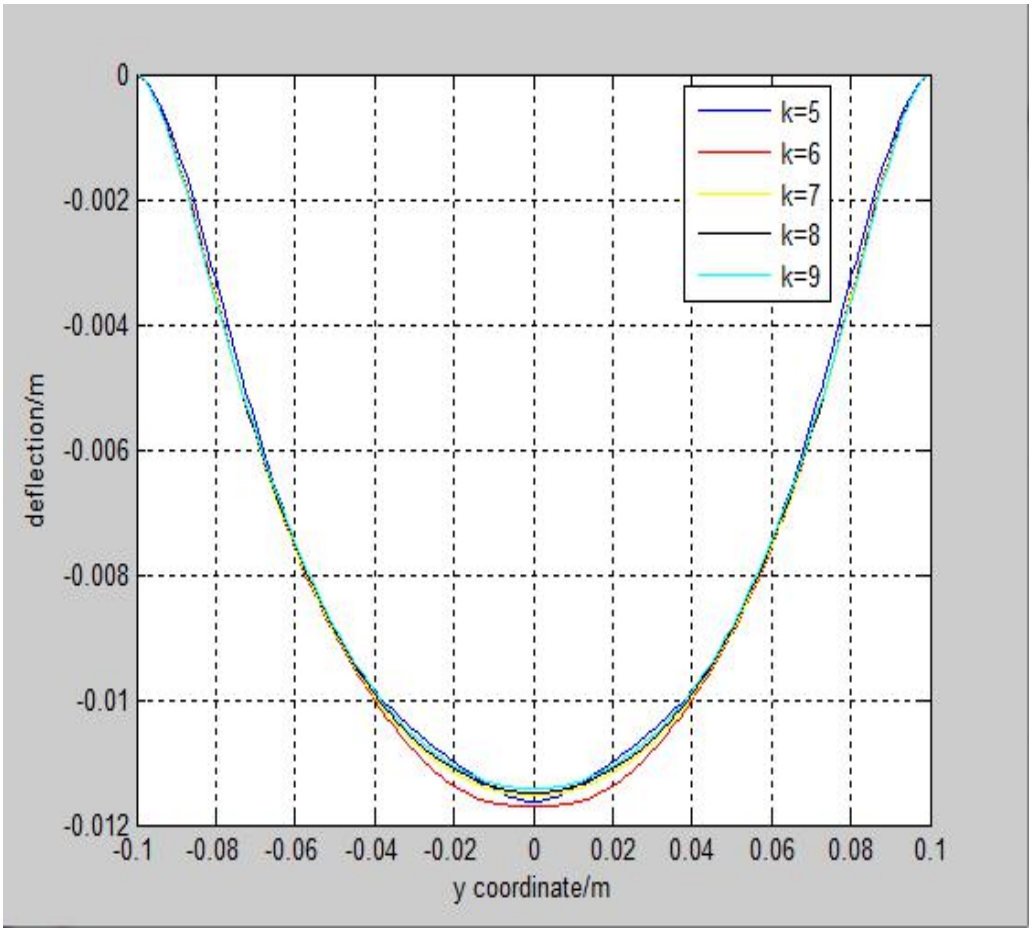

Figure 70 Convergence study for the in-plane displacement

The in-plane displacement order is the displacement basis function order along the plate's plane dimensions. For the plate, it is the displacement order for x and y direction. For the stiffener, it is the displacement order in the stiffener's axial direction.

The transverse displacement contours are shown from Figure 71-78 for different water pressures.

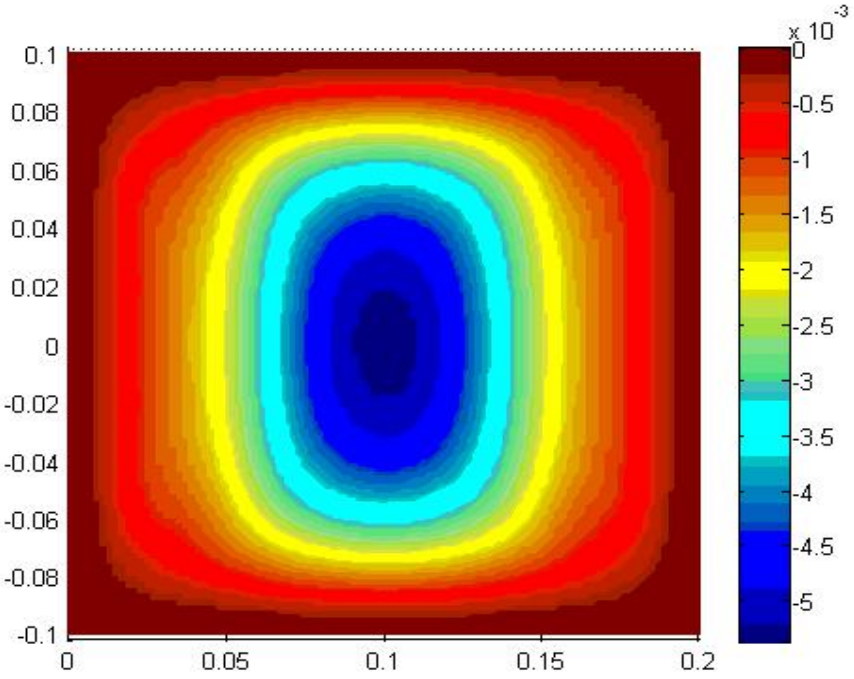

Figure 71 The deflection (unit: Meter) contours obtained using the present approach at pressure of 5MPa

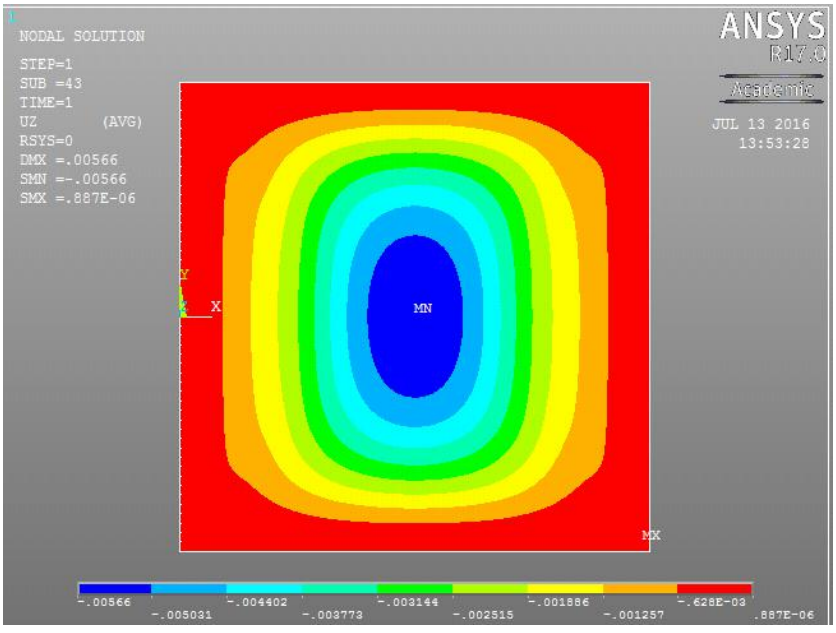

Figure 72 The deflection (unit: Meter) contours obtained from ANSYS Riks at pressure of 5MPa

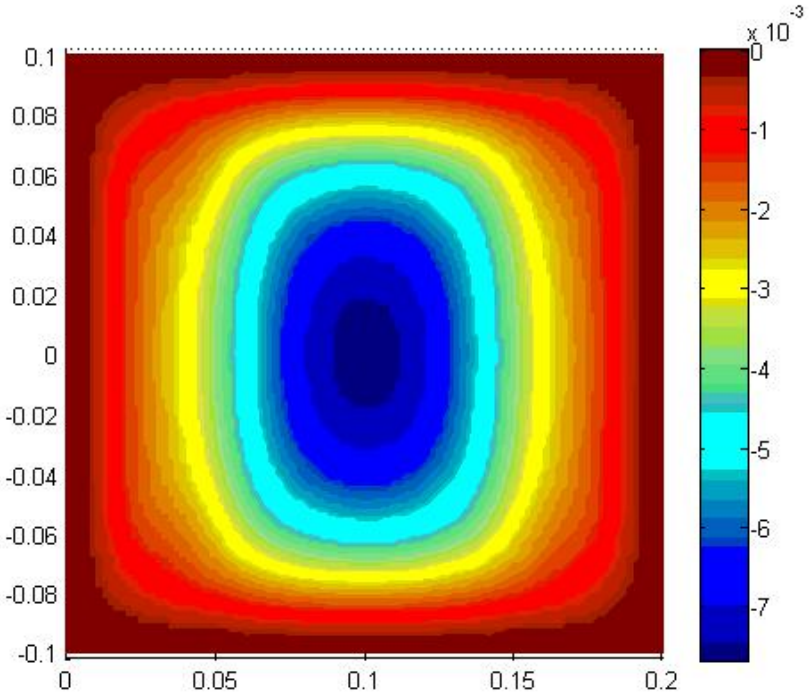

Figure 73 The deflection (unit: Meter) contours obtained using the present approach at pressure of 10MPa

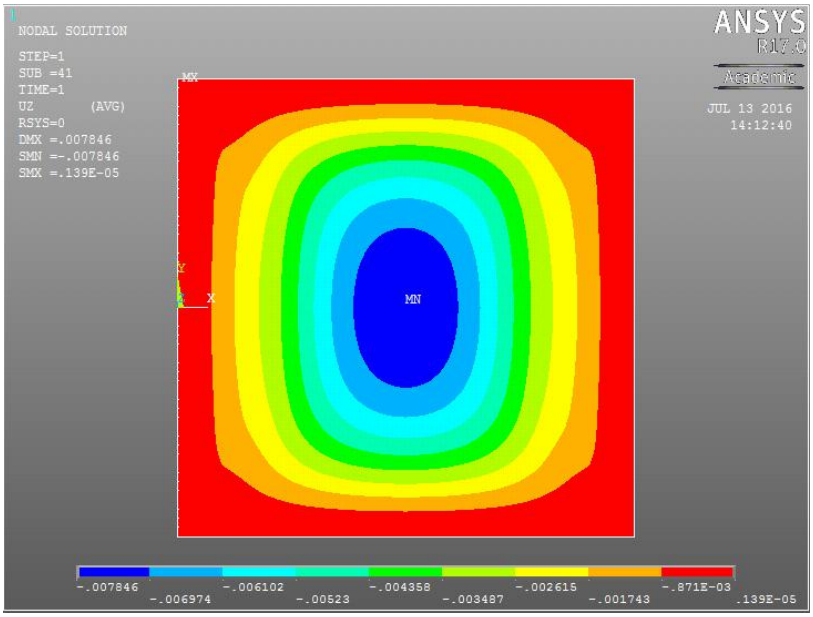

Figure 74 The deflection (unit: Meter) contours obtained from ANSYS Riks at pressure of 10MPa

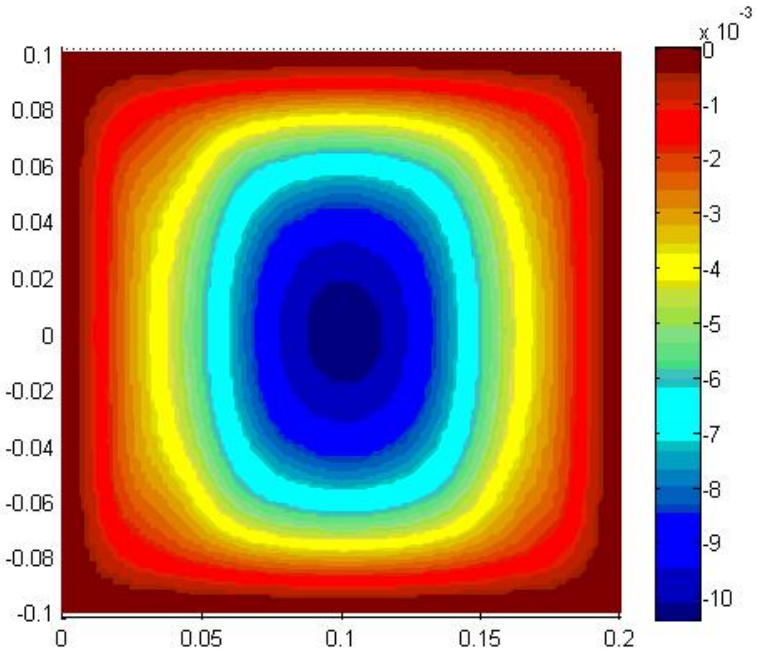

Figure 75 The deflection (unit: Meter) contours obtained using the present approach at pressure of 20MPa

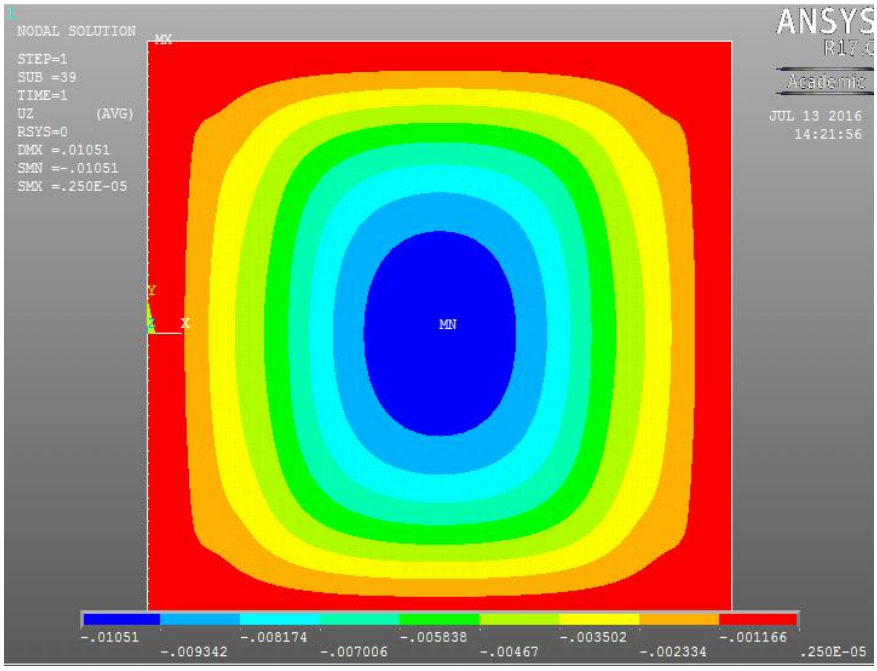

Figure 76 The deflection (unit: Meter) contours obtained from ANSYS Riks at pressure of 20MPa

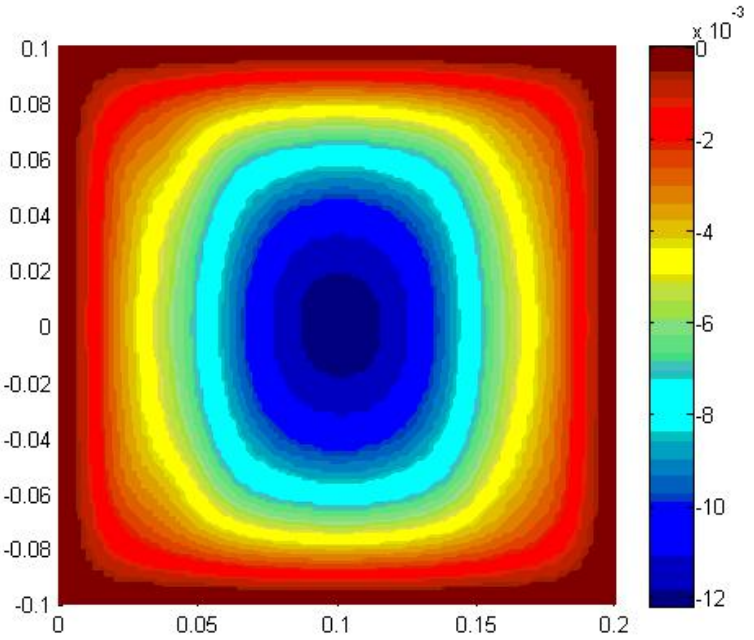

Figure 77 The deflection (unit: Meter) contours obtained using the present approach at pressure of 30MPa

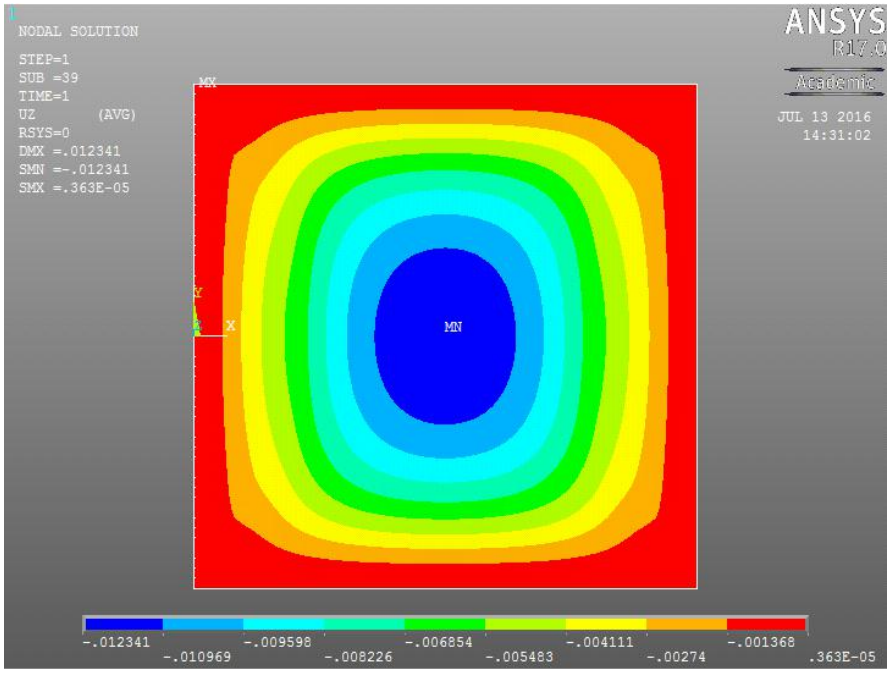

Figure 78 The deflection (unit: Meter) contours obtained from ANSYS Riks at pressure of 30MPa

From Figures 71-78, it is verified that the method is accurate when compared to those obtained in ANSYS. More stiffened plate structures are solved by using different stiffener structures.

The parameter d_p is 60mm. In this case, the stiffener is described in Figure 79. The applied water pressure is 30MPa.

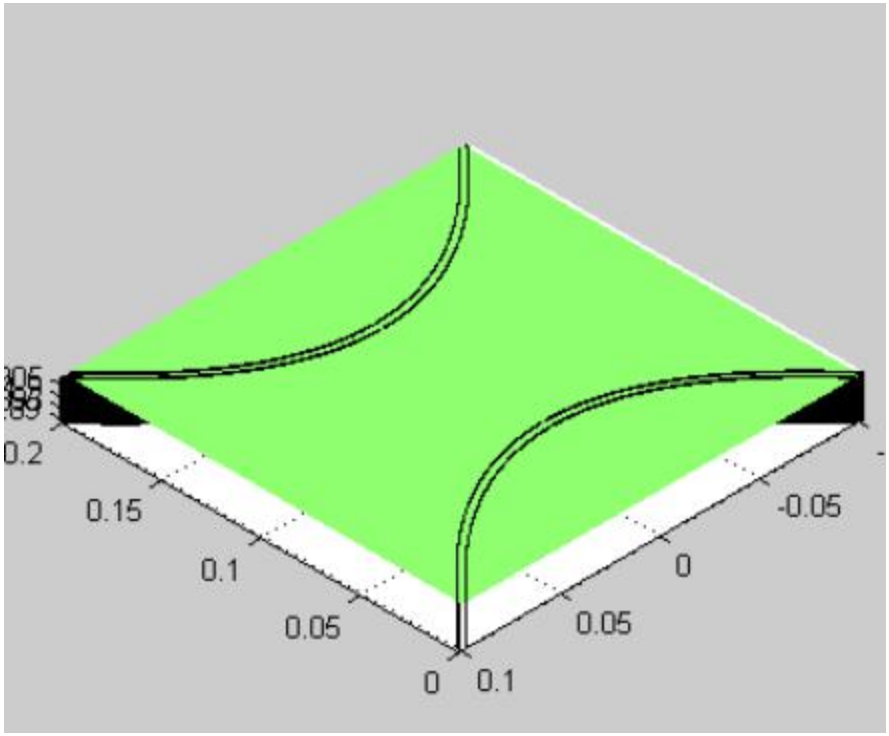

Figure 79 Stiffened plate structure for $d_p = 60mm$

The deflection is plotted and compared with that obtained using ANSYS as shown in Figure 80a and 80b.

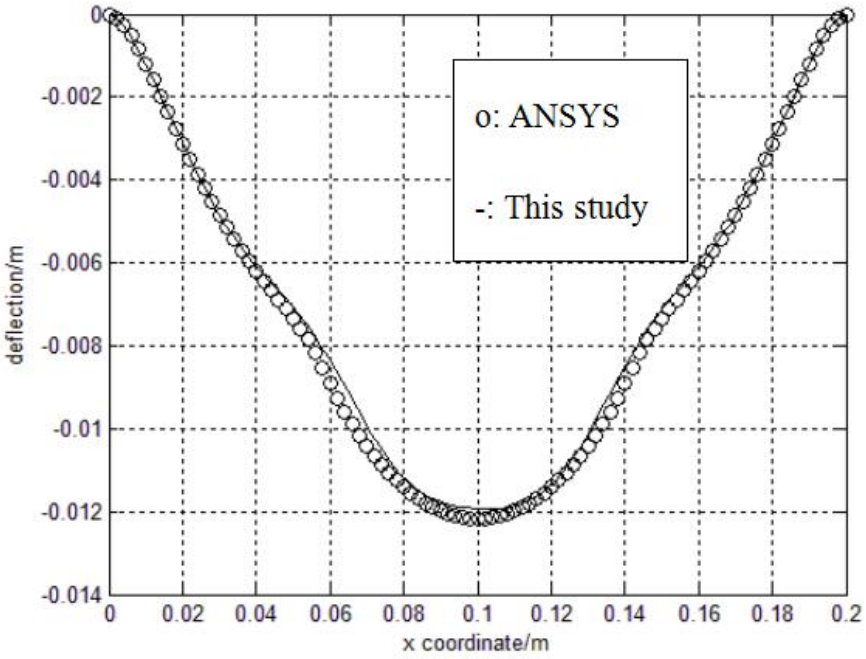

Figure 80a The deflection plot comparison (y=0) using ANSYS and the present approach

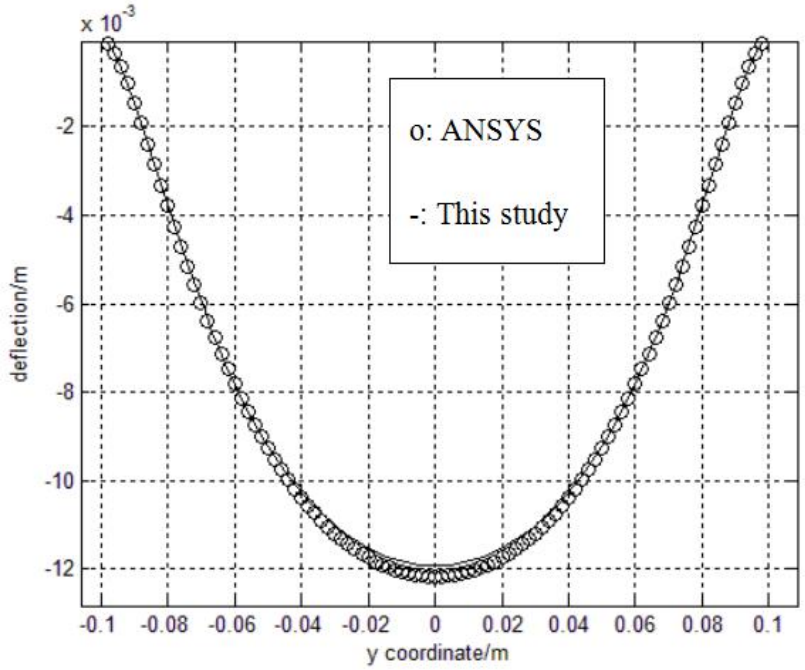

Figure 80b The deflection plot comparison (x=0.1) using ANSYS and the present approach

The deflection contours are shown and compared in Figure 81a and Figure 81b under 30MPa water pressure.

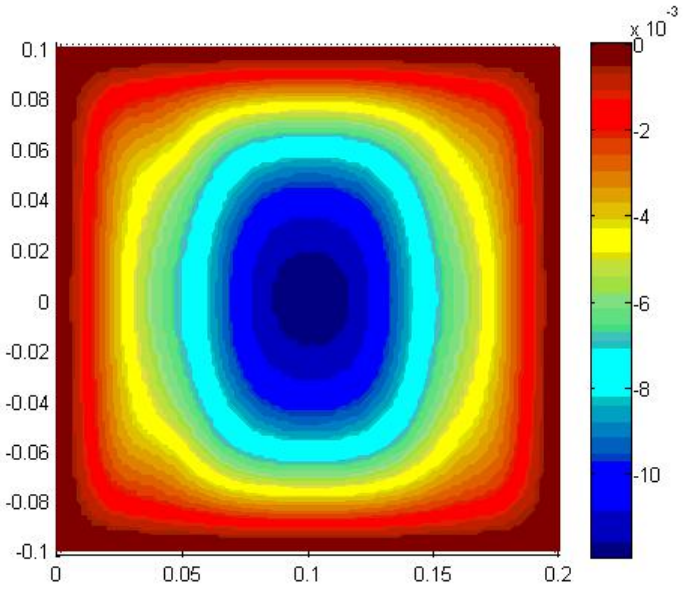

Figure 81a The deflection (unit: Meter) contours obtained using the present approach at pressure of 30MPa

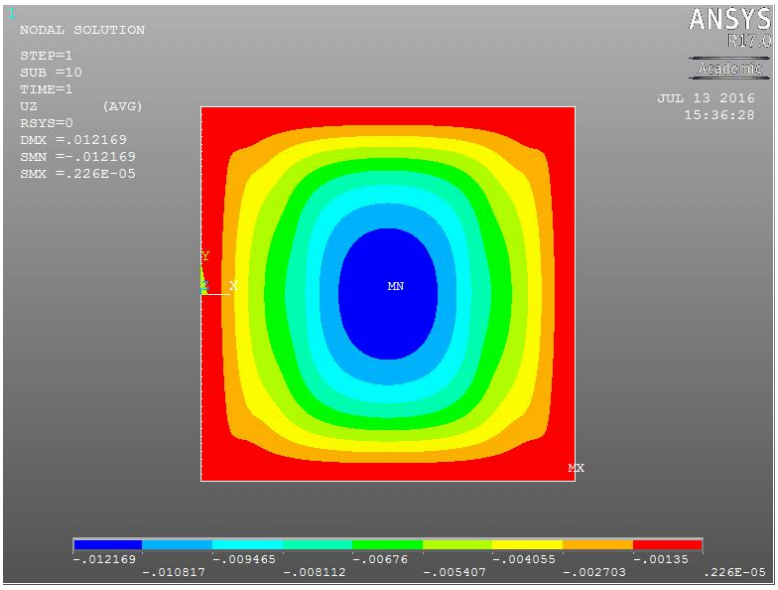

Figure 81b The deflection (unit: Meter) contours obtained using ANSYS Riks at pressure of 30MPa

The parameter d_p is changed to 70mm. In this case, the stiffener is shown in Figure 82.

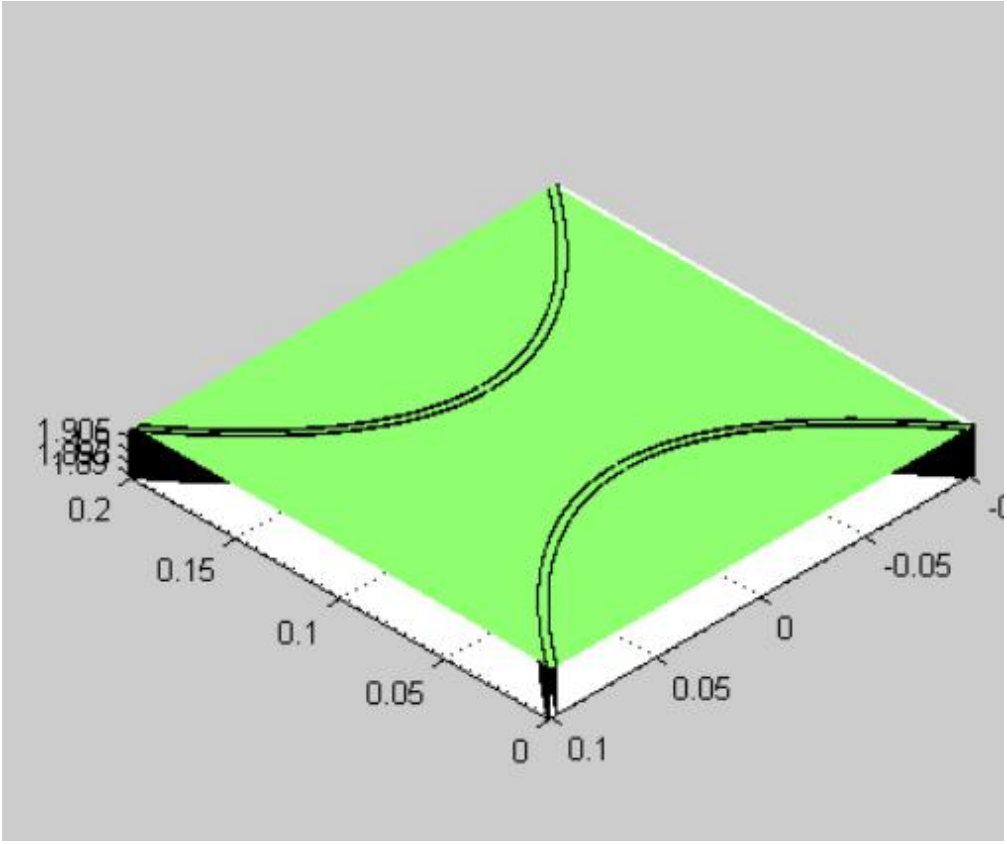

Figure 82 Stiffened plate structure for $d_p = 70mm$

The deflection is plotted and compared with the results obtained from ANSYS in Figure 82a, b. The deflection contours are shown in Figure 83a, b. From the comparison, it is proven to be accurate.

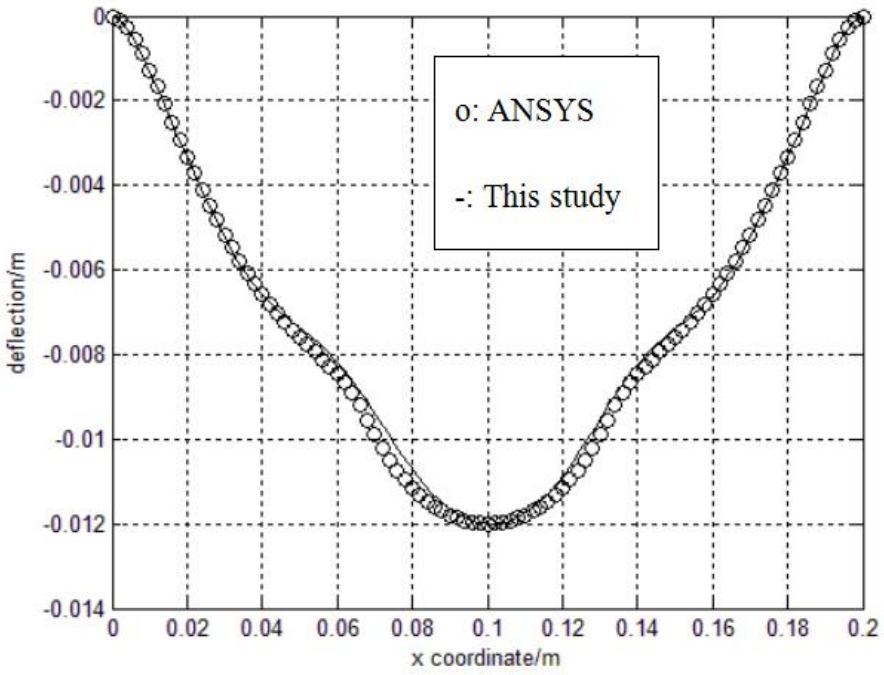

Figure 83a The deflection plot comparison (y=0) using ANSYS and the present approach

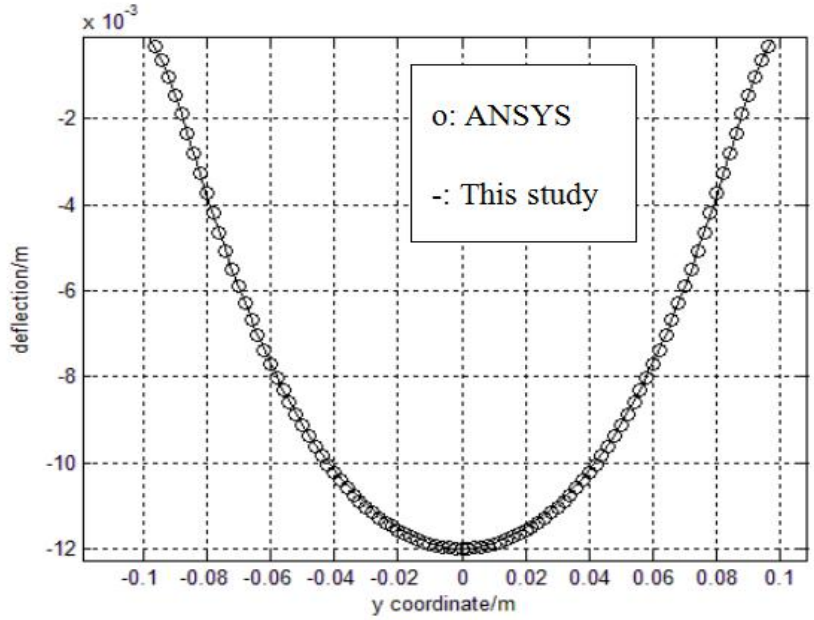

Figure 83b The deflection plot comparison (x=0.1) using ANSYS and the present approach

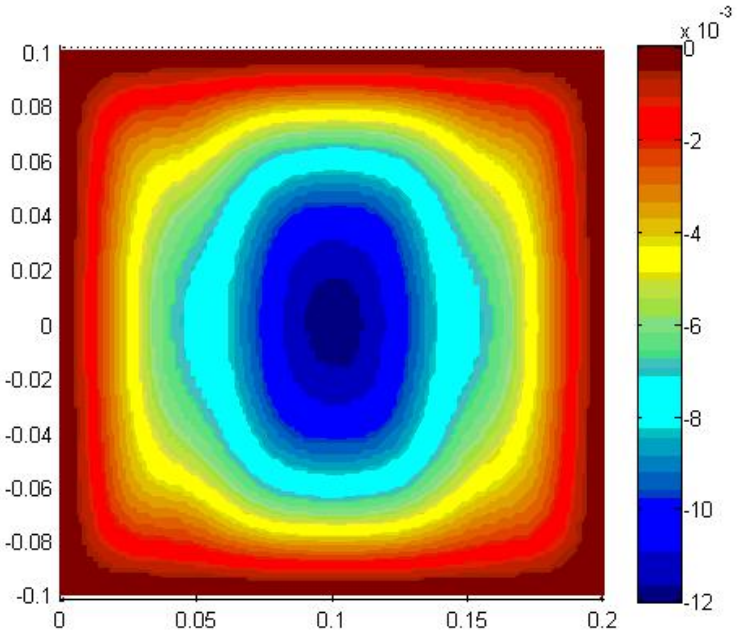

Figure 84a The deflection (unit: Meter) contours obtained using the present approach at pressure of 30MPa

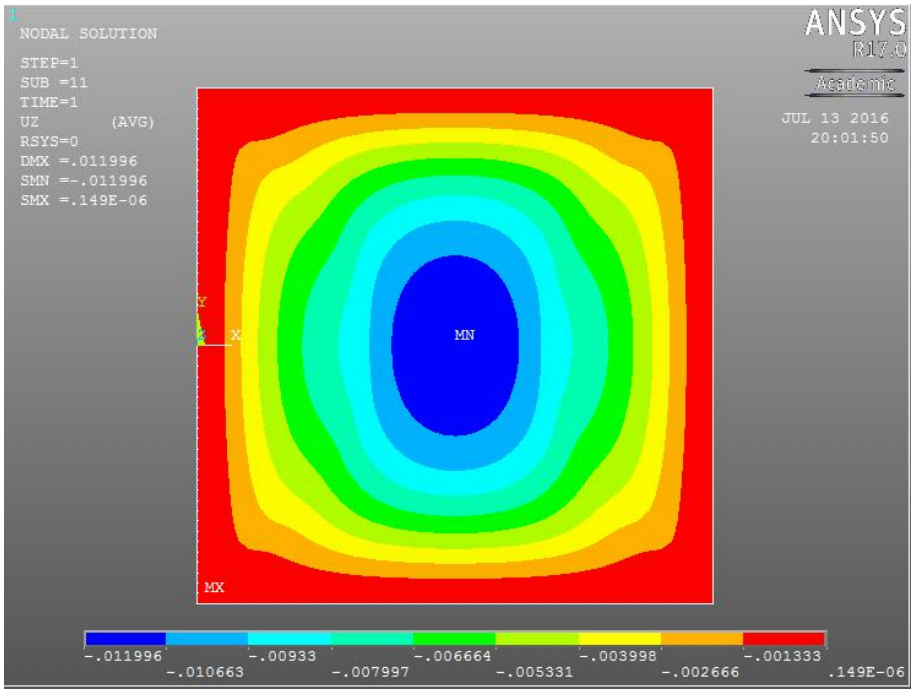

Figure 84b The deflection (unit: Meter) contours obtained using ANSYS at pressure of 30MPa

The parameter d_p is changed to 80mm. In this case, the stiffener is described in Figure 85.

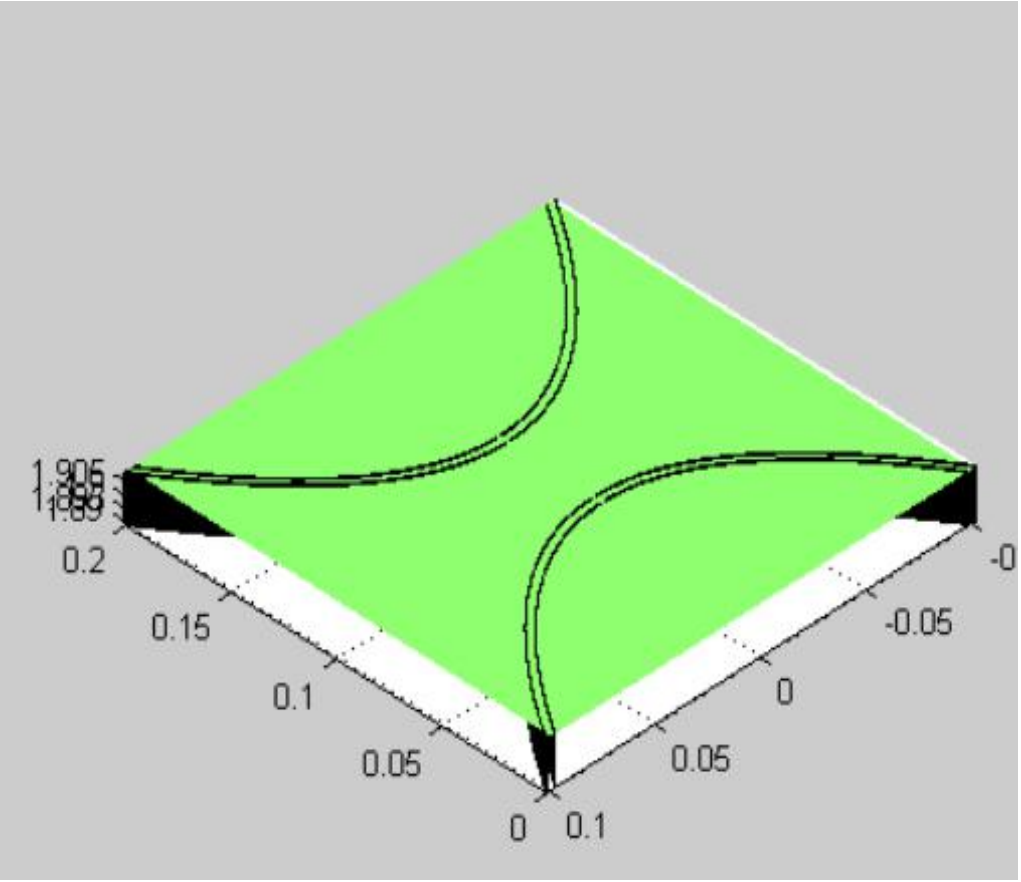

Figure 85 Stiffened plate structure for $d_p = 80mm$

The deflection of the plate is plotted and compared with ANSYS in Figure 86a, b.

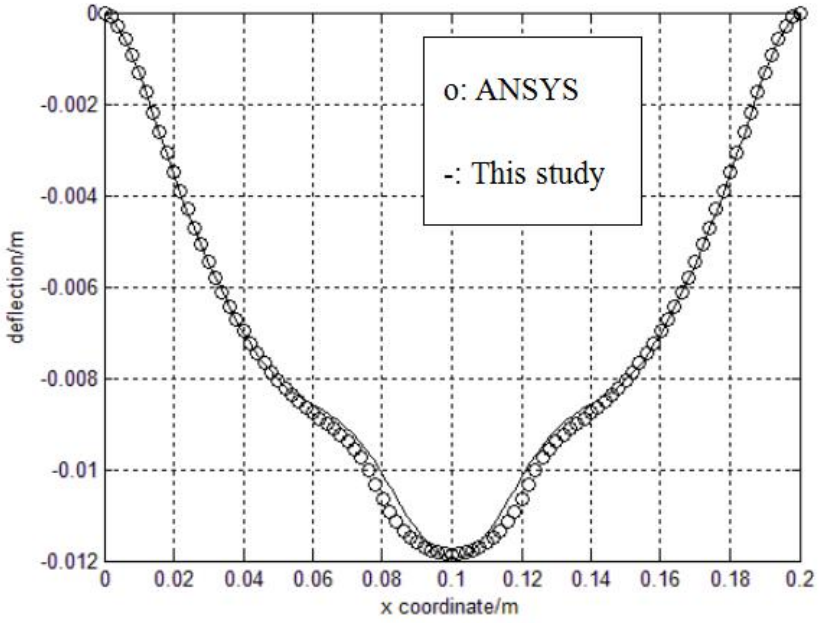

Figure 86a The deflection plot comparison (y=0) using ANSYS and the present approach

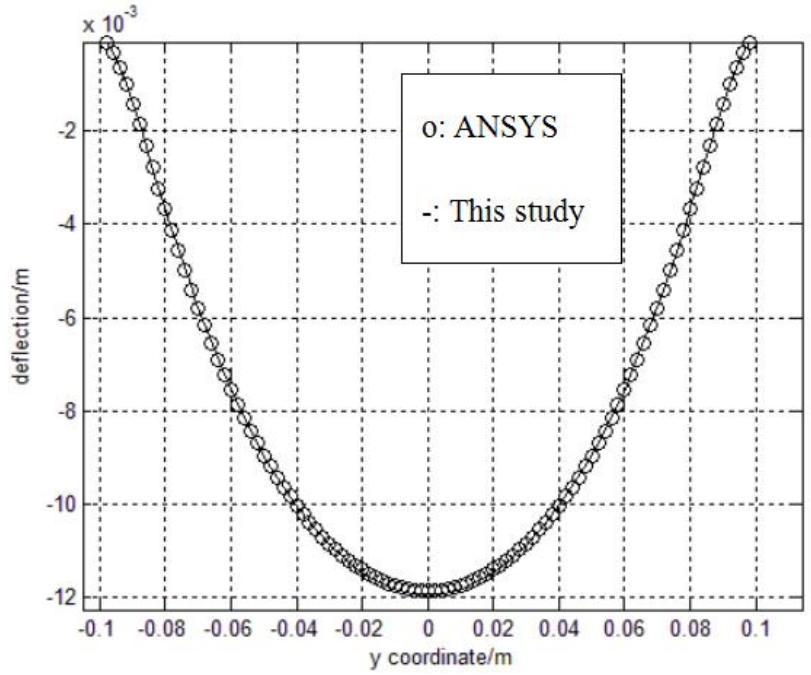

Figure 86b The deflection plot comparison (x=0.1) using ANSYS and the present approach

The deflection contours are shown in Figure 87a, b.

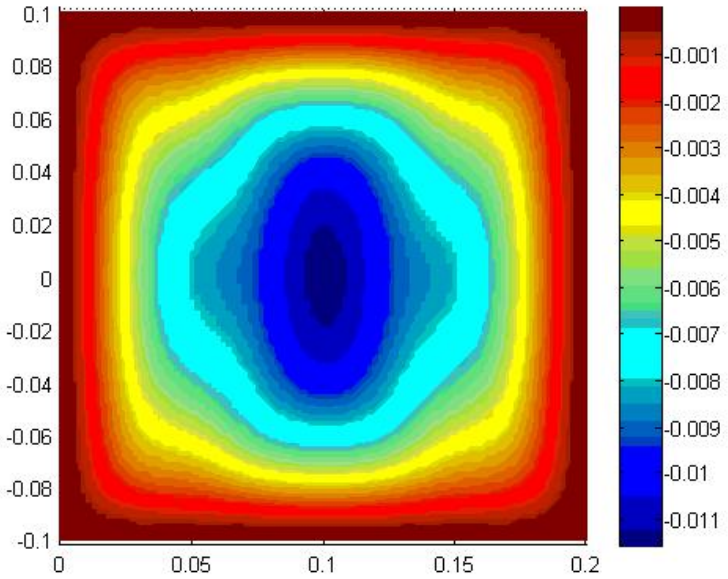

Figure 87a The deflection (unit: Meter) contours obtained using the present approach at pressure of 30MPa

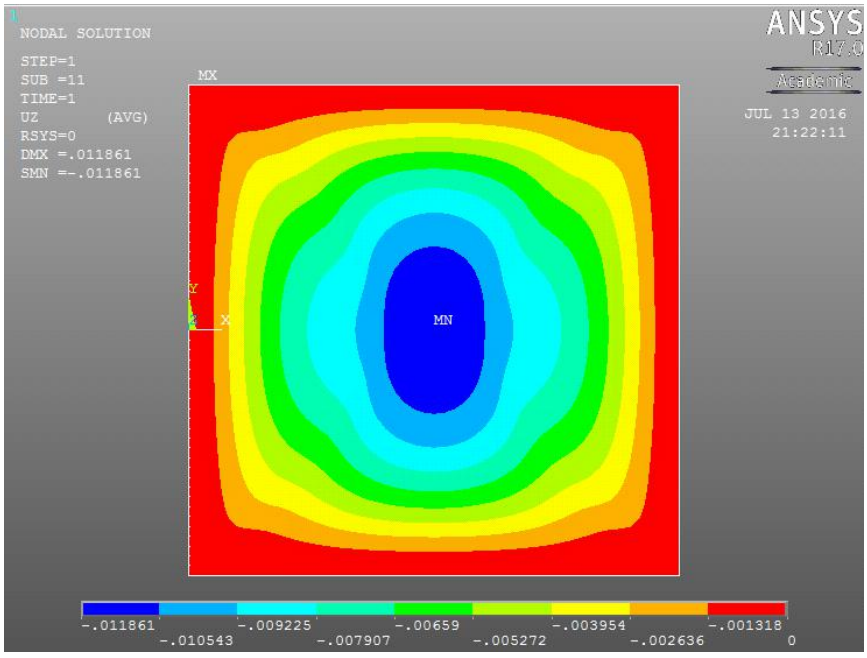

Figure 87b The deflection (unit: Meter) contours obtained using ANSYS at pressure of 30MPa

The parameter d_p is changed to 90mm. The stiffener is shown in Figure 88.

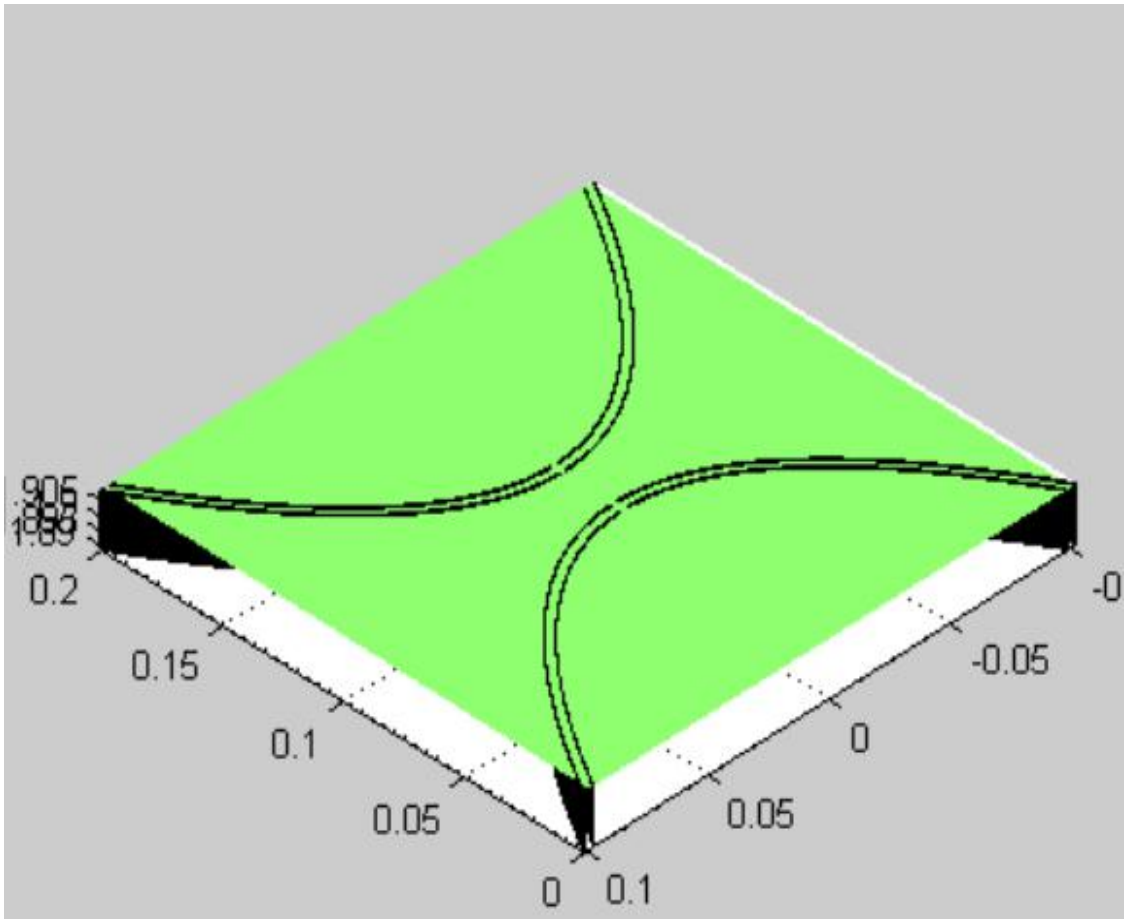

Figure 88 Stiffened plate structure for $d_p = 90mm$

The deflection of the plate is plotted and compared with ANSYS in Figure 89a, b.

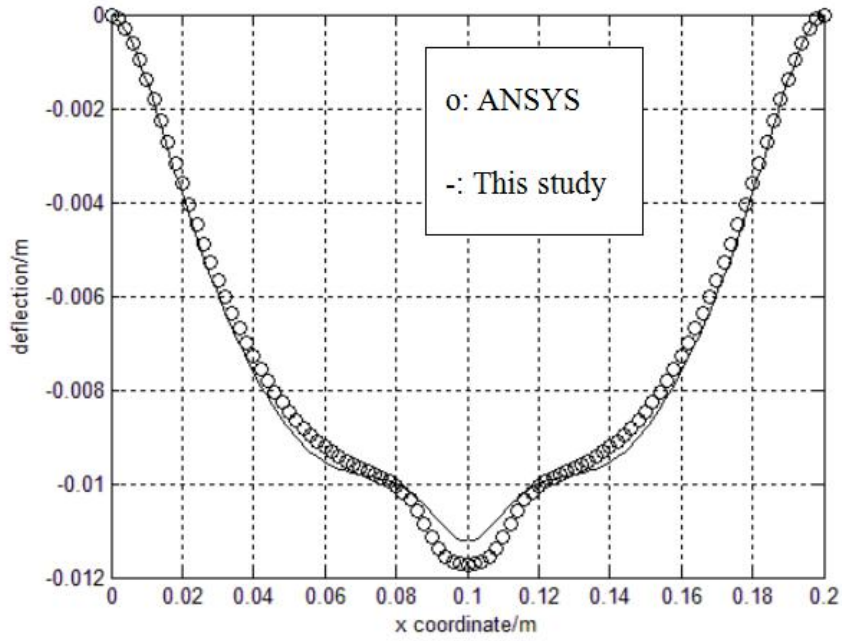

Figure 89a The deflection plot comparison (y=0) using ANSYS and the present approach

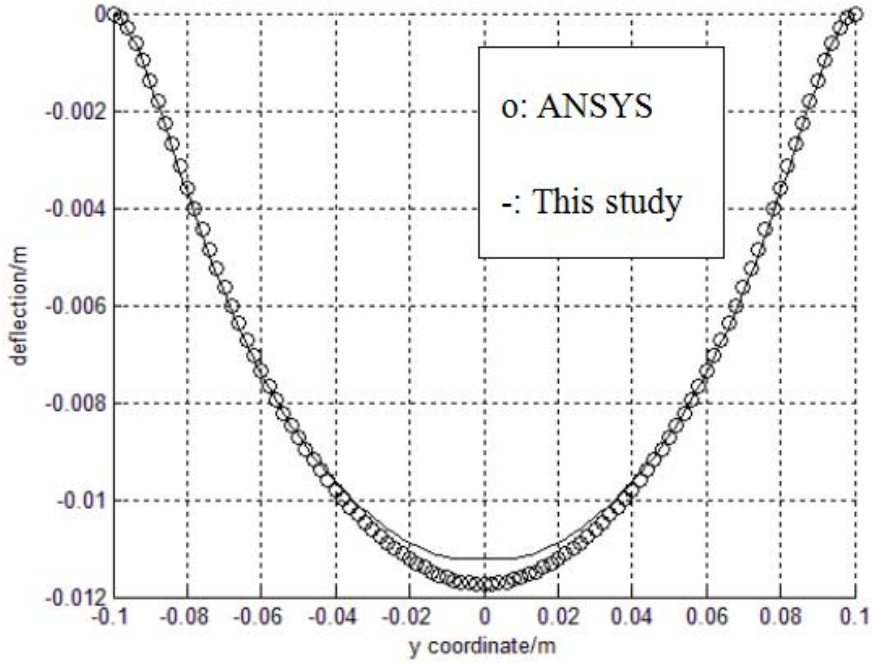

Figure 89b The deflection plot comparison (x=0.1) using ANSYS and the present approach

The deflection contours are shown in Figure 90a, b.

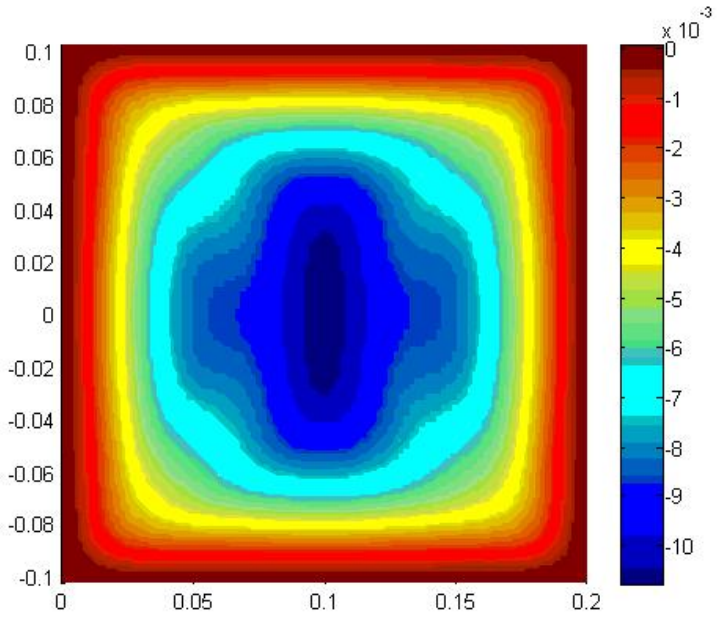

Figure 90a The deflection (unit: Meter) contours obtained using the present approach at pressure of 30MPa

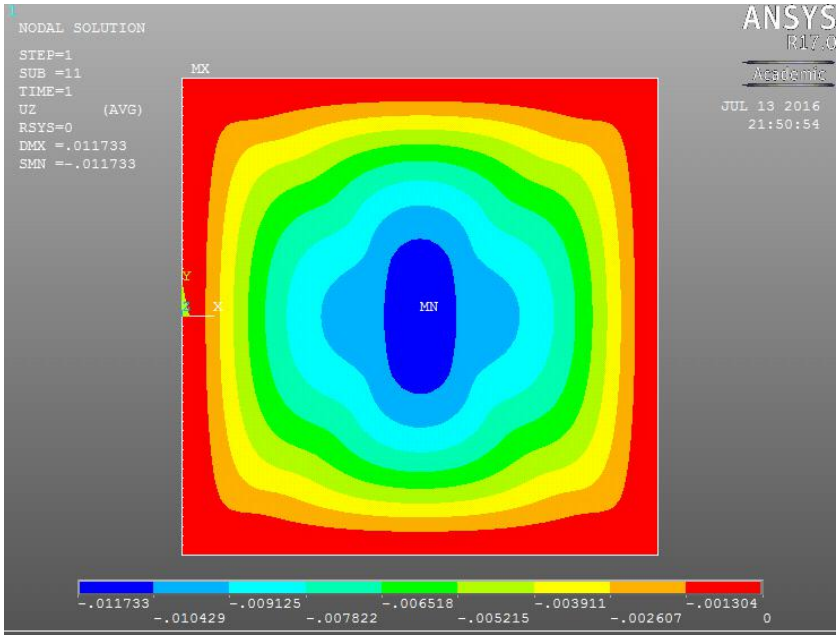

Figure 90b The deflection (unit: Meter) contours obtained using ANSYS Riks at pressure of 30MPa

The parameter d_p is changed to 100mm. In this case, the stiffer is described in Figure 91.

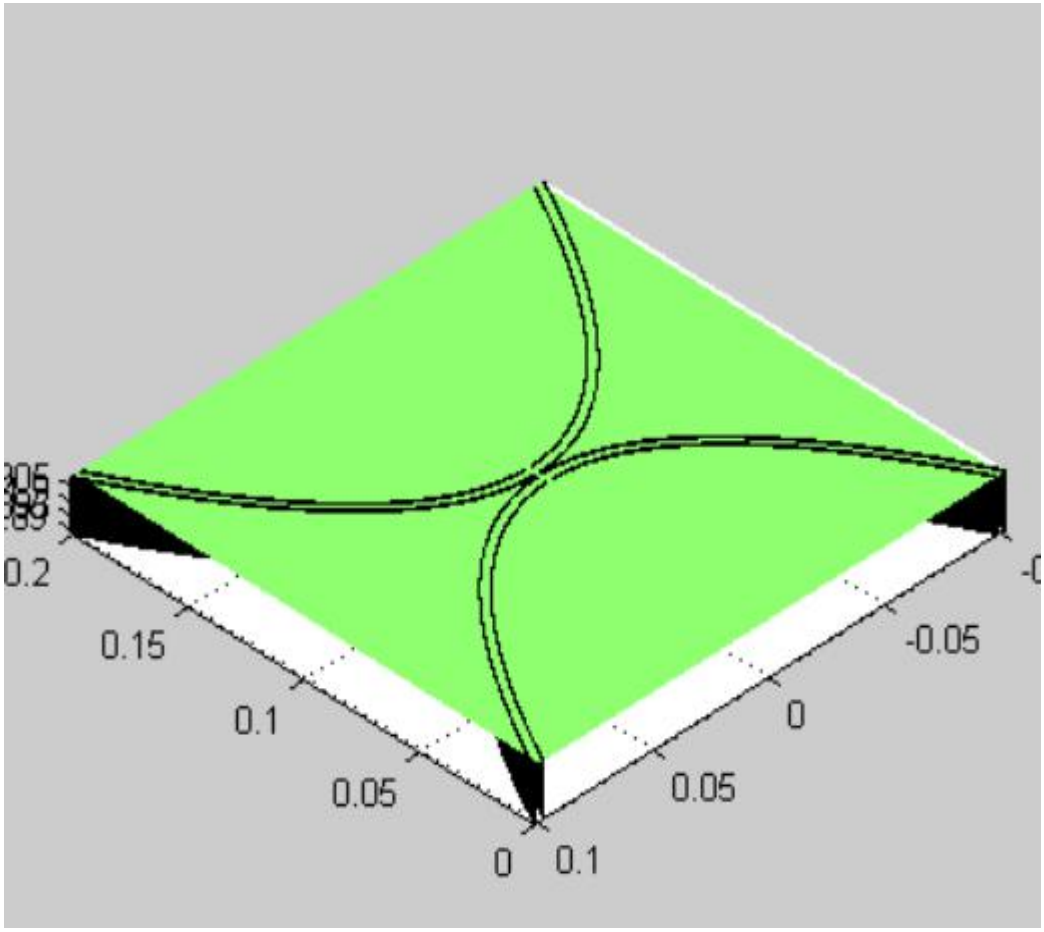

Figure 91 stiffener shape $d_p = 100mm$

The deflection of the plate is plotted and compared with ANSYS in Figure 92a, b.

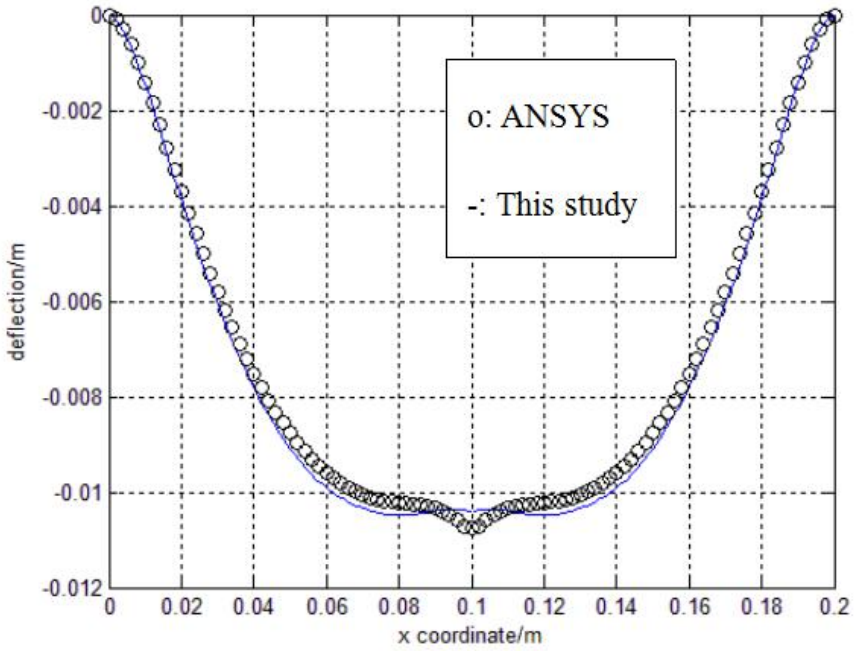

Figure 92a The deflection plot comparison (y=0) using ANSYS and the present approach

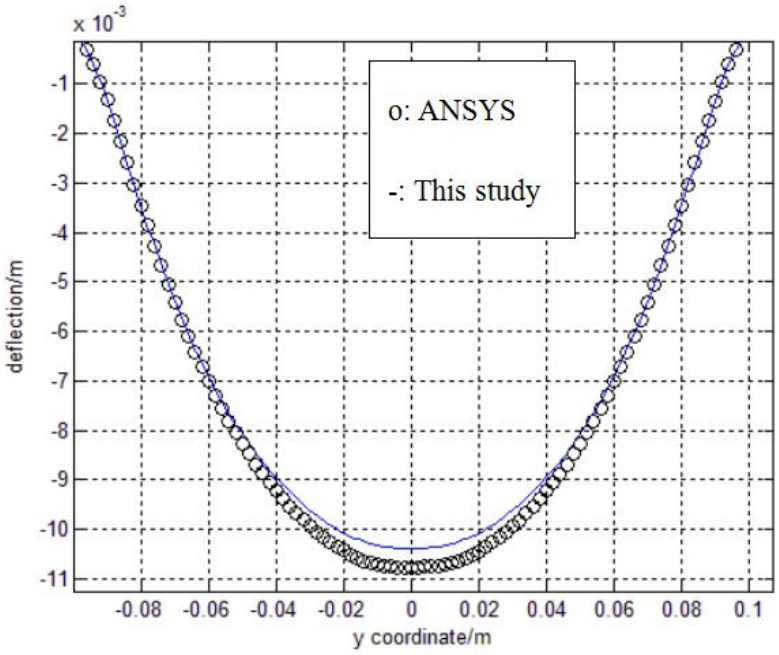

Figure 92b The deflection plot comparison (x=0.1) using ANSYS and the present approach

The deflection contours are shown in Figure 93a, b.

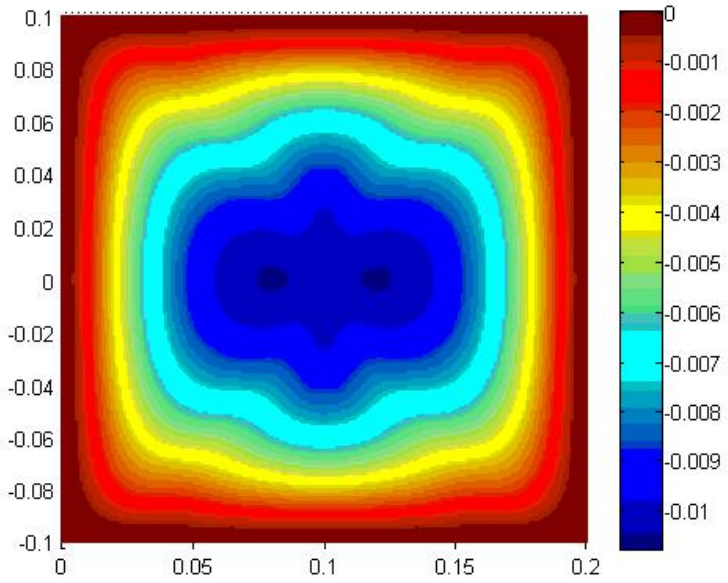

Figure 93a The deflection (unit: Meter) contours obtained using the present approach at pressure of 30MPa

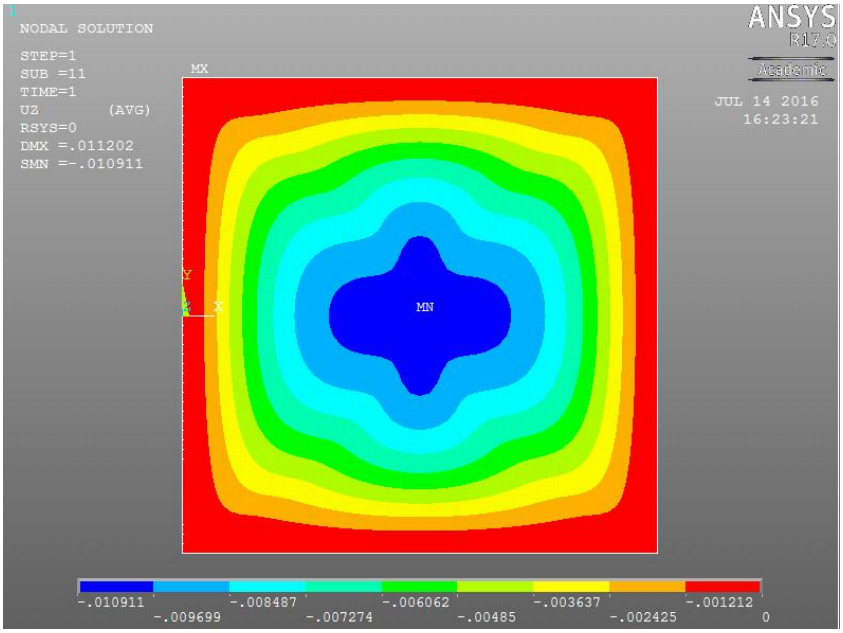

Figure 93b The deflection (unit: Meter) contours obtained using ANSYS Riks at pressure of 30MPa

From the numerical simulation results, it is observed that the method is accurate for various stiffened plate structures. The large deformation occurs for this thesis.

6.5 Stiffened hydrofoil shell

In this part, the buckling collapse analysis of the multi-layered hydrofoil structure is presented. The hydrofoil element is employed. As an illustration example, we use the NACA-0012 hydrofoil. The cross section of the NACA-0012 hydrofoil is described by:

$$z = \frac{h_w}{20}\left(0.2969 y_t^{1/2} - 0.1260 y_t - 0.3516 y_t^2 + 0.2843 y_t^3 - 0.1015 y_t^4\right) \qquad (253a, b)$$
$$y_t = y / L_c$$

The motivation for this analysis arises from recent development of ocean gliders [30, 31]. The underwater glider's wing structure is working under the deep ocean environment, where a large water pressure is applied on the outer surface of the wings (hydrofoil structures). A single layered hydrofoil buckling analysis under water pressure with large-deformation is presented in Test 13. In actual practice, the hydrofoil is always a multi-layer shell. Thus, the multi-layer hydrofoil buckling analysis is presented in Test 14. Also the hydrofoil structure is always supported by stiffeners and ribs. Thus, the stiffened hydrofoil structure under water pressure is analyzed in Test 15 and Test 16. In Test 15, we assume the stiffener is undeformable. In Test 16, we remove this assumption and the stiffener is deformable with hydrofoil shells. In Test 17, a more realistic 3-D hydrofoil model is developed. Throughout this section 6.5, the load is the water pressure applied on the outer surface.

Test 13: Single layer hydrofoil buckling analysis

The water pressure is applied on the outer surface of the hydrofoil. The boundary conditions will be:

$$\begin{aligned} x=0&: u_2=0, u_3=0 \\ x=c&: u_2=0, u_3=0 \end{aligned} \tag{254a, b}$$

Thus, the boundary condition functions are defined as:

$$f_{u_2}^{\xi_2}=f_{u_3}^{\xi_2}=\xi_2\left(1-\xi_2\right) \tag{255}$$

The following parameters are:

$$t_p=0.01m$$
$$L_c=1m$$

Where t_p is the wall thickness of the hydrofoil.

For the material property, the Ramberg-Osgood model is applied with the parameters:

$$n=10.7$$
$$\beta=3/7$$

The nominal yield stress is 488MPa.

The height of the hydrofoil h_w is changed and the critical buckling pressure is recorded in Table 5.

Table 5 The critical buckling pressure of the single-layer hydrofoil structure

h_w/m	Hybrid DG-FEM/1×10^5 Pa	ANSYS/1×10^5 Pa
0.1	1.77	1.83
0.12	2.03	2.09

0.14	2.26	2.32
0.16	2.47	2.50
0.18	2.66	2.66
0.2	2.81	2.78

where h_w is the maximum height of the hydrofoil.

The pressure curves for various h_w are shown in Figure 94.

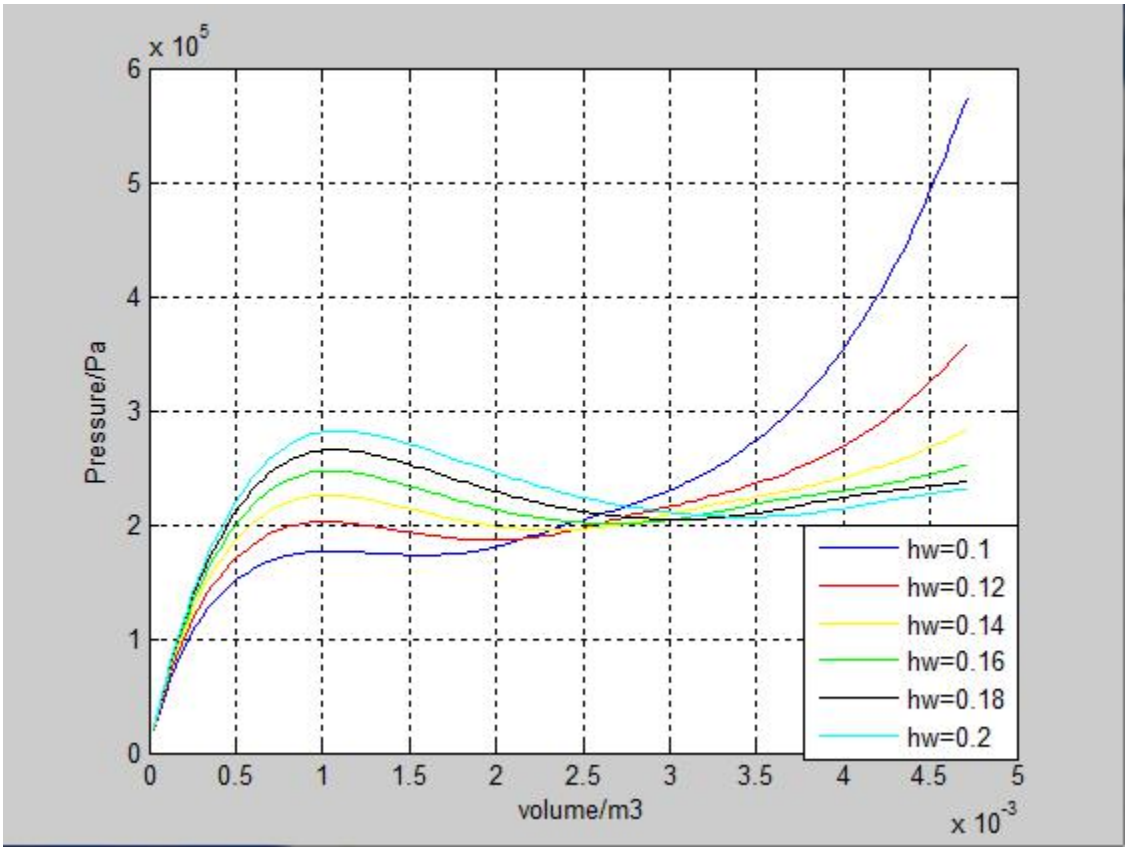

Figure 94 Pressure curves for different heights of hydrofoil structures

The convergence study is presented in Figure 95. For the case $h_w = 0.2m$, by using different circumferential displacement order k, we can get the pressure curves in Figure 95.

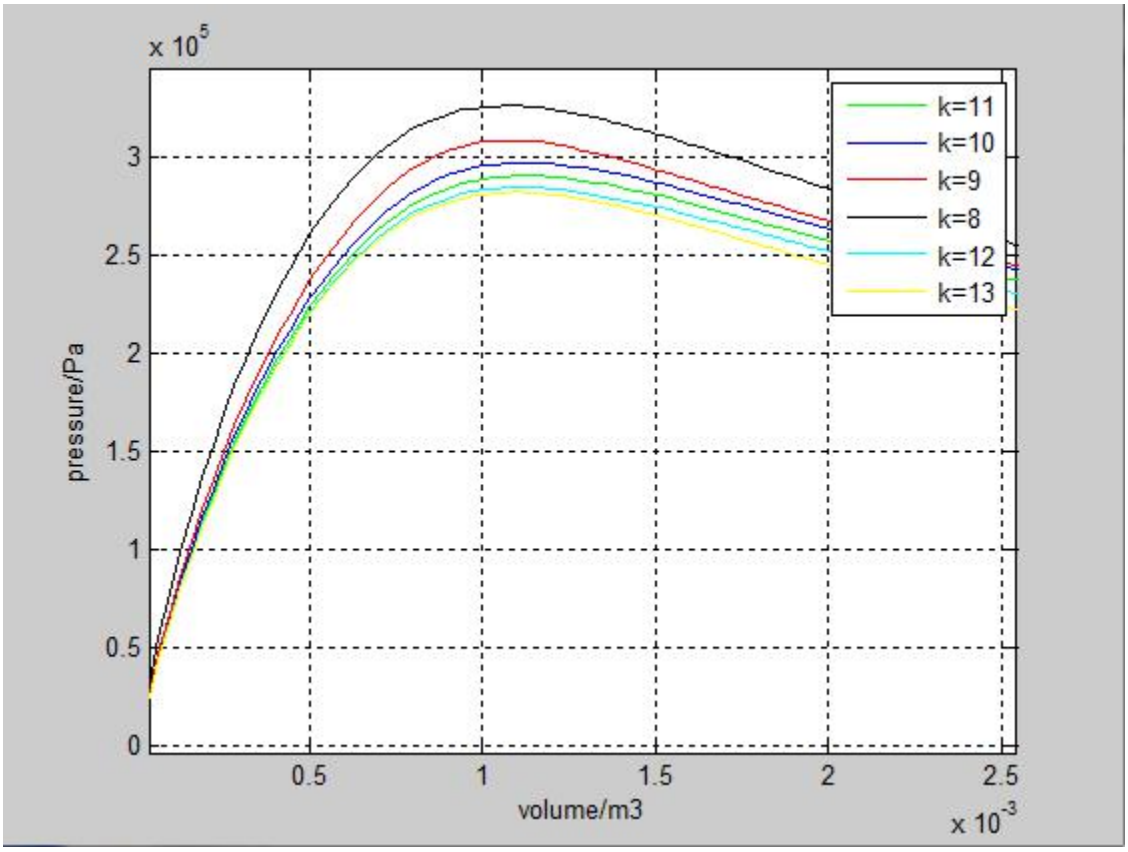

Figure 95 Convergence study of circumferential displacement order

It is observed that, with the increase of the displacement order, the pressure curves tend to be identical.

Test 14: Multi-layer hydrofoil analysis

A two-layered hydrofoil structure is analyzed next. The first layer is assumed to be elastic material and the second layer is assumed to be plastical. The Young's Modulus is 206GPa and the Poisson ratio is 0.3 for both the layers. For the second layer, the nominal yield stress is 488MPa.

The results of critical buckling pressure are listed in the Table 6. The post buckling pressure curves are given in Figure 96.

Table 6 The critical buckling pressure of the 2-layer hydrofoil structure

h_w / m	Hybrid DG-FEM/1×10^5 Pa	ANSYS/1×10^5 Pa
0.1	1.82	1.85
0.12	2.09	2.11
0.14	2.35	2.35
0.16	2.58	2.56
0.18	2.80	2.74
0.2	3.00	2.89

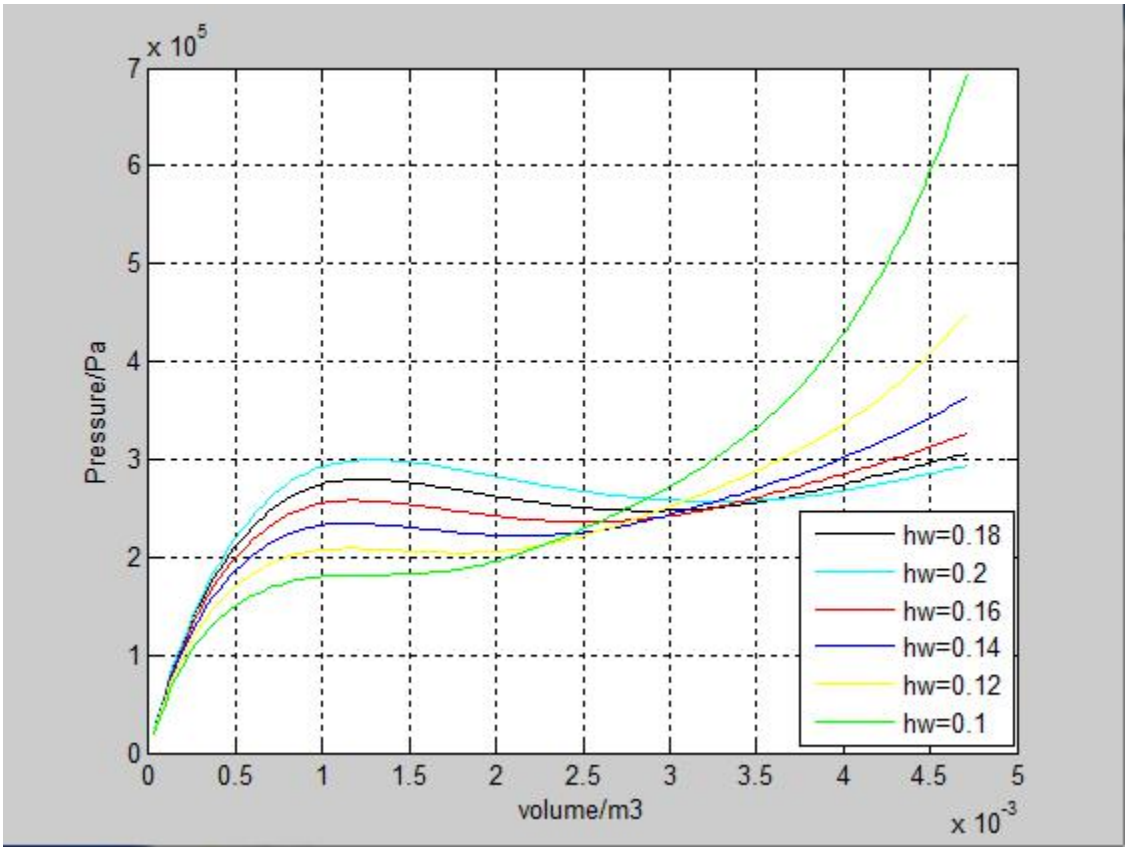

Figure 96 Pressure curves for different heights h_w / m (2-layer hydrofoil)

The post buckling profile of the multi-layer hydrofoils is shown in Figure 97.

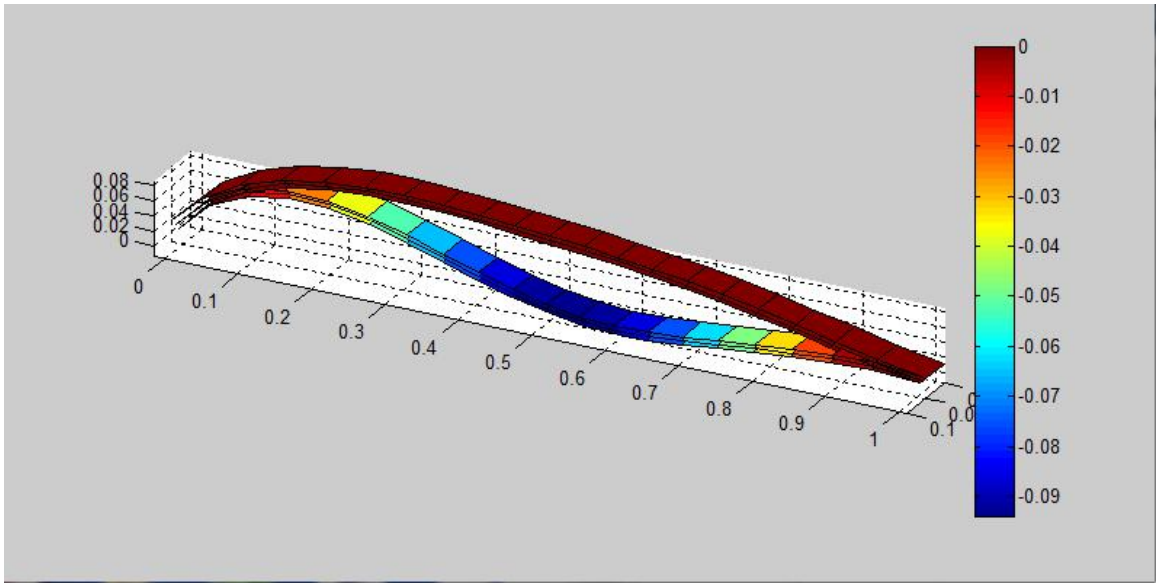

Figure 97 Post buckling profile (unit: Meter) of the multi-layer hydrofoil structure

Test 15: Simplified stiffened hydrofoil model (rigid stiffeners)

Stiffened hydrofoil structures are next analyzed. In this case, the multi-layered hydrofoil structure is supported by ribs (stiffeners). We assume that the ribs are strong enough such that the ribs are rigid. The material are both assumed to be elastic. The Young's modulus is 206GPa and the Poisson ratio is 0.3.

The distance between the adjacent ribs is changed and the maximum deflection under 5MPa are listed in the Table 7 and compared in Figure 98.

Table 7 Maximum deflection of stiffened hydrofoil with rigid ribs under 5Mpa

$d_{rib}(m)$	Hybrid DG-FEM(m)	ANSYS(m)
0.24	0.00220	0.00213
0.36	0.00789	0.00779
0.48	0.0148	0.0149
0.6	0.0224	0.0224

0.72	0.0308	0.0307
0.84	0.0393	0.0396
0.96	0.0483	0.0487
1.08	0.0575	0.0579

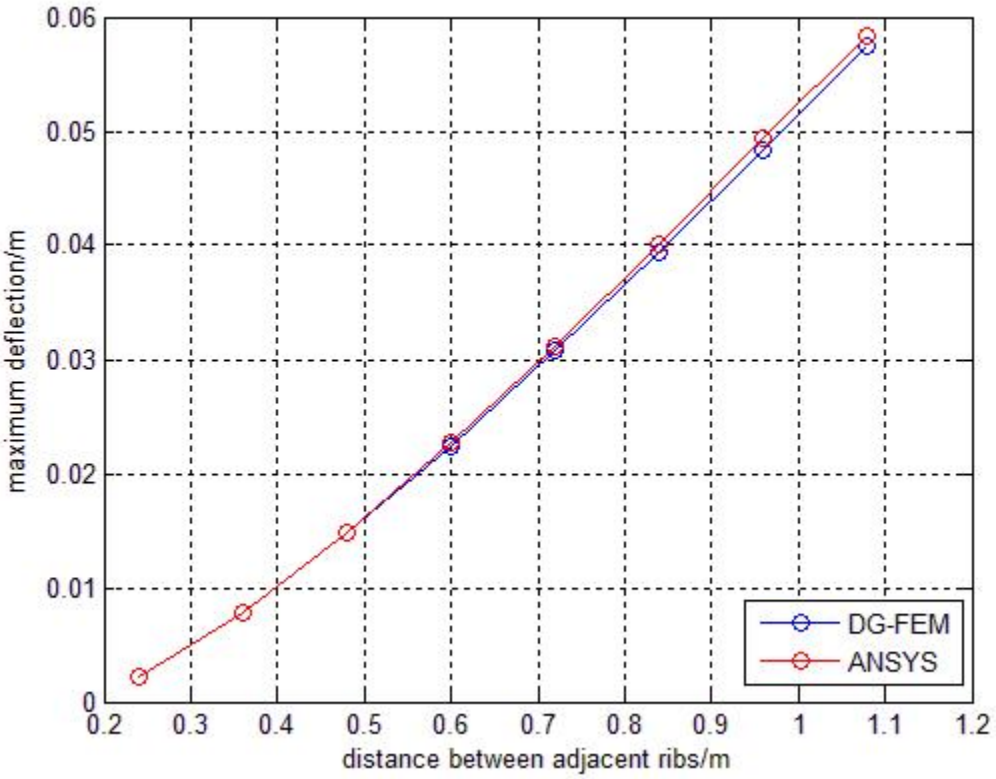

Figure 98 Maximum deflection for the stiffened hydrofoil structure with rigid ribs

The displacement contour is shown in Figure 99.

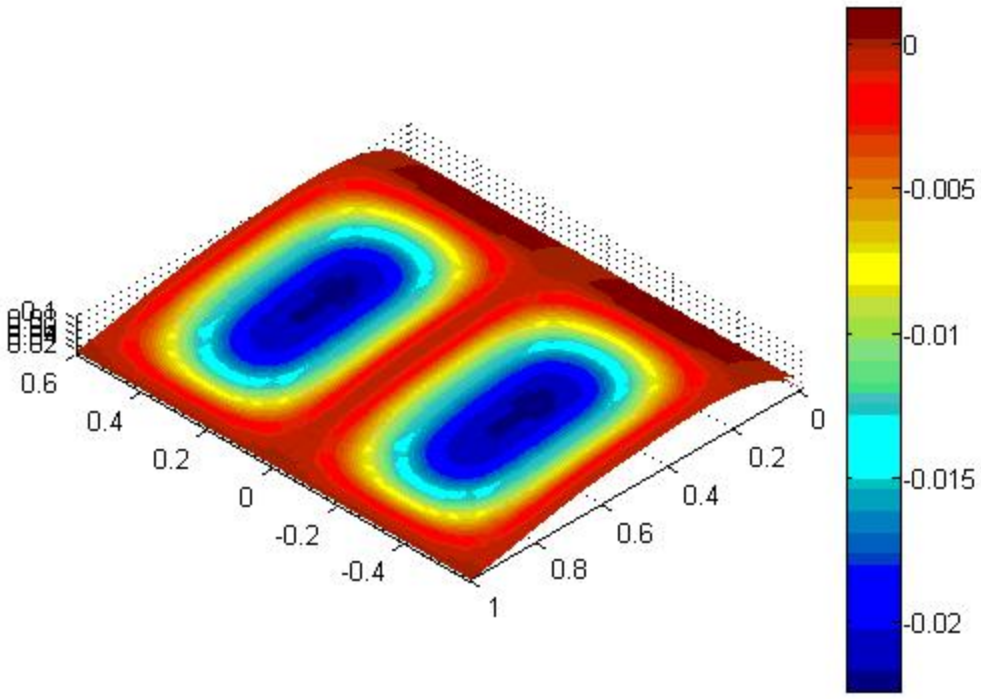

Figure 99 Deflection contours (unit: Meter) for stiffened hydrofoils with rigid ribs under water pressure

Test 16: Simplified stiffened hydrofoil model (deformable stiffeners)

Stiffened hydrofoil structures with deformable stiffeners are analyzed in this section. In this case, the multi-layered hydrofoil structure is supported by ribs (stiffeners). In this test, the ribs are flexible and thus will also deform along with the hydrofoils. The distance of adjacent ribs is varied. The rib's cross-section is a rectangular, whose width and height are 4cm and 2cm, respectively. The deflection of the stiffened hydrofoil under water pressure is shown in Figure 100.

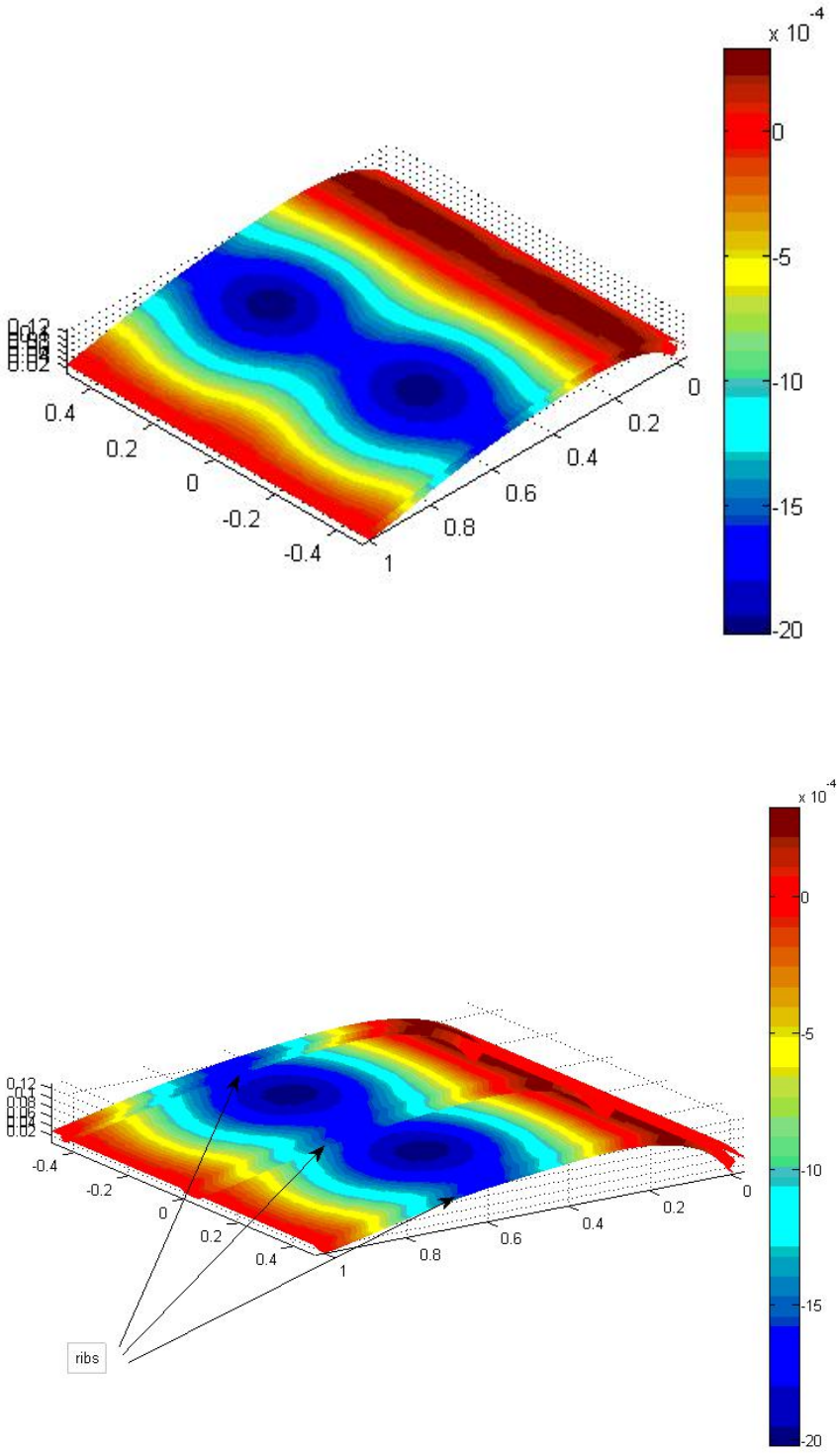

Figure 100 Deflection contours (unit: Meter) for stiffened hydrofoils with flexible ribs under water pressure

The distance between adjacent ribs is changed and the critical buckling pressure is calculated under water pressure, as shown in Table 8. The results are also compared in Figure 101.

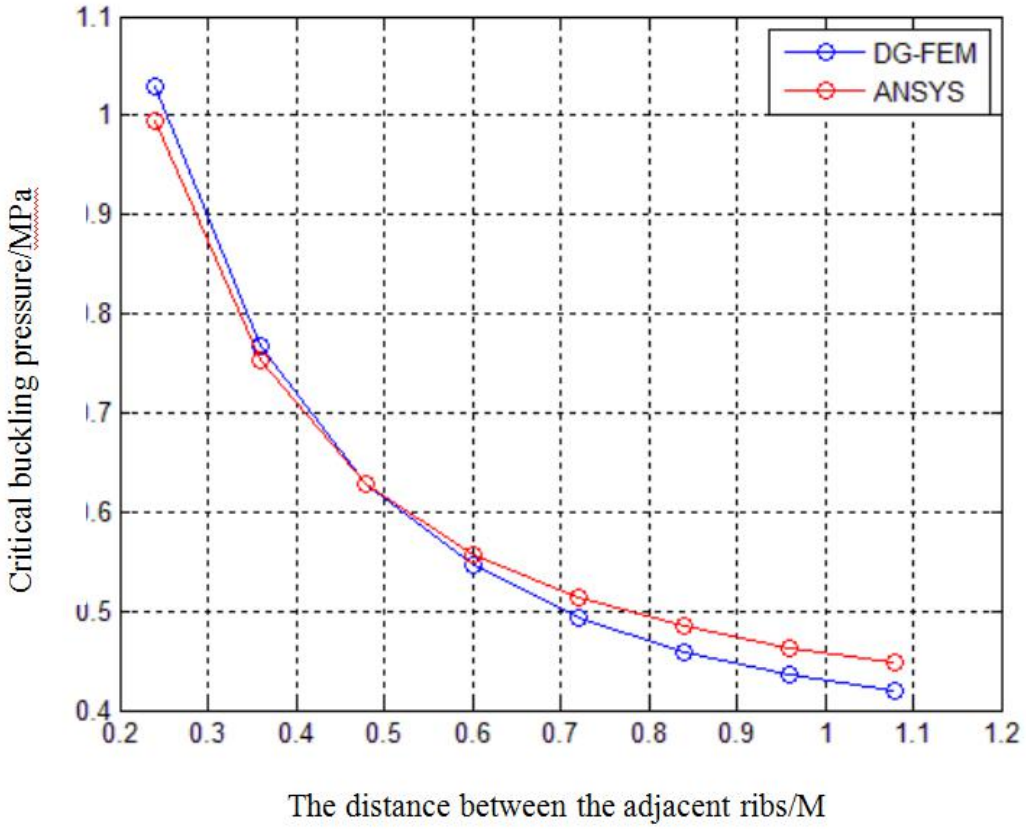

Figure 101 Critical buckling pressure for the stiffened hydrofoils with deformed ribs

Table 8 Critical buckling pressure for stiffened hydrofoils with deformed ribs

d_{rib}/m	DG-FEM/$1\times10^6 Pa$	ANSYS/$1\times10^6 Pa$
0.24	1.0284	0.9943
0.36	0.7675	0.7530

0.48	0.6288	0.6287
0.6	0.5457	0.5574
0.72	0.4931	0.5135
0.84	0.4590	0.4845
0.96	0.4358	0.4633
1.08	0.4185	0.4475

Test 17: 3-D realistic stiffened hydrofoil analysis

In this test, a whole 3-D realistic stiffened hydrofoil is developed for a more realistic analysis. The model is shown in Figure 102. The underwater glider wing's buckling analysis is presented.

In this case, the fixed boundary condition is applied on one side of the hydrofoil. For the other boundaries, the displacement boundary condition will be free. The water pressure is applied on the outer surface. The rib's cross-section will be a rectangular, whose edges are all 3cm. The distance between the adjacent ribs is changed and the pressure buckling curve is obtained.

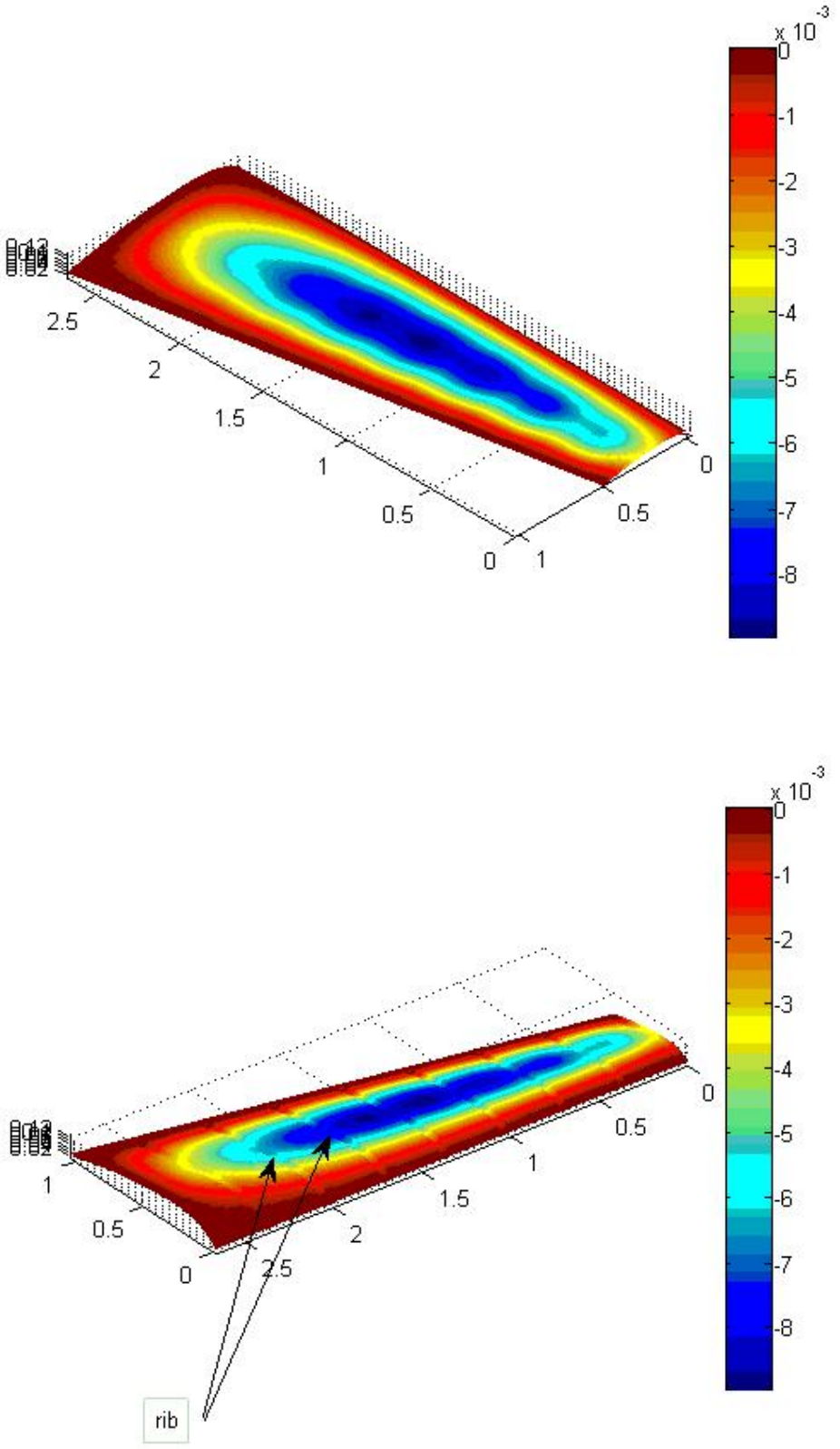

Figure 102 3-D realistic whole hydrofoil structure with stiffeners (ribs)

When the distance between adjacent ribs is $d_{rib} = 0.3m$, the pressure curve in Figure 103.

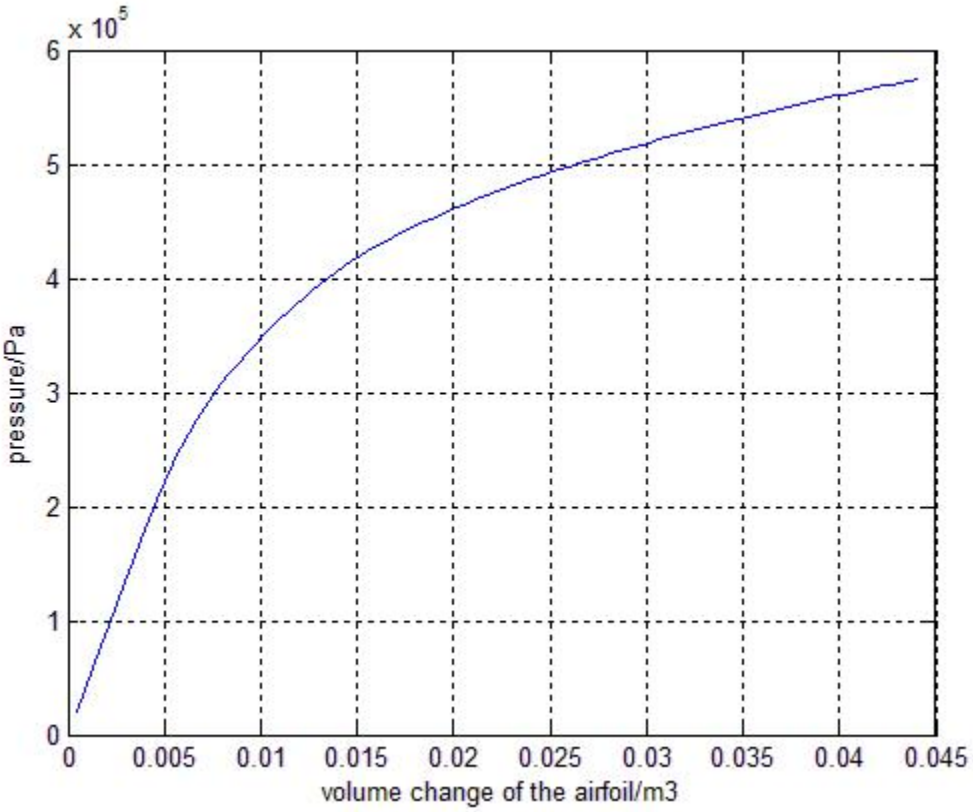

Figure 103 Pressure curve for the 3-D whole hydrofoil structure stiffened by ribs with a distance of 0.3m

When the pressure is 0.575MPa, the hydrofoil has totally collapsed (the contact between the hydrofoil inner surfaces is initiated). The deflection contour is presented in Figure 104.

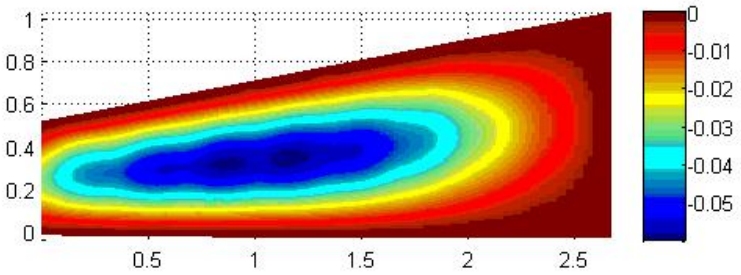

Figure 104 Deflection contours (unit: Meter) when the pressure is 0.575Mpa

The deflection curves for several cross-sections of the underwater glider wing are plotted in Figure 105.

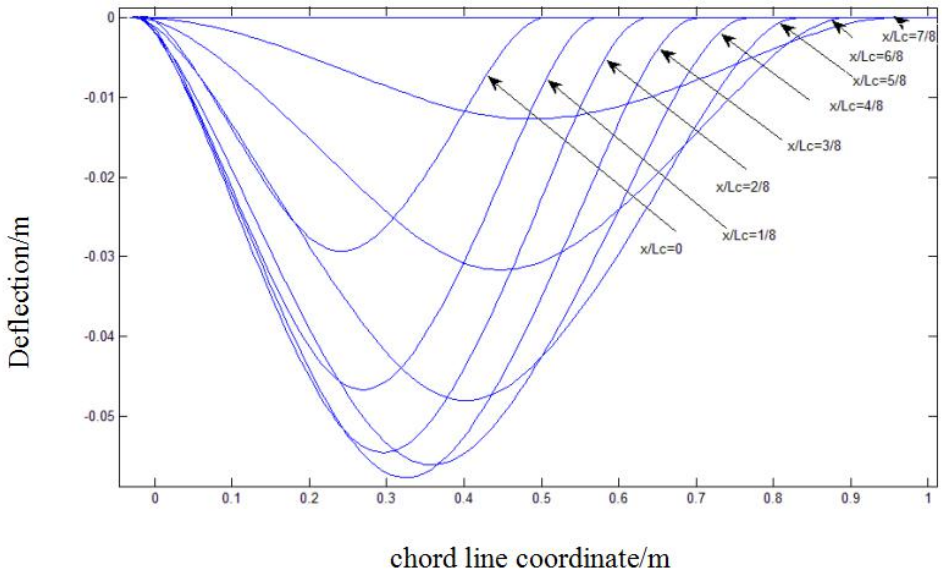

Figure 105 Deflection curves at several locations along the underwater glider wing

In Figure 105, L_c is the span length of the hydrofoil, x will be the span direction coordinate. The deflection curves are all plotted against chord-line coordinates.

When the distance between adjacent ribs is $d_{rib} = 0.23m$, the pressure curve is given in Figure 106.

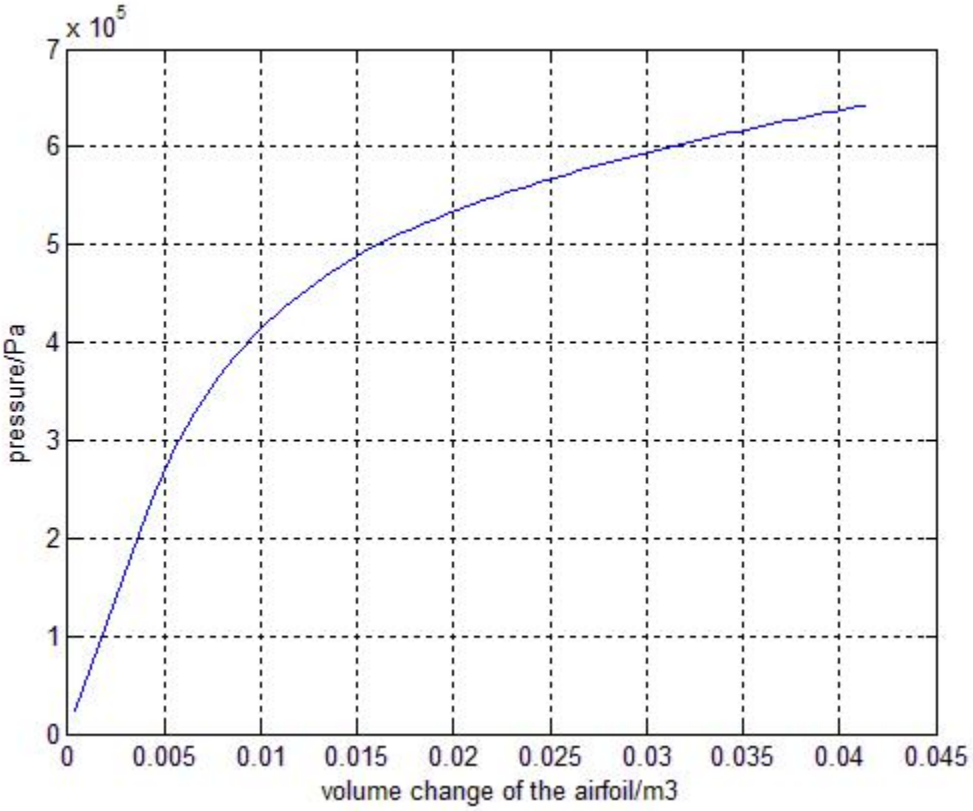

Figure 106 Pressure curve for the 3-D whole hydrofoil structure stiffened by ribs with a distance of 0.23m

When the pressure is 0.642MPa, the hydrofoil has totally collapsed (the inner surface of hydrofoils will contact). The deflection contour is given in Figure 107.

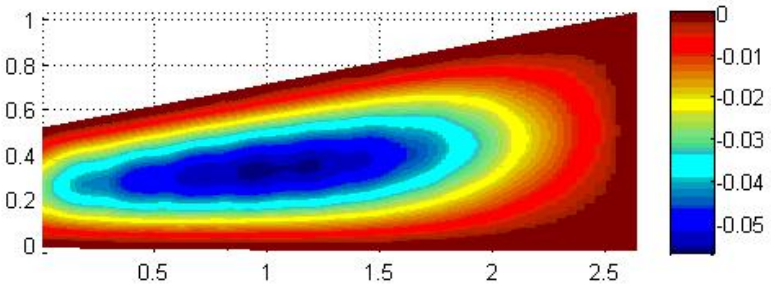

Figure 107 Deflection contours (unit: Meter) when the pressure is 0.642Mpa

The deflection curves for several cross-sections of the underwater glider wing are plotted in Figure 108.

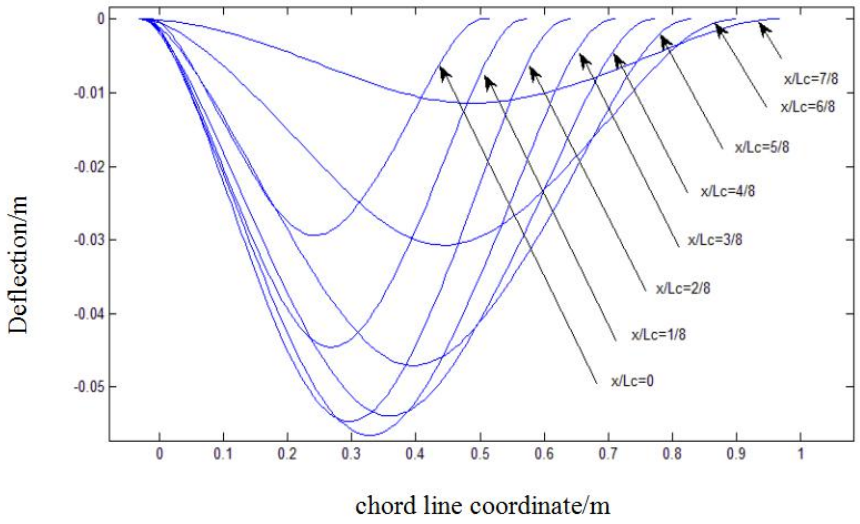

Figure 108 Deflection curves at several locations along the underwater glider wing

When the distance between adjacent ribs is $d_{rib} = 0.17m$, the pressure curve is given in Figure 109.

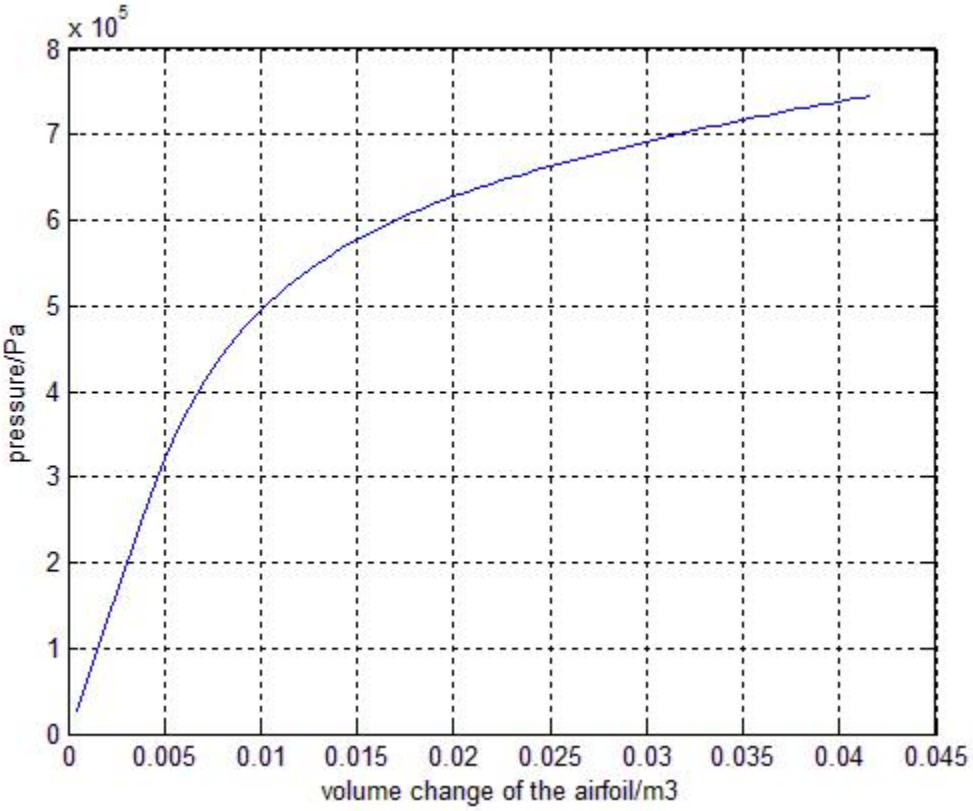

Figure 109 Pressure curve for the 3-D whole hydrofoil structure stiffened by ribs with a distance of 0.17m

When the pressure is 0.745MPa, the hydrofoil is totally collapsed (the contact between the inner surfaces is initiated). The deflection contours are shown in Figure 110.

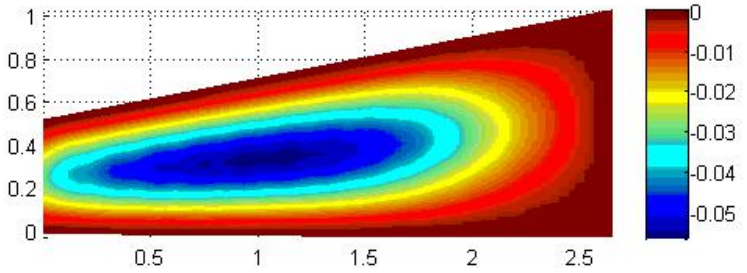

Figure 110 Deflection contours (unit: Meter) when the pressure is 0.745MPa

The deflection curves for several cross-sections of the underwater glider wing are plotted in Figure 111.

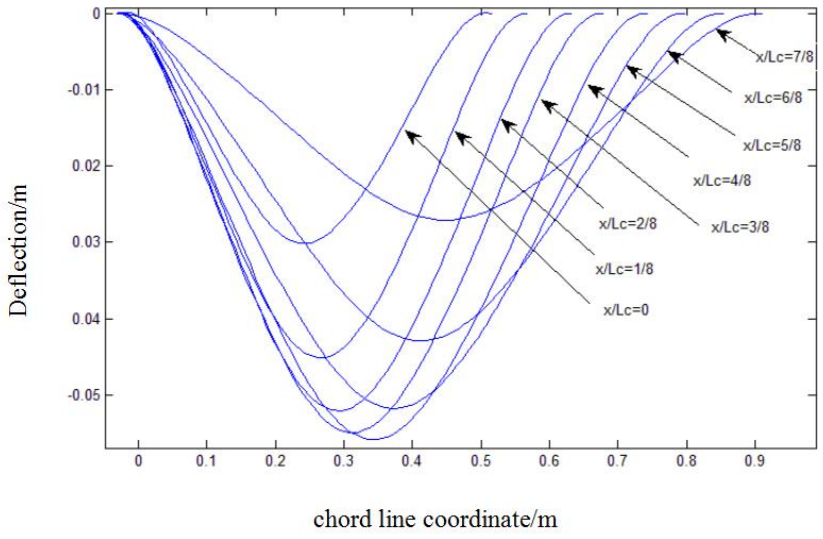

Figure 111 Deflection curves at several locations along the underwater glider wing

In this part, the stiffened hydrofoil structure model is developed. From the simplified hydrofoil slide model to realistic 3-D hydrofoil model with stiffeners, the method has been verified to be accurate when comparing with those from ANSYS. By using the stiffened hydrofoil element, the 3-D realistic hydrofoil collapse analysis is also presented.

For all the examples studied in Chapter 6, the order of the displacement basis function of the proposed hybrid DG-FEM is compared with that of traditional FEM in Table 9. From the comparison, it is observed that a high order resolution is obtained.

Table 9 Comparison of displacement order between this thesis and ANSYS

	Hybrid DG-FEM	Traditional finite element
3-D sandwich plate	6-6-3	2-2-2
2-D multi-layer collapse	8-5	2-2
3-D multi-layer buckling	2-8-5	2-2-2
Single layer hydrofoil	3-16-3	2-2-2
Multi-layer hydrofoil	3-16-3	2-2-2
Stiffened hydrofoil	3-16-4	2-2-2
Stiffened plate	3-9-9	2-2-2

In the Table 9, $a-b-c$ refers to the displacement order in the 3 dimensions for 3-D structure and $a-b$ refers to the displacement order in the 2 dimensions for 2-D structure.

For the order of traction, it is same as the displacement order in the interface.

The number of degree-of-freedom is compared in Table 10. The proposed DG-FEM uses a much fewer number of DOF to obtain the accurate results.

Table 10 Comparison of the number of DOF between this thesis and ANSYS

	Hybrid DG-FEM	Traditional finite element
3-D sandwich plate	972	39015
2-D multi-layer collapse	120	540
3-D multi-layer buckling	9600	54000
Single layer hydrofoil	8640	96000
Multi-layer hydrofoil	17280	96000
Stiffened hydrofoil	8640	96000
Stiffened plate	2187	96000

Chapter 7 Conclusion

In this thesis, a hybrid DG-FEM is developed for the analysis of the multi-layered structures. Five types of problems in the field of multi-layered structures are solved: sandwich plates, 2-D multi-layer pipes, 3-D multi-layer pipes, stiffened plates and stiffened multi-layer hydrofoils. Different from most previous investigations on these problems, this thesis focuses on large deformations leading to geometrically nonlinear problems. For verification, the results are compared with experiment results from other studies or numerical simulation results obtained using ANSYS.

In the hybrid DG-FEM method developed in this thesis, the displacement order can be higher than the traditional finite element. The structure configurations considered here are smooth with no geometrical discontinuities. For all examples studied, the number of DOF in this study is much fewer than that of traditional finite element method, as shown in Table 10. For the structures with multi-layers and stiffeners, the DG-FEM has the advantage in the freedom in selecting the displacement basis functions. The traction field (shear force and normal force) are also induced as additional DOF to be solved. Thus, the displacement conforming condition is not required in the selection of displacement basis function. A dedicated orthogonal basis function space is also developed. For different structures and/or different boundary conditions, a unique basis function space is developed.

Reference:

[1] K.J. Bathe, Finite Element Procedures, Prentice Hall, 1996.

[2] Kapania, R.K. and Raciti, S., 1989. Recent advances in analysis of laminated beams and plates. Part I-Shear effects and buckling. AIAA Journal, 27(7), pp.923-935.

[3] Kapania, R.K. and Raciti, S., 1989. Recent advances in analysis of laminated beams and plates, Part II: Vibrations and wave propagation. AIAA Journal,27(7), pp.935-946.

[4] Simo, J.C., Hughes, T.J.R., 1998. Computational inelasticity. Springer.

[5] Goyal, V.K. and Kapania, R.K., 2007. A shear-deformable beam element for the analysis of laminated composites. Finite Elements in Analysis and Design, 43(6), pp.463-477.

[6] Kapania, R.K. and Yang, T.Y., 1987. Buckling, postbuckling, and nonlinear vibrations of imperfect plates. AIAA Journal, 25(10), pp.1338-1346.

[7] Nosier, A., Kapania, R.K. and Reddy, J.N., 1993. Free vibration analysis of laminated plates using a layer wise theory. AIAA Journal, 31(12), pp.2335-2346.

[8] Zhao, W. and Kapania, R.K., 2016. Buckling analysis of unitized curvilinearly stiffened composite panels. Composite Structures, 135, pp.365-382.

[9] Kapania, R.K., Soliman, H.E., Vasudeva, S., Hughes, O. and Makhecha, D.P., 2008. Static analysis of sandwich panels with square honeycomb core.AIAA journal, 46(3), pp.627-634.

[10] Kapania, R.K. and Yang, T.Y., 1986. Formulation of an imperfect quadrilateral doubly curved shell element for postbuckling analysis. AIAA Journal, 24(2), pp.310-311.

[11] Saigal, S., Yang, T.Y. and Kapania, R.K., 1987. Dynamic buckling of imperfection-sensitive shell structures. Journal of Aircraft, 24(10), pp.718-724.

[12] Hammerand, D.C. and Kapania, R.K., 1999. Thermoviscoelastic analysis of composite structures using a triangular flat shell element. AIAA Journal, 37(2), pp.238-247.

[13] Hammerand, D.C. and Kapania, R.K., 2000. Geometrically nonlinear shell element for hygrothermorheologically simple linear viscoelastic composites.AIAA Journal, 38(12), pp.2305-2319.

[14] Cho, M. and Parmerter, R., 1993. Efficient higher order composite plate theory for general lamination configurations. AIAA Journal, 31(7), pp.1299-1306.

[15] Murakami, H., 1986. Laminated composite plate theory with improved in-plane responses. Journal of Applied Mechanics, 53(3), pp.661-666.

[16] Toledano, A. and Murakami, H., 1987. A composite plate theory for arbitrary laminate configurations. Journal of Applied Mechanics, 54(1), pp.181-189.

[17] Barbero, E.J. and Reddy, J.N., 1991. Modeling of delamination in composite laminates using a layer-wise plate theory. International Journal of Solids and Structures, 28(3), pp.373-388.

[18] Cho, M. and Parmerter, R.R., 1992. An efficient higher-order plate theory for laminated composites. Composite Structures, 20(2), pp.113-123.

[19] Reddy, J.N. and Khdeir, A., 1989. Buckling and vibration of laminated composite plates using various plate theories. AIAA Journal, 27(12), pp.1808-1817.

[20] Jonnalagadda, K.D., Blandford, G.E. and Tauchert, T.R., 1994. Piezothermoelastic composite plate analysis using first-order shear deformation theory. Computers and Structures, 51(1), pp.79-89.

[21] Han, J.H. and Lee, I., 1999. Optimal placement of piezoelectric sensors and actuators for vibration control of a composite plate using genetic algorithms.Smart Materials and Structures, 8(2), p.257.

[22] Oh, I.K., Han, J.H. and Lee, I., 2000. Postbuckling and vibration characteristics of piezolaminated composite plate subject to thermo-piezoelectric loads. Journal of Sound and Vibration, 233(1), pp.19-40.

[23] Li, T., On the formulation of a pipe element for a pipe structure with variable wall thickness. Ocean engineering 117 (2016) 398-410.

[24] Tassoulas, J.L., Karamanos, S.A., Mansour, G.N., Nogueira, A.C., 1997. Finite element analysis of tube stability in deep water. Computers and Structures. 64, 791-807.

[25] Kwang S. Woo, Jae S. Ahn, Seung H. Yang, 2016. Cylindrical discrete-layer model for analysis of circumferential cracked pipes with externally bonded composite materials. Composite Structures. 143, 317-323.

[26] Gergely Czéla, T. Czigánya, 2014. Finite element method assisted stiffness design procedure for non-circular profile composite wastewater pipe linings. Composite Structures. 112, 78-84.

[27] R. Ansari, F. Alisafaei, P. Ghaedi, 2010. Dynamic analysis of multi-layered filament-wound composite pipes subjected to cyclic internal pressure and cyclic temperature. Composite structures. 92, 1100-1109.

[28] Lee, L.-H., Kyriakides, S., Netto, T.A., 2008. Integral buckle arrestors for offshore pipelines: enhance design criteria. Int. J. Mech. Sci. 50, 1058-1064.

[29] Kyriakides, S., Netto, T.A., 2000. On the dynamics of propagating buckles in pipelines. Int. J. Solids Struct. 37, 6843-6867.

[30] MA, D.M., Ma, Z., Zhang, H. and Yao, H.Z., 2007. Hydrodynamic analysis and optimization on the gliding attitude of the underwater glider. Journal of Hydrodynamics (Ser. A), 6, p.005.

[31] Wang, S.X., Sun, X.J., Wang, Y.H., Wu, J.G. and Wang, X.M., 2011. Dynamic modeling and motion simulation for a winged hybrid-driven underwater glider. China Ocean Engineering, 25, pp.97-112.

[32] Shi, P., Kapania, R.K. and Dong, C.Y., 2015. Vibration and Buckling Analysis of Curvilinearly Stiffened Plates Using Finite Element Method.AIAA Journal, 53(5), pp.1319-1335.

[33] Kyriakides, S. and Corona, E., 2007. Mechanics of offshore pipelines: volume 1 buckling and collapse (Vol. 1). Elsevier.

[34] Fried, I. and Malkus, D.S., 1975. Finite element mass matrix lumping by numerical integration with no convergence rate loss. International Journal of Solids and Structures, 11(4), pp.461-466.

[35] Taylor, M.A. and Wingate, B.A., 2000. A generalized diagonal mass matrix spectral element method for non-quadrilateral elements. Applied Numerical Mathematics, 33(1), pp.259-265.

[36] Sprague, M.A. and Geers, T.L., 2008. Legendre spectral finite elements for structural dynamics analysis. Communications in Numerical Methods in Engineering, 24(12), pp.1953-1965.

[37] Sprague, M.A. and Purkayastha, A., 2015. Legendre spectral finite elements for Reissner–Mindlin composite plates. Finite Elements in Analysis and Design, 105, pp.33-43.

[38] Peet, Y.T. and Fischer, P.F., 2014. Legendre spectral element method with nearly incompressible materials. European Journal of Mechanics-A/Solids,44, pp.91-103.

[39] Rekatsinas, C.S., Nastos, C.V., Theodosiou, T.C. and Saravanos, D.A., 2015. A time-domain high-order spectral finite element for the simulation of symmetric and anti-symmetric guided waves in laminated composite strips.Wave Motion, 53, pp.1-19.

[40] Karniadakis, G. and Sherwin, S., 2013. Spectral/hp element methods for computational fluid dynamics. Oxford University Press.

[41] Hughes, T.J., Cottrell, J.A. and Bazilevs, Y., 2005. Isogeometric analysis: CAD, finite elements, NURBS, exact geometry and mesh refinement.Computer methods in applied mechanics and engineering, 194(39), pp.4135-4195.